Nanoporous Transparent Conducting Oxides and New Solid Acid Catalysts

by

Daniel Mieritz

A Dissertation Presented in Partial Fulfillment
of the Requirements for the Degree
Doctor of Philosophy

Approved August 2016 by the
Graduate Supervisory Committee:

Dong-Kyun Seo, Chair
William Petuskey
Pierre Herckes

ARIZONA STATE UNIVERSITY

December 2016

ABSTRACT

New sol-gel routes were developed to fabricate transparent conducting oxide coatings for energy applications. Sol-gel synthesis was chosen because the metal oxide products have high surface area and porosity. Titanium sol-gel chemistry was the main focus of the studies, and the synthesis of macroporous antimony-doped tin oxide was also explored. The surface chemistry and band characteristics of anatase TiO_2 show promise for solar energy purposes as photoelectrodes in DSSCs and as photocatalysts to degrade organic dyes and to split water. Modifying the band structure by increasing the conduction band edge energy is specifically of interest for reducing protons in water. To this end, a new sol-gel method was developed for incorporating Zr-dopant in nanoporous anatase TiO_2. The products follow Vegard's law up to 20 atom%, exhibiting surface area of 79 m^2/g and pore volume of 0.20 cm^3/g with average pore diameter of 10.3 nm; the conduction band edge energy increased by 0.22 eV and the band gap increased by 0.1 eV.

In pursuit of a greener sol-gel route for TiO_2 materials, a solution of $TiOSO_4$ in water was explored. Success in obtaining a gel came by utilizing hydrogen peroxide as a ligand that suppressed precipitation reactions. Through modifying this sol-gel chemistry to obtain a solid acid, the new material hydrogen titanium phosphate sulfate, $H_{1-x}Ti_2(PO_4)_{3-x}(SO_4)_x$, $(0 < x < 0.5)$ was synthesized and characterized for the first time. From the reported synthetic route, this compound took the form of macroscopic agglomerates of nanoporous aggregates of nanoparticles around 20 nm and the product calcined at 600 °C exhibited surface area of 78 m^2/g, pore volume of 0.22 cm^3/g and an average pore width of 11 nm. This solid acid exhibits complete selectivity for the non-oxidative dehydrogenation of methanol to formaldehyde and hydrogen gas, with >50% conversion at 300 °C.

Finally, hierarchically meso-macroporous antimony doped tin oxide was synthesized with regular macropore size around 210 nm, determined by statistical dye trajectory tracking, and also with larger pores up to micrometers in size. The structure consisted of nanoparticles around 4 nm in size, with textural mesopores around 20 nm in diameter.

DEDICATION

Dedicated to the stars and supernovas that created our atoms, so that we may study them.

“For every atom belonging to me as good belongs to you.” -Walt Whitman, Song of Myself

ACKNOWLEDGMENTS

First I must thank my mother who showed me the value of obtaining a PhD by driving 1.5 hours each way to CU Boulder during her 20 hour days. She instilled in people a sense of working in good-faith and maintaining a sense of urgency. Her vision of integrated and community-based public schools lives on with my father who I must thank equally. By his actions he showed me what work ethic is possible, and how to garner relationships by caring about people. Thanks to my sister for being my friend.

I thank Don for reinforcing the values that my parents held, and for showing me how to do science and at the same time how to cross a river in the dark. He showed me how to make time, how to use curiosity to surpass my imagination, and how we can correctly identify our guiding light by playing with numbers. We keep growing through criticism, and what a gift we have in anyone who will spend their energy to push us!

Thanks to Professors Stephen Boyes, John Venables Matthew Liberatore, and to Sifu Daniel Lee Ha, who mentored me and showed me what high quality work is.

My labmates who were my family in charting new territory in materials science, and who took me around the world with their presences, discussions, languages and cuisines: Dinesh Medpelli, Ki-Wan Jeon, Alex Volosin, Danielle Ladd, Jung-Min Seo, Taisiya Skorina, Milad Mesgar, Ebi, Barun Das, Adéle Renaud, Shaojiang Chen, Shanika Abeysooriya, Haojie Zhang, Runli Liang, Timur Boskalio, Carlos Hernandez.

Nicholas Spencer, Chris Potts, Brenton Hammer, George Chang, and my classmates.

TABLE OF CONTENTS

Page

CHAPTER

APPENDIX

LIST OF TABLES

Table Page

LIST OF FIGURES

Figure Page

Figure Page

Figure Page

Figure Page

Figure Page

Figure Page

CHAPTER 1

INTRODUCTION

1.1 Classification of Porous Materials

By definition, a pore is a minute opening in a material,[1] although the size is not specified by the definition. Since size is relative, we may consider a 'minute' size from different perspectives. For example, rivers or highways may appear minute from high above in an airplane, and capillaries can appear relatively large to a red blood cell. However, the function of these 'pores' is to facilitate diffusion, whether it is water or traffic or nutrients. Pores appear in everyday life in many ways; we experience the wicking power of capillary action as water is drawn in by a sponge or by wood, or by the soil. Pores in biology are ubiquitous, from membrane proteins controlling the traffic in and out of cells to skin pores to blood veins that that branch from arteries to vessels to capillaries. This latter example is especially illustrative to highlight the facility of a hierarchical pore structure, where a high flowrate through the large arteries eventually feeds the capillaries that have a high surface. The high surface area is important to allow molecular diffusion between blood and the surrounding cells, and a similar phenomenon is observed with our lungs in that the alveoli provide a high surface area that allows oxygen to diffuse into our blood at a sufficient rate. As both controlling mass transport kinetics and achieving a high surface area are essential in technology, imparting an effective pore structure to a material is of significant interest.

Pore size regimes are generally divided into three categories, micropores, mesopores and macropores, each of which presents unique properties for a wide range of applications based on tailoring their pore properties. Smaller than 2 nm, micropores present the highest specific surface area to materials, and are most frequently referenced for zeolites[2] (BET surface area > 1000 m^2/g)[3] and metal-organic frameworks (BET surface area ~ 2000 m^2/g)[4]. Mesopores are defined as between 2 nm and 50 nm, and in this pore regime both high surface area and generally sufficient diffusivity are co-present, and the material may be transparent or highly translucent.[5] Macropores, which are larger than 50 nm, provide adequate mass transport kinetics for larger molecules, such as biomacromolecules like proteins and DNA origami structures, and reduce the translucency of the material. Larger pores have been called gigapores,[6] and are often present in porous polymers.[7] There may also be the presence of pores with a multimodal distribution, which is the characteristic of a hierarchically porous material. For instance, the micropores of zeolites are often largely inaccessible due to the slow diffusivity, although introducing mesopores to the microcrystalline zeolites shows vast improvements in performance because the internal microporosity can be utilized.[8-14] Macroporous materials can also benefit from the copresence of mesopores to increase the specific surface area of the materials.[9,15-20]

In addition to the size of the pores, their connectivity and morphology are also important factors to consider based on the desired applications. Some pores may be isolated from other pores, which are called closed pores and serve to reduce the density and increase the buoyancy and resistance to heat transfer through the material. However, closed pores are to be avoided when diffusivity through the pores is important. Another type of pore morphology that is partially blocked or only accessible by a narrow neck is called 'ink-bottle', and is associated with sub-optimal diffusion.[21,22] Open pores are required to sustain the performance for applications that rely on sufficient diffusivity. In these cases, the pores may have various types of connectivity, which is also related to the pore ordering or periodicity. Ordered pores have predictable size, shape and connectivity, and may be spherical pores from an opal template[23,24] or emulsion template,[25,26] or a bicontinuous network of pores generated by spinodal decomposition,[27] or from a self-assembled surfactant template which is often a diblock[28-30] or triblock copolymer.[31] Although materials with ordered pores may exhibit the best diffusivity according to certain models,[32,33] it was also indicated that the pore ordering was a minor contributor to the diffusivity through the pores.[32] In another case, the pores may be random in nature, and may be well-connected. Although the rigid control over pore connectivity is not achieved for these materials, average pore size and fractional porosity can be controlled in random porous materials by modifying the synthetic conditions. Self-assembly is an initial step when synthesizing the templates for ordered porous materials, and the uniformity of the morphology is strongly dependent on the synthetic conditions. The time and resource intensive nature of synthesizing ordered porous materials that may reduce the scalability, as well as the high sensitivity to reaction conditions that may reduce the reproducibility, made random porous materials the target of the sol-gel routes that we designed.

Figure 1 shows a chart with scanning electron microscope and transmission electron microscope images of porous materials. The images are positioned according the pore size along the *x*-axis which is logarithmic and the images are labeled by their material and with a scale bar. The first image shows the intracrystalline micropores of MFI zeolite.[34] The following examples of mesoporous micron-sized particles of Sm_2O_3,[35]

TiO_2,[36] Bi_2WO_6,[37] $MgCo_2O_4$,[38] $NiCo_2O_4$,[39] Mn_2O_3,[40] and Co_3O_4[41] were chosen to emphasize the range of metal oxides that have been synthesized as well as the range of novel morphologies. Specifically, mesoporous micron-sized particles are of interest because as they pack together, the interparticle voids form macropores; the resulting hierarchically meso-macroporous material may potentially be applied as a coating by making a paste with the particles. SiO_2 with three pore size regimes is shown,[42] and the macroporous VO_x,[43] Fe_2O_3,[44] MgO,[45] and Bi_3NbO_7[46] and electrospun $La_{0.6}Sr_{0.4}Co_{0.2}Fe_{0.8}O_3$[47] also have a meso-macroporous hierarchy. CuO[48] and $CoMn_2O_4$[49] hollow micron-sized particles with mesoporous walls introduce intraparticle macropores in the hierarchical meso-marcoporous pore network. Freeze-cast Al_2O_3[50] has the largest average pore size shown on the chart.

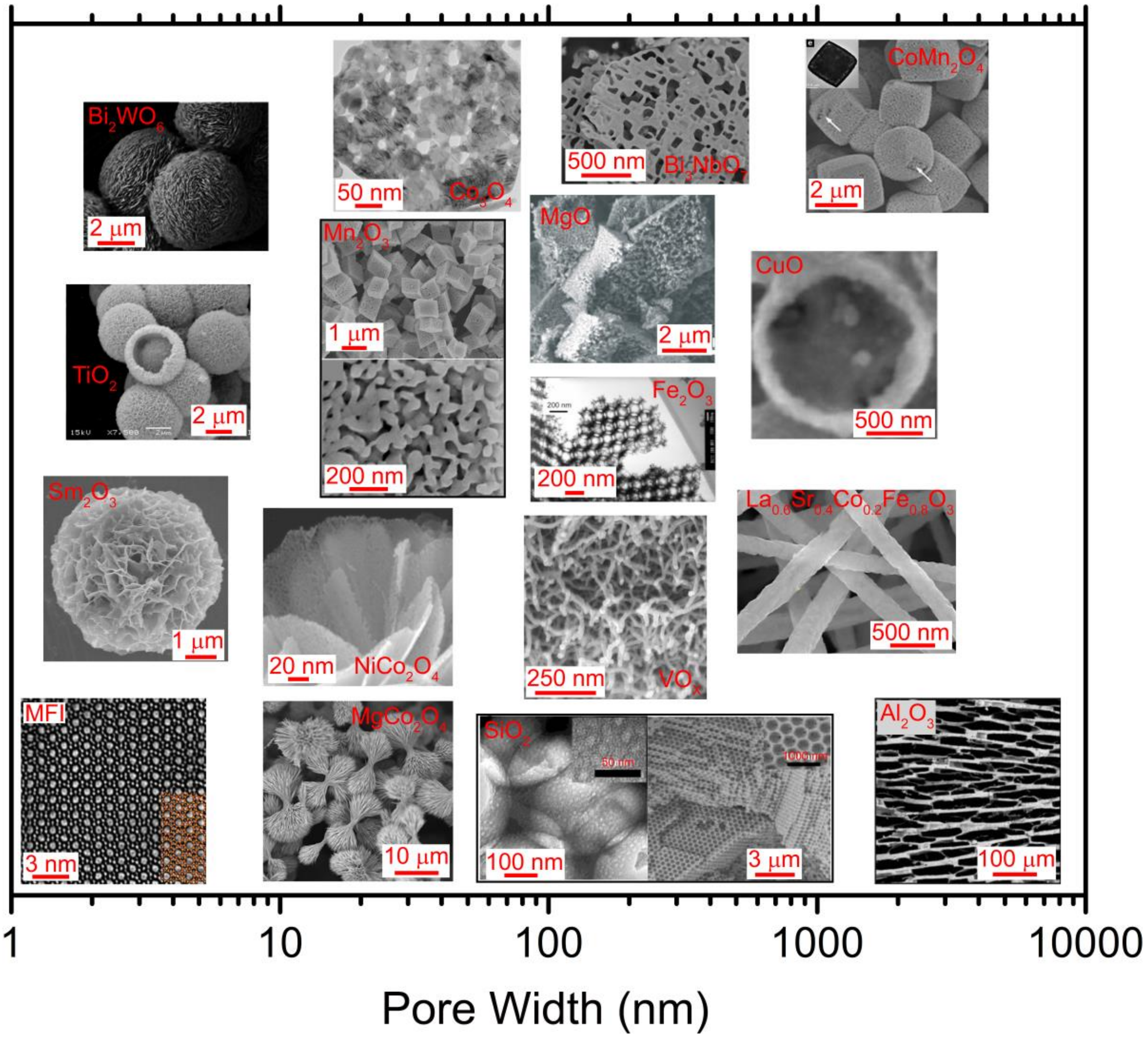

Figure 1. Some examples of porous metal oxides previously reported in the literature, including pore sizes ranging from micropores to macropores; the images are roughly aligned along the *x*-axis with their respective pore sizes. See the text for references.

Nanoporous materials can be synthesized by a wide range of techniques to impart controlled pore characteristics to the material. While a wide range of pore morphologies has been achieved for the monolithic and powder compounds, their application as films or coatings on glass is of particular interest because of the electrochemical interface that can be achieved with conducting materials. However, depending on the applications, synthesis of porous coatings on glass is limited by several factors including the ability of the porous material to make a uniform coating that adheres to the surface, and the maximum calcination temperature (~600 °C).

Figure 2 is a diagram showing electron microscopy images of some reported porous metal oxide films and coatings on glass substrates, arranged according to their pore width. Most images have two parts, which are the cross-section of the coating (bottom) and a top-view of the coating (top); otherwise, the cross-section is shown. While the free-standing metal oxides show a wide variety of compositions, porous coatings on glass have mostly been fabricated from conducting compounds to use as electrodes in applications such as electrochemistry and photovoltaics. One exception shown is the NaA zeolite membrane[51] which has micropores and is free of cracks or pinholes to be effective as a gas separation membrane. Mainly, other compounds shown are the conducting antimony-doped tin oxide (ATO),[52-56] tin-doped indium oxide (ITO)[57] and TiO_2.[58,59] Also shown are examples of SnO_2[60] which may be an electrode for water oxidation, and of V_2O_5[61] which is an electrochromic material. Mesoporous coatings of ATO have a random pore structure, while V_2O_5 exhibits ordered mesopores. The ordered macropores of the meso-macroporous ATO with an average width around 300 nm, and of TiO_2 with an average width around 2 μm, were fabricated by the only reported method for meso-macroporous coatings on glass with ordered macropores, which is by using self-assembled opal templates. Self-assembled polymer microbeads were also used to template the ITO coatings,[57] although their macropores are not ordered due to the shrinking and cracking of the coating, leading to disorder of the pores. In another example, large macropores were introduced to the TiO_2 coating by electrospinning.[59]

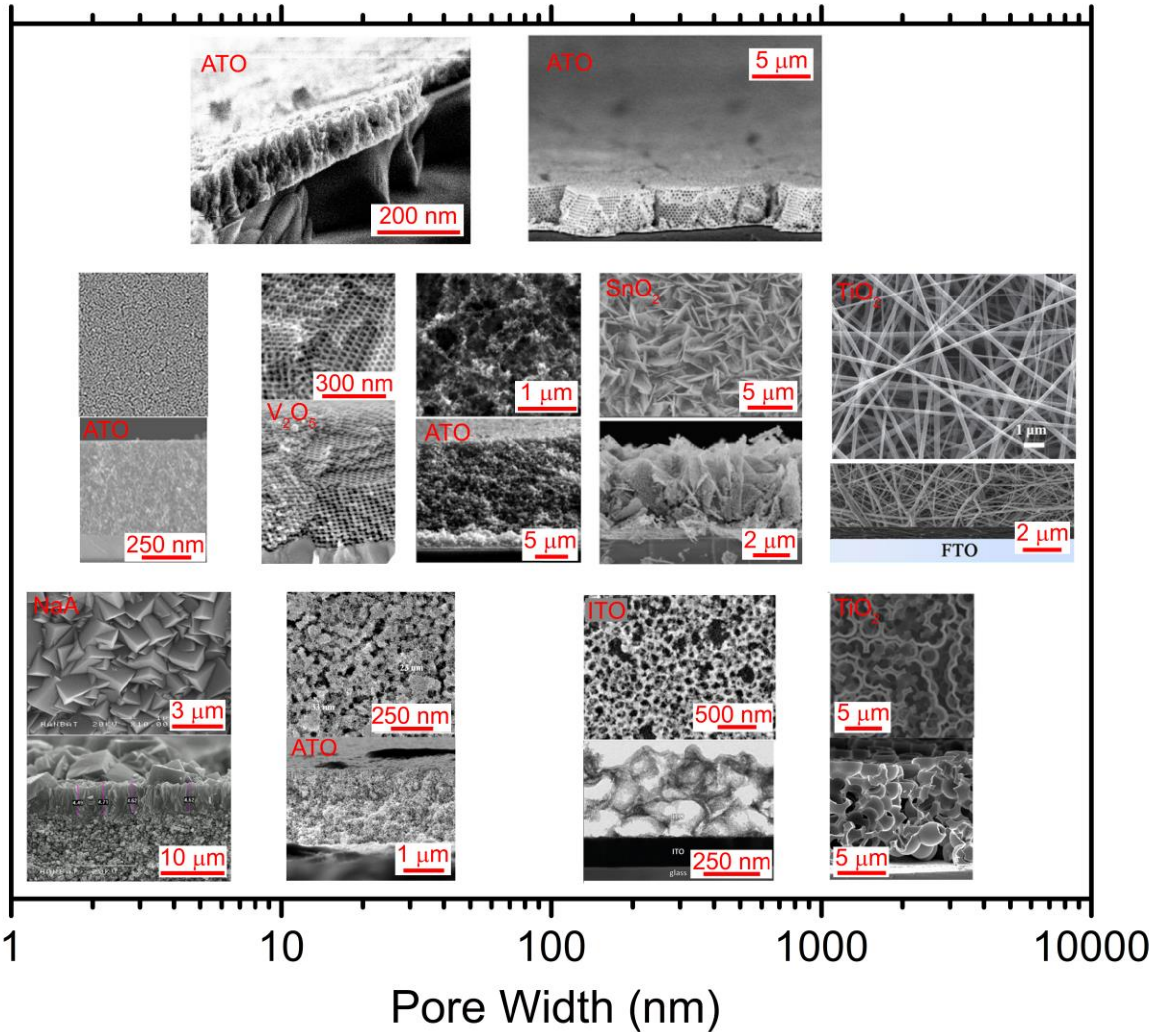

Figure 2. Porous metal oxide coatings on glass substrates (except NaA); the images are roughly aligned along the *x*-axis with their respective pore sizes. See the text for references.

1.2 Synthetic Methods for Porous Materials

Porous materials can be used as catalysts,[2,62] separation media,[2] thermal insulation,[63,64] biomedical scaffolds for tissues,[7] collecting space dust,[65] sensors,[66] chemical storage (i.e. H_2, CH_4),[67-70] supercapacitors,[5,20] battery materials,[5,71,72] templates,[73,74] and fuel cells.[5,75,76] Regarding the properties of porous metal oxides, it is especially important to consider about the details of their synthesis. Fabricating the porous metal oxides as films or coatings allows them to be used as electrodes.

Specifically, making the porous films and coatings on glass enables transparent electrodes that can be employed in devices such as solar cells,[5,77,78] sensors,[79,80] and protein electrochemistry.[57,81-85] Higher surface area provided by smaller pores is utilized by species that have adsorbed to the surface, however sufficient diffusion kinetics through the pores is also necessary both for the accessibility of the surface sites and for the removal of desorbed species such as products of catalysis. While fast mass transport rates and high sorption capacity are essentially mutually exclusive for a porous material, balancing the highest surface area and diffusivity is a central problem to address when designing porous materials. Therefore, developing synthetic methods that provide control over the pore characteristics is important for achieving the best performance.

In a solution-based synthetic route of porous materials, solids are formed from a solution of molecular precursors, and their unique properties are being exploited for existing and emerging technologies. While closed pores are suited for applications such as floatation and thermal insulation, where the air or vacuum in the pores act to reduce the overall density and to resist heat transfer, 3D openly connected pores allow for mass transport through a solid. Porous polymers are also synthesized by solution-based methods, but the focus of further discussion will be specifically on the synthesis of metal oxides. One distinguishing aspect between polymers and metal oxides from solution is that the metal oxides generally have a high specific surface area due to the nanoscale texture whereas polymers are often relatively smooth on the nanoscale. While the porous network should provide for good mass transport, the solidity of the material must be retained.

Metal oxides found in nature are generally mechanically robust and chemically stable in air up to relatively high temperatures, and are often colored and strongly absorbing. Additionally, the high electronegativity and charge density of the oxide ligand cause a strong interaction with the metal centers, generally leading to semiconducting materials. Oxygen generally makes ionic bonds with metals, in which the compound's valence shell is the O 2p that is fully occupied, leaving the conduction band for the charge carriers. In some cases, especially for d^{10} metal centers, the valence shell may be at a similar energy as the O 2p electrons, and the holes associated with d^9 centers such as Cu^+ will be the charge carrier acceptor and donors.[86]

A wide range of metal oxides are available from the periodic table, and each has not only a unique electronic structure, but also a unique synthetic behavior. As the simple metal oxides have been well studied, the metal oxide compounds that comprise more than one metal element are being explored actively in current literature reports. These include doped metal oxides and mixed metal oxides. Doped metal oxides are those that have the same crystal structure as the native oxide, however a fraction of the metal cations are replaced by another metal which is the dopant. In contrast, mixed metal oxides are those which form a new structure or stoichiometry that would not be formed by the native metal oxide. Each mixture of metal oxides will produce a different binary phase diagram. The line compounds from these phase diagrams are generally crystalline and with a unique composition, and therefore will have a unique set of properties. Compounds with the same stoichiometry but different compositions often form the same crystal structures, such as delafossites ($M^IM^{III}O_2$), spinels ($M^{II}M^{III}_2O_4$) and perovskites ($M^{II}M^{IV}O_3$). Different polymorphs can also have disparate properties, for example cubic

$LiCoO_2$ showed better electrocatalytic activity than the layered rhombohedral $LiCoO_2$ that leached Li^+ to a larger extent during the experiment.[87] During the synthesis of doped and mixed metal oxides, the compositional homogeniety is a crucial synthetic parameter to achieve in order to realize the desired properties of the target compounds.

Due to our interest in designing procedures that utilize green chemistry, we used aqueous solvent systems. Water itself is an important ligand, and can solubilize polar and charged species. Since oxide in water is usually the most negative species of any solute/solvent, it will generally replace ligands such as chloride, nitrate, or other organic species with nitrogen or oxygen. Specifically, metal cations will be chelated by the oxide of water to form aquo-complexes. As the oxide of the -aquo ligand is polarized by the metal cation, it may be hydrolyzed to produce an acidic proton while reducing the overall charge of the metal complex (**eq. 1**). The remaining hydroxo- ligands are prone to react with neighboring metal complexes to expel a water molecule, thus forming a bridging oxide **(eq. 2**).

$$\mathrm{M(OH_2)_6}^{n+} + \mathrm{H_2O} \rightarrow \mathrm{M(OH_2)_5(OH)}^{(n-1)+} + \mathrm{H_3O^+} \qquad \textbf{eq. 1}$$

$$-\mathrm{M}-\mathrm{OH} + -\mathrm{M}-\mathrm{OH} \rightarrow \mathrm{M}-\mathrm{O}-\mathrm{M}- + \mathrm{H_2O} \qquad \textbf{eq. 2}$$

Different species undergo hydrolysis to different extents, as a function of the pH. The hydrolysis ratio (h, $[H^+_{Hyd}]/[M_{Tot}]$) of an aquo-metal complex is given by **eq. 3**.[88] Here, the concentration of protons due to hydrolysis is a function of the metal concentration ($[M_{Tot}]$), the electronegativity of the meal (χ^*_M), the charge of the metal ion (z), and the coordination number of the metal complex (N). The various terms essentially describe the partial charge remaining on oxygen after electronegativity equalization, which directly controls the ratio between oxo-, hydroxo- and aquo- ligands in an aqueous system.

$$\frac{[\mathrm{H}^{+}_{Hyd}]}{[\mathrm{M}_{Tot}]} = h = \left[\frac{1}{1+0.41\mathrm{pH}}\right]\left[(1.36z - \mathrm{N})(0.236 - 0.08\mathrm{pH}) - \frac{(2.621 - 0.02\mathrm{pH} - \chi^{*}_{M})}{\sqrt{\chi^{*}_{M}}}\right] \qquad \textbf{eq. 3}$$

In water, there are two main reactions that lead to condensation. Olation occurs when an aquo-ligand hydrogen bonds to an adjacent metal complex with a hydroxo-ligand. This creates a bridging $(O_2H_3)^-$ ligand, and the condensation reaction (**eq. 4)** occurs as water leaves to produce a bridging –OH ligand.[88] Where a metal center has hydroxo- but not aquo-ligands, it may undergo condensation by oxolation (**eq. 5**) which proceeds by forming hydroxyl bridged metal centers followed by the proton transfer from the bridging hydroxyl to an adjacent hydroxo-group to form an aquo- ligand that leaves as water. Smaller and more highly charged metal ions, with higher hydrolysis ratios, are prone to condense by oxolation reactions. Hydrolysis leads to a decreased pH due to the elimination of acidic protons from the aqueous coordination sphere around metal centers. The dissolved species are positively charged in acidic conditions, and negatively charged under basic conditions. However, the concentration of zero-charge precursors can be increased by controlling the pH. For example, as the pH increases in an acidic solution of metal cation complexes, the formation of condensed species will proceed.[89] The pH and metal will decide whether olation or oxolation will predominate.

$$-\mathrm{M}-\mathrm{OH}+\mathrm{M}-\mathrm{OH}_2 \rightarrow \mathrm{M}-\mathrm{OH}-\mathrm{M} + \mathrm{H}_2\mathrm{O} \qquad \textbf{eq. 4}$$

$$-\mathrm{M}-\mathrm{OH}+\mathrm{M}-\mathrm{OH} \rightarrow \mathrm{M}-\mathrm{O}-\mathrm{M} + \mathrm{H}_2\mathrm{O} \qquad \textbf{eq. 5}$$

Figure 3 has 5 regions, *I* – *V*, divided by lines drawn with respect to the electronegativites of the metals. The points labeled by the elements represent the behavior of zero-charge precursors of their ions with aquo- and hydroxo- ligands. The line that defines region *I*, labeled as χ_B, represents the electronegativity of the metals where the zero-charge precursor will be strongly basic and exist as a monomeric species. This solubility is due to the relatively low positive charge and electronegativity of the metal ions, that do not polarize the oxide of aquo-ligands enough to cause them to dissociate, such as NaOH and $Ba(OH)_2$. Similarly, the zero-charge precursors will remain as soluble monomers above the boundary χ_A. However, in contrast to region *I*, the cations have both high charge and electronegativity, and the highly polarizing species will form strongly acidic and soluble oxoanions by completely hydrolyzing aquo-ligands, and further dissociating the hydroxo-ligands, for example H_2SO_4 and $HClO_4$. There are colored boxes around six elements in **Figure 3** that indicate the element groupings of interest in the various chapters in this thesis: Zr and Ti in green for $Zr_xTi_{1-x}O_2$, Sn and Sb in purple for $Sb_xSn_{1-x}O_2$ and P and S in red for $H_{1-x}Ti_2(PO_4)_{3-x}(SO_4)_x$.

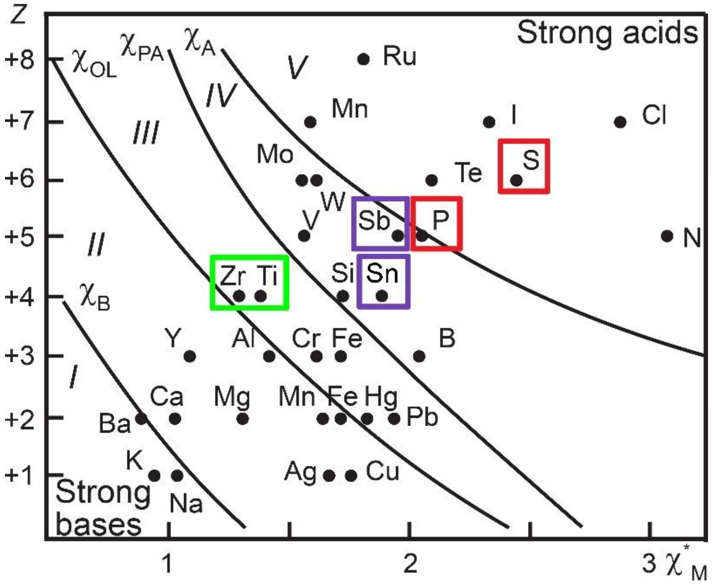

Figure 3. Electronegativities of metals vs. their cationic charges, with contour lines that approximate their dominant condensation reaction types (adapted from Jolivet).[88]

The condensation reactions between molecular precursors are dependent on the types of ligands in the coordination sphere, which are determined by the type of metal and by the pH in an aqueous solution. Electronegativity of the metal affects the magnitude of negative charge on the chelating oxides, which along with the pH (indicative of the activity of protons in solution) determines the speciation in the coordination sphere between aquo-, hydroxo- and oxo- ligands. Above the line χ_B, the cations cause hydrolysis of the aquo-ligands, because the higher charge and electronegativity polarize the oxide of the aquo-ligand enough that the proton affinity is lower than that of water. As water abstracts a proton from the species, the –OH ligand is formed that can undergo condensation with an intermolecular –OH ligand. In region *II*, the condensation reactions generally happen by the entire aquo-ligand leaving, and the upper bound for region *II* is the line χ_{OL} at which the aquo-ligands exhibit zero charge. In this region, compounds such as $[Al_2(OH)_2(OH_2)_8]^{4+}$, $[Al_4O(OH)_{10}(OH_2)_5]^0$, and

$[Al_4(OH)_{12}(OH_2)_4]^0$ may form. Region *III* is bounded by χ_{OL} and χ_{PA}, where the line χ_{PA} represents the line along which hydroxo-ligands will have a zero-charge in the zero-charge precursor. In this region, the condensation reactions can take place both by olation and by oxolation, between species such as $[(TiO)_8(OH)_{12}]^{4+}$,[90] $[Zr_4(OH)_{16}(OH_2)_8]^0$ or $[Zr(OH)_2]_2^{4+}$.[91] In region *IV* whose upper bound is χ_A, the high charge and electronegativity of the metal centers are strongly hydrolyzing, and aquo-ligands are unstable. Therefore, oxolation occurs in this region forming species such as $[V_{18}O_{42}]^{12-}$.[92] The various colored boxes correspond to the elements used in the various synthesized samples that will be discussed later in detail. While the lines in **Figure 3** are for zero-charge precursors with an aqueous coordination sphere, the solution-based synthetic conditions are highly tailorable with various cosolvents and additives to control the hydrolysis and condensation chemistries.[93]

Since the solids begin to form at the molecular level, the formation of nanoparticles is an inherent step of solution-based routes. In addition to the metal center's electronegativity and oxidation state, factors that affect the ligands in the coordination sphere include the solvent system, pH and temperature of the solution and other additives.[88,93] By controlling these synthetic factors, dispersions of nanoparticles have been synthesized with a high degree of control over the composition,[94-98] morphology[94,98-100] and surface properties.[101,102] These modifications can lead to beneficial properties such as high specific surface area,[95] unique surface chemistry,[100,103] size-dependent and dimensionality-dependent electronic properties[104] and the stabilization of certain crystal structures[105-108]; they also have distinct drawbacks including their difficulty to separate from the dispersant, often requiring centrifugation,[109,110] and poorly characterized environmental and health risks which may be severe, tied to the tendency of their readily becoming airborne or dispersed in water.[111,112] These risks can be mitigated while retaining the benefits of nanoparticles when the high surface are is presented as an internal surface area of a nanoporous material. Such nanoporous materials can generally be synthesized by controlled aggregation of nanoparticles,[30] and therefore the same synthetic factors can be manipulated to control the properties of porous materials as for nanoparticles.

Several synthetic methods have been successful for producing mixed metal oxides from aqueous solutions, and popular methods include hydrothermal, co-precipitation, Pechini method and sol-gel chemistry. Hydrothermal synthetic routes are carried out in an autoclave, and the high temperature and often extreme pH conditions facilitate an equilibrium condition that favors dissolution of the precursors and crystallization of the target phase according to Ostwald's rule.[113] Larger particles grow at the expense of smaller particles.[114] Therefore, high surface area materials are usually not synthesized by hydrothermal routes.

Co-precipitation is generally carried out by adding a base solution containing NH_4OH or NaOH to an acidic solution of metal salts. Precipitates rapidly form as amorphous metal oxy-hydroxides in the location of base addition, which are separated from the supernatant and subjected to thermal treatment for dehydration and crystallization.[88,98] In both hydrothermal and co-precipitation routes, the phase separation of solids from the supernatant may cause a different elemental ratio in the solids, and absolute compositional control is generally not achieved. Pechini routes generally use aqueous precursor solutions containing ethylene glycol and metals stabilized by citrate ligands.[115] Subsequent thermal treatment to induce the condensation polymerization between citrate and ethylene glycol creates a hard solid with uniformly distributed metal ions that yields oxide nanoparticles after calcination along with porous pieces. In the context of this thesis, sol-gel chemistry occurs when a precursor solution forms a homogeneous gel that occupies the entire volume of the precursor solution.[116] It is noteworthy that the Pechini route can be modified to achieve more desirable porous materials and even to apply coatings of porous metal oxides,[117] although at what point the modified Pechini route becomes more sol-gel-like is a gray area.

Although they are often referred to as sol-gel, possibly due to the fact that they form high-surface-area and nanostructured products, the co-precipitation and Pechini methods have synthetic steps that distinguish them from sol-gel chemistry. The procedure for co-precipitation can be applied to a wide range of metal ion solutions, although the products are relatively dense compared to sol-gel products, and the compositional uniformity is not ensured. The Pechini route is also robust in that it can be applied to synthesize a wide range of mixed metal oxides, however there is a low extent of sintering of the citrate-capped particles rather than a pre-formed porous network, and the generation of gasses as the polymer matrix decomposes may break up the delicate porous structure. Advantages of sol-gel derived products include the wide range of synthetic condition options that provide a high degree of flexibility, the high surface area and porosity, the ability to adjust the pore characteristics, the homogeneous distribution of the precursors in the gel, as well as a wide variety of processing options of the gel.

Sol-gel chemistry can be explored by finding conditions under which the volume-filling gel is formed.

1.2 Sol-Gel Synthetic Route for Porous Metal Oxides

Gelation occurs when a fluid solidifies. Various areas in the literature adhere to a different definition of what a gel is. In a liquid, the phase transition from fluid to solid is one depending on particle connectivity rather than a thermodynamic transition, where the strength of the interaction between the particles (U) and the volume fraction of solids in the liquid (ϕ) are main determiners for the gelation behavior.[118] **Figure 4a**[119] depicts this gelation behavior, where the black line indicates the transition from a fluid to solid. Even when the particles are non-interacting, gelation occurs as ϕ approaches ~ 0.58 due to the arrested dynamics of nanoparticle diffusion.[118] At low ϕ values, gelation can still occur with the high interaction parameter between the nanoparticles, as clusters grow with fractal dimensions. One illustration of the gel transition is shown in **Figure 4b**,[118] where the black curve shows the conversion of epoxy monomers with time, shown with images of the epoxy at various times of reaction. The liquid phase is a dispersant to the growing clusters, and a network is suddenly formed that pervades the entire volume. This liquid with a continuous network of solids is a gel. As may be expected from hydrous metal oxide nanoparticles, the surface interaction between neutral particles may be quite strong due to hydrogen bond interactions. However, a surface charge that is associated with the pH of solution can counteract the attractive interaction between the particles.

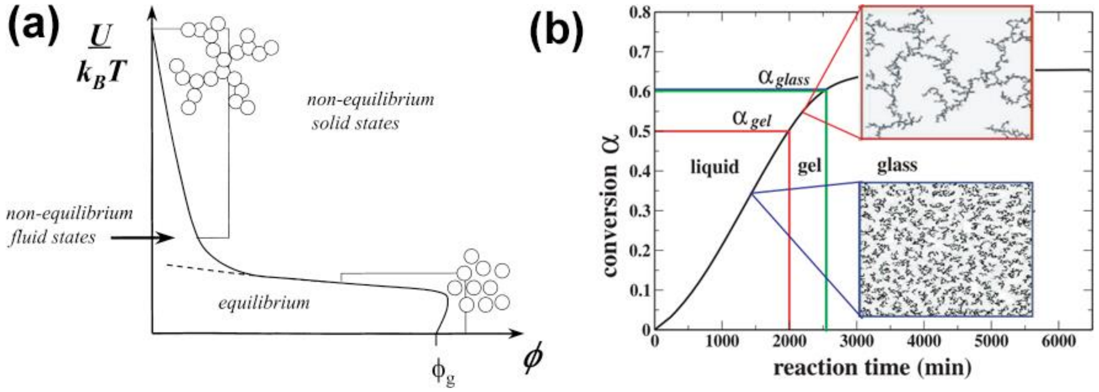

Figure 4. a) Sol particle packing density vs. surface interaction strength, illustrating the connectivity of the sol particles in different regimes (adapted from Trappe *et al.*).[119] b) The gel transition is illustrated by images, and the curve shows how conversion increases with reaction time, and at what point gelation occurs (adapted from Zaccarelli).[118]

During sol-gel chemistry, the initially soluble molecular precursors slowly become insoluble either by forming zero-charge precursors or by losing their stabilizing ligands. Condensation reactions between the insoluble metal complexes produce sol nanoparticles, which reduce the surface area to reduce the surface free energy, γ (**eq. 6**). As nanoparticles tend to aggregate to minimize their surface energy, so will the sol dispersion destabilize. However, by adjusting the conditions while maintaining homogeneity, for example by increasing the pH or by decomposing the stabilizing ligands or capping agents, the solidification can suddenly pervade the entire volume at once. Formation of the insoluble species can be controlled in various ways. Increasing the pH can lead to forming zero-charge precursors, and this can be accomplished uniformly throughout the volume by using organic species such as epoxides that act as an acid scavenger. For example, since the reaction rate of propylene oxide with acids is relatively slow compared to dissolved $NaOH_{(aq)}$ or $NH_4OH_{(aq)}$, it can be completely solvated before the reaction proceeds to a significant degree,[43,89,120] and can be further slowed by using an epoxide with an electron-withdrawing group such as chloride in epichlorohydrin.[121] Another way to increase the pH uniformly is by including a solute that can generate base *in-situ* such as urea that will react with water to form ammonia.[117] Aside from controlling the pH, gelation can be induced by removing ligands that stabilize the metal species in solution, for example peroxo-ligands can be decomposed with mild heating.

$$\gamma = (\partial G/\partial A)_{n,T,P} \qquad \textbf{eq. 6}$$

Different types of condensation reactions can take place based on the chelating species, as is well-known for the hydrothermal synthesis of zeolites with amine-based structure-directing agents.[122] Also, with limited to no water for hydrolysis, alcohols may be a leaving group during condensation reactions; for example titanium *n*-butoxide will react to form dimers and cyclic trimers in *n*-butanol, where *n*-butanol is the leaving group.[123,124] Part of the tendency to form dimers and trimers is to increase the coordination number around the metal center, which is only 4 for the monomeric metal alkoxide precursor but is most stable as 6. In the presence of water, hydrolysis and condensation take place, although the condensation can be decoupled from the hydrolysis reactions by providing sufficient acidity.

In both aqueous metal cation solutions and in metal oxide compounds, due to the ligand field stabilization energy, many metal centers are most stable when they are octahedrally coordinated by oxide ligands as MO_6. However, in solution the MO_6 exist as molecular species with various degrees of hydration, where the oxide may exist as an aquo-ligand ($-OH_2$), hydroxo-ligand (-OH) or oxo-ligand (=O), whereas oxide ligands bridge the metal centers in solid metal oxides. Metal oxides, and specifically mixed metal oxides, will exhibit the desired properties only when the distribution of metal ions is uniform throughout the solids.[125] Brownian motion guarantees that the distribution of soluble species will be homogeneous on the atomic scale. Since the soluble metal ions are already uniform in the gel on the molecular level, and their octahedral coordination is roughly the same in the gel and in the metal oxide, only a minimum thermal treatment is required to achieve an atomically homogeneous composition.

After gelation, we generally want to remove the solvent without disrupting the open pore structure of the wet gel. This presents a challenge because solvent removal coincides with pore collapse due to capillary pressures exerted on the pore framework at the liquid-vapor interface. The capillary pressure (p_c) is the result of a higher interfacial energy between the solid and vapor compared to that between the solid and liquid,[126] and can be expressed in **eq. 7**, where the surface energy at the liquid-vapor interface is given by γ_{LV}, θ is the contact angle, and r_P is the radius of the capillary pore.[127] Since the hydrous metal oxide gels are typically hydrophilic, the interfacial energy between polar solvents and the gel surface will be especially low and will produce a pronounced meniscus. Nanopores wick the fluid quickly, and since the wicking action is the result of a strong interaction between the liquid and the solid surface, drawing the liquid into the capillary exerts an inward stress on the pores which can cause them to collapse.

$$p_C = \frac{2\gamma_{LV} cos\theta}{r_p} \qquad \textbf{eq. 7}$$

The solvent removal and subsequent processing strongly affect the morphology and pore characteristics of the final product. Gels can be molded into virtually any shape, although ageing may cause the gel to shrink while it retains that shape.[128] However, cracking attributed to the different capillary forces on pores with different radii can be a difficult problem to overcome without supercritical solvent removal.[129,130] Films and coatings can be fabricated without cracking and peeling,[129,131,132] due to the resistance to lateral shrinkage provided by the substrate. In other sol-gel processes, components can be added to the sol including: 1. Those which may modify the properties of the liquid before gelation, for example the viscosity for producing self-standing coatings, 2. Those which may be used to control or preserve the pore structure such as multi-block copolymer surfactants[31,133] or condensation polymers,[43,134] 3. Those which may impart additional porosity as sacrificial templates such as polymer beads, silica beads or carbon black,[23,24,135,136] 4. Those which may be functional components in the final product, for example rutile nanoparticles in DSSCs to facilitate better absorption,[33,137] 5. Other components that will dissolve in the solution for exploratory syntheses, for example phosphoric acid or boric acid, that will not be removed during calcination. After the gel formation, ageing typically occurs as condensation reactions continue to expel water and cause shrinkage of the gel structure. Ageing conditions can be an important aspect in the synthetic procedure, because the connectivity between nanoparticles increases which translates to higher mechanical strength and conductivity of the final gel products, and can also improve the final porosity by preventing pore collapse.[138] Subsequent solvent removal has been carried out by various methods, some of which are described in more detail in **Section 1.4**.

Depending on the metal species and the desired porosity and crystal structure, calcination temperatures ranging between 450 and 900 °C are typically used for dehydration and crystallization of the gel products. This is in contrast to traditional solid-state routes that take place at higher temperatures (~1000 °C) to allow for atomic diffusion, when the precursors are initially mixed on the macroscale. These solid-state routes generally result in dense materials. A major limitation for these solid-state routes is that they are poor for synthesizing porous materials with a high surface area. Exploration of new solution-based synthetic routes for porous metal oxides was carried out with green chemistry in mind. The green aspects include that high calcination temperature is avoided, and that the procedures are generally scalable and can be carried out in water and biorenewable alcohol solvents.

1.3 Sol-Gel Chemistry of Titanium and Tin

Titanium dioxide has been the subject of heavy study especially since it was first shown that water splitting occurs at the surface under UV illumination,[139] and for dye-sensitized solar cells (DSSCs).[140] SnO_2 is also of interest for water splitting as a water oxidation catalyst,[141] and as a parent oxide for doping with Sb^{5+} for fabricating transparent conducting oxides (TCOs).[134]

Sol-gel methods that used precursors containing Ti^{4+} (75 pm) and Sn^{4+} (83 pm) were investigated. While the ions have the same charge, one reason that their aqueous chemistries are unique is due to the size difference. Fajans' rules suggest that the small and highly charged Ti^{4+} cations will interact strongly with the hydrous ligands, while the bonds between the larger Sn^{4+} cations and hydrous ligands will show more covalent character.[142] In addition to the ionic size and charge, the electronic configuration can be used to understand the differences in the chemical behavior, as Ti^{4+} is $3d^0$ and Sn^{4+} is $5p^0$. Also, the different electronegativies contribute to determining the reactivity with water.

Furthermore, the synthetic conditions that achieve gelation will be affected differently by criteria including the solvent, pH, additives, concentration, and conditions during drying and calcination. The conditions under which the proper gelation takes place are disparate for the two metal systems which may be understood by their chemical identities.

In water, Ti^{4+} mainly undergoes oxolation reactions unless the conditions are highly acidic. These oxolation reactions are hardly reversible,[88] indicated by the forward reaction arrows in **eqs. 8** and **9**, and the chemical reaction will proceed to the products as water is added, due to the formation of hydrolyzed Ti species that react with each other by oxolation. On the other hand, the solution of Sn^{4+} is stable at pH ~ 2,[134] and while it undergoes oxolation reactions due to the high electronegativity and charge, olation reactions also occur due to its large size[88] in addition to oxolation reactions. Since the bonds formed by olation are more labile than those formed by oxolation, the equilibrium exists between condensed and hydrolyzed species and is indicated by the right-left harpoon arrows in **eq. 10** and **11**. So, in the case of aqueous tin chemistry, the gelation can be slowed by adding water according to LeChatlier's principle.

$$\mathrm{Ti(OBu)_4 + 6\ H_2O \rightarrow Ti(OH_2)_2(OH)_4 + 4\ BuOH} \qquad \textbf{eq. 8}$$

$$\mathrm{2\ Ti - OH \rightarrow Ti - O - Ti + H_2O} \qquad \textbf{eq. 9}$$

$$\mathrm{SnCl_4 + 6\ H_2O \rightleftharpoons Sn(OH_2)_3(OH)_3 + 4\ HCl} \qquad \textbf{eq. 10}$$

$$\mathrm{Sn - OH + Sn - OH_2 \rightleftharpoons Sn - OH - Sn + H_2O} \qquad \textbf{eq. 11}$$

TiO_2 made by sol-gel protocols generally exhibits the anatase crystal structure ($\rho_{anatase,TiO2}$ = 3.89 g/cm^3)[143] which is depicted in **Figure 5a**. Due to the Ostwald step rule,[144] formation of anatase occurs despite the fact that the most stable bulk TiO_2 polymorph is rutile under ambient conditions, whose structure shown in **Figure 5b**

($\rho_{\text{rutile,TiO2}}$ = 4.25 g/cm^3).[143] Rutile is also the common crystal structure of SnO_2 ($\rho_{\text{rutile,SnO2}}$ = 6.99 g/cm^3) shown for comparison in **Figure 5c**. Both anatase and rutile are tetragonal crystal structures; anatase TiO_2 has the space group $I4_1/amd$ with a = 3.7848 Å and c = 9.5124 Å,[145] while the rutile crystal structure has the space group $P4_2/mnm$ with a = 4.5931 Å and c = 2.9588 Å for TiO_2,[145] and a = 4.7374 Å and c = 3.1863 Å for SnO_2.[146] In both crystal structures, the tetravalent metal centers are octahedrally coordinated by oxide ligands, although in anatase the octahedra share 4 edges with other octahedra while in rutile the octahedra form linear chains by sharing opposite equatorial edges with two other octahedra, and the axial oxide ligands are corner-sharing between the linear chains.

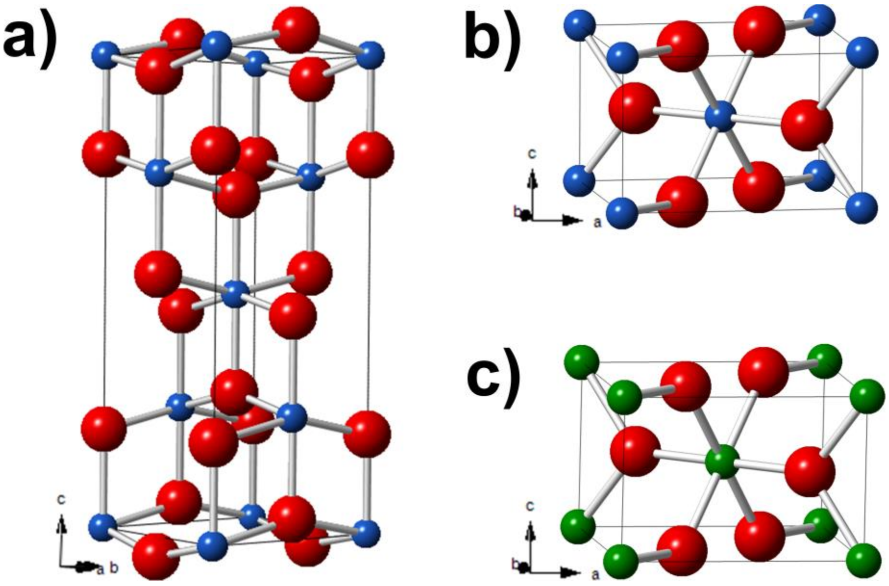

Figure 5. Crystal structures of a) anatase TiO_2, b) rutile TiO_2, and c) rutile SnO_2.

Anatase forms before rutile from amorphous titania because the surface energy of anatase is lower than that of rutile,[147] and therefore the crystallites will have a lower overall energy when the surface area is high enough. **Figure 6** depicts the relative overall enthalpies for the three common TiO_2 polymorphs with three lines for anatase, brookite and rutile, and the heavy trace follows the phase that will have the lowest enthalpy with respect to the specific surface area.[105,106] Because the bulk energy of anatase is higher, the rutile phase is thermodynamically favored, and will undergo a phase transition with kinetics that are highly dependent on the synthetic method[143] and that begins at higher temperatures for smaller nanoparticles.[148]

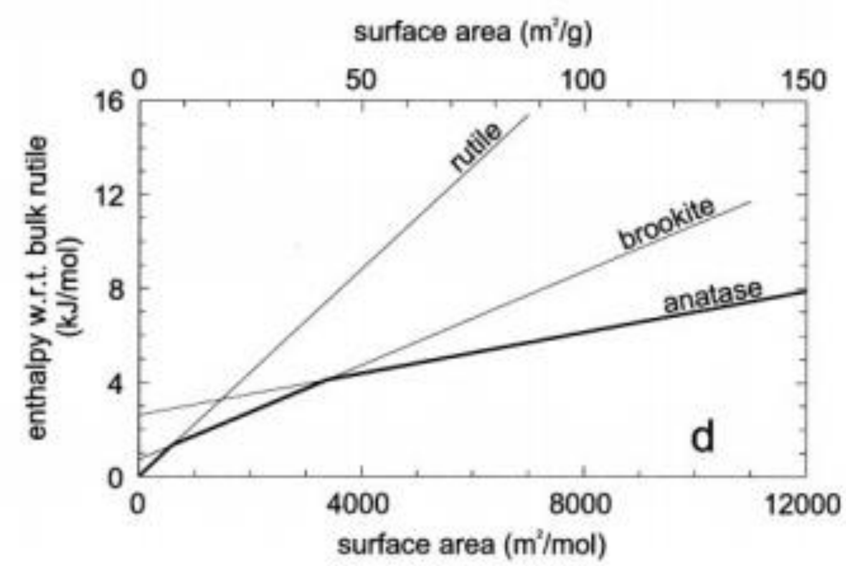

Figure 6. Enthalpy of TiO_2 polymorphs exhibiting a range of surface areas, with respect to bulk rutile. The heavy line indicates the most thermodynamically stable phase with a given surface area (adapted from Navrotsky).[106]

For sol-gel synthesis of TiO_2, molecular titanium species are stabilized both by controlling the amount of water to prevent complete hydrolysis before gelation, and by maintaining highly acidic conditions because the nucleophilic condensation is greatly inhibited by protonation of the ligand oxides. One of the highest porosities of TiO_2 was achieved by Campbell *et al*.[149] who used methanol as a solvent, ~ 0.5 *M* titanium *n*-butoxide ($Ti(OBu)_4$) as the Ti-source, a water/Ti ratio of 4, and HNO_3 as a catalyst for gelation with a ratio of H^+/Ti of 0.125. **Figure 7a** shows the gel time in methanol for various ratios of water/Ti with the H^+/Ti ratio set to 0.1, and the gel product was processed into an aerogel. The 'best' gel from this set of experiments had a water/Ti ratio of 4, which was chosen as the ratio for testing the effect of H^+/Ti on gelation. The highest porosity was found for the gel with H^+/Ti = 0.125 shown in **Figure 7b**, which exhibited a surface area of 220 m^2/g and a pore volume around 0.6 cm^3/g after calcination at 500 °C for 3h. While the precursors appear to form a solution, gelation occurs spontaneously which suggests that a true solution is never obtained; even at a H^+/Ti ratio of 0.175, gelation occurs spontaneously shown in **Figure 7b**.[149] Our own experiments to reproduce this gel revealed that several hours after forming, the gel dissolved back in the acidic mother liquor. If the acidity is reduced after gelation, for example by replacing the solvent, the gel is stable.

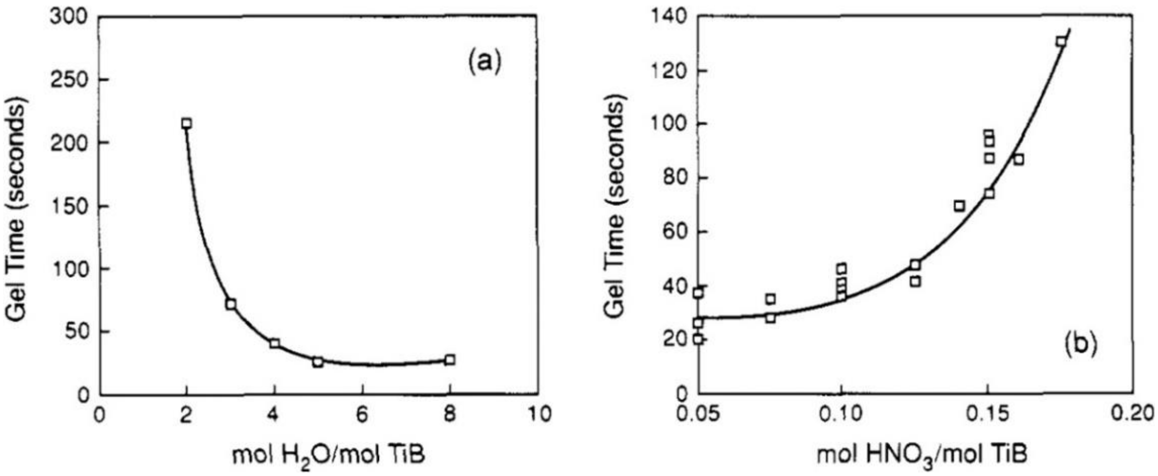

Figure 7. Experimental results for a solution of ~ 0.5 *M* $Ti(OBu)_4$ in methanol as data points, with fitted curves, of gel time as it depends on a) the water/titanium ratio with H^+/Ti = 0.1, and on b) the acid/titanium ratio with water/Ti = 4 (adapted from Campbell *et al.*).[149]

At 10 times lower H^+/Ti ratios than reported by Campbell *et al.*, work by Kallalla *et al.* examined the condensation behavior of $Ti(OBu)_4$ in butanol with various amounts of water and acid using small-angle X-ray scattering (SAXS) to monitor the average size of inhomogenieties as the solution was destabilized and formed solids.[124] The smallest inhomogenieties were observed in cases with high acidity. As condensation reactions occur, the bridging oxide ligands become increasingly more acidic, and will preferentially undergo further condensation with respect to the less acidic monomers. The higher Brønsted acidity of bridging oxides than non-bridging oxides causes them to exhibit a faster condensation rate, while condensation is more inhibited for the non-bridging oxides. The faster reaction rates of more condensed species create a propensity for dense growth, leading to reactions that form precipitates. Since a high acidity results in inhibiting the condensation reactions equally regardless of the degree of bridging of the reactants, gels were only obtained with $H^+/Ti > 0.005$, seen in **Figure 8**. At a water/Ti ratio of 2, **Figure 8** shows that precipitates are formed where the acidity is not sufficient, in the dark gray region. Excess acid can prevent the condensation reactions from forming solids, which is also related to the concentration of the Ti^{4+} precursor. The concentration around ~ 0.5 *M* seems to be near the lower end required to form a gel at all.

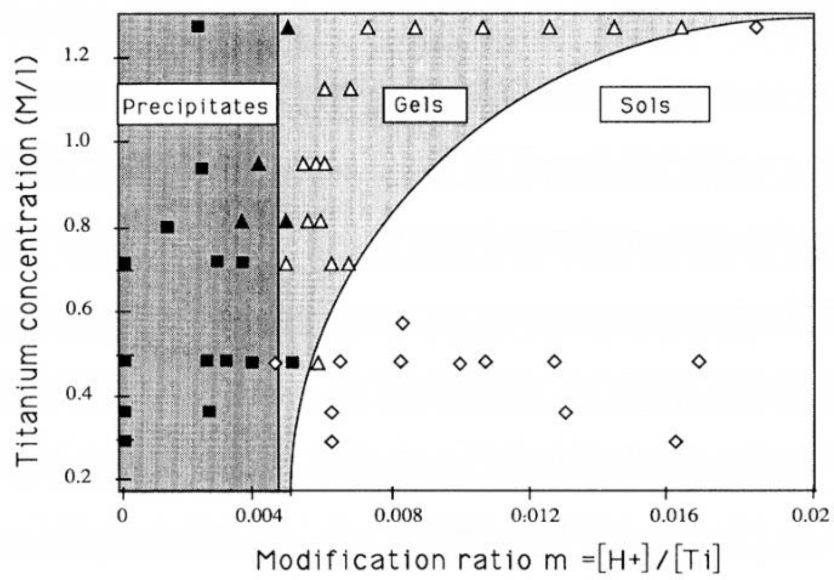

Figure 8. Form of solids present in solutions of $Ti(OBu)_4$ at various concentrations and at various acid/titanium ratios, showing regimes for precipitates, gels and sols (adapted from Kallala).[124]

Both of these studies on titanium sol-gel chemistry underscored the importance of high acidity for our sol-gel design. However, in both studies the pH was kept constant and gelation was spontaneous. We avoided this spontaneous gelation (dense growth) by ensuring that the solution was stable before gelation by adding sufficient acid to protonate the oxide ligands, and by not over-adding water. By starting with a stable sol, we induced gelation by increasing the pH and thereby deprotonated the oxide ligands. To prevent the growth of dense inclusions, it was crucial that the reaction proceeded slowly to allow for an equilibrium between condensation and re-hydrolysis reactions. We accomplished this during the development of two synthetic routes, one in methanol by thermal decomposition of dissolved urea, and another in ethanol by the addition of the proper amount of epichlorohydrin. While these gelation characteristics are important for the uniform porous structure of TiO_2 itself, in the case that dopants such as Zr^{4+} are introduced it is important to maintain atomic-scale homogeniety in the gel. The Zr-precursor $ZrCl_4$ was hardly soluble in the methanol-based solvent system, although $ZrCl_4$ hydrolyzed and dissolved well in the ethanol-based solvent system. Following the gelation, solvent removal was performed to prevent the severe pore collapse.

Simple evaporation of the solvent from the wet gel leads to a ‘xerogel’ that still has a high surface area, however the pore volume is greatly reduced from the wet gel.[130] The aqueous mother-liquor may also be switched by performing a solvent exchange with a less polar solvent such as alkanes that do not strongly interact with the hydrous metal oxide, and that evaporate with a lower extent of pore collapse to yield an ‘ambigel’.[130] ‘Aerogels’ are synthesized by replacing the solvent with liquid CO_2 that becomes supercritical at room pressure and temperature and evaporates without interacting with the pore walls, and generally produces materials with the highest porosity.[130] In another example that can produce materials with porosity comparable to aerogels, and that was pioneered by our research group, the mother-liquor is ultimately replaced by an oil solution in tetrahydrofuran (THF), from which the THF is evaporated under ambient conditions. The remaining substance has pore walls coated by oil, termed an ‘olegel’, which is combusted.[150] In some cases, residual carbon remains after solvent removal, and the products are generally amorphous. Calcination is finally performed to remove carbon and to crystallize the dry gel products.

The hydrous Ti gel obtained in methanol was interesting, and it was processed into highly mesoporous monoliths by both the aerogel and the pyrogel routes. For fabrication of the aerogel, solvent exchange was carried out with acetone and subsequently with CO_2, which was removed supercritically to produce highly mesoporous (BET surface area ~ 520 m^2/g, pore volume ~ 2.9 cm^3/g, pore diameter ~ 22 nm), centimeter-sized yellow monoliths. **Figure 9a** provides a visual summary of the acidic TiO_2 gel formed in methanol from urea decomposition. After the supercritical solvent removal, the TEM image in **Figure 9b** shows the microstructure of the aerogel, with the inset of a photograph of the aerogel monolith. The PXRD pattern in **Figure 9c** shows the amorphous nature of the aerogel with very broad Bragg peaks associated with anatase TiO_2; after calcination at 500 °C, the pores coarsened to reduce the surface area and increase the pore diameter (BET surface area ~ 110 m^2/g, pore volume ~ 1.2 cm^3/g, pore diameter ~ 42 nm) and anatase crystallites were formed.

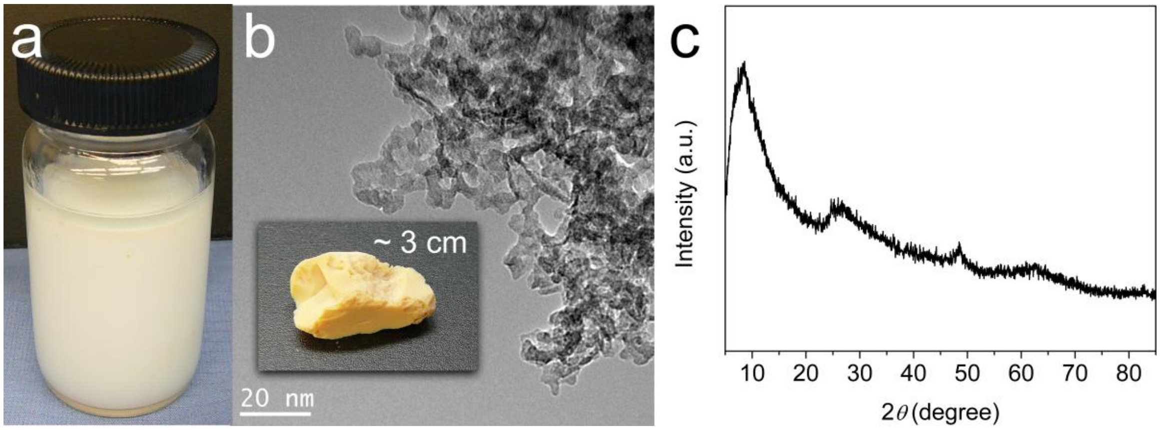

Figure 9. a) Hydrous titanium oxide gel in methanol, b) TEM image of the aerogel (scale bar = 20 nm) with an inset image of an aerogel monolithic particle, and c) PXRD of the aerogel.

From the same methanolic gel in **Figure 9a**, highly mesoporous and transparent monoliths were produced through the pyrogel route using mineral oil rather than canola oil.[150] **Figure 10** shows a microscope image of pyrogel pieces (BET surface area ~ 80 m^2/g, pore volume ~ 0.8 cm^3/g, pore diameter ~ 30 nm), and its photocatalytic activity (crushed and sieved to < 100 µm particles) compared to Degussa P-25. There is a substantial benefit to the porous pyrogel when compared to the Degussa P-25 nanoparticles, which is that separation of the photocatalyst occurs by gravity, or can be achieved by filtration; centrifugation is not needed as it is with nanoparticles. The high activities of both Degussa P-25 and of the pyrogel photocatalyst for degradation of organics seem to rely on the copresence of the anatase and rutile crystal structures. The phase composition that shows the best performance for methyl orange decomposition is around 85% anatase and 15% rutile. However, the phase transition from anatase to rutile takes place above 500 °C, and hot-spots during the combustion step likely limited the reproducibility of achieving the proper phase ratio. It is also noteworthy that including 2.5 atom% Zr in the pyrogel synthesis produces a material that shows the same activity as Degussa P-25, although the PXRD pattern of the product reveals that some Baddelelyite-type phase is present in addition to anatase and rutile.

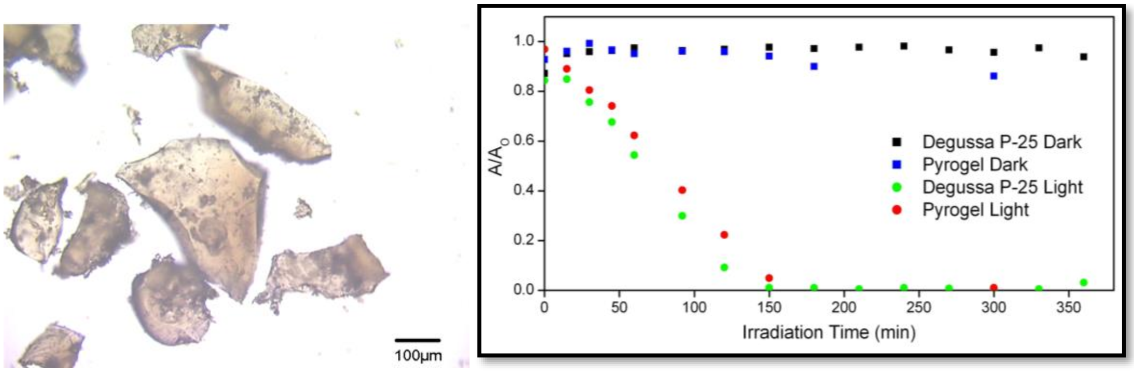

Figure 10. (left) Optical image of transparent pieces of the TiO_2 pyrogel (scale bar = 100 µm), and (right) photocatalytic performance of the pyrogel in decomposition of methyl orange, compared to Degussa P-25.

Another titanium precursor, $TiOSO_4$, requires a highly acidic and polar solvent to dissolve, and the precursor powder itself comes with some excess sulfuric acid to facilitate the dissolution in water without adding extra acids. Also, the highly polar solvent is required and alcoholic solutions of $TiOSO_4$ do not form. As such, epoxides are not sufficient to increase the pH to make insoluble species. Thermal decomposition of urea to generate ammonia was effective to produce insoluble species, although they appeared in the form of precipitates and not as a gel. A similar precipitation behavior was observed by diluting the dissolved $TiOSO_4 \cdot 0.18\ H_2SO_4$ to less than ~ 1 *M* of [Ti]. Since $TiOSO_4$ is a feedstock chemical for producing TiO_2 by the sulfate process,[151] and it is soluble in water, we want to do use it to develop a greener synthetic route to sol-gel TiO_2 than by using the more highly processed and reactive alkoxide precursor. Along the same lines, we want to minimize the use of organics altogether. To overcome the challenge of forming a precipitate rather than a gel, hydrogen peroxide was introduced that complexes with the TiO^{2+} in solution.

Evaporating the water from the titanyl peroxo complex yields a red and clear gel (**Figure 11a)**, and subsequent calcination at 700 °C leads to a sulfate-free TiO_2 solid, with many closed large pores, that retains the shape of the gel (**Figure 11b**). The large closed pores result from trapped oxygen gas that is released as peroxide ligands decompose, and the high viscosity of the hydrous titanyl peroxo sulfate that retains the bubbles. Furthermore, various additives could be included in the precursor solution to modify the physical characteristics of the gel. **Figure 11c** and **d** show calcined products of samples synthesized with the additives of polyethylene glycol and Jeffamine, respectively. PEG imparts closed pores with some clear pore walls, and Jeffamine produces open pores with more elongated and needle-like pore walls. Adding phosphoric acid to the synthesis yielded a new product altogether that will be discussed at length in **Chapter 5**.

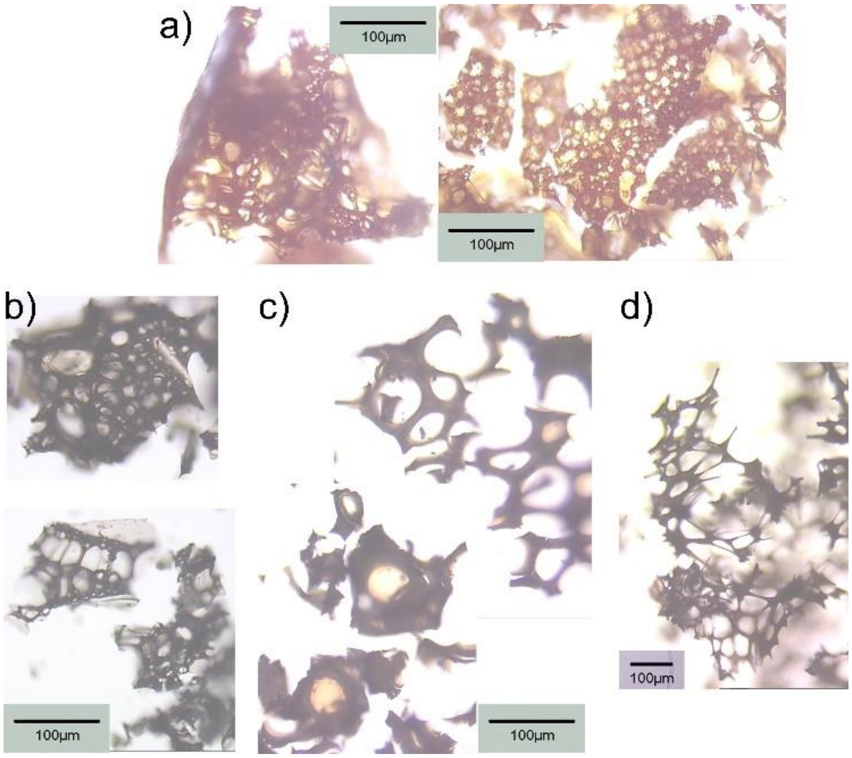

Figure 11. a) Clear, red dry gel of hydrous titanyl peroxo sulfate, b) hydrous titanyl peroxo sulfate gel calcined at 700 °C, c) PEG-added hydrous titanyl peroxo sulfate gel calcined at 700 °C, d) Jeffamine-added hydrous titanyl peroxo sulfate calcined at 700 °C.

Synthesis of SnO_2 aerogels was previously reported by using the epoxide gelation route.[120] ATO aerogels have also been synthesized by a different route, in which the metals do not begin as molecular precursors, but instead as pre-synthesized ATO nanoparticles prepared by the Müller technique.[97,152] Although it is non-aqueous and the product is nanoparticles rather than porous monoliths, our specific interest in TCOs makes it necessary to mention the Müller technique because of the versatile and novel options it lends to fabrication of TCO monoliths[53] and coatings, especially as an ink. This facile approach entails dissolving the metal chloride precursors in benzyl alcohol, which is subjected to heating before purifying the product; it is noteworthy that the crystalline product is formed at 100 °C. We also extended this synthetic route to fabricate nanocrystalline TiO_2 within mesoporous Al_2O_3 using a microwave reactor.

1.4 Porous Transparent Conducting Oxides

Transparent conducting oxides (TCOs) are employed in photovoltaic[153,154] and solar fuel conversion[155] devices, display technology[153,156,157] and other optoelectronic interfaces. Sol-gel procedures can impart desired characteristics to the metal oxides including atomic homogeniety and uniform microstructure, and we wanted to control the pore characteristics and to provide versatile processability of the final nanostructured metal oxides. Sol-gel techniques are amenable to being used along with additives, since other reagents can be in solution that do not disrupt the sol-gel chemistry. Polymers or carbonaceous materials can be additional components in the sol-gel reaction mixture enabling coatings for architectural glass[158] with photochromic[159] or self-cleaning properties[160,161] and as circuitries including as electrodes.[81,154,156] The porous aspect of the conducting oxide coatings is important for applications that require diffusion of molecules and ions within the pores, such as the I^-/I^{3-} redox couple that is commonly used for DSSCs.[154,162-164] Mesoporous coatings have a high specific surface area that is important for the adsorption of active species to the surface of the electrode. Most porous TCOs are mesoporous, however in some cases the adsorbing molecule is too large to have good diffusivity through mesopores. In these cases, it is important to produce TCOs with macropores, which have been sparsely reported, and are generally not much thicker than 1 μm which limits the surface coverage of sorbants.[57,135]

Figure 12 depicts the band structure of an *n*-type semiconductor under three conditions. In **Figure 12a**, the central features of the electronic structure of the semiconducting materials are labeled: the band gap (E_g) and the Fermi energy (E_F). Roughly, the conduction band edge energy (E_{CB}) and the valence band edge energy (E_{VB}) can be approximated by **eq. 12** and **eq. 13**, respectively, where χ is the geometrical average electronegativity of the elements in the compound in eV.[165] Mulliken electronegativites are used, which are defined by **eq. 14**, where χ is the elemental electronegativity, and IE and EA are the ionization and electron affinity energies, respectively.[166] **Figure 12b** shows the band edge energy diagram of *n*-type Sb-doped SnO_2, where one of the five electrons occupies the antibonding orbital with oxide. Therefore, the Fermi energy increases to between the donor Sb^{5+} and the Sn^{4+} antibonding orbitals with oxide, and with a small amount of thermal energy the electrons can be injected into the bulk rutile conduction band. The injection of an electron into the conduction band can also occur by a photoexcited chromophore, which is depicted as DYE in **Figure 12c** in which the Fermi energy is at the bottom of the conduction band.

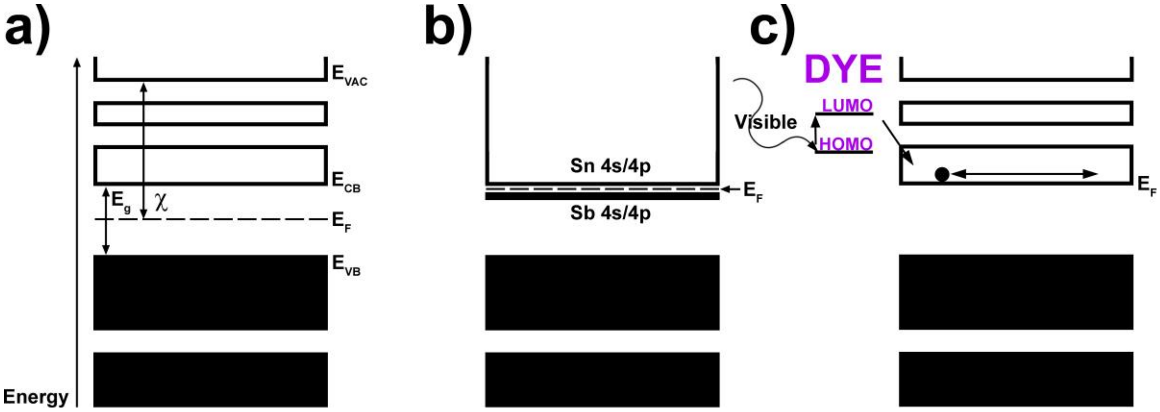

Figure 12. a) Typical band structure of a transition-metal oxide semiconductor, where the Fermi level can be predicted by the electronegativites of the elements, b) Sb-doping in

SnO_2 produces mobile charge carriers in the conduction band, c) mobile charge carriers in the conduction band of TiO_2 after an electron from a photoexcited adsorbed dye molecule was injected.

$$E_{CB} = -\chi + \frac{1}{2} E_g \qquad \textbf{eq. 12}$$

$$E_{VB} = -\chi - \frac{1}{2} E_g \qquad \textbf{eq. 13}$$

$$\chi = \frac{1}{2} (IE + Ea) \qquad \textbf{eq. 14}$$

Advancements in TCOs have come in the forms of new materials and new synthetic techniques, to reduce the overall cost and improve the scalability of the TCO fabrication. The most common and best performing TCO material is indium tin oxide, which is a solid solution consisting of 90 wt% In_2O_3 and 10 wt% SnO_2 that is generally deposited by sputtering techniques.[167] Sputtering techniques require an ultrahigh vacuum and a high voltage supply, which makes the relatively thin (~35 – 1000 nm)[157] TCOs expensive to fabricate. One major reason that sputtering methods are used to deposit TCOs is the atomic homogeniety that can be achieved without high temperature treatment (<200 °C for ITO) as the gaseous species directly form solids on the substrate. Sputtered coatings are non-porous which is the best for conductivity but limits the applicability in advanced devices that require controlled diffusion and high surface area.[97] For achieving a homogeneous composition on the atomic level, solution-based chemistry is an alternative to vacuum-based deposition techniques.[168] Liquid coatings of ATO precursor can be deposited by several techniques including dip-coating,[169-176] spin-coating,[177-180] doctor-blading,[121,181] that are subsequently processed to remove the solvent and produce a porous coating. Both premade nanoparticle 'inks'[97,167,182] and gels formed on the surface [81,121,183] have been used to deposit the transparent conducting oxide layers from solution. The subsequent processing should preserve the pore structure, which entails both minimizing the pore collapse during solvent removal and ensuring the sufficient connectivity between the nanoparticles that the coating has solidity and conductivity.[184] The latter process is generally accomplished by thermally induced sintering of the nanoparticles, however the upper limit for the thermal treatment is ~ 600°C due to the softening and melting of the glass.

Not only is indium expensive, but also global supplies may be exhausted in a decade.[167] Recently, new materials have been investigated to replace ITO, and one of the most promising candidates was reported to be Al- or Ga- doped ZnO.[157] Many other metal oxides have also been explored as TCOs,[156,185] including *p*-type ZnO, CdO and delafossites such as Cu(Sr, Fe, Al, Ga, Cr)O_2,[168,186-189] and *n*-type such as RuO_2,[5] (Sb, In, Nb, Ta)$_x Sn_{1-x}O_2$,[170,184,185,190-192] F:SnO_2,[193] In_{2-x}(Sn, Ga,)$_x O_3$,[194,195] $Ba_{1-x}La_xSnO_3$,[196] $Nb_{12}O_{29}$,[197] ZnO, ZnO-In_2O_3-SnO_2,[198,199] and $Zn_{1.824}In_{4.336}Ge_{1.84}O_{12}$.[153] Of these, a wide range have been synthesized by sol-gel methods[168,170,186,187,192,196,200] which opens the option of synthesizing them as porous coatings. Our main interest was the synthesis of thicker $Sb_xSn_{1-x}O_2$ (ATO) coatings with controlled pore characteristics in the mesopore and macropore regimes, that could uptake macromolecules with sufficient diffusivity while also achieving a high surface coverage.

While the deposition of TCOs through a sol-gel process offers a variety of morphologies, thicknesses and processing options, there are several challenges associated with producing the porous TCOs that may be employed in devices. When the coatings exceed ~ 1 um in thickness, severe cracking often occurs during the solvent removal and thermal treatment that may be associated with delamination.[127,131,132] Also, as the pores are infiltrated with electrolyte or solvent, pore collapse may occur that may also cause peeling of the coating. If the coating is too fragile, or if the diffusivity is too low, the coatings may not be practical for applications. Also, a high transparency can reduce the amount of light that can be absorbed which limits the usefulness as DSSC electrodes, although some applications can use the highly transparent electrodes such as tandem photovoltaic devices (i.e. electrode 3 in **Figure 13**)[77]. We developed synthetic methods that can produce porous TCO coatings to overcome these problems, from both TiO_2 and SnO_2 based materials.

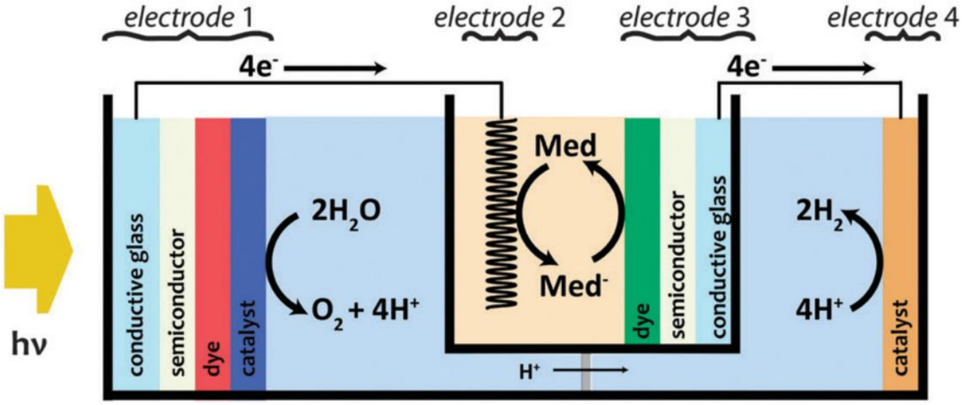

Figure 13. Schematic for a water-splitting tandem solar cell (adapted from Sherman *et al.*).[77]

The majority of porous TCOs are specifically mesoporous. This mesoporosity is the result of textural pores among the nanoparticles that formed in solution, and since mesopores are smaller than the diffraction limit of visible light, the light does not scatter and produces a transparent electrode. **Figure 14a** shows photographs of the transparent ZTO coating with the reflection such that the coating can be seen. The slight variations in thickness of the coating can be seen by the variations of color in the magnified image of ZTO coatings in **Figure 14b**, with a scale bar of 100 µm. Synthesis and characterizations of these coatings will be covered in detail in **CHAPTER 3**.

Figure 14. a) Photographs of transparent nanoporous Zr-doped TiO_2 films on conducting glass substrates, and b) the color variation caused by slight thickness variations, seen under an optical microscope (scale bar = 100 μm).

Due to its band structure and surface chemistry, TiO_2 is the primary material used for porous DSSC electrodes,[140,164,201] in photocatalytic reactions for self-cleaning surfaces[202] and water splitting[139,160,161,202], and is also used as a UV detector[203-205] and gas sensor.[206,207] The performance of TiO_2 in these devices can be enhanced by various treatments including doping to modify the electronic band structure. For example, increasing the conduction band edge energy increases the open circuit voltage of DSSCs, and the efficiency with which the electrode 3 can reduce protons into hydrogen in **Figure 13**. Furthermore, widening the band gap results in a wider range in UV detection than intrinsic TiO_2. In one case, Al-doping at 3 atom% in TiO_2 increased the open circuit voltage in DSSC tests by ~ 0.03 V.[208] Zr-doping in TiO_2 has also been shown to increase the conduction band edge energy by 0.11 eV at 5 atom%, although literature reports have not shown the corresponding increase in the voltage of a DSSC made with $Zr_xTi_{1-x}O_2$.[163] SnO_2 has also been employed as a DSSC electrode,[209] but the efficiency was significantly lower than TiO_2 electrodes which has been attributed to the better grafting of -COOH functional dye molecules to anatase TiO_2 surface than to the SnO_2 surface.[210] Depositing a thin layer of SnO_2 on the surface of TiO_2 DSSC electrodes greatly improves the performance by preventing electron transfer from the TiO_2 to the solvent.[211] Generally for these applications, the mesopores are ideal because of the high surface area and due to the fact that the diffusing species are relatively small molecules. As the size of the diffusing molecules becomes larger, approaching the size of the pores, diffusivity will be substantially hindered.[9]

Another important TCO material is $Sb_xSn_{1-x}O_2$ (ATO), which shows promise as a substitute for ITO. A solution based, dual-gel method for synthesizing highly mesoporous ATO has been well established[134] and well characterized including both by DNA-origami size exclusion studies[181] of the pores with controlled diameters as well as the fabrication of films by doctor-blading.[121] As mentioned for DSSCs and as illustrated by DNA-origami size exclusion studies, the mesopore diameter limits the molecules that can access the pores.[181] Macroporous ATO,[53,54] and coatings thereof,[55,57,82,135] have been fabricated in previous reports. However, both the homogeneity of the macropore distribution and the coating solidity are difficult to ensure without significantly complicating the synthetic route. For example, polymer[135] or silica[55] colloids have been used as sacrificial templates to impart a periodic macropore structure, although these methods have several drawbacks.

Primarily, these methods rely on self-assembly of the colloids that is time consuming and may leave dense regions. Also, the high cost of the colloidal templates and the use of hazardous HF for removing silica are undesirable. Additionally, the pre-fabrication of ATO nanoparticles increases the synthetic intensiveness, and it is unclear what major advantages the ordered pore structure exhibits over a random pore structure.

Another strategy that employed the assembly of ATO nanoparticles into a random macroporous network by the aerogel technique, with subsequent calcination, produced high surface-area, macroporous monoliths with the co-presence of macropores and mesopores.[212] However, there were still relatively dense regions present, and the material was not applied as a coating. Template-free routes relying on spinodal decomposition have been explored for the synthesis of various monolithic, macroporous metal oxides,[213] however there are no reports of macroporous ATO coatings produced by this route.

Considering the challenges for the scalable fabrication of macroporous ATO coatings, we explored a new aqueous sol-gel based method that used carbon black as a sacrificial template and acidic metal chloride precursors. Because of the strong phobic interaction between carbon black and water, a surfactant was required to produce a homogeneous dispersion; the homopolymer PEG compound (~98% with bisphenol-A and epichlorohydrin) was effective and not cost prohibitive as multi-block polymer templates can be. In the literature, carbon black has been applied as a template for monolithic metal oxides, often to improve diffusivity through microporous materials such as zeolites by imparting pores.[11,13,214-217] Also, high-surface-area metal oxides have been synthesized with carbon black template,[136,218-224] but not as coatings.

We studied the viscometry of the solvent and template system used for the synthesis of meso-macroporous ATO, across various concentrations and ratios of carbon black and PEG. Based on these studies, we think that the carbon black and PEG template forms a continuous network throughout the volume of the reaction mixture. After removal of the template, the pores form a well-connected network that is hierarchical, comprising mesopores and macropores. The hierarchical pore structure consisting of both macropores and mesopores balances sufficient diffusion with high surface area. Further, the thick (2 – 20 µm) macroporous coatings can be applied without peeling from the substrate.

The carbon-black templating method was also applied to make macroporous TiO_2 and $Zr_{0.1}Ti_{0.9}O_2$ coatings that were tested as electrodes for DSSCs. In the literature, larger nanoparticles and small microparticles are added to the DSSC electrode paste,[137] although the macropores may accomplish the same light-scattering effect. These DSSCs will be discussed further at the end of **CHAPTER 4**.

1.5 Mixed Oxoanion Compounds

While oxide is a polarizing ligand, tetrahedral oxoanions are generally more polarizing, due to electron withdrawing of the oxygen electron cloud by the high-valent covalent cation at the center. This leads to more ionic bonding between the transition metal and the oxygen in the oxoanion and thus the metal centers become more reducible. Such oxoanions include, in order of the electronegativity of the tetrahedral center, SO_4^{2-}, PO_4^{3-}, AsO_4^{3-}, MoO_4^{2-}, GeO_4^{4-}, SiO_4^{4-}, VO_4^{3-}. While the metal compounds with oxoanions have found applications in catalysis,[225-227] ion conductivity,[228,229] ion exchange,[230-234] low thermal expansion materials,[235] battery materials,[236-240] sensors,[241-245] and ion-selective electrodes[246,247] it has been found that the mixed oxoanions can improve certain properties for these applications. The compound $Na_{(1+x)}Zr_2(PO_4)_{3-x}(SiO_4)_x$ exhibits exceptional conductivity of Na^+, for which it earned the name of sodium superionic conductor, or NASICON for short. **Figure 15** depicts the NASICON-type structure, which has three components: tetrahedral oxoanions (XO_4, gray) alternately corner sharing with octahedrally coordinated metal cations (M, blue), which form a rigid framework of lantern units with ion channels connected in three-dimensions that hosts the alkali cations (A, pink). **Figure 15a** shows the view down the *c*-axis that shows the rhombohedral symmetry well. **Figure 15b** shows the profile view of a NASICON-type unit cell that reveals the connectivity of the polyhedra, which will be described in more detail in **Section 5.3**.

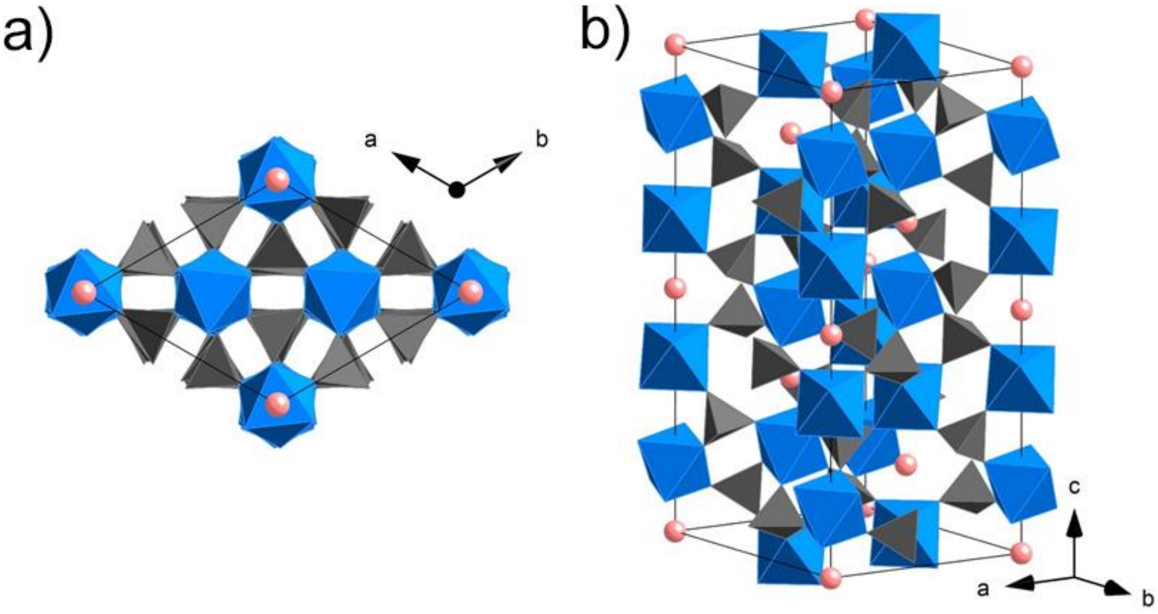

Figure 15. NASICON-type unit cell a) down the *c*-axis, and b) side view.

Following the discovery that ionic conductivity and capacity could be greatly enhanced by oxoanion mixing, a wide range of compounds with the NASICON-type structure have been explored, based on group IV metals. Parent compounds that have been synthesized include: $AHf_2(PO_4)_3$; (A = Li^+, Na^+, K^+, Rb^+, Cs^+, Ag^+, $Ca^{2+}_{0.5}$, $Sr^{2+}_{0.5}$, Cu^+, ($Cu^+_{0.5}H^+_{0.5}$), $Cu^{2+}_{0.5}$, $Cd^{2+}_{0.5}$),[248-253] $Na_4Hf_2(GeO_4)_3$,[254] $Na_4Zr_2(GeO_4)_3$,[254]

$AZr_2(AsO_4)_3$; (A = Li^+, Na^+, K^+, Rb^+, Cs^+, $Sr^{2+}_{0.5}$),[255-257] $Na_4Zr_2(SiO_4)_3$,[258,259] $AZr_2(PO_4)_3$; (A = H^+, H_3O^+, NH_4^+, Li^+, Na^+, K^+, Rb^+, Cs^+, $Mg^{2+}_{0.5}$, $Ca^{2+}_{0.5}$, $Sr^{2+}_{0.5}$, $Ba^{2+}_{0.5}$, $Sc^{3+}_{1/3}$, $Cr^{3+}_{1/3}$, $Mn^{2+}_{1/2}$, $Co^{2+}_{1/2}$, $Ni^{2+}_{1/2}$, Cu^+, $Cu^{2+}_{0.5}$, $Zn^{2+}_{0.5}$ $Cd^{2+}_{0.5}$, $Al^{3+}_{1/3}$, $Eu^{2+}_{0.5}$, $Eu^{3+}_{1/3}$, $Gd^{3+}_{1/3}$, $Er^{3+}_{1/3}$, $Tm^{3+}_{1/3}$, $Yb^{3+}_{1/3}$, $Lu^{3+}_{1/3}$, $Pu^{4+}_{1/4}$, $Am^{3+}_{1/3}$, $Y^{3+}_{1/3}$, $Zr^{4+}_{1/4}$),[231,250,251,255,260-279] $ATi_2(AsO_4)_3$; (A = Li^+, Na^+, K^+, Ag^+, $Mg^{2+}_{0.5}$, $Ca^{2+}_{0.5}$, $Sr^{2+}_{0.5}$),[280,281] $ATi_2(PO_4)_3$; (A = Li^+, Na^+, K^+, Rb^+, $(Rb_{0.8}Cs_{0.2})^+$, NH_4^+, $Mg^{2+}_{0.5}$, $Ca^{2+}_{0.5}$, $Sr^{2+}_{0.5}$, $Ba^{2+}_{0.5}$, $Sc^{3+}_{1/3}$, $Fe^{2+}_{1/2}$, $Co^{2+}_{1/2}$, Ni^{2+}, $Cu^{2+}_{0.5}$, Cu^+, Ag^+, $Cd^{2+}_{1/2}$, $Pb^{2+}_{1/2}$, $(Na_{0.25}Eu_{0.25})^+$),[225,231,235,282-294] $Na_3Ti_2(PO_4)_3$,[295] $Na_4Ti_2(PO_4)_3$,[295] $NaTi_2(SO_4)_3$,[296] $Ti_2(SO_4)_3$.[265,296] Size effects primarily govern the phase formation, as seen by the inability of Cs^+ to fully occupy the Ti-based frameworks, although 20 atom% Cs^+ substitution for Rb^+ was achieved in $Rb_{0.8}Cs_{0.2}Ti_2(PO_4)_3$ to produce an isotropic low-thermal expansion material. Also, Na^+ conduction is high in the Hf- and Zr-based frameworks with respect to that in $NaTi_2(PO_4)_3$, which is attributed to the smaller ion channels and resulting increased activation energy for ion transport. Despite the propensity of the d^0 cations to form NASICON-like structures with oxoanios, the stability limits are shown by the inability to form certain compounds; for example, germinates only form with Hf and Zr, and the vacant sulfate compound is only formed with Ti. Sulfate has the strongest electron-withdrawing character of the viable oxoanions and is therefore of interest for producing polyoxometallates,[297-299] proton- and ion-transport materials,[300-302] solid acid catalysts[116,303-309] and high voltage ion-battery materials.[310,311]

By controlling the oxoanion content, certain properties of the parent NASICON-type compounds can be improved. A clear example is the voltage increase exhibited during Li^+-battery tests of $Fe_2(MoO_4)_3$ and $Fe_2(SO_4)_3$, which show voltages of 3.0 and 3.6

V, respectively.[312,313] Although Ti-based NASICON-type structures are at the forefront of alkali ion-battery research, sulfate has not been reported to occupy tetrahedral sites within Ti^{4+}-based compounds. Partial oxoanion substitution is known to improve ionic conductivity properties over the parent materials: Na^+ conductivity is improved in zirconium phosphate silicates[230,255] and titanium phosphate arsenates,[314] and Li^+ conductivity is improved within titanium phosphate frameworks doped with silicate,[315-317] vanadate,[315,318-320] and niobate.[315,318-320] Additionally, phosphate molybdates of Zr have been studied for their range of catalytic activity, with the non-oxidative dehydrogenation of methanol improving with mixed oxoanions,[277,321] and vacant frameworks isostructural to monoclinic $Sc_2(WO_4)_3$ have been studied for negative thermal expansion properties including $Zr(PO_4)_2MoO_4$,[322] $Zr(PO_4)_2WO_4$,[323-325] $Hf(PO_4)_2MoO_4$, $Hf(PO_4)_2WO_4$,[326] $Zr(PO_4)_2SO_4$, and also a rhombohedral phase of $Zr(PO_4)_2SO_4$.[327,328] Two distinct NASICON-like structures of $Zr(PO_4)_2SO_4$ were reported; the monoclinic and denser of the two was a result of direct sulfate substitution in zirconium phosphate during a sulfuric acid reflux, and sulfate is presumed to be randomly distributed from the emission profile.[327,329] A second compound shares the $R\bar{3}c$ symmetry of NASICON, and was prepared by a reported sol-gel route where the gel pieces were calcined to form the less-dense phase of $Zr_2(PO_4)_2SO_4$.[230]

CHAPTER 2

CHARACTERIZATION METHODS

I used the following characterization methods for analyzing the properties of the materials that I synthesized: ultraviolet/visible (UV/VIS) diffuse reflectance spectroscopy (DRS) and transmission spectroscopy, solid-state nuclear magnetic resonance (SS-NMR) spectroscopy, Raman spectroscopy, energy dispersive spectroscopy (EDS), inductively coupled plasma with optical emission spectroscopy (ICP-OES), scanning electron microscopy (SEM), transmission electron microscopy (TEM), scanning transmission electron microscopy (STEM), Mott-Schottky (MS) spectroscopy. Also the diffraction and scattering based methods that I used included optical profilometry, powder X-ray diffraction (PXRD) with Rietveld refinement, dynamic light scattering (DLS), and electrophoretic light scattering (ELS) in conjunction with autotitration. Additionally, the physical-based methods that I used included stylus profilometry and nitrogen gas sorption. The relatively unique characterization methods are described below, which are PXRD and Rietveld refinement, Mott-Schottky analysis, nitrogen gas sorption measurements and dynamic light scattering determination of size and zeta potential of dispersed particles.

As most of the characterizations that I used are common, I will not describe the details of all measurements except the ones in the following sections.

2.1 Mott-Schottky Measurements

While crystalline compounds have characteristic band edge energies, this is a bulk property. Measuring the band structure characteristics by electrochemical impedance spectroscopy (EIS) is complicated because the electrochemical signal can only communicate with the bulk by charge transfer at the surface. An energy diagram of the EIS setup for probing the electrochemical properties of the semiconductor is depicted in **Figure 16**. The semiconductor conduction band energy (E_{CB}) and Fermi energy (E_F) are shown at the left of the figure, and they are separated by a value of ΔE_F that is systematically around 0.1 – 0.2 eV for *n*-type semiconductors. E_F is measured by the workfunction of the semiconductor electrode ($\phi_{SC)}$ through the electrolyte with the same workfunction (ϕ_{EL}).

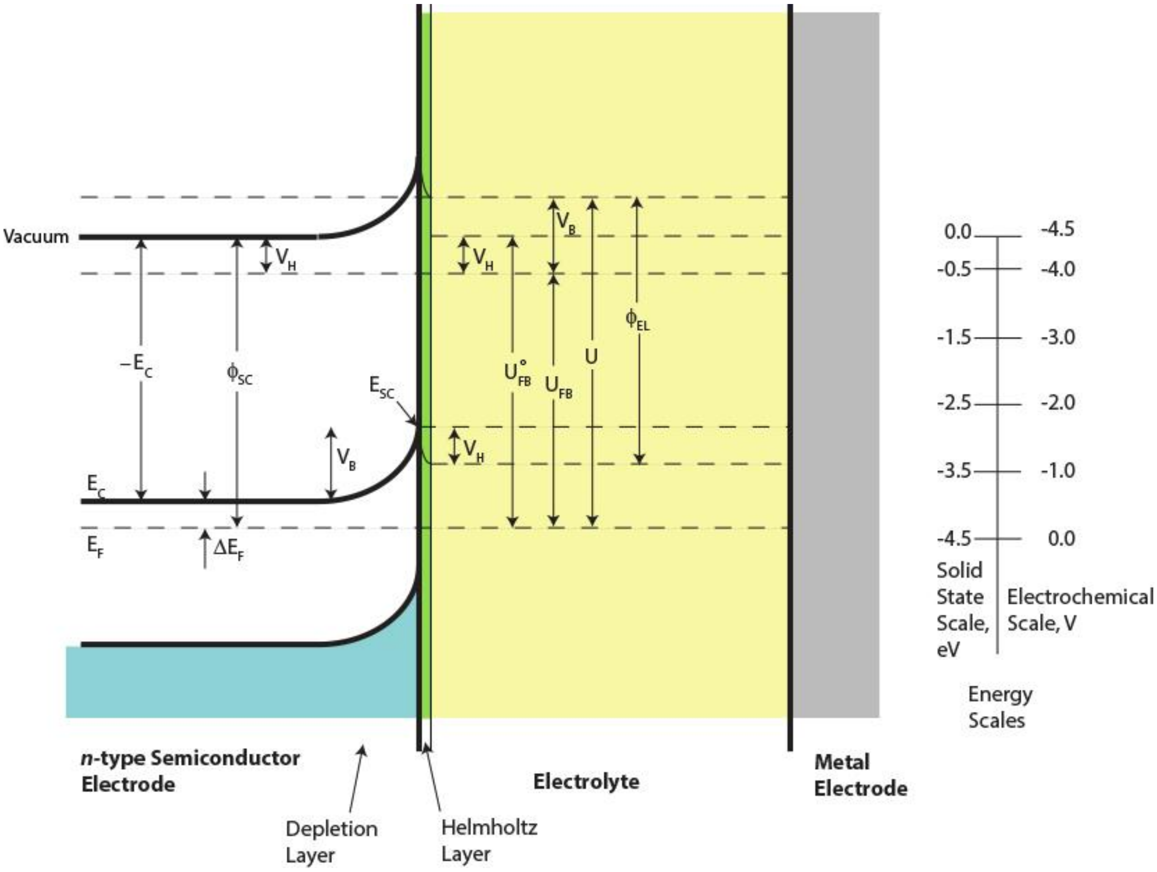

Figure 16. Schematic diagram showing the setup for a Mott-Schottky measurement, where energy increases vertically. The *n*-type semiconductor electrode is on the left, exhibiting band bending at the interface with the electrolyte, through which the electrochemical impedance is applied by the metal electrode.

We want to measure the flat band potential, U_{FB}, and ultimately calculate the standard flat band potential for the material, U_{FB}^{0}. In order to account for the voltage of band bending (V_B) caused by the depletion layer, an experiment is performed by modulating the applied potential (U) and monitoring the space charge capacity (C_B) of the depletion layer. A useful equation for analyzing the experimental data is derived from Poisson's equation that employs Gauss's law, and that is examined at the surface of the semiconductor, where E_{SC} is the conduction band edge energy at the surface. Thereby, the Mott-Schottky equation (**eq. 15**) is derived.[330]

$$C_B^{-2} = \left(\frac{2}{qN_{SC}\kappa\epsilon_0 A^2}\right)\left(E_{SC} - \frac{kT}{q}\right) = \left(\frac{2}{qN_{SC}\kappa\epsilon_0 A^2}\right)(U - U_{FB} + V_H - \frac{kT}{q}) \qquad \textbf{eq. 15}$$

Here, N_{SC} is the density of immobile charge in the space charge region, κ is the dielectric constant, ϵ_0 is the permittivity of free space, and A is the contact area between the semiconductor and the electrolyte. The Helmholtz potential, V_H (**eq. 16**), is caused by a gradient in the chemical potential through the solvent due to the effects of accumulated charge at the semiconductor surface from a difference between the pH in the electrolyte, and the pH of zero charge (PZC) of the semiconductor surface.[331]

$$V_H = 2.303kT(PZC - pH_{electrolyte}) \qquad \textbf{eq. 16}$$

As **eq. 15** reveals, the plot of C_B^{-2} vs. U should produce a linear region that extrapolates to 0 when $U = U_{FB} + V_H$, assuming that the term kT/q is negligible. An example plot, known as a Mott-Schottky (M-S) plot, is instrumental in determining the conduction band edge energies of semiconductors by EIS. The effect of pH on the flat band potential of an electrode is illustrated in **Figure 17** from the reported supporting information, where the measured flat band of '5% Zr-added TiO_2' decrease in potential as the pH increases. The surface measurement is influenced not only by the pH, but also by the material composition, the exposed crystal faces, surface morphology and structuration, and the electrolyte system. In our case, we approximated the PZC as the pH of zero zeta-potential (PZZP), which was measured using electrophoretic light scattering coupled with autotitration, described later in **Section 2.4.**

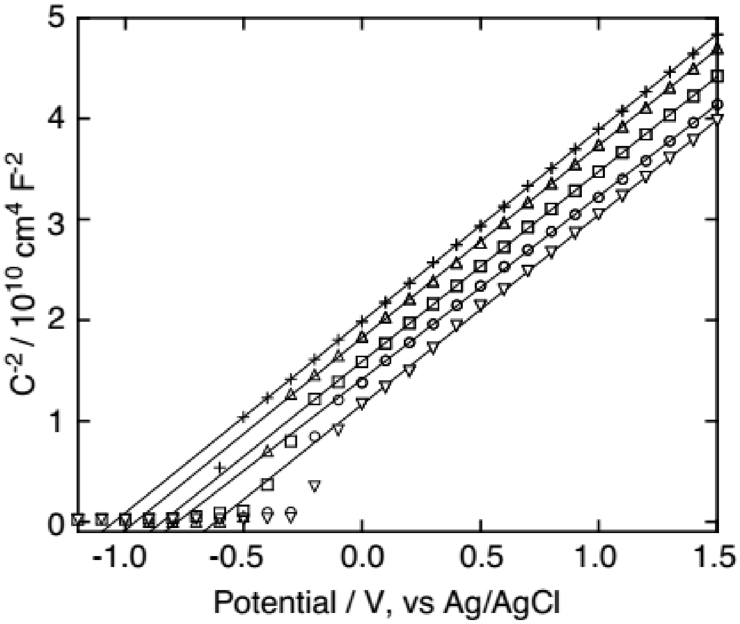

Figure 17. Mott-Schottky plots for ‘5% Zr-added TiO_2’ electrodes electrolyte pH = 2.0 (downward triangle), 3.4 (circle), 5.2 (square), 6.6 (upward triangle), and 9.3 (cross) (adapted from Imahori *et al.*).[163]

2.2 Inductively Coupled Plasma – Optical Emission Spectroscopy (ICP-OES)

A straightforward and versatile approach to high throughput elemental analysis is ICP-OES. The versatility comes from using a plasma to excite all of the elemental species simultaneously, and detecting the signal emitted as the excited atomic species relax. Atomic emission lines are narrow, and complex mixtures of elements can be evaluated quantitatively due to the low amount of spectral overlap. For most elements, elemental analysis can be carried out by the ICP-OES technique with a precision around ppm to ppb. For analysis, the samples are first acid-digested using a microwave-assisted route to produce an analyte solution. In our case dealing with Ti-based oxide and phosphate compounds, the acid digestion required HF and a multiple heating steps to 180 °C for 15 min.

Subsequent analysis begins with nebulizing the analyte solution, and the nebulized droplets enter a chamber with Ar-plasma. The elements are delivered to the plasma in the nebulized droplets, the contents of which are atomized and ionized by the high-energy environment. As the excited atomic species relax by emitting a characteristic spectrum, detection is performed at the known atomic emission wavelengths. Due to the fluctuating nature of both plasma and nebulization processes, as well as to matrix effects, the analysis requires calibration before each use. With the blank matrix solution used during analysis as the diluent, calibration is performed at the chosen atomic emission wavelengths by serial dilutions of a known standard. Two or three emission lines are used. This calibration curve can drift during analysis, and therefore quality checks must be performed periodically to prevent inaccurate data collection.

Limitations of ICP-OES include that some elements cannot be analyzed (such as O, H, Ar), and others have relatively high detection limits such as S. Chemistry between certain species may also cause unintended atomic interactions in the plasma that reduce the atomic emission signal. To account for all of the factors, method development was performed for each new system of analytes. Generally, method development is straightforward and involves selecting the atomic emission lines to use for analysis, and finding the correct concentration for analysis. The concentration range of the calibration curve is centered on the target concentration, and the software carries out the quantitative analysis. In our application, this was the case when titanium and zirconium were the only analytes.

During method development for our samples, we discovered that the copresence of titanium and phosphate in the analyte solution necessitated higher R/F power for plasma than normally used. This requirement was attributed to the strong tendency of Ti and P species to complex which interfered with the atomic emission. The signal for both species was dramatically lower than expected and the calibration plot was highly irregular. The calibration plot became linear and the elemental ratios were reasonable after increasing the R/F power to 1200 W, while 1150 W was used otherwise.

2.3 Powder X-ray Diffraction (PXRD) and Rietveld Refinement

Diffraction occurs with radiation at many length scales, from neutron diffraction that reveals magnetic structural information to electron diffraction that can be used to probe nanoscale crystallinity to X-ray crystallography that can be used for complete and high-throughput crystal structure determination. Single-crystal X-ray diffraction scans in 3D to produce a 2D, centrosymmetric diffraction pattern, from which a crystal structure can be solved. However, without a femtosecond X-ray laser, large crystals (~1 um) are required for single-crystal analysis. A wide range of information is accessible from XRD including lattice strain, epitaxial layer thickness, surface reconstructions with low-energy[33] and tomographic distribution of defects.[33] Another indispensable tool for solid-state materials characterization is X-ray diffraction on powders, which is sufficient for the precise determination of the unit cell parameters, using an internal standard for which we used silicon.

The cathode ray tube used to provide X-rays is illustrated on the left of **Figure 18**, where a high tension (~50 keV) is applied to a Cu target, and the electrons incident on Cu ionize core electrons. In an event pictured in the right of **Figure 18**, the outer electron relaxes from the L to the K shell, and releases Cu Kα X-rays with an average wavelength of λ = 1.5418 Å. Due to the non-degenerate 2p-orbitals in the L shell, both Cu $K\alpha_1$ and Cu $K\alpha_2$ radiations will be produced with characteristic wavelengths of λ = 1.54056 and Å; λ = 1.54439 Å, respectively; Kβ radiation is also emitted when an M-shell electron relaxes to the vacancy in the K-shell, with λ = 1.392 Å for Cu Kβ radiation. Since the wavelength of X-rays is on the same order as the angstrom-length atomic spacing in solids, a wavefront of X-rays travelling through a solid will diffract. Conditioning the primary beam is generally performed in some fashion, although the components such as collimators, slits and filters also attenuate the beam, and their implementation is widely varied across diffractometers. For example, a Ni-filter is often employed, which absorbs the Cu Kβ radiation along with some of the Cu Kα2.

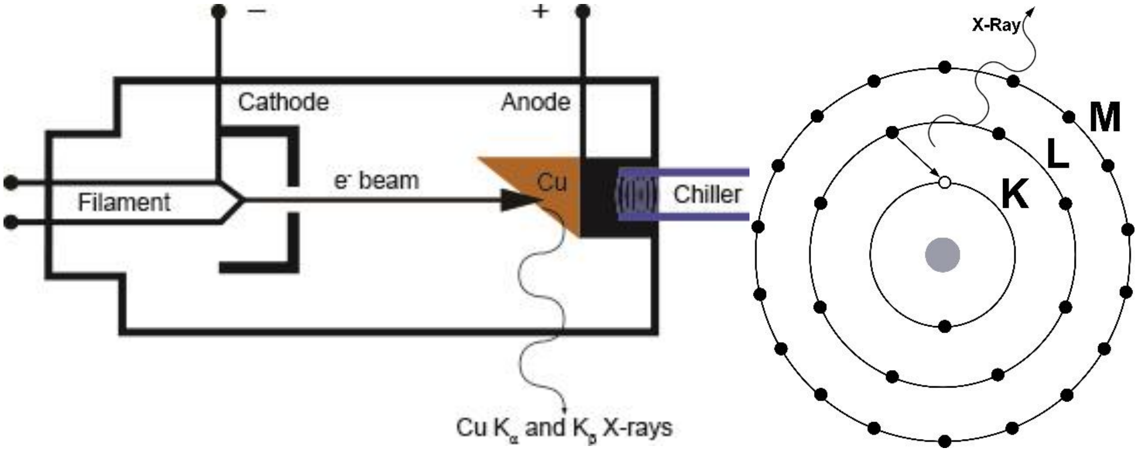

Figure 18. (left) Drawing of a cathode ray tube, (right) illustration of a vacancy in the K shell, and a Cu Kα transition that correlates to the emission of a characteristic X-ray.

X-rays were detected either by a gas-flow detector or an intrinsic Li-drifted Si (Si(Li)) detector. In the former, a gas of 90% Ar and 10% methane gas runs through a cathodic tube, and a wire runs concentrically through the tube, which is the anode. As X-rays bombard the gas, the Ar is ionized with ~ 15.7 eV per event. A potential is applied between the anode and the cathode to attract the electrons electrons to the anode, where they produce a signal, and the Ar^+ ions travel to the cathode to be reduced. The applied bias accelerates the ionized electrons enough that they can ionize subsequent Ar atoms, producing a cascade of further ionization events, and it is held at a potential at which there is a proportional response between the number of incident X-rays and the detected signal. The UV-photons generated during the cascade are absorbed by methane to eliminate uncharacteristic signals from being detected. Si(Li) detectors use intrinsic Li-drifted Si that is sandwiched in a *p*-i-*n* junction across which a bias is applied. The average absorption event within the Si is ~ 3.6 eV, and the complete absorption of the keV X-ray happens through millimeter scales, to produce a number of electron-hole pairs equal to the incident energy divided by ~ 3.6 eV. Electrons travel to the cathode and the holes travel to the anode producing a voltage dependent on the energy of the incident X-ray with an energy resolution of ~ 3.6 eV.

Diffractograms were collected using the Bragg-Brentano configuration (**Figure 19**) that is common for PXRD. The apparatus consists of a cathode-ray tube that emit X-rays from a Cu target to generate the primary beam at an angle of elevation from the sample of θ. Detection of the secondary beam is carried out with the detector also at an angle of elevation of θ. Therefore, as the X-ray tube and the detector move along the goniometer circle, while maintaining both angles at θ, the measurement takes place by scanning 2θ.

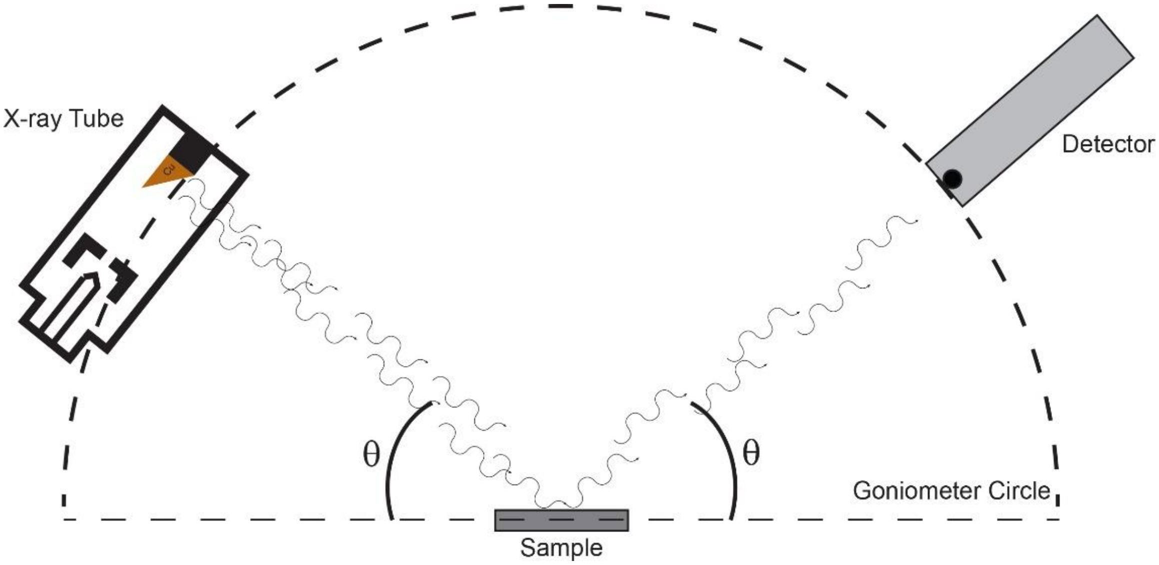

Figure 19. The Bragg-Brentano geometry for PXRD analysis.

In a diffraction experiment, signal's amplitude in reciprocal space is measured. In the simplest case, a primary beam impinges a 1D array of scatterers, which are respectively X-rays and electrons in our case but which could also be visual light on a diffraction grating or water waves and wooden posts on a pier. The important aspect of diffraction is that the wavelength of the primary beam should be close to the spacing of the obstacles, and this is the case with X-rays and atomic spacing in condensed matter. The coherent scattering of an X-ray with intensity I_0 by an electron produces a scattered intensity (I) given by the Thompson equation (**eq. 17**) in which the scattering angle is θ, K is a constant (7.94×10^{-30} m^2) and r is the distance between the electron and the detector.

$$\mathrm{I} = \mathrm{I}_0 \frac{K}{r^2}\left(\frac{1+\cos^2 2\theta}{2}\right) \qquad \textbf{eq. 17}$$

Figure 20 shows a periodically spaced line of electrons (black dots) that scatter the incident X-ray beam (gray circles). There is an angle at which the scattered waves will interact with each other constructively, shown as 2θ in the diagram below; due to destructive interference, the signal will be negligible at all other angles than 2θ as given by the **eq. 18** and increases.

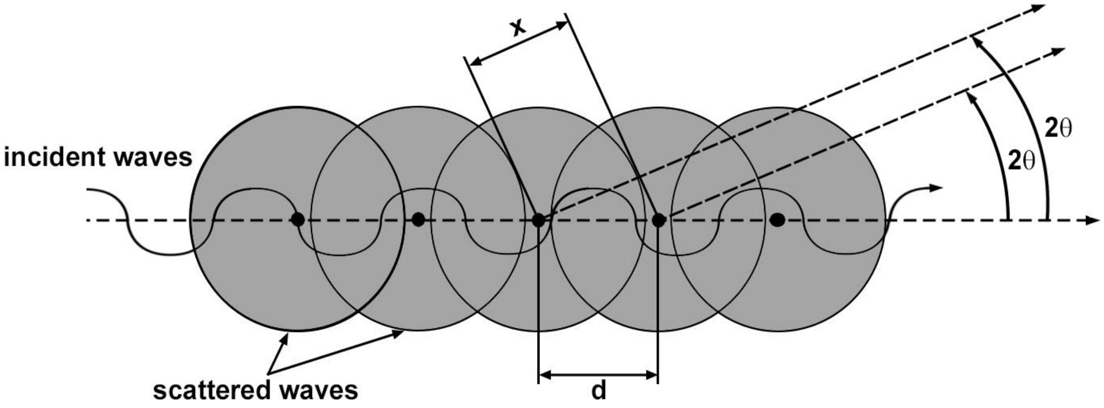

Figure 20. Diffraction from a line of scattering points irradiated along their axis of alignment (adapted from Pecharsky *et al.*).[332]

$$\varphi = 2\pi\left(\frac{\mathrm{d}-x}{\lambda}\right) = 4\pi\left(\frac{\mathrm{d}\sin^2\theta}{\lambda}\right) \qquad \textbf{eq. 18}$$

In the above scenario, the phase angle, φ, defines the relationship between the intensity observed at a given angle of theta and the distance between the scatterers. When the incident wave is propagating along a vector that is not along the direction of the periodic spacing, the variable ψ is introduced to define this angle (**Figure 21**), with ‘a’ as the spacing of the scatterers in the h direction, the phase relation becomes defined as **eq. 19**. The 3D ordering of atoms in solids, and the constructive interference occurs where the phase angles from all 3 dimensions intersect. The Laue equations (**eq. 19 – eq. 21**) summarize the condition under which the diffracted beam is observed from a single crystal; only along the direction where all three Laue equations are satisfied will diffraction peaks be detected.

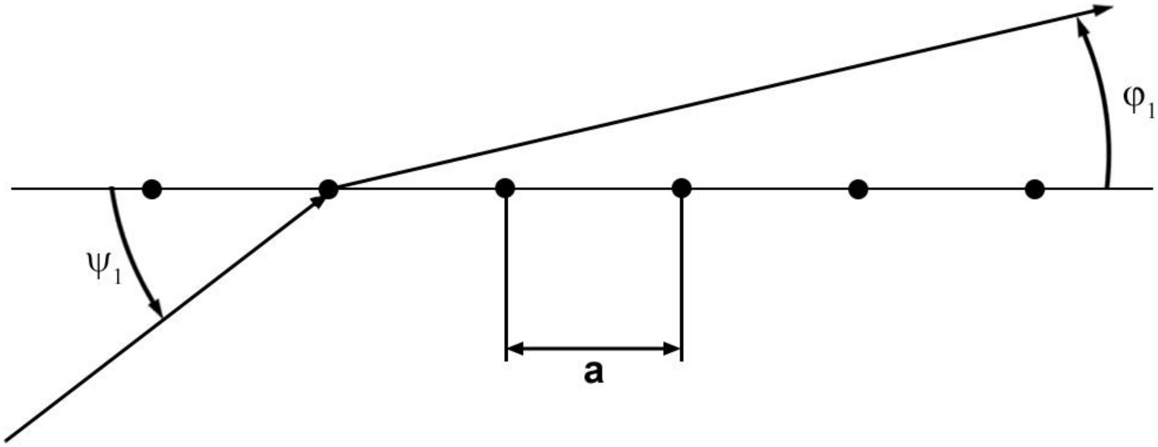

Figure 21. Diffraction from a line of scattering points irradiated from an angle ψ_1.

$$a(\cos\psi_1 - \cos\varphi_1) = h\lambda \qquad \textbf{eq. 19}$$

$$b(\cos\psi_2 - \cos\varphi_2) = k\lambda \qquad \textbf{eq. 20}$$

$$c(\cos\psi_3 - \cos\varphi_3) = l\lambda \qquad \textbf{eq. 21}$$

While the Laue equations define narrow conditions for the directions along which diffraction spots (Laue spots) will be seen for single crystals, a fine powder contains a statistical number of individual crystallites that are positioned in random orientations. Rather than Laue spots in reciprocal space, diffraction from a fine powder will produce Laue rings. Taking advantage of this aspect of powders, reciprocal space can be scanned in only one dimension, 2θ as depicted in **Figure 22**, to gain 3D structural information about the crystal. Laue equations are condensed to Bragg's law (**eq. 22**) for PXRD, which treats the atomic planes as reflectors of the X-rays. As the X-ray wavefront is reflected from a certain atomic plane, it has travelled farther than the wave reflected from the previous atomic plane by a length of 2Δ. Given the ability of modern diffractometers to scan 2θ with a small step size, unit cell parameters can be especially well refined as they are calculated from the set of measured d_{hkl}.

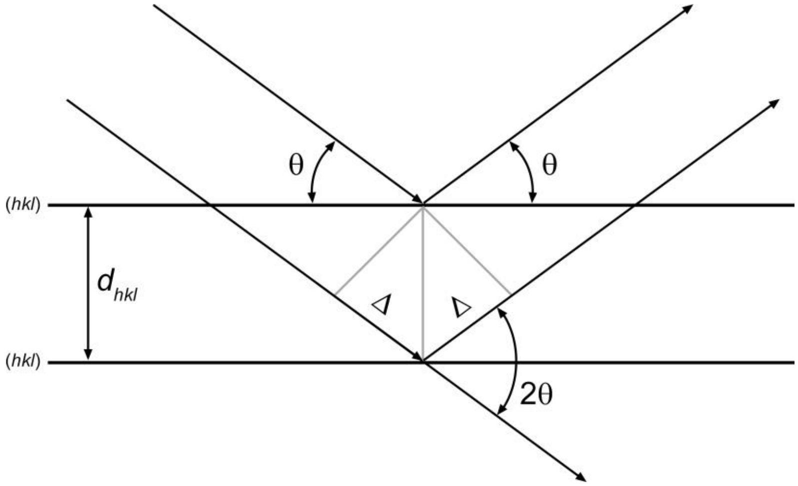

Figure 22. Illustration of Bragg's law for diffraction from crystal planes with index *hkl* in PXRD.

$$n\lambda = 2d\sin(\theta) \quad \textbf{eq. 22}$$

Through this relationship, the wavelength of radiation (λ) determines the scaling in reciprocal space, and the order of a certain reflection is given by n. The Miller index of a Bragg peak in (h, k, l) represents the order of the reflection along the a, b and c directions, respectively. In a scan of 2θ, the associated d-spacing of a Bragg peak decreases with increasing 2θ values, and also with increasing Miller index values. For a given set of Bragg peaks, the unit cell parameters can be refined. For example, in the case of triclinic crystal structures (**Figure 23**) which have the lowest symmetry, the unit cell parameters $a, b, c, \alpha, \beta,$ and γ can be determined by **eq. 23**, where V is the unit cell volume.

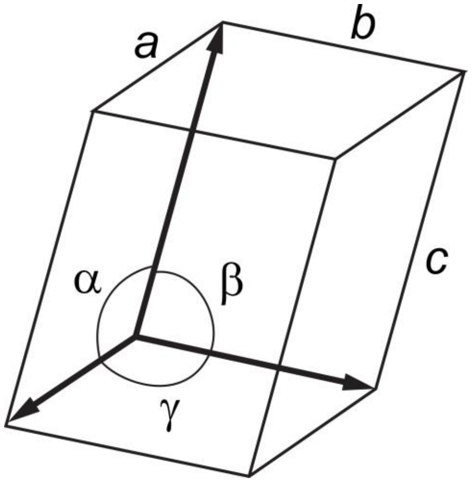

Figure 23. A triclinic unit cell with the unit cell parameters labeled.

$$\frac{1}{d^2} = \frac{1}{V^2}\Bigg(\left(b^2c^2\sin^2\alpha\right)h^2 + (a^2c^2\sin^2\beta)k^2 + (a^2b^2\sin^2\gamma)l^2 + \left(abc^2(\cos\alpha\cos\beta - \cos\gamma)\right)hk + \left(a^2bc(\cos\beta\cos\gamma - \cos\alpha)\right)kl + \left(ab^2c(\cos\gamma\cos\alpha - \cos\beta)\right)hl\Bigg) \qquad \textbf{eq. 23}$$

As crystal structures exhibit a higher symmetry, the equation will simplify significantly, and reduces to **eq. 24** for orthorhombic space groups as an example.

$$\frac{1}{d^2} = \frac{h^2}{a^2} + \frac{k^2}{b^2} + \frac{l^2}{c^2} \qquad \textbf{eq. 24}$$

To illustrate the *d*-spacings of the Miller planes, a 6 × 12 projection of atomic columns down the *c*-axis of an orthorhombic lattice is shown in **Figure 24** with three different *d*-spacings indicated. Also, the unit cell is indicated in the bottom left, labeled with the parameters *a* and *b*, with *c* normal to the screen.

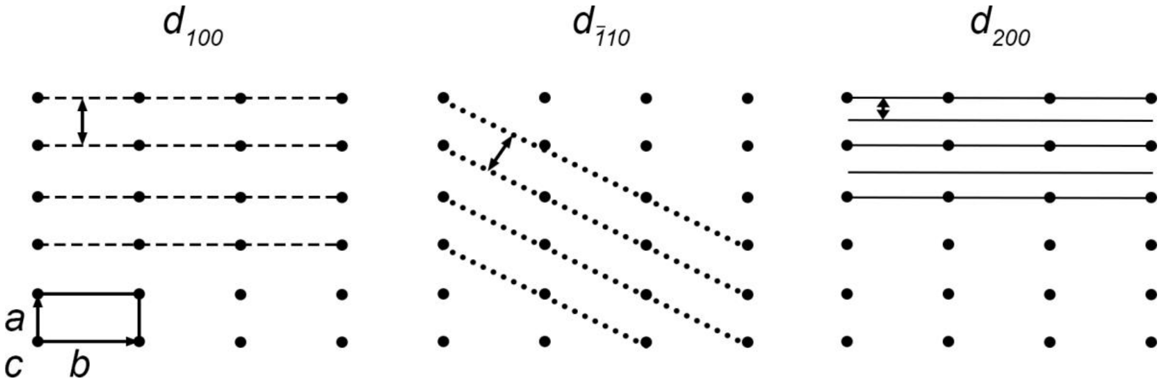

Figure 24. 2D projection down the *c*-axis of an orthorhombic lattice, indicating the indexed planes which are separated by the corresponding *d*-spacings.

While the peak positions can be used to solve for the unit cell parameters, the space group cannot always be pinpointed by PXRD due to the overlapping peaks in the 1D diffractogram. Inversely, we may take a known structure and simulate a PXRD pattern for comparison with the experimental pattern. In doing this, Bragg's law (**eq. 22**) is used to simulate peak positions, and the relative intensities of the peaks are directly proportional to the structure factor, $|F_{hkl}|^2$ which is the absolute value of the square of the structure amplitude of the j^th^ atom at the fractional coordinates *x, y* and *z*.(F_{hkl}, **eq. 25**) In this expression, *n* is the total number of atoms in the unit cell, *g* is the partial occupancy (often 1), *t*(*s*) is the thermal parameter, *f*(*s*) is the atomic scattering factor, and $s = \sin\theta_{hkl}/\lambda$.

$$F_{hkl} = \sum_{j=1}^{n} g^j t^j(s) f^j(s) \exp\left[2\pi i\left(hx^j + ky^j + lz^j\right)\right] \qquad \textbf{eq. 25}$$

At higher temperatures and for lighter elements, atoms become perturbed from their lattice points to a greater degree. With an assumption of a spherical electron cloud, the thermal vibrations will effectively enlarge this sphere by the average magnitude of displacement. For an isotropic displacement, the root mean square deviation, U_{iso} (Å^2), can be used to express the thermal parameter as **eq. 26**.

$$t^{\mathrm{j}} = \exp\left[-U^{\mathrm{j}}_{iso}\frac{\sin^2\theta}{\lambda^2}\right] \tag*{\textbf{eq. 26}}$$

A more accurate thermal parameter can also be considered, in which the anharmonic displacement parameters, β_{11}, β_{22}, β_{33}, β_{12}, β_{13}, β_{23}, are employed that describe an ellipsoid of electron density of the scatterers (**eq. 27**), rather than the spherical electron density of U_{iso}. With 1D PXRD data, accurately modeling the details of thermal atomic motions is not meaningfully carried out with higher order anharmonic displacement parameters; refining β values is necessary to obtain a satisfactory fit with the experimental data, but must be used mindfully as they are unavoidably somewhat of a fudge factor for peak shape.

$$t^{\mathrm{j}} = \exp\left[-(\beta^{\mathrm{j}}_{11}h^2 + \beta^{\mathrm{j}}_{22}k^2 + \beta^{\mathrm{j}}_{33}l^2 + \beta^{\mathrm{j}}_{12}hk + \beta^{\mathrm{j}}_{13}hl + \beta^{\mathrm{j}}_{23}kl)\right] \tag*{\textbf{eq. 27}}$$

The atomic scattering factor of atom j (f^{j}, **eq. 28**) expresses how the electron cloud will scatter the X-ray photon. Species with higher atomic numbers are stronger scatterers, and the scattering events can be expressed in terms of the parameters c_0, a_1 – a_4, b_1 – b_4 for the various elements, that are reported in the international crystallographic tables,[333] as are approximations of the anomalous scattering parameters $\Delta f^{\mathrm{j}\,\prime}$ and $\Delta f^{\mathrm{j}\,\prime\prime}$.

$$f^{\mathrm{j}} = c^{\mathrm{j}}_0 + \exp\sum\nolimits_{i=1}^{4} a^{\mathrm{j}}_i \exp\left[-b^{\mathrm{j}}_i \sin\frac{\theta}{\lambda}\right] + \Delta f^{\mathrm{j}\prime} + \mathrm{i}\Delta f^{\mathrm{j}\prime\prime} \tag*{\textbf{eq. 28}}$$

Phase identification is one primary application of PXRD data, where crystal structures have characteristic Bragg peak positions that can be cross-referenced with databases. Where an unknown crystal structure is analyzed, PXRD is faced with difficulties. First, given that the sample is phase-pure, the peaks and the peak positions can be fit with different space groups using Le-Bail or Pawley full pattern decomposition methods, which simulate a PXRD pattern to match the experimental pattern using non-linear least squares, although no structural information is included in the refined phase. Using these pattern analysis methods, the unit cell parameters can be determined from the Bragg peak positions. Also, the peak broadness can be used to quantify the crystallinity by the average crystallite domain size, which is interpreted as the nanoparticle size from the peak broadness.

In addition to the peak positions and relative peak intensities, accurately simulating a PXRD pattern from a structural model requires accounting for parameters outside of those that describe the crystal structure. Aspects of the sample need to be considered such as small particle size leading to broadening of Bragg peaks, preferential orientation that effects relative peak intensities, and sample thickness effects that may impart a shift in 2θ to the entire pattern. Besides the sample itself, contributions to the detected X-ray intensity include not only the Bragg peaks, but also the background signal, the instrumental parameters including beam attenuators, collimators or monochromators that affect the peak shapes, or other misalignments to offset the peak positions. All of these parameters can be included in a structural model, where they can be modified independently by an iterative process that seeks to minimize the value of Φ in **eq. 29**. This method is known as Rietveld refinement, and it is emphasized that before trusting the result of a refinement it should be carried out multiple times on the same

PXRD pattern to ensure the reproducible result. Also, multiple PXRD patterns of a sample should be analyzed before drawing solid conclusions.

$$\Phi = \sum_{i=1}^{n} w_i (Y_i^{obs} - Y_i^{calc})^2 \qquad \textbf{eq. 29}$$

This brute-force approach to analyzing PXRD patterns is based on analysis of the difference between the experimental intensities (Y_i^{obs}) and those calculated from a structural model (Y_i^{obs}). Each point is weighted by w_i, which is $(Y_i^{obs})^{-1}$. Before doing refinement on the structural model based on the experimental data, the data can be pre-conditioned, for example by correcting the pattern based on an internal standard by applying a shift in 2θ such that the Bragg peaks associated with the internal standard appear at the correct positions. Also, some peak resolution can be gained at the expense of signal/noise ratio by stripping the PXRD pattern of the Cu $K\alpha_2$ radiation. In addition, regions at either end of the pattern (roughly $2\theta < 15°$, $2\theta > 80°$), can be omitted from the refinement when no peaks appear there, which helps improve the stability of the background refinement. When the pre-treatment of the PXRD pattern is complete, an initial structural model is refined by iteratively decreasing the value of Φ by refining certain parameters. These parameters include the background, phase composition, scaling, unit cell parameters, peak shape, preferential orientation, site occupancy, fractional coordinates, instrumental parameters and thermal parameters.

Rietveld refinement was carried out in a software program such as FullProf, Topas, Panalytical X’Pert Pro, Match!, or GSAS. Initial inputs were the raw PXRD data, and structural information including the space group and occupancy. The background was refined based on a Chebyshev polynomial, which was usually chosen to be 5th or 6th order depending on the goodness of fit, and could also be summed with a 1/x term where x was refined along with the polynomial. The background was refined independently, and fixed during the refinement of other parameters. When the background was not being refined, the scaling was always refined, as it accounted for the various factors that affect the intensity across the entire range of 2θ, including the polarization factor, phase composition, and various instrumental factors such as beam attenuation or collimation, and goniometer radius. Next, the phase composition was refined, followed by the unit cell parameters and then the peak shape. The peak shape in PXRD patterns is not a regular function (i.e. Gaussian nor Lorentzian) and often several options are available for model peaks with refinable parameters to attempt to match peak shapes. By incorporating some Guassian and some Lorentzian character in the peaks, a more adequate model is generated to match PXRD peaks, such as the Pseudo-Voigt peak-shape function (**eq. 30**), where $C_G = 4\ln 2$, H is the full width at the half-maximum peak intensity (FWHM) and is expressed as $H = (U\tan^2\theta + V\tan\theta + W)^{1/2}$ where U, V and W are refinable parameters, $\eta = \eta_0 + \eta_1 2\theta + \eta_2 2\theta^2$ where η_0, η_1 and η_2 are refinable, $C_L=4$, and $x = (2\theta_i - 2\theta_k)/H_k$ where $2\theta_i$ and $2\theta_k$ are the Bragg angles of the i^{th} point of the experimental PXRD pattern and the calculated Bragg angle of the k^{th} Bragg reflection, respectively.[332]

$$y(x) = \eta \frac{C_G^{1/2}}{\sqrt{\pi}H} \exp\left(-C_G x^2\right) + (1-\eta) \frac{C_L^{1/2}}{\pi H} \left(1 + C_L x^2\right)^{-1} \qquad \textbf{eq. 30}$$

Refining the peak shape often involves only refining the value of U, as refining V or W, or the η parameters can create a diverging iterative calculation. After initial refinement of the peak positions and shapes, all parameters are fixed except for the background which is refined again. Alternating refinements of the background and peak position/shape can be performed with diminishing returns. Although the peak broadening is caused by any type of disorder, the limited crystallinity can be expressed as an average crystallite size by the Debye-Scherrer equation, **eq. 31** where the average thickness of the crystalline domains (*t*, nm) is expressed as a function of the Bragg angle (θ) and the shape factor, K, that is 1 for spherical crystallites, although we usually used 0.9 for manual calculations.

$$t = \frac{\mathrm{K}\lambda}{\mathrm{FWHM}\ \cos\theta} \qquad \textbf{eq. 31}$$

Fixing these peak shape parameters, the next step is to refine the fractional coordinates and fractional occupancies of the atoms in the unit cell. This can be challenging with large unit cells that contain many atoms, as refining them all together can produce the wrong result, but refining them individually is time consuming as they must be alternately refined. The peak shapes can then be refined again, because the fractional coordinates and occupancies affect the structure factor. Instrumental parameters can be input and refined but generally will not significantly alter the refinement when the sample was nanoparticles, presumably due to the somewhat low signal to noise ratio caused by wider Bragg peaks. The final parameter to refine is the thermal parameter, which will try to fit the simulated and experimental PXRD patterns in a relatively unconstrained manner. If thermal parameters turn out to be negative after refinement, it is an indication that other parameters may have been refined incorrectly.

In the software programs, the refinement proceeds with the experimental PXRD pattern on-screen, overlaid with the simulated PXRD pattern as it is refined. Visual comparison gives an accurate impression about the validity and the quality of fit between the simulated and experimental patterns that can be quantified by the figure of merit, R_{wp}, given in **eq. 32**. Generally, R_{wp} less than 10% may be considered acceptable, however the visual comparison is an important aspect of assessing the quality of fit.

$$R_{wp} = \left[\frac{\sum_{i=1}^{n} w_i (Y_i^{obs} - Y_i^{calc})^2}{\sum_{i=1}^{n} w_i (Y_i^{obs})^2}\right]^{1/2} \times 100\% \qquad \textbf{eq. 32}$$

Figure 25 shows example PXRD patterns (various colors) of TiO_2, $Ti_{0.9}Zr_{0.1}O_2$, $Ti_{0.8}Zr_{0.2}O_2$ and $Ti_{0.7}Zr_{0.3}O_2$ calcined to 500 °C, overlaid by the refined, simulated PXRD patterns (red lines), below which are gray curves that represent the difference between the two. The R_{wp} values are between 4 and 10 for these fits. There are broad peaks belonging to the nanoparticulate samples, as well as narrow peaks that belong to the Si internal standard, that is also included as a structure in the refinement although its unit cell parameters are not refined. Instead, before refinement, the entire pattern was shifted to make the Bragg peak position match the known peak position of the strongest Si reflection at 28.44 degrees. In the examples below of $Ti_{0.8}Zr_{0.2}O_2$ and $Ti_{0.7}Zr_{0.3}O_2$, there is a broad peak from $2\theta = 20$ to 40° from the Zr/TiO_2 that has a low crystallinity. These examples illustrate a pitfall for Rietveld analysis of PXRD data, and especially for phase composition analysis, which is that PXRD with the Bragg-Brentano geometry fails to characterize the amorphous phase content well, especially when it is copresent with a crystalline phase. In this configuration, the detector becomes saturated at small angles, requiring the scan to start from no smaller than $2\theta \sim 5°$. This limitation also makes it less convenient to analyze structures with large *d*-spacings such as some hydrous layered compounds or zeolitic materials.

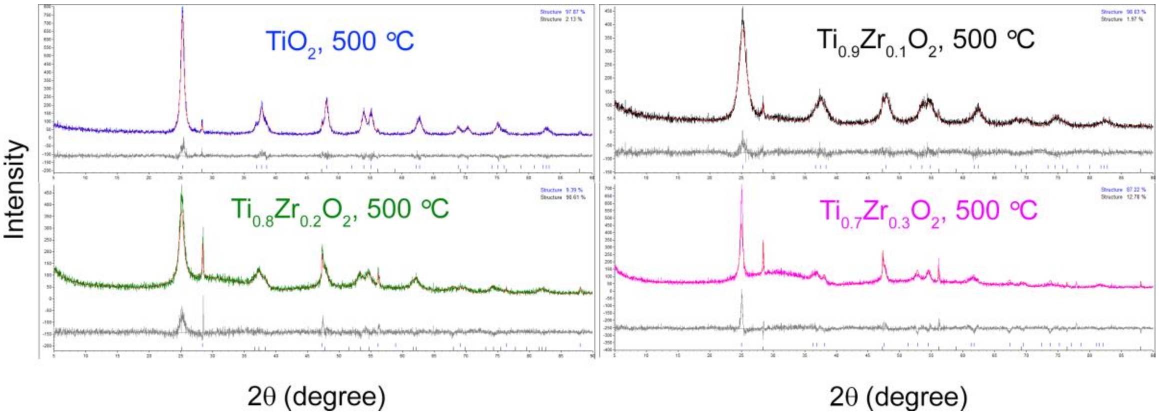

Figure 25. Rietveld refinement results for various Zr-doped TiO_2 samples calcined to 500 °C. The gray line beneath the PXRD pattern is the difference between the experimental pattern (diffractogram) and the simulated curve (red line).

2.4 Gas Sorption Techniques

Interpretation of gas sorption experiments is subject to a great deal of scrutiny, due to several factors. First, the statistical nature of the measurement does not account for heterogeneities in the sample. Next, a physical model must be applied to understand the shape of the sorption isotherm which makes assumptions that are not realistic. Also, the upper limit to pores that can be recognized by nitrogen gas sorption are ~ 150 nm, and many porous materials have larger pores. Finally, the quality of measurements can be difficult to ensure, due to experimental parameters such as limited measurement container size, extremely small sample weights and incomplete degassing. However, there is no substitute for the type of comparative analysis that can be done between isotherm data from samples of the same type. The richness of the data allows for development of increasingly complex models by which to compare important parameters of the materials, and also those numbers can be interpreted in conjunction with characterization techniques such as SEM, TEM, zeta potential, and XRD. Furthermore, chemical analysis of surfaces can be carried out by sorptive techniques; we analyzed the solid acidity by temperature programmed desorption of ammonia gas (NH_3-TPD), for example.

Primarily, sorption measurements were carried out with nitrogen gas at 77 K. Before sorption studies, the sample was heated to at least 100 °C (generally 150 – 200 °C) under either vacuum or flowing nitrogen to remove adsorbed molecules from the surface. The experiment was conducted with the sample initially under vacuum and cooled to liquid nitrogen temperature (77 K) in an analysis tube. A pressure transducer monitored the pressure in the head space while quantized amounts of nitrogen gas were introduced. Between injections of nitrogen gas, the pressure was allowed to equilibrate and the data point of partial pressure (p/p_0) and total quantity of nitrogen were recorded. The resulting curve contains information about various aspects of the sample. After the pressure of nitrogen was increased to near atmospheric pressure, a vacuum was gradually pulled on the analysis tube and data collection continued as nitrogen was removed incrementally.

There are three main regions in a gas sorption isotherm that each contains unique information about the pore characteristics at different length scales. Where $p/p_0 < 0.05$, micropores (<2 nm) will become filled, then between $0.05 < p/p_0 < 0.3$ monolayer coverage is generally achieved and multilayer sorption begins. Then when $p/p_0 > 0.3$, pores begin to fill and a hysteresis may be observed between the adsorption and desorption isotherm branches.

Based on the characteristics in these partial pressure regimes, gas sorption isotherms have been categorized into 6 main groups by IUPAC, shown in **Figure 26**.

The rapid onset of amount adsorbed with increasing relative pressure is indicative of micropores, such as in isotherm type I, II and IV. Materials that have macropores are shown in isotherm types II and III. The shape of an overall exponential increase in the type III isotherm results from the weak interaction between the substrate and the adsorbate compared to the interaction of the sorbate with itself hence multilayer sorption predominates. The hysteresis shown between the adsorption and desorption branches in type IV and V isotherms is characteristic of mesopores, and the interaction between adsorbates is stronger in type V behavior.

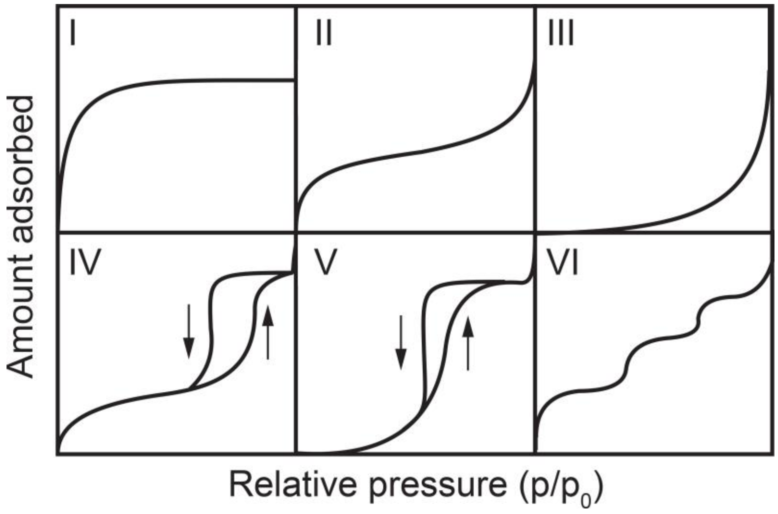

Figure 26. The six types of isotherms as defined by the IUPAC standards from p/p_0 from 0 to 1: I) micropores with single pore width; II) large mesopores and macropores with a strong interaction between the liquid and pore walls, III) large mesopores and macropores with a weak interaction between the liquid and pore walls, IV) smaller mesopores with a strong interaction between the sorbent and the pore walls, V) smaller mesopores with a weak interaction between the sorbent and the pore walls, VI) well defined sorption events, such as multilayers on graphene.[334]

At the pressure p, and considering a liquid that has a vapor pressure of p_0, molar volume of V_m and surface tension of γ, the equilibrium will be established to satisfy **eq. 33**. The Kelvin equation (**eq. 33**) shows that in a liquid-vapor system, the equilibrium will favor liquids as the droplet size becomes smaller, which may be defined by the radius of a confining pore, r. The BET setup that we used, with nitrogen gas as the adsorbate and cooled to LN_2 temperatures, is convenient because p_0 is 1 atm.

$$\ln\left(\frac{p}{p_0}\right) = \frac{2\gamma V_m}{rRT} \qquad \textbf{eq. 33}$$

Given this relationship, it is evident that with increasing partial pressure, the equilibrium will begin to favor condensation in small pores first. With this in mind, the shapes of the isotherms are understandable with respect to the pore size. If micropores are present, initial dosing of nitrogen gas into the sample tube does not lead to an increase in pressure. Rather, at $p/p_0 < 0.05$, nitrogen gas will fill the micropores. While we may gain some insight into the micropore volume, nitrogen filling micropores does not necessarily take place with efficient molecular packing, and is interpreted more meaningfully with more data points at low pressure enabled by low-pressure transducers (that we did not have) and also data analysis by density functional theory. While sol-gel materials have some micropores, the textural porosity is mainly due to mesopores.

The resulting isotherms can be interpreted by applying various models to them. The simplest model is the Langmuir model (**eq. 34**) which describes the kinetics of monolayer sorption at a given temperature. In this model that is depicted in **Figure 27**, the enthalpy difference between free and adsorbed molecules ($h_f – h_{a)}$ is q, and the mass of adsorbed species is a function of the pressure and of the reciprocal half-loading pressure, termed the Langmuir parameter (b), given in **eq. 35**.[335] While this model was groundbreaking in 1916, it does not describe the scenarios beyond monolayer sorption and interaction strength between the adsorbates and the substrate. Indeed, a Langmuir isotherm can relatively accurately describe cases with only monolayer coverage as in the Type I isotherm in **Figure 26**, and even at low partial pressures for other isotherms such as types II and IV where multilayer sorption is negligible. However, as the partial pressure is exceeded where significant amounts of multilayer adsorption occur, there is an inflection point in the isotherm (seen, for example, in the Type II isotherm in **Figure 26**) that is not described by the Langmuir model.

$$m = m_l \left(\frac{\mathrm{bp}}{1+\mathrm{bp}}\right) \qquad \textbf{eq. 34}$$

$$\mathrm{b(T)} = \frac{1}{\mathrm{p}_0}\sqrt{\frac{\mathrm{T}_0}{\mathrm{T}}}\exp\left(\frac{\mathrm{q}}{\mathrm{RT}}\right) \qquad \textbf{eq. 35}$$

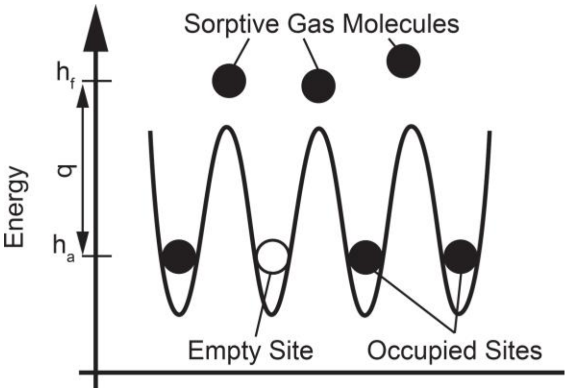

Figure 27. Schematic diagram of the Langmuir sorption model, where energy increases with the vertical axis (adapted from Keller *et al.*).[334]

An additional detail of gas sorption is that the interaction between adsorbates will effectively modify the surface properties before monolayer coverage is achieved. To account for this changing surface chemistry, the Halsey correction for heterogeneous surfaces was also used in determining surface area, where *k* is a correction factor less than 1, and *s* is a non-integer number determined by plotting $\log(\log(p_0/p))$ vs. $\log n$ where *n* is the number of adsorbed molecules. Since the nature of the heterogeniety is difficult to model, semi-empirical fitting (**eq. 36**) can improve the performance of the model.

$$\ln\left(\frac{\mathrm{p}_0}{\mathrm{p}}\right) = \frac{k}{\left(\frac{\mathrm{bp}}{1+\mathrm{bp}}\right)^s} \qquad \textbf{eq. 36}$$

As described by **eq. 37**, the inflection point can be accounted for by the BET model that considers multilayer sorption of gas molecules. For this model, the C parameter (**eq. 38**) is used to determine the pressure to form a monolayer, p_l for a gas with saturation pressure p_s. **Figure 28** shows the case of multilayer sorption on surface sites, where the adsorbates will bind to both occupied and to empty surface sites. The driving force for adsorption is the enthalpy difference between free and adsorbed molecules, $(h_f - h_a)$ for surface admolecules and $(h_f - h_l)$ for multilayer adsorption. The weaker interaction of nitrogen molecules with themselves (causing multilayer sorption) than with the surface is seen by the smaller value of $(h_f - h_a)$ than $(h_f - h_l)$. C is also exponentially proportional to the net molar energy of adsorption E_{NME} termed by Rouquerol *et al*. If C < 2, the inflection point is not pronounced enough to use the BET model, although we generally used a cutoff of C > 80.[335]

$$\frac{n}{n_l} = \frac{\mathrm{C}\left(\frac{\mathrm{p}}{\mathrm{p_s}}\right)}{\left(1-\frac{\mathrm{p}}{\mathrm{p_s}}\right)\left(1+\frac{(\mathrm{C}-1)\mathrm{p}}{\mathrm{p_s}}\right)} \qquad \textbf{eq. 37}$$

$$\mathrm{C} = \left(\frac{\mathrm{p}_s}{\mathrm{p}_l} - 1\right)^2 = 1 + \gamma^{3/2} \approx \exp\left(\frac{\mathrm{E_{NME}}}{\mathrm{RT}}\right) \qquad \textbf{eq. 38}$$

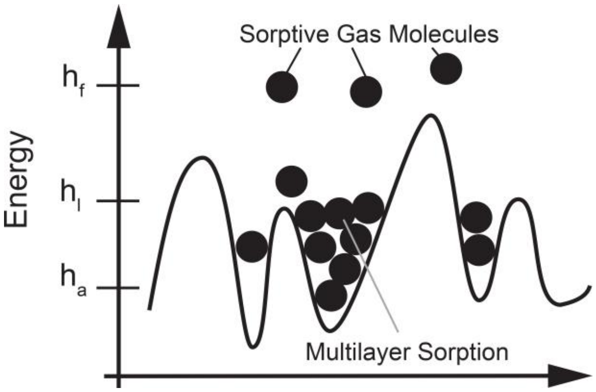

Figure 28. Schematic diagram of the BET model for multilayer sorption, where energy increases with the vertical axis (adapted from Keller *et al.*).[334]

In the pressure regime around $0.05 < p/p_0 < 0.3$, a linear and nearly flat region exists during which monolayer adsorption and desorption is occurring. At the inflection point, the analysis of monolayer coverage is carried out from the modeled C parameter, and the BET specific surface area (S_{BET}, m^2/g) is determined by the relationship given in **eq. 39**, where the specific surface area can be calculated by determining the mass of a monolayer of N_2 gas determined using the BET model ($m_{l, BET}$) nitrogen gas in the cross sectional are of an N_2 molecule is $\sigma_{N2} = 0.162$ nm^2, the molar mass of N_2 is $M_{N2} = 28$ g/mol and m_l is the mass of a monolayer of N_2 gas.

$$S_{BET} = \frac{\sigma_{N2}\, m_{l,BET}}{M_{N2}} \qquad \textbf{eq. 39}$$

The size (nm) of the primary nanoparticles can also be estimated by the specific surface area as measured by N_2 sorption studies using S_{BET} by **eq. 40**, which is derived assuming that the particles are individual spheres.

$$\text{size} = \frac{6000}{\rho\, S_{BET}} \qquad \textbf{eq. 40}$$

The Faas correction was also applied in the case where multilayer sorption was considered, as the ASAP 2020 user's manual describes that it models statistical thickness well, and it is often used in the literature.[336] An integrative approach was taken to analyze the pore size distribution within porous materials (Barrett-Joyner-Halenda, BJH) that treats the pores as cylinders with certain radii that contain differential volumes that sum to the total pore volume. However, the upper limit of capillary condensation for liquid nitrogen is 150 nm.

Evaluation of pore size distribution from the isotherm data is carried out using BJH analysis which is an iterative method. The analysis begins by defining the radius of pore confinement by the Kelvin equation. At a given pressure, pores with smaller radii than this are considered as being filled. The amount of gas is translated to a pore volume by considering it as a liquid, and filling a cylinder with the thickness calculated using **eq. 33**. The next iteration starts by defining the new pore radius and determining the partial pressure required to fill these pores.

Another useful quantity calculable given the density of a material is the fractional porosity (Porosity) that can be expressed by **eq. 41**, where the density of the material is ρ in g/cm^3, and the total pore volume (Pore Volume) is in cm^3/g. The total pore volume is the total quantity of gas adsorbed at the highest relative pressure.

$$\text{Porosity} = \frac{\text{Pore Volume}}{\text{Pore Volume} + \frac{1}{\rho}}$$ **eq. 41**

2.5 Particle Size Analysis by Dynamic Light Scattering (DLS)

The Stokes-Einstein equation (**eq. 42**), gives the relationship between the size and speed of a diffusing particle, where the hydrodynamic radius (size) is inversely proportional to the translational diffusion coefficient (D_t). The relationship is through the Boltzmann constant (k_b) and the temperature (T) and assumes spherical particles and Brownian motion. Measuring the diffusion constant of particles requires knowing the viscosity of the medium (η), and leads directly to knowing the particle size.

$$\text{size} = \frac{k_b \mathrm{T}}{3\pi\eta D_t} \qquad \textbf{eq. 42}$$

Measuring the diffusion constant of particles is carried out by the experimental setup shown in **Figure 29.** Monochromatic laser light illuminates a dispersion, and the scattered intensity is detected at a certain angle θ from the incident beam. Dynamic light scattering (DLS) experiments are carried out by measuring the intensity of scattered light at this angle, which is a function of the scattering vector q **(eq. 43)** where λ_0 is the wavelength of incident light in a vacuum and n is the refractive index of the medium. The optics will be revisited in **Section 2.5** to discuss zeta potential measurements that utilize the reference beam.

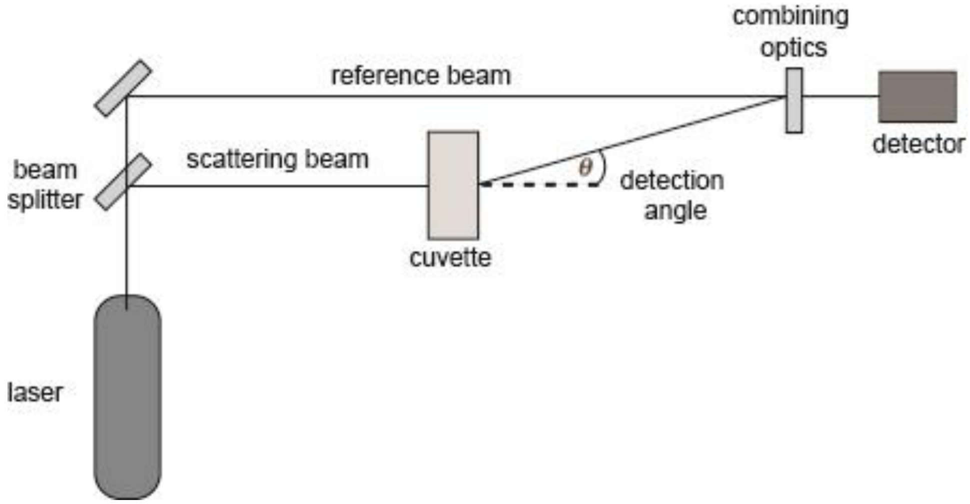

Figure 29. Optics used for the DLS and electrophoretic light scattering (ELS) measurements (adapted from Kaszuba *et al.*).[337]

$$q = \frac{4\pi n}{\lambda_0} \sin\frac{\theta}{2} \qquad \textbf{eq. 43}$$

As a dispersion is illuminated by monochromatic light, the scattered light from two particles will interfere coherently when they are separated by roughly the wavelength of the laser. Speed is related to size by **eq. 42**, and two coherently scattering particles will fall out of phase on a shorter timescale with faster diffusion based on **eq. 44** in a system undergoing Brownian motion. That is to say, the diffusion constant can be calculated by the decay rate constant (Γ) of the coherent scattering.

$$\Gamma = D_t q^2 \qquad \textbf{eq. 44}$$

The intensity correlation function ($G_2(\tau)$) **eq. 45**, is the weighted average of the fluctuations in the intensity with the delay times τ between readings. A useful way to examine the data is by Siegert's relationship that introduced A and B as experimental parameters to normalize the signal and to accounting for background signal, respectively.[338]

$$\mathrm{G}_2(\tau) \approx \frac{1}{\mathrm{N}} \sum_{i=1}^{N=large} \boldsymbol{I}(t_i)\boldsymbol{I}(t_{i+\tau}) = A\left[1 + Be^{-2\Gamma\tau}\right] \qquad \textbf{eq. 45}$$

Siegert's relationship is expanded to **eq. 46**, which is the form to be used in cumulants analysis. The additional parameter μ_2 allows for the model to account for polydispersity.

$$\mathrm{G}_2(\tau) = A\left[1 + Be^{\left(-2\Gamma\tau + \mu_2\tau^2\right)}\right] \qquad \textbf{eq. 46}$$

Second-order cumulants analysis is carried out by rearranging **eq. 46**, and setting it equal to a second order polynomial, as shown in **eq. 47**, in which the term a_0 is 0 when the signal is normalized and background-corrected, and μ_2 is 0 for monodisperse samples.[339]

$$\frac{1}{2}\ln[AB] - \Gamma\tau + \frac{\mu_2}{2}\tau^2 = a_0 + a_1\tau + a_2\tau^2 \qquad \textbf{eq. 47}$$

Fitting the data accordingly leads to the value for Γ, by which D_t can be calculated using **eq. 44**, and also the polydispersity (PDI) is expressed as **eq. 48**.[340] Having solved for D_t, the particle size can also be calculated by **eq. 42**.

$$\mathrm{PDI} = \frac{2a_2}{{a_1}^2} \qquad \textbf{eq. 48}$$

2.6 Zeta Potential Analysis

While the random and uncorrelated motions that occur during Brownian motion are analyzed by cumulants analysis of the fluctuating scattered intensity, the zeta potential measurement is carried out by heterodyning in ELS. In this technique, an electric field is applied across the dispersion of particles, and the induced movement of the particles will also cause a Doppler shift in the frequency of the scattered light (Δv) according to the equation **eq. 49**. While the instrument's detector is not geared to detect this low of a frequency shift, an interferogram is produced by combining the scattered light with the primary laser. The resulting beating wave pattern can be analyzed to extract the frequency shift.

$$\Delta \upsilon = 2\mathrm{U_E}\frac{\sin\left(\frac{\theta}{2}\right)}{\lambda} \qquad \textbf{eq. 49}$$

The cuvette used to measure zeta potential (**Figure 30, left**) is a folded capillary cuvette with electrodes at either side off the capillary. As a voltage is applied across these electrodes, the particles will experience a force proportional to the charge on their surface, that will impart movement based on the electrophoretic mobility ($U_{E)}$ described by **eq. 50** and shown in the middle of **Figure 30**. Here, ζ is the zeta potential, κ is the Debye length, a is the particle radius, η is the viscosity and f(κa) is Henry's function. A close-up of the negatively charged particle surface in the right of **Figure 30** shows various layers of interest within the diffuse layer. The surface charge will be compensated by relatively strongly associated, positively charged species such as cations, referred to as the Stern layer. The so-called 'double layer' is created due to the second anionic layer that forms on top of the Stern layer. The electric field from the particle surface is screened by the solvent and ions, and the thickness of the double-layer is determined by the inverse Debye length, which is also simplified for water at 298 K in **eq. 51**, where N_A is Avogadro's number, e is the electronic charge, ε_0 and ε_r are the permittivity of free space and of the liquid, respectively, and I is the molar ionic strength. The zeta potential is defined at the plane where ions no are no longer associated with the particle strongly enough to move with it in solution, which is defined by the Helmholtz layer. This layer is also called the surface of hydrodynamic shear or the slipping plane.

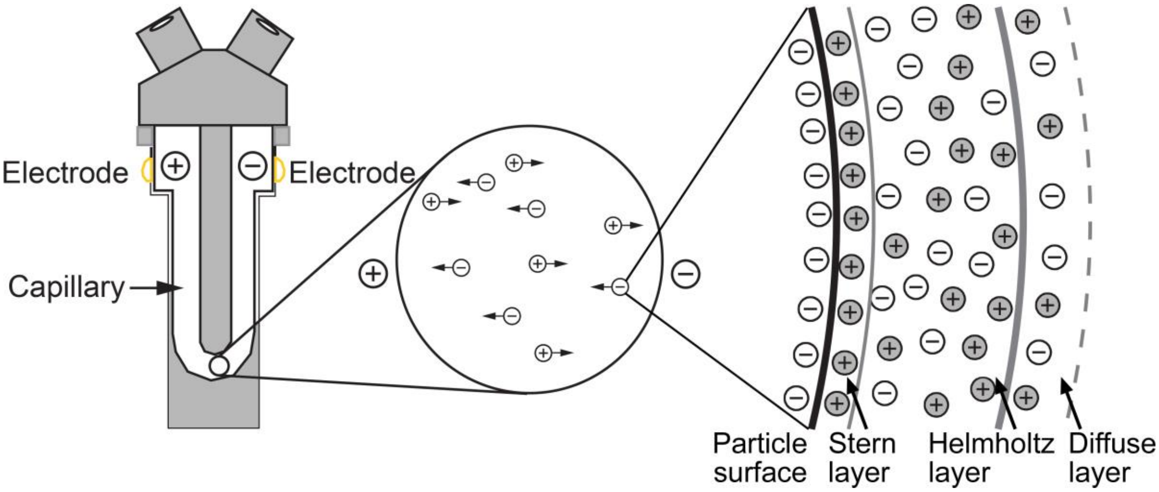

Figure 30. Folded capillary cuvette (left) used for ELS measurements. Electrophoresis toward the respective electrodes is shown in the middle circle, and the layers of electrolyte ordering within the diffuse layer around a charged particle is shown on the right.

$$U_E = \frac{2\varepsilon\zeta f(\kappa a)}{3\eta} \qquad \textbf{eq. 50}$$

$$\frac{1}{\kappa} = \sqrt{\frac{\varepsilon_0\varepsilon_r kT}{2000N_A e^2 I}} \cong 0.304\left(I^{-0.5}\right) \qquad \textbf{eq. 51}$$

The diffusion of a spherical particle in solution with mobile ions will be limited by the viscosity of the solution interacting with the particle, and by the mobile ions interacting with the diffuse layer. In the extremes where one of these forces is dominant, a different of Henry's functions is used to describe the electrophoretic mobility. In the case that the Debye length is large compared to the particle radius (Huckel limit), Henry's law will take the form of **eq. 52**, whereas when the Debye length is relatively small (Smoluchowski limit), Henry's law will be used in the form of **eq. 53**.[330]

$$\kappa\mathrm{a} > 1; \mathrm{f}(\kappa\mathrm{a}) = \frac{3}{2} - \frac{9}{2\kappa\mathrm{a}} + \frac{75}{2\kappa^2\mathrm{a}^2} - \frac{330}{\kappa^3\mathrm{a}^3} \qquad \textbf{eq. 52}$$

$$\kappa\mathrm{a} < 1; \mathrm{f}(\kappa\mathrm{a}) = 1 + \frac{(\kappa\mathrm{a})^2}{16} - \frac{5(\kappa\mathrm{a})^3}{48} - \frac{(\kappa\mathrm{a})^4}{96} + \frac{(\kappa\mathrm{a})^5}{96} - \left[\frac{(\kappa\mathrm{a})^4}{8} - \frac{(\kappa\mathrm{a})^6}{96}\right] e^{\kappa\mathrm{a}} \int_{\infty}^{\kappa\mathrm{a}} \frac{e^{-1}}{t}\, dt \qquad \textbf{eq. 53}$$

The pH will also have a critical effect on the zeta potential, as different materials exhibit different aqueous surface chemistry. As mentioned in **Section 2.2**, one important parameter of the surface chemistry is the pH of zero zeta potential (PZZP), that approximates at what pH the particle surface has zero charge. Due to the setup of the folded capillary cuvette shown in **Figure 30**, a liquid can be continuously pumped in and out of the cuvette through the openings at the top of the capillary and connected to a titration device. This setup not only enables not only the facile determination of the PZZP of dispersions, but also the titrant can be another additive such as a metal salt to modify the ionic strength, or a surfactant etc.

CHAPTER 3

SYNTHESIS AND CHARACTERIZATION OF TRANSPARENT AND NANOSTRUCTURED FILMS OF TiO_2 AND OF $Zr_xTi_{1-x}O_2$

3.1. Introduction

Due to its abundance, stability and desirable electronic structure, TiO_2 has been explored for various photochemical and photoelectrochemical applications including solar water splitting and as electrodes in devices such as dye sensitized solar cells. In light of these promising traits, transition-metal dopants can be chosen to beneficially modify the optical and morphological properties of TiO_2 for the applications. Among various dopants, isovalent Zr^{4+} has been a desirable one as its vacant 4*d* orbitals with a high energy may lead to a conduction band with a higher energy in Zr-doped TiO_2 (ZTO, or more precisely a solid solution $Ti_{1-x}Zr_xO_2$) than that of TiO_2.[341,342] Supported films (coatings) of nanoporous ZTO have been explored as electrodes in devices such as dye sensitized solar cells (DSSCs) and UV detectors,[154,163,204,205,343] owing to the higher conduction band and open circuit voltage, and improved responsivity to UV light. In DSSC applications, it has been indicated that Zr-doping effectively raises the conduction band energy and thus increases the open circuit potential of the devices.[154]

Despite the importance of the material, systematic studies on how the Zr-doping affects the band energies of ZTO have been missing in the literature. More fundamentally, there have been inconsistencies in the correlations between Zr-doping level and lattice parameters among different reports and also in the maximum level of Zr-doping (or Zr-substitution) in ZTO.[30,204,205,344-351] For example, the highest doping limits (~ 30 at%) have been reported based on powder X-ray diffraction (PXRD) studies on thin films of ZTO.[205] However, a much lower maximum doping amount (7.5 at%) has been reported for bulk samples through a systematic examination of the correlation between the Zr-doping level and the unit cell constants. Namely, the unit cell constants changed more or less linearly up to 7.5 at% within the experimental error limit, following Vegard's law.[133] Despite this trend, the results were unusual because the *c*-axis showed a decrease upon doping while the *a* axis increased without an apparent reason or explanation. Moreover, the corresponding unit cell volume change was negligible and did not show a Vegard's behavior, unlike the unit cell parameters, even below the suggested maximum doping limit. These incoherencies in the literature reflect the lack of a congruous trend among the reported optical band gaps,[203,205,345,346,352-358] and peculiarly large[203,205,353,359] or small[357] band gaps even for undoped samples. Further anomalous and inconsistent reports of Brunauer-Emmett-Teller (BET) surface area and pore characteristics exacerbate the difficulty of comparing the results from literature in terms of the influence of the nanostructures from various synthetic procedures.[345,349,352,354,356,357,360-366]

One possible reason for the inconsistencies could be related to the fact that different works employed different synthetic methods, although they can all be categorized as sol-gel methods. Sol-gel methods are advantageous for synthesis of nanostructured metal oxides because they allow relatively low calcination temperatures to retain the gel nanostructures without significant sintering and consolidation of gel-network nanoparticles. Furthermore, as far as synthesis of ZTO is concerned, sol-gel methods appear to allow a high degree of doping and maintain the anatase structure, unlike other methods that rely on co-precipitation or high-temperature calcination conditions.[367,368] However, high-valent metal ions such as Ti^{4+} and Zr^{4+} are known to undergo rather uncontrollable hydrolysis and polycondensation in typical sol-gel synthetic conditions, undermining the intended advantages of sol-gel processes.[369] Chelation of the metal ions with organic ligands may help in alleviating the problem, and yet it is not clear if the aqueous chemistries of Zr^{4+} and Ti^{4+} complexes are similar enough to provide the required homogeneity of metal ion distribution after the gelation. The inhomogeneity at various levels will lead to inconsistent results in terms of the lattice parameters, particle sizes and phase impurities in the products as well as their physicochemical properties.

The epoxide method reported by Baumann *et al.* provides a convenient means to increase pH at a controlled rate throughout the body of acidic metal precursor solutions in order to form a uniform gel.[89] By initiating the gelation with epoxides, the dissolved metal species with disparate reactivities gelate with a uniform composition at the atomic scale.[350] The method has been adapted to incorporate (dope) Sb into SnO_2 in a form of dense thin films with a relatively uniform distribution of the doping ions, resulting in desired electrical properties.[170] More recently, we have reported synthesis of highly porous Sb-doped SnO_2 films, through a modified epoxide method where inorganic/polymer dual gel network structures are utilized to preserve the porosity of the gel to the greatest extent. The interpenetrating gel structures in the dual gel support each other during solvent removal and reduce the shrinkage while retaining 3-D connectivity.

By adapting the inorganic/polymer dual gel method, herein we report systematic preparation and characterization studies of nanoporous ZTO both in bulk and in thin film forms, with a doping content from 0 to 30 at%. Various synthetic parameters including calcination temperature have been examined to establish the possible doping concentration range while preserving the porosity of the materials. After firmly establishing the relationship between the doping levels and the phase behavior, we have observed a strong violation of scissor relationship in the electronic band edge energies of the ZTO with different doping levels based on optical and electrochemical impedance spectroscopy studies.

3.2. Experimental

3.2.1 Materials Synthesis

Samples were prepared by varying the synthetic parameters of the amount of dopant and calcination temperature, which is denoted in **Tables 1** and **2**. In the sample nomenclature in the tables, the first number represents the at% of Zr doping, which was varied from 0 – 30%, and the second number stands for the temperature of calcination. Various calcination temperatures were used up to 850 °C. Further detailed characterizations and data analysis are given for the samples from the lowest calcination temperatures that could produce pure phases, as those samples have the highest porosity for our purpose. The concentrations of the organic components including resorcinol (R), formaldehyde (F) and polyethylene glycol (PEG) were fixed to [R] = 0.45 *M*, [F] = 0.90 *M* and [PEG] = 6.6 wt%, as was the total concentration of the metal ions ([Ti] + [Zr] = 0.50 *M*). The precursor amounts for the samples are given in **Table 1**.

Table 1. Nominal precursor weights (in grams) used for the synthesis of nanoporous TiO_2 and selected ZTO samples.

Precursor	TiO_2	10% ZTO	20% ZTO	30% ZTO
$Ti(OBu)_4$	6.93	6.24	5.55	4.85
Ethanol	14.47	14.36	13.51	13.14
HNO_3	2.49	2.49	2.49	2.49
$ZrCl_4$	0	0.48	0.96	1.44
H_2O	3.20	3.20	3.20	3.20
R	2.00	2.00	2.00	2.00
PEG	2.98	2.98	2.98	2.98
ECH	9.52	10.51	12.62	14.00
F	3.04	3.04	3.04	3.04

For a typical procedure, using sample 10-500 as an example, 6.24 g (18.3 mmol) of titanium *n*-butoxide ($Ti(OBu)_4$) (Mw = 340.32 g/mol; Sigma-Aldrich, 97%) was added to 14.4 g absolute ethanol (Koptec, 200 proof) in a 70 mL-glass bottle, and the solution was acidified with 2.49 g (27.5 mmol HNO_3) concentrated nitric acid (EMD, 15.7 *M*). In a separate bottle, 0.48 g (2.0 mol) of $ZrCl_4$ (233.04 g/mol; Alfa-Aesar, 99.5+%) was hydrolyzed by 3.20 g of deionized water (*Caution*: exothermic reaction). Once the solution cooled down, it was added to the $Ti(OBu)_4$ ethanolic solution with swirling. 2.98 g of polyethylene glycol copolymer (PEG) (Sigma-Aldrich, 15-20 kDa) and 2.00 g (18.2 mmol) of resorcinol (110.1 g/mol; Sigma-Aldrich, 99%) were dissolved while magnetically stirring up to an hour to yield an orange, clear solution. The solution bottle was placed in an ice bath for about 15 minutes before 10.51 g (113.6 mmol) of ±-epichlorohydrin (92.52 g/mol; Fluka, ≥99%) and subsequently 3.04 g (37.4 mmol HCHO) formaldehyde solution (Sigma-Aldrich, 37 wt% in water with 10 – 15 wt%

methanol) were weighed into the solution. The solution was then put in the ice bath for another 10 minutes. It is noted that epichlorohydrin must be added prior to formaldehyde solution. Otherwise, only precipitates would form instead of the desired monolithic gel.

When the solution was taken out from the ice bath and was gradually warmed up to room temperature, the pH of the solution slowly increased from zero to four, which was accompanied by an increase in viscosity and by turning from transparent orange to translucent deep red. After about four hours, the solution formed a soft gel which was then aged for one day to yield a translucent, maroon-colored monolith. The color change suggests some degree of R-F polymerization. This gel was heated to 70 °C for three days to produce a hard, red-brown composite gel. The monolith was then broken up and dried ambiently for at least one day. Subsequently, this composite xerogel was heated in an ashing furnace (Carbolite, AAF1100) at a rate of 100 °C per hour to 500 °C, where it was calcined for 10 hours.

To prepare films of the same materials, the precursor solution was deposited on a fluorine-doped tin oxide glass (FTO) (Hartford Glass, Tec 7) substrate. To prepare the substrate, FTO slides were washed with soapy water, rinsed well, and sonicated in an acetone bath for five minutes. A scotch tape mask was applied to cover three edges of an FTO slide to define both the coverage area and the thickness of the final nanoporous films. The doctor blading technique was employed to apply the film. A small amount of the precursor solution was dropped on the edge opposite to the un-masked edge, and drawn smoothly and quickly across the slide with a Pasteur pipette. The wet films were immersed in mineral oil (Spectrum, extra heavy) within about 10 seconds after the deposition and heated at 70 °C in a laboratory oven. After the films were taken out from the oil bath, the tape was removed and residual mineral oil was rinsed off with hexanes before calcination.

3.2.2 Materials Characterization

Powder X-ray diffraction (PXRD) was conducted on a Bruker D8 diffractometer using Cu Kα radiation. Both primary and secondary goniometer radii were 205 mm, and the Si-strip linear position sensitive detector had a forward dispersion slit angle of 1° and a beam spill of 12 mm. The crushed bulk sample was spread on a quartz plate, and the data presented was acquired by scanning 2θ from 5 to 90°, with a step size of ~ 0.016° and a scan time of 60 minutes. The samples were pre-mixed carefully with a silicon powder internal standard (Deane K. Smith; X-ray diffraction accessories). The (111) Si reflection at $2\theta = 28.443°$ was used as a reference for sample peak positions. The full-width half-maximum of the microcrystalline silicon standard was measured to be $2\theta = 0.1°$, which was subtracted from the full-width half-maximum of the measured Bragg peak before applying the Scherrer equation for particle size estimation. The unit cell constants of the anatase-type products were determined from all the indexed Bragg reflections in $2\theta = 15 – 90°$ by using TOPAS 4.2 Software program (Bruker). Elemental analysis was performed on a Thermo iCAP6300 inductively coupled plasma optical emission spectrometer, (ICP-OES).

Nitrogen sorption isotherms were collected on a Micromeritics TriStar II 3020 Surface Area and Porosity Analyzer at 77 K. Samples were degassed under flowing N_2 at 150 °C for 8 hours. For surface area calculation, the Brunauer-Emmett-Teller (BET) model was applied to the adsorption branch in the partial pressure range of 0.05 – 0.2 and all samples showed the C value in the range from 80 to 110. The Barrett-Joyner-Halenda (BJH) model was applied to the desorption branch to calculate pore-size distribution using the Halsey thickness curve, heterogeneous surfaces and Faass correction to account for multilayer desorption in estimating the thickness of the adsorbed nitrogen.[370] Total pore volume was approximated by the total quantity of gas adsorbed at the data point closest to $P/P_o = 0.98$ on the desorption branch.

Scanning electron microscopy (SEM) studies were performed on films on FTO and on dry-ground samples on carbon tape using an FEI XL-30 Environmental SEM using 10 keV electrons. For transmission electron microscopy (TEM) and high-resolution TEM (HR-TEM) studies, samples were prepared by dry-grinding and dusting onto TEM grids. High resolution TEM and scanning TEM (STEM) images, as well as small-angle electron diffraction (SAED) patterns and electron dispersive X-ray spectra (EDS), were collected on a JEOL 2010F at an accelerating voltage of 200 kV. UV/Vis absorption spectra of the transparent thin films were obtained on a Shimadzu UV-1601 UV-Vis spectrophotometer using quartz cuvettes as sample holders, and the corresponding reflectance spectra were obtained on a Perkin Lambda 18 spectrophotometer equipped with a Spectralon reflectance sphere accessory.

Electrochemical impedance spectroscopy (EIS) measurements were carried out on thin films on FTO glass and also on dense pellet electrodes immersed in $LiClO_4$ (1 *M*) aqueous solution with a platinum counter-electrode and an Ag/AgCl reference electrode. Pellets were produced as working electrodes by pressing dried and well-ground powder samples (0-500, 10-500 and 20-600) around 6000 psi and sintering at 450 °C for two hours in air. Then, each pellet was connected to a copper wire with carbon paste, mounted in a chemical epoxy resin (CaldoFix-2 kit, Struers) and polished (SiC paper, grid 1200 and 4000) to give a smooth electrode surface. A potentiostat/galvanostat (CH Instruments, model 600 d) was used in the frequency range of 10 Hz to 100 kHz for the measurements, in which an AC voltage (5 mV in amplitude and a frequency range of 1 to 10 kHz) was imposed in a potential range of – 0.8 ~ 0.2 V vs. Ag/AgCl.[188] Subsequently, the interface semiconductor/electrolyte capacitance (c) was determined according to the imposed potential (e) using a simplified Randles equivalent circuit represented in **Figure 31**,[371] where the diffusion (the Warburg) in the faradic part was neglected at high frequencies (0.8 – 10 kHz) because it was not visible in the Nyquist diagram. Thus, it consists of a series resistance (R_S), representing mainly the faradaic and contact resistances and the resistance of the electrolyte, in series with a constant phase element (CPe), namely a pseudo-capacitance (Q), which is in parallel with the charge transfer resistance (R_{CT}) associated with the electron transfer between the semiconductor and the electrolyte. The impedance of the CPE is given by $Z_{CPE} = 1/(Q(j\omega)^{\alpha})$, where j, ω and α represent the imaginary unit, the pulsation frequency and the difference from an ideal capacitance (when $\alpha = 1$), respectively. The flat band potential (U_{fb}) and the charge carrier density ($N_{a)}$ were then deduced from the Mott-Schottky plot (C_{SC}^{-2} vs. E) which utilizes Mott-Schottky equation for an *n*-type semiconductor: $\frac{1}{C_{SC}^2} = \frac{2}{\varepsilon\varepsilon_0 e A^2 N_D}(EUE_{fb} - \frac{kT}{e})$, where C_{SC} is capacitance in the space charge region of the semiconductor, A the interfacial surface area between the semiconductor electrode and the electrolyte, k the Boltzmann constant, T the temperature, *e* the electron charge, ε_0 the vacuum permittivity and ε the relative permittivity of the semiconductor. For the calculations, C_{SC}^{-2} was approximated to be C^{-2} due to the large capacitance of the Helmholtz layer, at the semiconductor surface in the electrolyte, in comparison to C_{SC}. Semiconductor capacitance (C) was then calculated according to the following formula derived from Brug *et al.*, and Mott-Schottky plots were obtained.[372]

$$C = Q^{\frac{1}{\alpha}} \left(\frac{1}{R_S} + \frac{1}{R_{CT}} \right)^{\frac{(\alpha-1)}{\alpha}}$$

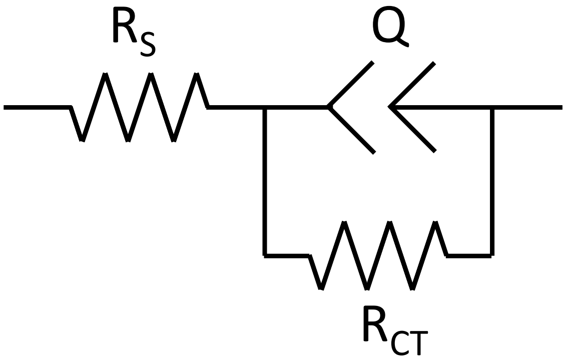

Figure 31. Model of the electrochemical circuit employed for impedance measurements on nanoporous ZTO materials.

3.3. Results and Discussion

3.3.1 Sol-Gel Synthetic Procedure

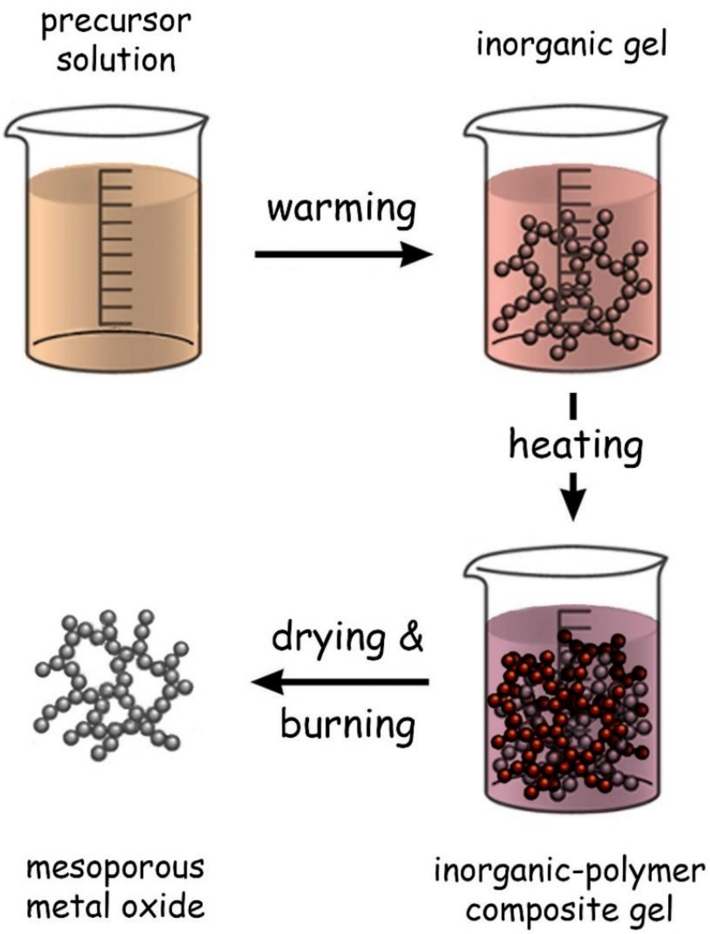

Figure 32. Synthetic Scheme of the porous ZTO materials.

The overall synthetic procedure to produce nanoporous TiO_2 and ZTO is depicted in **Figure 32**, which is adapted from Volosin *et al*.[134] This procedure has been essential in production of highly nanoporous metal oxides with uniform chemical compositions despite the high-temperature calcination in a later step. Subsequent inorganic gelation and organic polymerization create a 3-D network of interpenetrating hydrous metal oxide and R-F polymer gels throughout the solution. Drying and calcination of this composite gel produces the nanoporous metal oxides during which the R-F polymer acts as a sacrificial buttress, keeping the porosity of the gel. The $Ti(OBu)_4$ and $ZrCl_4$ precursors are hydrolyzed in the acidified water/ethanol mixture solvent and the initial pH of the precursor solution was adjusted to be about 0.15 based on the estimation from the concentrations of the precursors. When the pH was higher than 0.18, the precursor solution turned to an opaque gel within a minute, which needs to be avoided. This pH-dependent stability of the solution is consistent with a previous work by Chong *et al.* in which the acidified precursor solutions of hydrolyzed $Ti(OBu)_4$ gelated even without an initiator when the solutions were prepared to have a pH above 0.22.[373-375] In comparison to the previous reports,[134,373,374,376] our synthesis employs a strongly acidic water/ethanol solution with a larger amount of water to promote a rapid hydrolysis and subsequently stabilize the hydrolyzed metal ions, which is critical for consistent results. To induce gelation by the inorganic precursors, the pH of the precursor solution was gradually increased by using epichlorohydrin as the acid-scavenger.[377] The gelation usually took a few hours at room temperature and the final pH was around 4. Propylene oxide was tested for acid scavenging but our preliminary results indicated that the epoxide was too reactive to achieve the desired gradual pH increase and resulted in inhomogeneous gels.

The precursor solution initially showed an orange color and the color intensified during gelation and aging of the inorganic gel at room temperature. After 24 hours of aging, the gel became rigid and deep red in color but translucent. In well-documented reaction mechanism of polymerization,[378] the condensation reaction of resorcinol with formaldehyde can produce methylene bridged resorcinolic resin structures in the presence of an acid catalyst. The deep red color of the gel, an indication of R-F polymerization, is caused by *o*-methide quinone by-product of the reaction at a low pH (~0.2 in our case).[379] In our experiments, the remaining mild acidity after gelation (pH ~ 4) might have been enough to catalyze the polymerization at an elevated temperature (70 °C). It is also plausible that the hydrous titania and zirconia species provided some acidity from hydrolysis of aquo- or hydro-ligands. Meanwhile, the initial orange color appears to be unrelated to the R-F polymerization process in our experiments, as it occurred only when the $Ti(OBu)_4$ and resorcinol were co-present even in the absence of formaldehyde. Without resorcinol, the resulting wet gels were pale yellow, which is the innate color of the gel as verified by a control experiment where the gels were prepared without any organic components except the $Ti(OBu)_4$.

Upon heating at 70 °C, the R-F polymerization was more complete, as expected from our previous work,[134] during which the gel became even darker and gained a texture like a hard rubber. After drying and calcination, the final products were white and the CHN analysis indicated that they were free of organics (**Table 2**). As shown in **Figure 33**, the relative amounts of Zr and Ti elements were consistent with the nominal compositions within the errors of 2.8%, from the ICP-OES results on two sets of independent sample batches. Although not detailed here, the TEM-EDS results were consistent with these results.

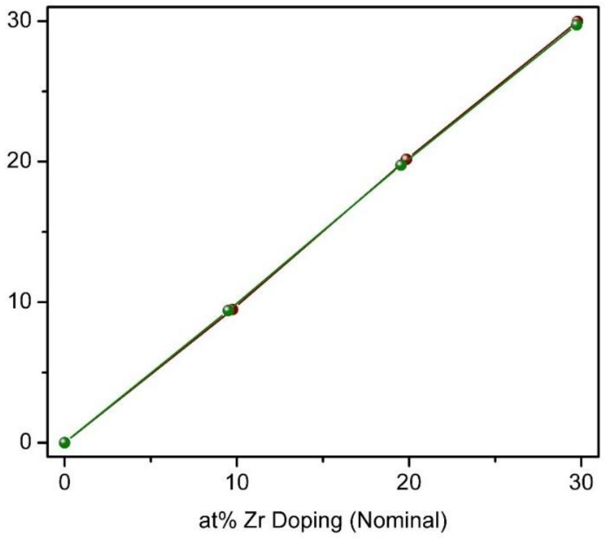

Figure 33. Elemental analysis results from optical emission spectra compared to the nominal elemental compositions for the nanoporous ZTO materials. Results from two individually prepared ZTO sample sets are shown in red and green.

Table 2. CHN elemental analysis on selected ZTO products.

Sample	Wt% C	Wt% H	Wt% N
0-500	0.117	0.372	0.015
10-500	0.034	0.233	0.004
20-600	0.064	0.245	0.014
30-500	0.1	0.29	0.015

3.3.2 Effect of Calcination Temperature on Phase Formation

The phase formation of TiO_2, 10%, 20% and 30% ZTO samples was examined at various calcination temperatures between 500 and 850 °C by using PXRD studies (**Figure 34**). Diffraction patterns in **Figure 34a** show that the Bragg peaks and intensities of the undoped sample match the simulated pattern of anatase, shown with vertical, red lines, and that the peaks become suddenly sharp above 600 °C. This nanocrystalline TiO_2 exhibits typical behavior for sol-gel produced TiO_2, in that the phase transition to rutile (diffraction peaks indicated by 'R') becomes visible in PXRD with calcination at 600 °C, and that the nanoparticles begin to sinter into a bulk material more significantly when held above 600 °C.[143] The coinciding phase transition and coarsening are dependent as described by Navrotsky *et al.*, and are difficult to pinpoint because the synthetic method strongly affects the thermal phase behavior of TiO_2 and ZTO materials.[105-107] In our synthesis, the phase transition does not occur below 600 °C, and coarsening of the anatase product is well suppressed like in previous sol-gel syntheses.[345,346,380-384]

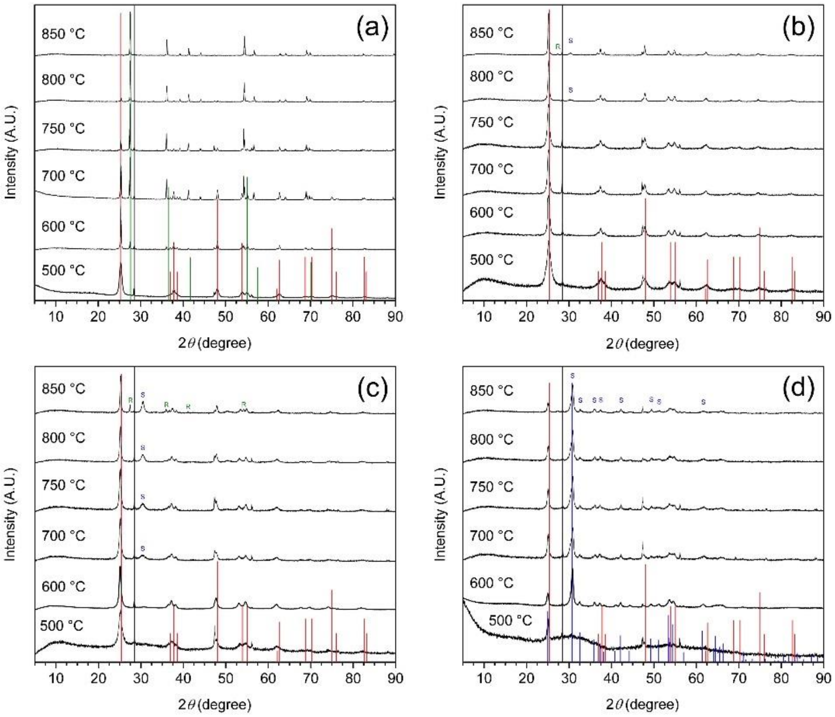

Figure 34. Powder XRD patterns of nanoporous ZTO samples after calcination at different temperatures. The patterns shown are (a) TiO_2, (b) 10% ZTO, (c) 20% ZTO, and (d) 30% ZTO. The silicon standard is marked by a vertical black line at $2\theta = 28.44°$, and the anatase Brag peaks are indicated by the red vertical lines. Rutile peaks are labeled with 'R', and srilankite peaks are labeled with 'S'.

In contrast to TiO_2, 10% ZTO undergoes almost no transformation into rutile TiO_2 (diffraction peaks indicated by 'R'),[30,203,344-350,354,357,359,361-366,380,385-390] while maintaining a small average crystallite size (<30 nm; see the sample 10-800 in **Figure 34b**), in agreement with previous works.[133,345,349,382] Above 750 °C, a small amount of srilankite $ZrTi_2O_6$ phase (Bragg peaks indicated by 'S') appears in the product. The srilankite phase has 33% Zr in the structure and the emergence of the phase appears to be at the expense of the Zr content in the anatase phase, as the major (101) anatase peak shows a small but apparent shift to a higher angle when calcined above 750 °C, especially at 850 °C. In other words, the single phase formation of the targeted 10% ZTO is possible only with the calcination temperature below about 800 °C.

Upon increasing the doping content to 20%, the phase formation exhibits a more complex behavior, as seen in **Figure 34c**. In the sample 20-500, the anatase phase is predominant but with a relatively poor crystallinity, while an amorphous component coexists as indicated by a broad hump with a low intensity centered around 30°. When calcined at 600 °C, the product shows only an anatase phase with a good crystallinity. However, the srilankite phase starts to appear above 700 °C, with an increasing amount as the calcination temperature increases. Like in the 10% Zr samples, the anatase phase loses its Zr by the increased formation of the srilankite, which is indicated by the higher-angle shift of the (101) Bragg peak. The pure anatase phase with the maximum incorporation of Zr is achieved at 600 °C.

Meanwhile, the phase formation behavior of the 30% ZTO samples indicates the anatase phase as a less stable one. The sample 30-500 shows weak anatase peaks, but with a significantly large broad hump centered around 30°. With a higher calcination temperature, the broad hump is replaced by a dominating peak at 30.8°. This peak and other new peaks can be assigned to the srilankite phase for all the 30% ZTO samples. Interestingly, the anatase peaks, as well as the srilankite peaks, do not show a shift above 700 °C, implying that the system is at its thermodynamic equilibrium as far as the chemical compositions are concerned. It was not possible to obtain a pure anatase product and in fact the srilankite phase was dominant at any temperature where the phase could be crystallized.

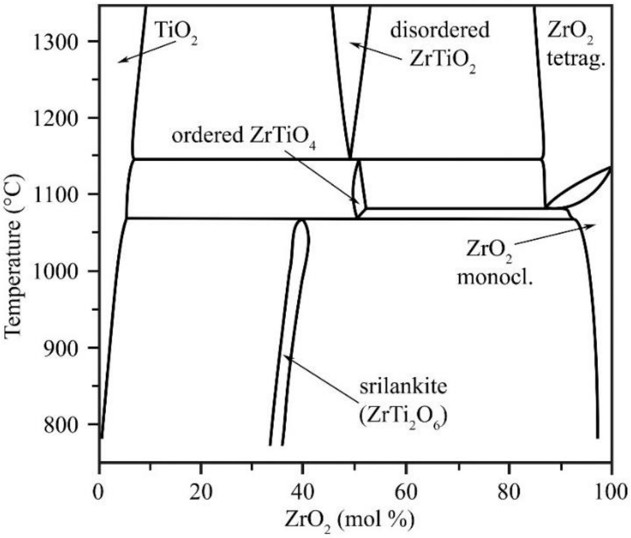

Figure 35. Phase diagram of ZrO_2 in TiO_2 at high temperatures, adapted from Troitzsch 2005.[391]

In the literature, it appears that the nature of the coexisting srilankite phase has not been clearly described. In one study, it was reported that $ZrTiO_4$, which is isostructural to the srilankite phase, was formed as a minor phase for the ≥ 30% ZTO compositions above 700 °C for one hour,[345] but a closer inspection of the Bragg peak positions indicates that the minor phase is actually closer to the srilankite. In another report,[350] the 30% ZTO product showed a $ZrTiO_4$ phase after calcination at 600 °C for 2.5 hours, and yet above 600 °C, co-presence of both srilankite and $ZrTiO_4$ phases was apparent based on the PXRD pattern. **Figure 35** shows the experimental TiO_2-ZrO_2 phase diagram at temperatures above ~ 750 °C.[391] No phase diagram is available at lower temperatures and the one in **Figure 35** serves only as a guide at the thermodynamic limit in which both Ti^{4+} and Zr^{4+} ions are stabilized in the most desired ligand environment. By extrapolating the phase diagram to lower temperatures, therefore, we expect that only the srilankite phase, not $ZrTiO_4$, would appear as a possible crystalline phase if the nominal Zr-loading turns out to exceed the highest Zr-content that can be achieved in the ZTO at the calcination temperature. This is indeed the case in our studies.

In any event, exhaustive comparison of our results with the literature indicates that the targeted anatase phase appears to be less thermally stable in our studies than what we expected from others, and the undesired srilankite phase starts to show up at a lower calcination temperature. It is noted that the calcination was carried out for 10 hours in our studies instead of one to three hours,[203,344,345,349,350] and thus the kinetics of the phase formation must play a role for the observed discrepancies. In previous differential thermal analysis (DTA) studies of ZTO, it has been concluded that the activation energy for crystallization of anatase phase increases as the Zr content in the ZTO increases.[347] All these point to the importance of a balance required between calcination temperature and duration, not to mention the relevance of the homogeneity of the metal ion distribution in the gel. While low temperature and short heating time for calcination are preferred for formation and stabilization of the targeted anatase phase, such conditions may not afford more equilibriated incorporation of Zr in the final anatase phase. Longer periods have been used in some studies for lower temperature calcinations (4 hours at 500 °C and 8 hours at 550 °C) in order to preserve the anatase structure, and yet it was not clear if the resulting anatase phase had the highest possible homogeneity in Zr distribution in the structure.[346,383]

In **Figure 36**, PXRD patterns of the samples 0-500, 10-500, 20-600 and 30-500 all calcined for 10 hours are shown together for comparison. The samples were chosen as they exhibited a single anatase phase (except for the 30% doping) after calcination at the lowest possible temperature for a reasonable crystallinity. **Figure 37** shows the trend of the unit cell lengths and volume as a function of the nominal Zr-loading in our studies (in red; a = 3.7855(22) Å, c = 9.5111(57) Å, V = 136.29(23) Å^3 for 0-500; a = 3.7985(30) Å, c = 9.5917(20) Å, V = 138.40(21) Å^3 for 10-500; a = 3.8136(25) Å, c = 9.6752(46) Å, V = 140.71(24) Å^3 for 20-600; a = 3.8122(18) Å, c = 9.7312(67) Å, V = 141.42(2.18) Å^3 for 30-500) together with the previous results in the literature.[133,350,381,386,388] The unit cell constants from the literature are fairly scattered and do not show a particular trend, although they tend to increase with the increase in the Zr-loading.

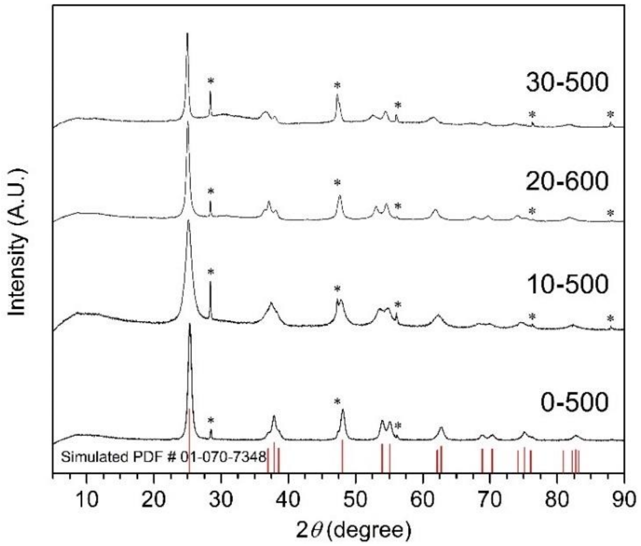

Figure 36. PXRD of nanoporous ZTO samples 0-500, 10-500, 20-600 and 30-500, in order from bottom to top. The red lines show the anatase Bragg reflections and the stars indicate the reflections from a Si standard.

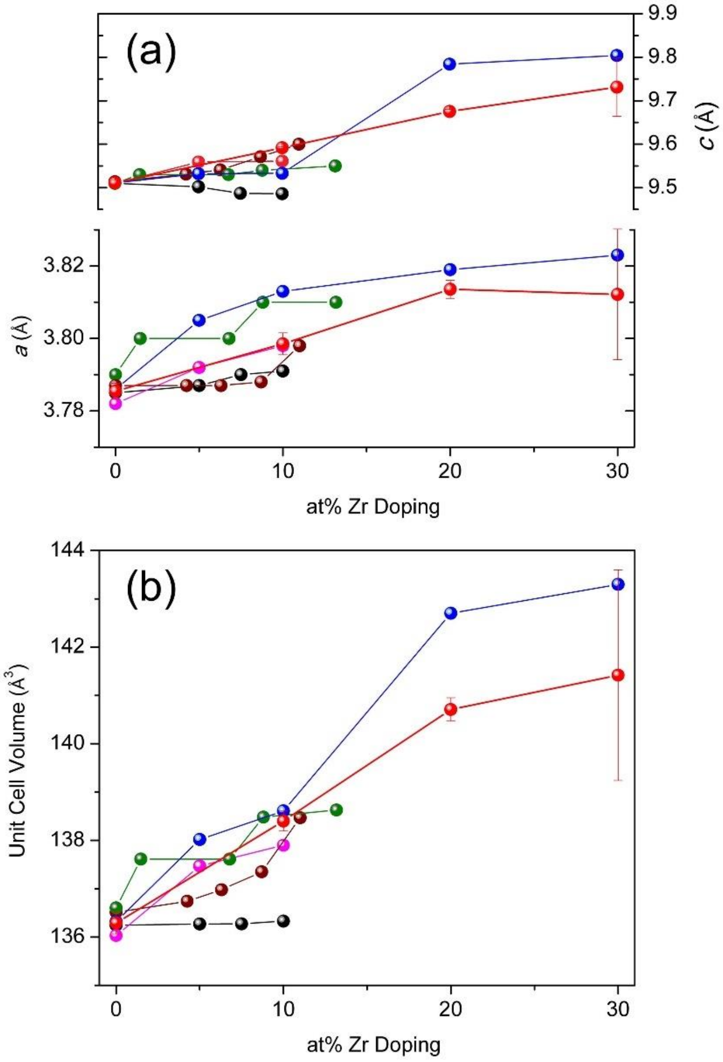

Figure 37. (a) Unit cell parameters and (b) unit cell volume for sol-gel derived ZTO materials, as a function of Zr loading. The nanoporous ZTO materials synthesized by the reported R/F method are shown with red spots connected by thick lines. Sol-gel products from the literature are shown as connected by narrow lines: Lejon *et al.* (green),[386] Lucky *et al.* (pink),[381] Wang *et al*. (blue),[350] Naumenko *et al.* (maroon),[388] and Yang and Ferreira (black).[133]

However, our results clearly show a linear relationship between unit cell parameters and the Zr-loading up to 20%, indicating that the ZTO system does follow Vegard's law up to a certain doping content. While not certain due to the large errors among the different batch samples, the deviation from the Vegard's law for the 30%

doping is understandable as the Zr amount in the anatase phase would be greatly affected by the co-existence of the srilankite as the major phase. Formation of the srilankite ($ZrTi_2O_6$) reduces the amount of Zr available for the co-existing ZTO and hence the Zr content in the ZTO would be lower than the nominal 30%. Based on the unit cell volume obtained at 30% in **Figure 38**, the actual Zr content in 30-500 is estimated to be 23% on average, from the extrapolation with unit cell volume which we obtained from the linear curve in **Figure 38b** (Unit cell volume ($Å^3$) = 0.221·(at% Zr) + 136.26 ($R^2 = 0.999$)). This value may be considered as the maximum Zr-loading for ZTO regardless of the co-presence of other phases in the products, although the large uncertainty of the unit cell constant estimation needs to be taken into account. If we assume the 23% ZTO and srilankite (33% Zr) as the only existing phases at the 30% nominal composition, the law of mass conservation indicates that the two phases amount to 1/3 and 2/3 of the total, respectively, although the exact amounts are not certain due to the small but non-negligible phase width of srilankite. These relative amounts are in agreement with the presence of the srilankite as the major phase as can be seen in the PXRD patterns of 30%-ZTO at the high temperatures (**Figure 34**) where the srilankite becomes crystallized.

One might be also intrigued about the maximum Zr-content achievable in the anatase at a high temperature where the system would behave more closely to the thermodynamics. Although not detailed here, the anatase in 10% ZTO sample maintained its Zr amount even at 850 °C, as interpolated from the refined unit cell parameters, while at the same temperature the 20% ZTO sample lost Zr down to 11% at the expense of the srilankite formation. These final Zr contents are much higher than the negligible Zr solubility (less than one at%) shown in the thermodynamic phase diagram

(**Figure 34**). The thermodynamic stability of ZTO in the anatase structure has not been explored, as the anatase in pure TiO_2 itself is stable only below 600 to 700 °C. Our work indicates that anatase ZTO can be stable above those temperatures with a Zr-content up to about 10 at% even after a reasonably prolonged calcination time.

3.3.3 Surface Area and Pore Structure from Nitrogen Sorption Experiments

Specific surface areas and pore characteristics are compared here for the samples 0-500, 10-500, 20-600 and 30-500: the ones that were calcined at the minimum temperature required to obtain phase-pure PXRD patterns of ZTO at a given Zr-loading. This also allowed for the resulting products to exhibit the highest possible surface areas and porosities, as we intended. The N_2-sorption isotherms of the samples are shown in **Figure 38a**, and the corresponding BET surface areas were 64, 136, 79 and 136 m^2/g, respectively (**Table 3**). The estimated surface areas are in the range reported from the previous works and also show a general trend of increased surface area upon Zr-doping for the same calcination temperature. Not surprisingly, a higher calcination led to a lower surface area (79 m^2/g for 20-600 vs. 148 m^2/g for 20-500). It is worth mentioning that the surface areas of our products are high overall in comparison to some of the previous reports both for TiO_2[352,354,362,363,383] and for ZTO.[345,356,357,362,382,383] We notice that most of the sol-gel-based TiO_2 and ZTO products exhibiting a high surface area, including the ones from our work, were prepared in a strong mineral acid medium during the sol-gel synthesis.[349,357,361,364]

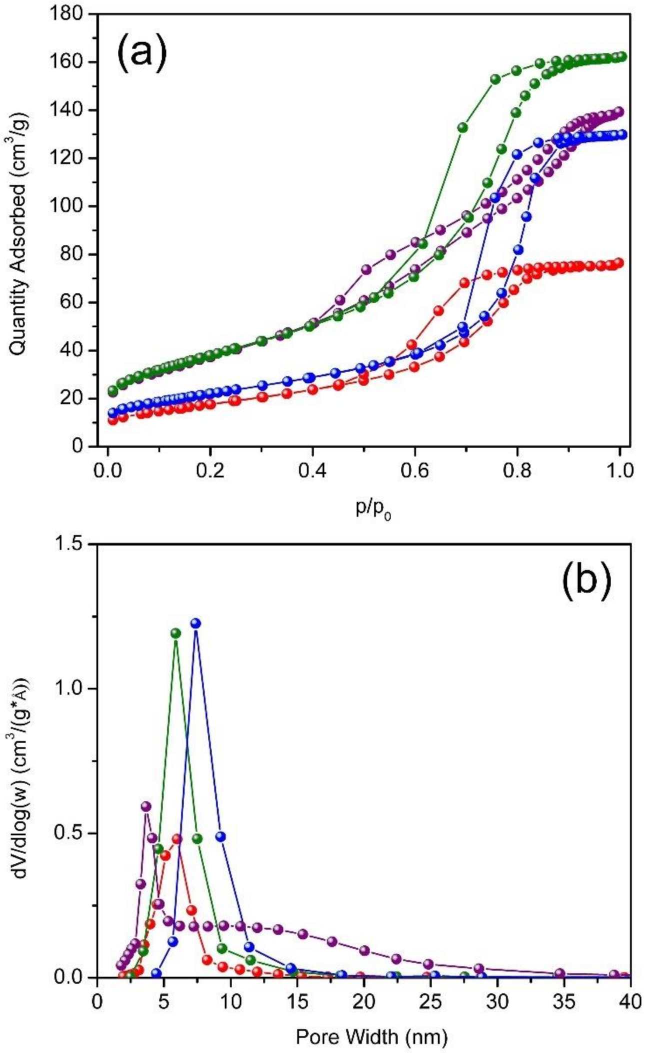

Figure 38. N_2 sorption isotherms (a) and BJH pore size distributions (b) for samples 0-500 (red), 10-500 (green), 20-600 (blue) and 30-500 (purple).

The presence of mesopores is evidenced by the observed type IV isotherms with H1-type hysteresis loops for 0-500, 10-500 and 20-600, and with a combination of H1- and H3-types[392] for 30-500 (**Figure 38a)**. The corresponding pore widths and total pore volumes are 7.2, 7.5, 10.3 and 6.3 nm, and 0.12, 0.26, 0.20, and 0.22 cm^3/g for 0-500, 10-500, 20-600 and 30-500, respectively (**Table 3**). For the same respective samples, the hysteresis loops are the widest around partial pressures of p/p_0 = 0.7, 0.7, 0.75 and 0.5, which are correlated with the peak positions in **Figure 38b** that shows the BJH pore size distributions of the samples.

It is emphasized that the high porosity of the samples could be achieved by using the R-F polymer gel network as a buttress (or template) to retain the porosity of the gel during the prolonged calcination. Without such a sacrificial porogenic component, the original gel porosity hardly remains unless the calcination is carried out at a very low temperature (lower than 500 °C) and for a short period of time (fewer than four hours).[349,357,364] This was clear in our control experiment in which the same synthetic procedure was followed but without PEG and R-F polymer precursors. The TiO_2 product calcined at 500 °C was dense with a final surface area of 2.1 m^2/g and a negligible pore volume (0.003 cm^3/g). The ZTO products calcined at the same temperature did show a high surface area (140, 128 and 149 m^2/g for 10, 20 and 30% Zr, respectively), but their pore volumes were still low (0.15, 0.10 and 0.05 cm^3/g) with small pore widths (not larger than 4 nm). Their N_2 isotherms and BJH pore distributions are shown in **Figure 39**, and the hysteresis loops are H2-type, indicating inhibited diffusion and some closed pores within the pore network.[393] In comparison to the control TiO_2, the starkly high surface areas of the control ZTO products is consistent with the previous observations[345,346,394] and highlights the effect that Zr incorporation preserves the nanoparticle size inherent from the sol-gel methods.

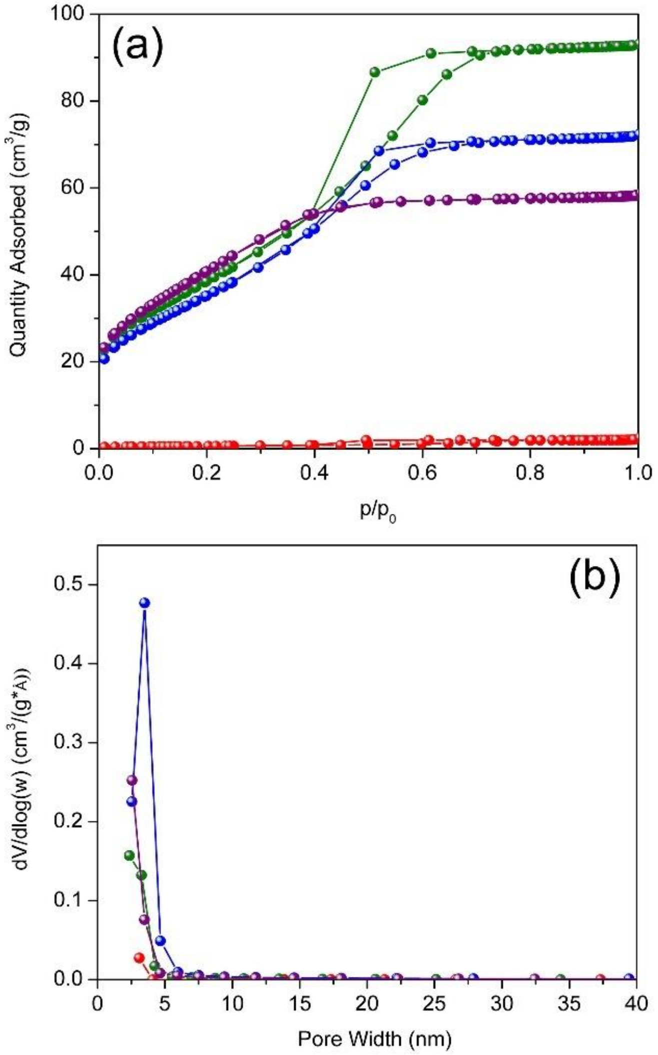

Figure 39. N_2 sorption isotherms (a) and BJH pore size distributions (b) for the dense samples TiO_2 (red), 10% ZTO (green), 20% ZTO (blue) and 30 % ZTO (purple).

3.3.4 Microscopic Morphologies from SEM and TEM Studies

Figure 40 shows the SEM images of 20-600 in bulk (lightly ground; **a** and **b**) and coated on FTO glass slide (**c** and **d**) as representatives, since all the samples appear to be similar under the SEM. The powder particles in **Figure 40a** show fractured surfaces which indicate the brittle nature of the material. In **Figure 40b**, their microstructure exhibits a homogeneous textural porosity among the individual particles with a particle size around 20 nm. In the form of a film, the sample shows a smooth and homogeneous surface (**Figure 40c**) whose higher magnification image indicates a uniform pore structure (**Figure 40d**).

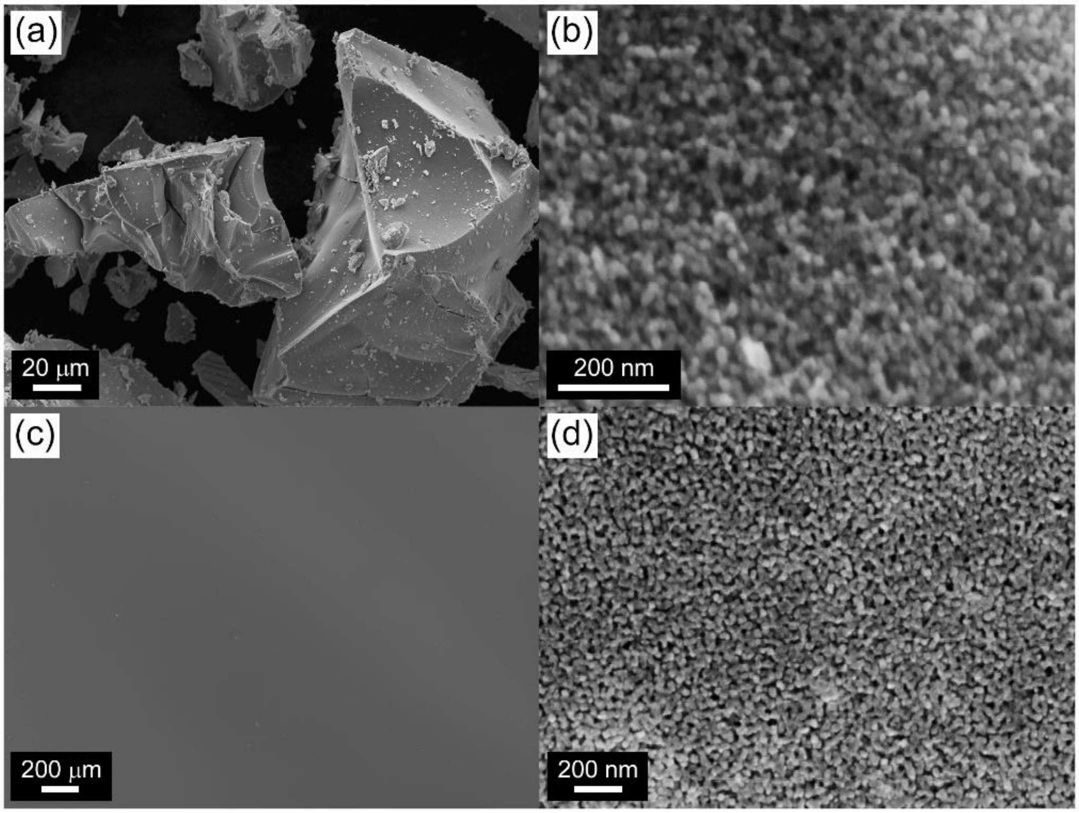

Figure 40. Scanning electron microscope images of the sample 20-600. Frames (a) and (b) are of the bulk material and the scale bars are 20 μm in (a) and 200 nm in (b). Frames (c) and (d) are of the thin film. The scale bars are 200 μm in (c) and 200 nm in (d).

Table 3. Surface areas and pore characteristics of the products. See the Experimental section for the sample naming convention. The samples in bold are extensively discussed throughout the text.

Sample	BET Surface Area (m^2/g)	Pore Volume (cm^3/g)	Average Pore Size[a] (nm)	Porosity[b] (%)	Crystallite Size (nm)[c]
0-500	64.3	0.12	7.2	33	18.9 ± 4.9
10-500	136	0.26	7.5	48	8.43 ± 1.2
20-500	148	0.23	6.1	49	14.3 ± 2.5
30-500	136	0.22	6.3	45	29.4 ± 3.8
0-600	44.9	0.10	8.5	29	60
10-600	113	0.24	8.4	49	21
20-600	78.7	0.20	10.3	43	24.3 ± 4.3
30-600	84.4	0.22	10.5	48	–
0-500-noRF	2.1	0.003	3.2	1.1	36
10-500-noRF	140	0.15	3.5	38	6.4
20-500-noRF	128	0.10	3.2	29	8.2
30-500-noRF	149	0.05	2.8	17	7.9

[a] 4·(total pore volume)/(BET surface area)

[b] Based on Porosity $= \frac{\text{Pore Volume}}{\text{Pore Volume} + \frac{1}{\rho_{ZTO}}}$ where ρ_{TiO2} = 3.90 g/cm^3 is assumed to be the density of TiO_2, ρ_{ZTO1} = 4.06 g/cm^3 is assumed to be the density of 10% ZTO, ρ_{ZTO2} = 4.19 g/cm^3 is assumed to be the density of 20% ZTO, ρ_{ZTO3} = 4.34 g/cm^3 is assumed to be the density of 30% ZTO.

[c] The values with standard deviations were an average from 3 to 5 samples from different batches.

More detailed structural features were revealed in the TEM studies for the samples 0-500, 10-500, 20-600 and 30-500 (**Figure 41**). The first three samples exhibit a grape-like network of spherical nanoparticles that are somewhat irregular and faceted in shape, and yet the textural porosity observed in all four samples is consistent with the results from the N_2 gas sorption measurements and analyses. All the particles in 0-500, 10-500 and 20-600 are crystalline, as concluded from the well-developed lattice fringes in the high resolution TEM images in insets of **Figures 41a** – **c** and also from sharp Laue rings and diffraction spots in the corresponding SAED patterns (**Figures 42a** – **c**). The sample 30-500 shows a significant heterogeneity, which will be discussed later.

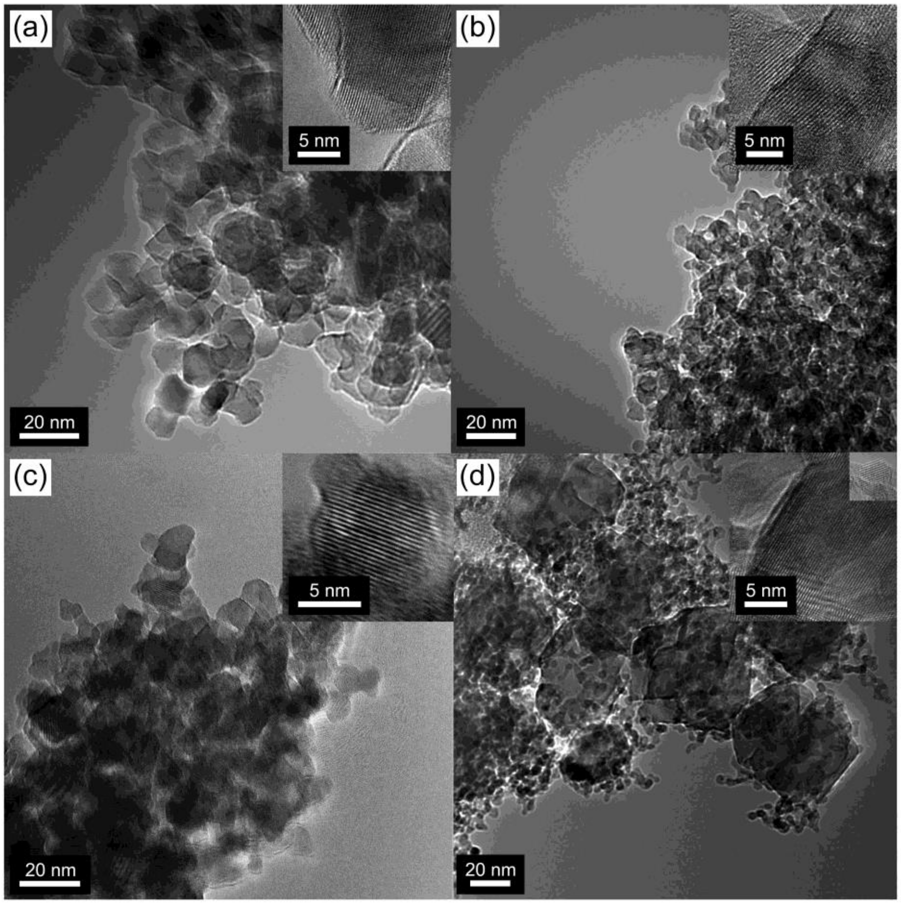

Figure 41. Transmission electron microscope images of the samples (a) 0-500, (b) 10-500, (c) 20-600 and (d) 30-500. The scale bars are 20 and 5 nm for the main and inset images, respectively.

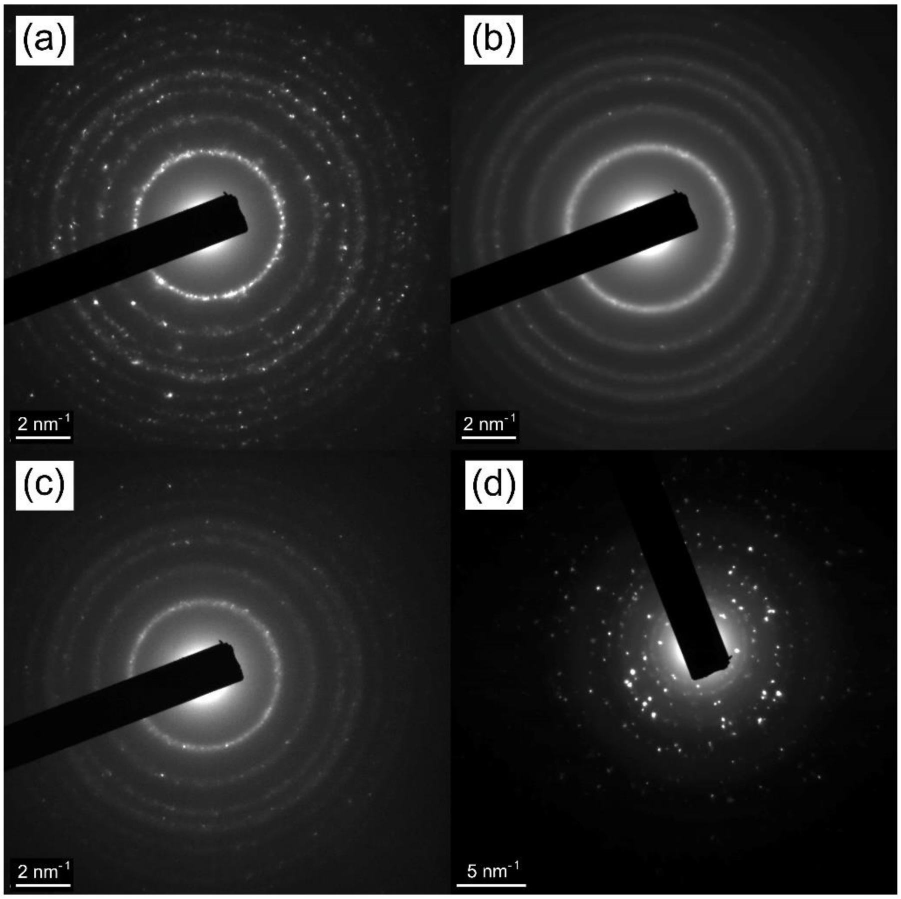

Figure 42. Selected area electron diffraction (SAED) patterns of a) 0-500, b) 10-500, c) 20-600 and d) 30-500. The scale bars in (a) – (c) are 2 nm^{-1}, and in (d) is 5 nm^{-1}.

For 10-500 and 20-600, the STEM-EDS results show that the Zr-doping was uniform nanoscopically with the average Zr contents of 11 ± 2 and 19 ± 2 at%, respectively. The particles in 10-500 are significantly smaller (5 – 10 nm) than those in 0-500 (10 – 20 nm), although they were calcined at the same temperature, and this is consistent with the crystallite sizes estimated from the Scherrer equation (**Table 3**). This suppressed coarsening has been attributed to the irregularity of the surfaces that is caused by surface stress or lattice strain from substituting relatively large Zr^{4+} ions (0.72 Å) for Ti^{4+} (0.61 Å),[395] which in turn inhibits diffusion and coalescence necessary for particle growth.[350,388] The 20-600 sample has larger particle sizes than 10-500, from both the TEM image (**Figure 41c**) and the Scherrer equation (**Table 3**). This is reflected in their SAED patterns where the small particle size of 10-500 gives nearly continuous and relatively wide Laue rings while the narrower Laue rings with discrete diffraction spots result from the large particle size of 0-500. The particle growth in 20-600 is certainly due to the higher calcination temperature but an additional reason is that the inhibitive effect of Zr doping on the particle growth is not quite present for the 20% doping. As indicated in **Table 3**, the 20-500 sample from calcination at 500 °C has an average crystallite size much larger than that of 10-500 and in fact only slightly smaller than what is estimated for 0-500. **Figure 43** shows a TEM image with a HRTEM inset of the lattice fringes, and the corresponding SAED pattern for ZTO 20-500, in which it appears that the nanoparticles are cemented into a 3D network where the individual nanoparticles are difficult to resolve. The copresence of wide Laue rings with bright Bragg spots in the SAED pattern suggests that the crystallites have a slight range of unit cell parameters and therefore different amounts of Zr-dopant. Both problems of the copresence of an amorphous component with the crystallites visible by PXRD, and the indication of inhomogeneous doping in the crystallites by SAED were solved by increasing the reaction temperature to 600°C to fully react the Zr-dopant with the TiO_2.

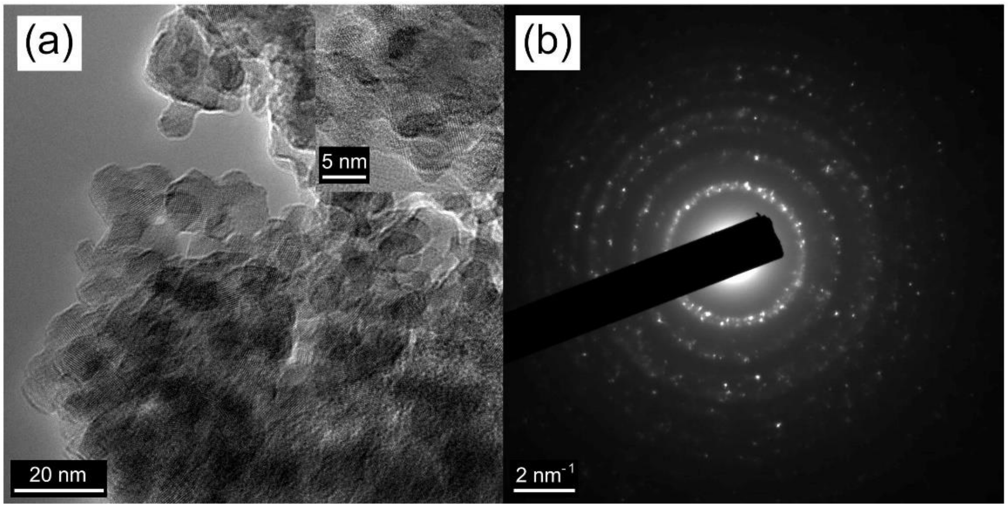

Figure 43. TEM micrographs ((a), scale bars = 20 nm, 5 nm inset) and SAED pattern ((b), scale bar 2 nm-1) of ZTO 20-500.

Among the four samples in **Figure 41**, 30-500 has a uniquely different morphology in that its TEM image (**Figure 41d**) shows two distinctively different types of particles, isolated ones with a large round shape (20 – 60 nm) and very small interconnected particles (~4 nm). The large particles are likely to be the anatase phase observed in the PXRD pattern of 30-500 (**Figure 36**), in that the crystallite size of the anatase estimated from Scherrer equation is about 30 nm, which is closer to the size of the larger particles in the TEM image. The representative high resolution TEM image of the larger particles in the inset of **Figure 41d** clearly shows lattice fringes, indicating a substantial crystallinity. This is also in agreement with large intense anatase diffraction spots observed in the corresponding SAED pattern (**Figure 43**). STEM-EDS analysis (**Figure 44**) found that the large and small 30-500 particles had the Zr contents of 20 ± 15 at% and of 53 ± 13 at%, respectively. The large uncertainties of the compositions may stem from the fact that the big and small particles are neither clearly separated nor homogeneously intermixed for the measurements. In any event, the heterogeneous microscopic morphology of 30-500 explains the co-presence of H1- and H3-type hysteresis loops in the N_2 sorption isotherm of the sample in **Figure 38a**. The textural porosity among the smaller particles is more likely to be responsible for the H1-type loop at $p/p_0 \sim 0.5$, while the H3-type loop in the higher pressure region may be due to the larger interparticle spacing among the large particles themselves or between the large and small particles.

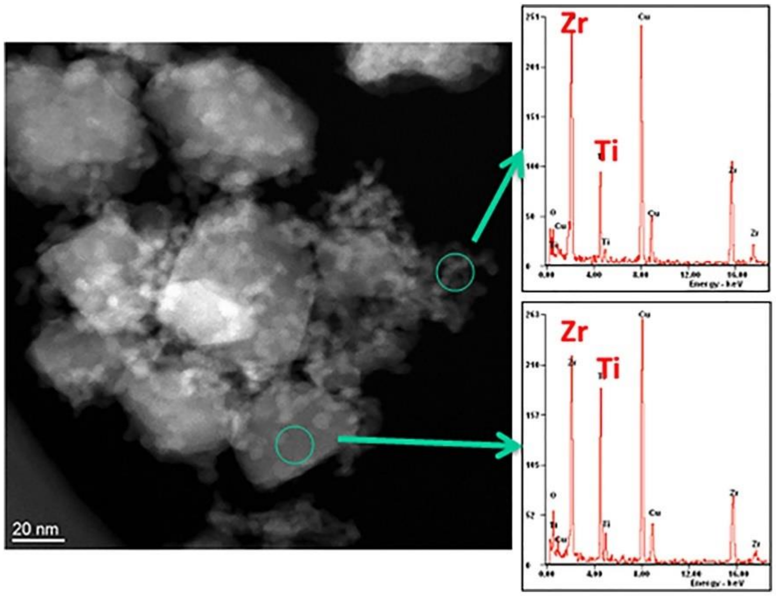

Figure 44. STEM image of 30-500 with corresponding EDS spectra of the different particle types.

3.3.5 Optical Band Gaps

Figure 45 shows UV-Vis diffuse reflectance spectra (DRS) of the pelletized bulk powders of 0-500, 10-500, 20-600 and 30-500 and their Kubelka-Munk transforms. The absorption edge increases in energy with the Zr amount, as we expected. From extrapolation, the band gap of the sample 0-500 was found to be 3.19 eV, which is consistent with the known value (3.2 eV) for anatase TiO_2.[396,397] For the ZTO samples, the band gap values are estimated to be 3.24, 3.29 and 3.38 eV for 10-500, 20-600 and 30-500, respectively. A sharper slope at the onset of absorption of 20-600 is likely related to its higher crystallinity due to the higher calcination temperature, as seen previously.[350] It is noted that the band gap increase is more severe from 20-600 (20 at% Zr) to 30-500 (30 at% Zr), but the band gap value obtained for 30-500 may not represent the innate optical property of the system, as the sample was not homogeneous. In our studies, therefore, we conclude that the near maximum 20% Zr doping in the anatase TiO_2 increases the optical band gap by 0.10 eV. This increase is smaller than what has been reported in other systematic studies.[203,345] In one study, the band gaps of TiO_2, 10%, and 20% ZTO were reported to be 3.06, 3.11 and 3.17 eV directly from DRS,[345] and in another 3.50, 3.57 and 3.63 from absorption spectra.[205] These discrepancies may be due to the different methods for band gap estimation, as we can see the inconsistent band gap values even for the pure anatase TiO_2.

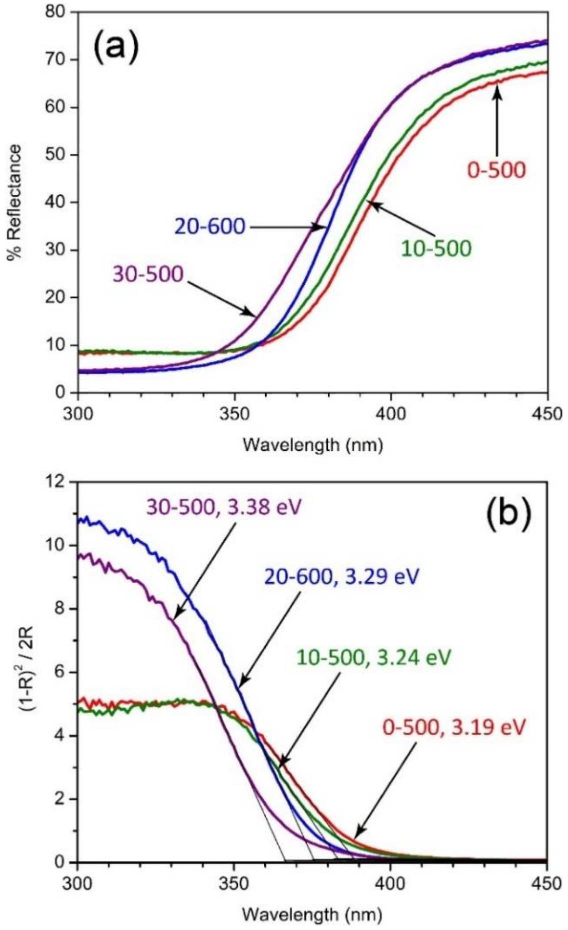

Figure 45. (a) Diffuse reflectance spectra, and (b) their respective Kubelka-Munk transforms, for 0-500 (red), 10-500 (green), 20-600 (blue) and 30-500 (purple).

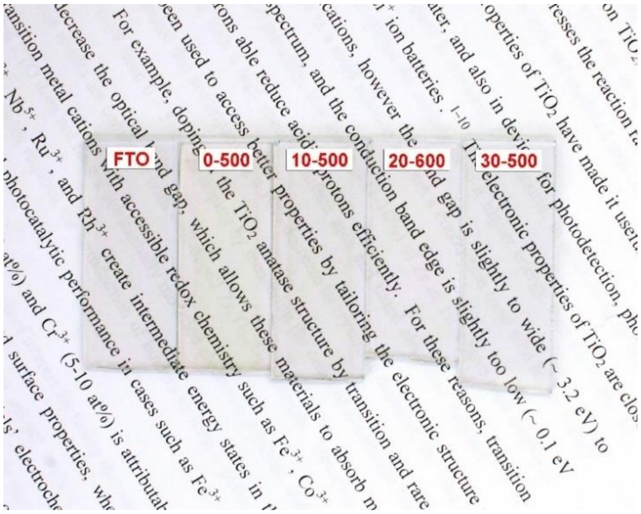

Figure 46. Photograph of plain FTO glass and FTO glass with thin films of 0-500, 10-500, 20-600 and 30-500 appearing from left to right.

Since our synthetic method allows preparation of thin films of the materials, their optical properties were further examined by taking the UV-Vis absorption spectra. To bare eyes, the materials are almost transparent and colorless, as shown in **Figure 46** for the films on FTO glass. The porous ZTO coatings cover the length of the slides except for the area spanning around 2 mm from one end. The Scotch® tape masks placed on the sides of the slides shaped the ZTO coatings in a stripe form with a width of ~ 15 mm. The prepared coatings exhibit consistent thicknesses of approximately 300 nm from profilometric studies. The 20-600 coating appears slightly yellowish compared to the others and is also slightly opaque, which may be due to the reaction of ZTO with FTO underneath during calcination. UV-Vis transmission spectra (**Figure 47a)** were analyzed based on Tauc models for both direct band gap and indirect band gap scenarios.

The direct band gap model resulted in band gap values of 3.69, 3.72, 3.76 and 3.83 eV for 0-500, 10-500, 20-600 and 30-500 (**Figure 47b**), respectively, while 3.39, 3.42, 3.27 and 3.50 eV resulted from the indirect band gap model (**Figure 47c**). For both models, the Tauc band gap values increase as the Zr content increases except for the 20-600 sample, which we suspect is the consequence of the yellow coloring of the sample. The Tauc band gaps from the transmission spectra are noticeably larger than what we obtained from the Kubelka-Munk transforms and this appears to be the consistent observation in the literature.[203,355,384,394]

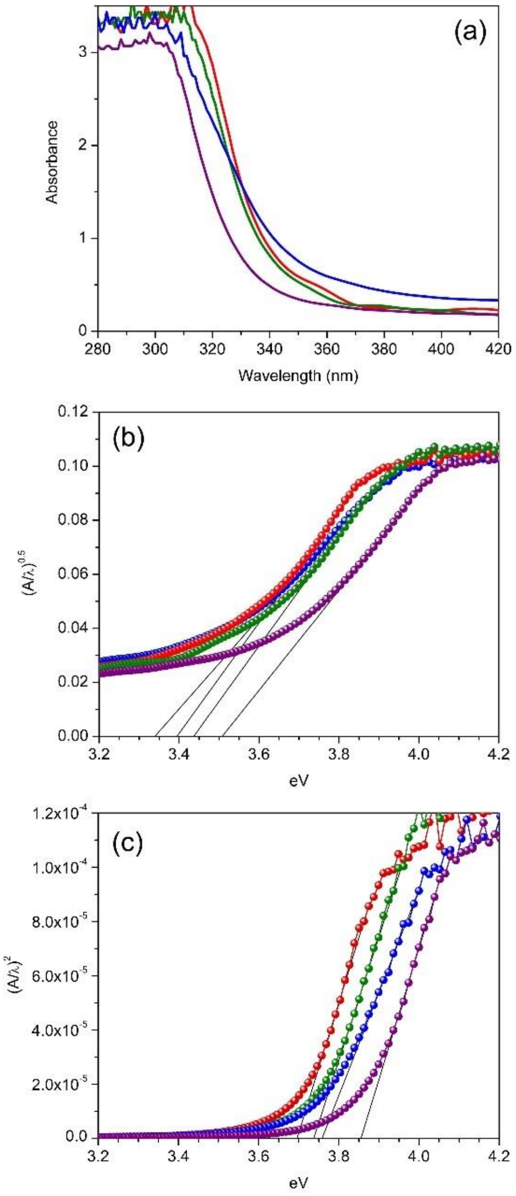

Figure 47. Tauc plots, with curves drawn from transmission data of films of 0-500 (red), 10-500 (green), 20-600 (blue) and 30-500 (purple), with linear regions indicated by solid lines whose x-intercepts estimate (a) the indirect band gaps and (b) the direct band gaps.

3.3.6 Flat Band Potentials and Band Edge Energies

Mott-Schottky analysis of electrochemical impedance spectra (EIS) was carried out to locate the flat band potentials, in order to approximate the conduction band edge energies of TiO_2 (0-500) and ZTOs (10-500 and 20-600), which are *n*-type, wide-band gap semiconductors.[398,399] **Figure 48a** shows the Mott-Schottky plots obtained with the simplified equivalent circuit (**Figure 31**). The plots show a linear relationship between C^{-2} vs. E, as C^{-2} approaches 0. The positive slope found for all the samples indicates *n*-type behavior in under-depletion conditions.[400] By extrapolating to $C^{-2} = 0$, therefore, the Mott-Schottky equation indicates flat band potentials (U_{fb}) of –4.26, –4.10 and –4.03 eV on the absolute vacuum scale (pH = 5.05; T = 25 °C) for TiO_2, 10% ZTO and 20% ZTO, respectively. By correcting the boundary layer contribution at the surface to the flat band potential values by employing the measured PZZP values (5.45, 5.45 and 5.58 for TiO_2, 10% ZTO and 20% ZTO, respectively, in our experiments),[331,401-403] the corrected flat band potential values (U_{fb}^0) in the scale of the absolute vacuum system (AVS),[331] for the "bulk" material, are –4.24, –4.08 and –4.00 eV, respectively. In the AVS scale, these corrected flat band potentials correspond to the Fermi energy of the bulk material which lies beneath the conduction band edge energy for *n*-type semiconducting materials (**Figure 48b**).[400] We assumed that the charge carrier density variation is negligible as all the metal ions have the same number of valence electrons. Furthermore, a typical correction factor of 0.10 eV[163,401,404,405] was applied to the U_{fb}^0 values to arrive at the reported conduction band edges (–4.14, –3.98 and –3.90 eV, respectively), the basis for which will be discussed later in this section.

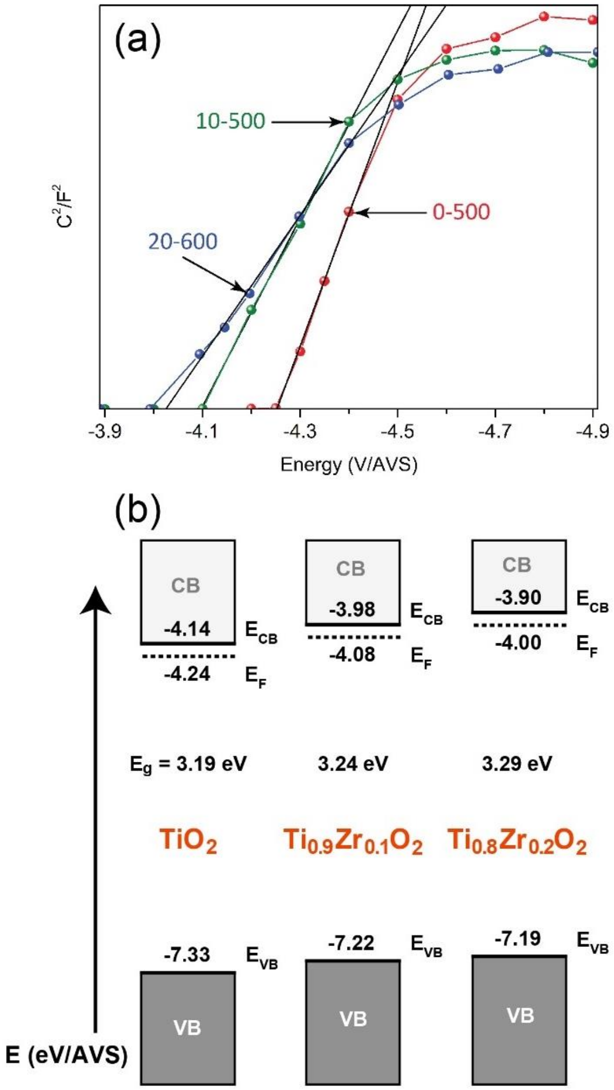

Figure 48. (a) Mott-Schottky plots obtained at a pH of 5.05 from dense pellets of the ZTO materials 0-500 (red), 10-500 (green) and 20-600 (blue). (b) Schematic band energy diagrams for the materials with the energy values estimated from the Mott-Schottky measurements and optical band gaps.

Figure 48b depicts schematic band energy diagrams for the samples based on the flat band potential values and the optical energy band gaps from the Kubelka-Munk transforms. As the Zr content increases, both the conduction and valence band edges increase in energy. The increase is slightly more for the conduction band edge by 0.24 eV from 0 to 20% Zr, while the valance band edge becomes more reducing by 0.14 eV.

The finding by Imahori *et al.*, that 5% Zr-doping results in an increase of flat band potential by 0.11 eV, is in agreement with our results although the work did not show the unit cell parameters for the samples.[163] For further substantiation of the results in our studies, similar measurements and analyses were carried out at pH of 7.5 for the corresponding nanoporous TiO_2 and ZTO coatings on FTO substrate and their Mott-Schottky plots are given in **Figure 49a**. Because the flat band energy is relatively small (–4.26 V at pH 7) for FTO compared to those of TiO_2 and ZTOs and thus does not interfere in the linear region of the plots.[406] The U_{fb} values of the nanoporous coatings of 0-500, 10-500 and 20-600 was extrapolated from the linear region near C^{-2} as –4.10, –3.92 and –3.84 eV, respectively. After correcting the pH-dependence of 59 mV/decade, the estimated U_{fb}^0 values were –4.12, –3.94 and –3.87 eV, respectively for 0-500, 10-500 and 20-600 (**Figure 49b**). These values are consistent with the ones for the dense pellets within the maximum deviation of 0.04 eV. The interpretation of the C^{-2} vs. E behavior in the plots is somewhat complicated because the capacitance is also contributed by the *n*-type semiconductive FTO substrate itself because the electrolyte liquid penetrates through the nanoporous coating down to the FTO surface and also because the depletion layer length becomes comparable to the nanoparticle size. However, the consistent behavior between the pellets and the nanoporous coatings may indicate that nanoparticles in the nanoporous coatings are well interconnected electrically by the calcination.

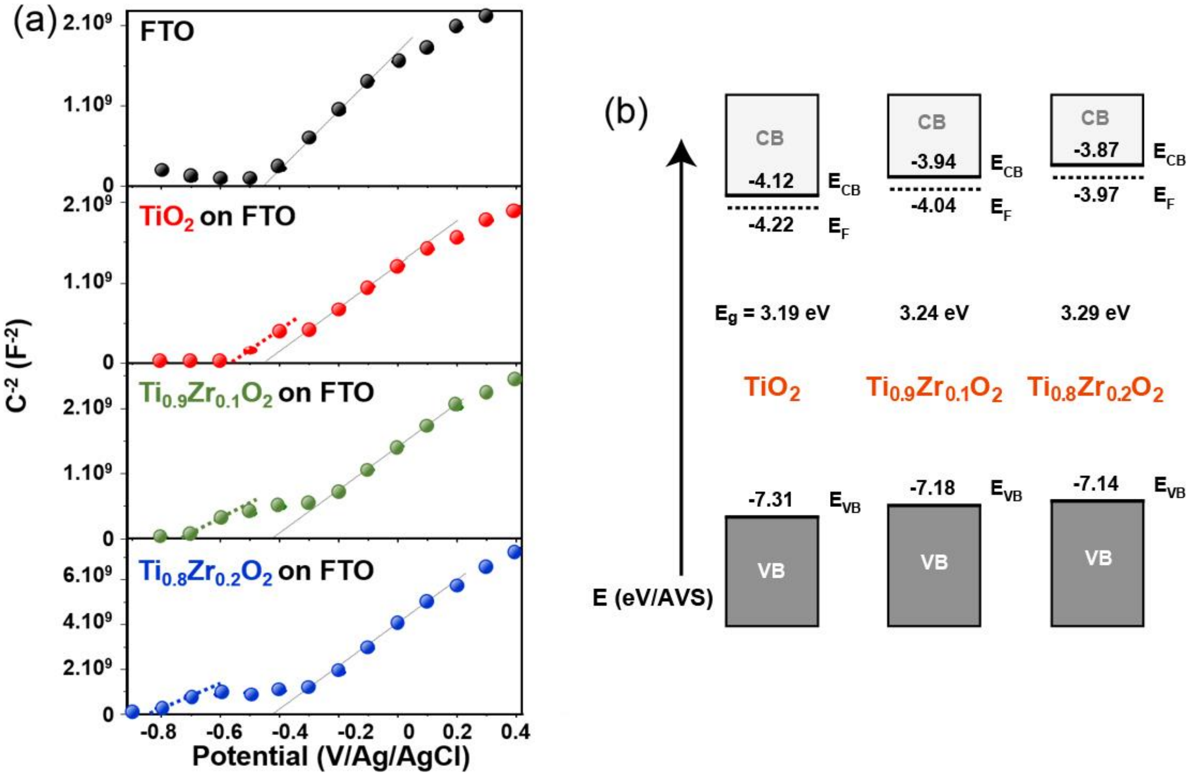

Figure 49. (a) Mott-Schottky plot, obtained at pH 7.48, from films of nanoporous ZTO material on FTO with increasing Zr doping, and (b) the estimated flat band potentials.

The measured Fermi energies (or the U_{fb}^0 values, to be more precise in our case) can be compared with their semiempirically predicted values (E_{CB}) by the scissor relationship between valence band (VB) edge and conduction band (CB) edge in the AVS scale:

$$E_{CB} = -\chi + 0.5E_g$$

$$E_{VB} = -\chi - 0.5E_g$$

where χ and E_g are the geometrical average electronegativity and the measured band gap of semiconductors.[401] The relationship where E_{CB} and E_{VB} are located symmetrically in energy with respect to χ value was originally suggested based on Mulliken's definition of the electronegativity of a neutral atom as the arithmetic mean of the atomic electron affinity and the first ionization energy.[407] For a semiconductor, the bulk electronegativity corresponds to the undoped Fermi energy or halfway between the bottom of the conduction band and the top of the valence band. Their electronegativity can be calculated as the geometric mean of Sanderson's electronegativities of the constituents.[404] Over the years, this relationship has been validated for a large number of semiconducting compounds,[33,331,404,408] although a caution must be paid as the model does not take into account the structural modification at the material/water interface, surface orientation and terminal groups.[409] **Figure 50** shows U_{fb}^0 vs. E_{CB} for our samples (in red squares) together with other compounds from the literature (see APPENDIX A).[163,331,376,400,401,404,410-415] The trend line (dark grey, solid line) was obtained by setting the slope to unity and finding the best linear relationship between U_{fb}^0 and E_{CB} for all the compounds except our samples. The intercept value of –0.10 eV was regarded as a universal difference between U_{fb}^0 and E_{CB} for all the compounds, and thus the value was used in our discussions above and also for **Figure 49b**. The value is close to the typical ones (0.1 to 0.3 eV) set out in the literature.[163,404,405]

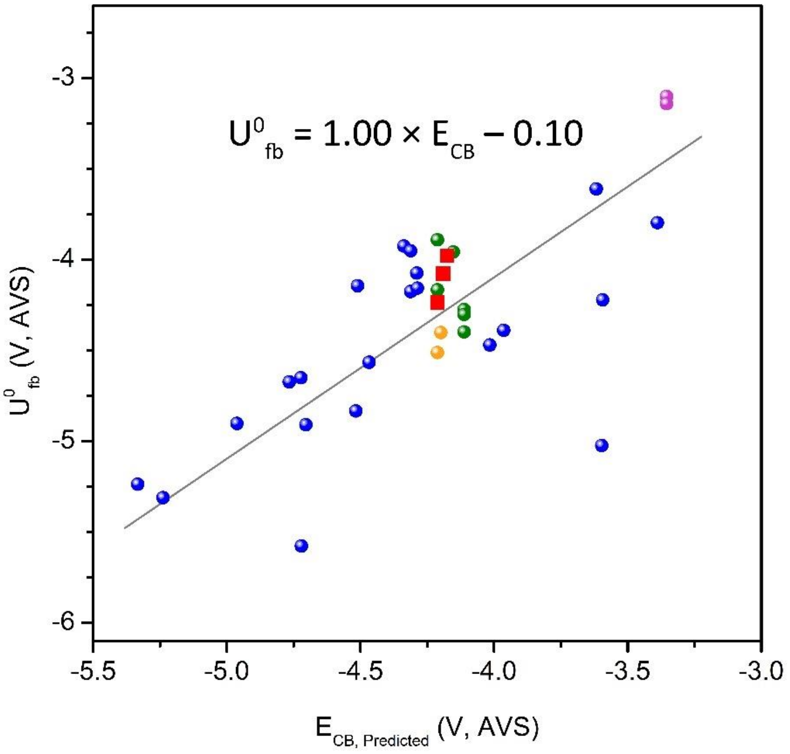

Figure 50. pH-corrected flat potential (U_{fb}^0) vs. the conduction band edge energy (E_{CB}) from the scissor relationship for various metal oxides; $Ti_{1-x}Zr_xO_2$ from this study (red squares) $Ti_{1-x}Zr_xO_2$ from ref. 163 (orange),[163] anatase TiO_2 (green),[376,412-415] ZrO_2 (pink)[400,404] and others (blue).[376,400,401,404,410,411,414] The grey line is from a linear fitting (see the text).

It is mentioned that the correlation between U_{fb}^0 and E_{CB} is rather poor among the various metal oxides in **Figure 50**. While this is not unreasonable considering of the nature of the simple semiempirical model, large discrepancies are still noticed even when we consider only the data for nanostructured anatase TiO_2 (in green dots) from the literature.[376,412-415] This scattered agreement underscores possible variations of the physicochemical properties of the materials prepared via different synthetic conditions. Considering only the ZTO samples prepared under the same synthetic condition in our study (in red squares), the Zr-doping in TiO_2 induces a steep increase in the energy of the conduction band edge, in comparison to the expected increase from the overall trend (the dark grey line) observed in **Figure 50**. A purblind extrapolation of the steep increase would lead to an unreasonably high conduction band edge energy for ZrO_2 and yet the previous experimental results[400,404] (shown in pink dots) indicate that ZrO_2 does not deviate much from the general trend. In other words, the conduction band edge of ZTO appears at a higher energy than what we expect from the increase in the electropositiveness of the Zr element or more precisely the higher 4*d* orbital energy of Zr^{4+} ion along with the optical energy gap. Although the absolute values are different, the same trend was observed upon doping at 5% Zr in a previous study (in orange dots).[163]

Though it is not clear, the observed high energies of the conduction band edge may be due to the fact that Zr^{4+} ions in ZTOs with the anatase structure do not have optimized bonds with the surrounding oxide ions. The metal ions in the anatase structure have a coordination number of six with a pseudo octahedral geometry, while Zr ions in ZrO_2 are surrounded by seven oxide ions (the structure is not shown here). Furthermore, the average M–O bond distances are much shorter (1.960 and 1.969 Å for 10% and 20% ZTO, respectively) than in baddeleyite ZrO_2 (2.158 Å)[416,417] and are in fact quite close to the average Ti–O bond distances in pure TiO_2 (1.946 – 1.949 Å[418-420] for anatase and 1.959 Å[419] for rutile). Previous first principle calculations have predicted that a hypothetical ZrO_2 in an anatase structure would have an average Zr–O bond distance of 2.121 Å, while the same calculation method provided an average Ti–O bond distance of 1.963 Å in the anatase TiO_2. Shorter coordination distances would lift the Zr 4*d* orbitals to a higher energy due to a stronger π^* interaction with oxygen ligand orbitals. Overall, the partial substitution of the Ti atoms with large-sized and more electropositive Zr atoms in the anatase increases the conduction band edge energy drastically, leading to electrode materials with a high reduction potential.

Interestingly, the measured change in the valance band edge energy is also quite significant compared to the increase (0.02 eV per 10 at% Zr) predicted from the scissor relationship in **Figure 50**. This indicates that the electropositiveness of Zr element or more precisely the higher 4*d* orbital energy of Zr^{4+} ion is not the only factor to consider in predicting or understanding the modification of the electronic band structure of anatase TiO_2 upon Zr doping. As the Zr content increases, the ionicity of the metal-to-oxygen (M–O) bond increases, leading to a larger electron density on the oxide ions. Since the valence band edge (the highest energy levels in the valence bands) of a metal oxide consists mainly of oxygen 2*p* orbitals with a nonbonding or weak π M–O bonding,[421] the valence band edge energy would increase upon the accumulation of the negative charge through increased electron-electron repulsion. In any event, the measured valence band edge energy of –7.27 eV for 20% ZTO is sufficiently low to oxidize water (~ –5.7 eV).[422]

3.4. Concluding Remarks

To summarize, we have investigated the effect of the Zr content in anatase-type nanoporous Zr-doped TiO_2 on the thermal stability, nanoscopic morphologies, unit cell parameters, optical energy gaps and band edge energies by developing a new sol-gel synthetic route designed for controlled hydrolysis and polycondensation of the metal precursors. For the first time, we have observed that the Zr-doped TiO_2 system follows Vegard’s law up to 20 at% Zr. Optical band gap energies were measured to increase linearly from 3.19 to 3.29 eV between TiO_2 and $Ti_{0.8}Zr_{0.2}O_2$. For the same respective compositions, conduction band edge energies increased from –4.14 eV to –3.90 eV. Mild calcination conditions provided by the sol-gel route reduce the extent of particle coarsening during the dehydration/dehydroxylation and crystallization. After calcination, therefore, the nanostructured TiO_2 and Zr-doped TiO_2 products in an anatase structure exhibited porosities up to 50 % and surface areas approaching 150 m^2/g. Despite the low calcination temperatures, Vegard's behavior of the final products suggests that Ti^{4+} and Zr^{4+} ions are homogeneously distributed in the final products and probably even in the initial gel products.

The unprecedented observation of a well-correlated relationship between the compositions and the unit cell parameters for the Zr-doped TiO_2 system accentuates the importance of a good synthetic control during the sol-gel process and also firmly establishes the relationships between the compositions and the optical and electronic properties not only for the bulk materials but also for the thin nanoporous films fabricated by the same synthetic method. Therefore, the findings in this study would be beneficial in employing the materials for various applications including UV sensors with a tunable energy detection range,[203,205] and dye-sensitized solar cells that can achieve a higher voltage,[154,163] as well as the solar fuel productions from water.[346,382,411,423]

CHAPTER 4

SYNTHESIS AND CHARACTERIZAION OF HIERARCHICAL MESO-MACROPOROUS SnO_2, $Sb_{0.071}Sn_{0.929}O_2$, TiO_2 AND $Zr_{0.1}Ti_{0.9}O_2$

4.1 Introduction

Porous transparent conducting oxides (TCOs) have recently started to emerge as materials for high surface area electrodes that capture biomacromolecules to harness their unique photochemical and electrochemical properties outside cellular environments.[52,57,81-85] Mesoporous TCO electrodes have been synthesized as thin films and their high uptake of small proteins has been demonstrated.[56] For example, we previously have reported that electrochemical characterization of cytochrome c protein (~3 nm diameter) adsorbed within a mesoporous electrode, featuring average pore width of 18 nm and a high surface area of 92 m^2/g, reveals a remarkably high surface coverage (1,000 pmol/cm^2) wherein all protein molecules are involved in electron transfer with the electrode surface.[81] More recently, a 600 pmol/cm^2 surface coverage of electroactive cytochrome c was achieved within ordered porous films with 10 nm pore width and a surface area of 120 m^2/g.[53,82] However, mesoporous materials are less than ideal for large biomacromolecules (>10 nm) because their comparably small pore sizes are expected to not allow appropriate diffusion and adsorption and thus will significantly reduce the loading efficiency. Indeed, it has been shown that biomacromolecules diffuse significantly more slowly as their size becomes comparable to that of the pore width; in the case of the ~ 4-nm globular protein lysozyme, for example, pores are virtually inaccessible to protein molecules that are 80% as wide.[9] Adsorbed biomacromolecules should also retain their singleness, as aggregation can greatly reduce the electrochemical response.[424]

Macroporous TCOs with pore diameters ranging from ~80 to 400 nm have been reported in the literature,[55,57,135] although their utilization in bioelectrochemistry has been rare.[57] The advantage of macroporosity as it pertains to biomacromolecules lies largely in the more effective diffusion kinetics of large molecules in the pores, as well documented for artificial tissues and drug delivery. For example, bovine serum albumin (BSA; ~7 nm) has a free diffusion constant of 60 $\mu m^2/s$,[425] but the protein was found to diffuse much more slowly at 5 $\mu m^2/s$ in ion exchange resins with pores smaller than 100 nm.[6,426] By contrast, in considerably bigger pores (10-40 µm), the hindrance in diffusion was less severe with BSA diffusion constants ranging from 10 to 30 $\mu m^2/s$.[427] We note that a detailed comparison is challenging due to the different porous materials used in the latter studies (methacrylate copolymer or polysaccharide based ion exchange resins compared to dextran-methacrylate hydrogels).

For the best performance of TCO electrodes interfacing with biomacromolecules, it is highly desirable to provide both macropores and mesopores with a hierarchical pore structure. While macropores facilitate efficient long-range diffusion of large molecules, mesopores connected with the macropores expand the surface area available for adsorption of biomacromolecules.[428] Various synthetic methods have been implemented to prepare such hierarchically porous TCO materials mainly from silica, titania,[42,429] and zirconia,[18,429,430] and, to a lesser extent, from other metal oxides.[40,429-432] However, it has been challenging to adapt the existing synthetic methods to fabricate hierarchically porous TCO coatings for electrodes, as the resulting products should have relatively uniform morphology and thickness and cover a large area of transparent substrate.

Herein we report the synthesis of highly uniform, hierarchically porous ATO coatings via a newly developed carbon black template method. We also provide a detailed structural and morphological characterization of the material through powder X-ray diffraction (PXRD), nitrogen sorption, profilometry, scanning electron microscopy (SEM), transmission electron microscopy (TEM), and infiltration with fluorophore-labeled DNA-nanotweezers that were used as single particle probes of diffusion through and adsorption in the pores. As demonstrated previously for either nano- and macroporous materials,[433-436] diffusion constants within different pore regimes can be explicated by such single-particle tracking. For our hierarchical meso-macroporous ATO coatings, we find two diffusion regimes, which correspond to free diffusion events in the large macropores that are inhibited by the physical interaction with the mesoporous walls, and to diffusion events of probes confined within the smaller and regularly appearing macropores of ~ 210 nm.

4.2 Materials and Methods

The synthesis of meso-macroporous ATO was carried out by modifying a previously established sol-gel route for producing more porous coatings.[121] In an Ultra-Turrax tube drive with a rotor-stator element, 0.05 g of $SbCl_3$ (Alfa Aesar, ≥ 99.9%) was dissolved in 6.50 g of *n*-BuOH (J.T. Baker, 99.9%) by shaking, followed by the addition of 1.00 g of $SnCl_4 \cdot 5H_2O$ (Alfa Aesar, 98%) and 1.00 g of deionized water. In a separate bottle, a paste was homogeneously blended consisting of 61.8 % (w/w) ±-epichlorohydrin

(Fluka, ≥ 99.9%), 25.8 % (w/w) polyethylene glycol bisphenol A, epichlorohydrin copolymer (PEG) (Sigma-Aldrich, 15-20 kDa) and 12.4 % (w/w) carbon black, acetylene (Alfa Aesar, 50% compressed ≥ 99.9%, surface area = 75 m^2/g, bulk density of 0.095 – 0.103 g/cm^3). Of this paste, 6.15 g was transferred to the metal salt solution in the tube drive. The rotor-stator element was then turned on for high-shear mixing with a setting of three for 10 seconds to initiate blending. After the initial blending, the tube was vigorously shaken and subjected to high-shear mixing with a setting of six for one minute. Next, the tube was vigorously shaken and finally subjected to high-shear mixing with the maximum setting of 9 for one minute to produce a viscous black liquid that was the precursor mixture. The precursor mixture was transferred to a separate vial.

For preparing coatings of the meso-macroporous ATO, cover glass (VWR, No. 1.5, 22 × 22 mm) was cleaned with soapy water and sonication in acetone, and then a double-layer of tape (Scotch Transparent Tape) was applied to cover about one or two mm on opposing sides, and a single tape layer was applied to a third edge opposite to the un-masked edge. Onto this third edge, a small amount of the precursor mixture was dropped, and drawn smoothly and quickly across the slide with a Pasteur pipette. After allowing to dry under ambient conditions for one hour, the slides were placed in a tube furnace and heated to 500 °C for five hours, with an oxygen atmosphere to oxidize the carbon. During this heating, the carbon black disappeared to yield translucent, pale blue coatings. Alternatively, the carbon black and sol-gel composite was dried and calcined under the same conditions to obtain bulk ATO powder for nitrogen sorption studies.

Powder X-ray diffraction (PXRD) was performed on a Siemens D5000 diffractometer using Cu Kα radiation. Five coatings were scraped from the cover glass substrates, and crushed well with a small amount of silicon powder as internal standard (a = 5.4301 Å); the resulting mixture was dispersed in ethanol and spread on a quartz plate. Data were acquired by scanning the 2θ angle from 5 to 90° with a step size of ~ 0.016° and a scan time of two hours. The (111) Si reflection at $2\theta = 28.443°$ was used as a reference during unit cell analysis, which was carried out using PANalytical X'Pert Pro Software. Stylus profilometry was carried out using a Dektak XT with a 12.5 µm diameter tip and two mg of force. The profile was obtained with a line scan across the ATO coating, beginning and ending on the cover class substrate. Optical profilometry was conducted with a ZeScope, using an objective lens. The ZeMap software was used to analyze a linear portion of the 3D map.

Nitrogen sorption isotherms were obtained from the bulk powder using a Micromeritics ASAP 2020 Surface Area and Porosity Analyzer at 77 K. The powder was degassed under vacuum at 250 °C for 8 h before data collection. The Brunauer–Emmett–Teller (BET) model was applied to the adsorption branch in the partial pressure range of 0.05-0.2. Pore size distribution was analyzed using the Barrett–Joyner–Halenda model applied to the desorption branch, with the Halsey thickness curve for non-uniform surfaces and the Faas-correction for multilayer desorption.[370] Total pore volume was estimated from the quantity of gas adsorbed at $P/P_0 \sim 0.99$.

Scanning electron microscopy (SEM) studies were conducted on ATO coatings on cover glass substrates and contacted by carbon tape, with an FEI XL-30

Environmental SEM using 20 keV electrons. To study the morphology of the carbon black and PEG template, the synthesis was carried out without the metal salts, and a coating was prepared in the same fashion. Transmission electron microscopy (TEM) was performed on the scraped ATO coating that was crushed lightly and dusted onto the TEM grid. For high-resolution TEM (HR-TEM) studies, the scraped ATO coating was sonicated in ethanol for 20 min, and the TEM grid was immediately immersed in the dispersion and air-dried. Images of carbon black were obtained by gently dusting the carbon black reagent onto a TEM grid. For a control experiment, the coating was pyrolyzed under an Ar atmosphere with the same heating procedure as the coatings calcined under an O_2 atmosphere. Micrographs were obtained on a JEOL 2010F at an accelerating voltage of 200 kV.

The zeta potential of samples dispersed in buffer solutions through 20 min of sonication was measured with a Malvern Zetasizer Nano. Subsequently, these dispersions were auto-titrated against a 0.50 *M* solution of $MgCl_2$ using the MPT-2 accessory, in increments of 1 m*M*, and the zeta potential was measured in triplicate between each addition. Data were collected using the Malvern software.

For single molecule fluorescence imaging, a previously reported DNA nanotweezer with Cy3 and Cy5 modifications[437] was utilized as fluorescent reporter to probe the meso-macroporous ATO coating by single molecule fluorescent particle tracking. The design and preparation of the DNA nanotweezer at a concentration of 5 n*M* followed the literature[437,438] (**Figure 52**). The DNA nanotweezer was then diluted to 200 p*M* into a final buffer of 1x PBS supplemented with 10% (w/v) PEG 8000 and 1 m*M*

$MgCl_2$ as the infiltration solution. 40 µL infiltration solution was placed on top of an ATO coating (~20 mm × 20 mm, coated onto a cover slip) and soaked at room temperature for one hour to maximize adsorption. After deposition, the remaining solution was removed by airflow and the ATO coating was washed twice with 40 µL imaging solution, composed of infiltration buffer supplemented with oxygen scavenger system, consisting of either 2.5 m*M* 3,4-dihydroxybenzoate, 25 n*M* protocatechuate dioxygenase, and 1 m*M* Trolox for imaging the mobile and immobile nanotweezer probes; or 0.63 m*M* 3,4-dihydroxybenzoate, 6.3 n*M* protocatechuate dioxygenase, 0.25 m*M* Trolox for photobleaching experiments. Finally, 20 µL imaging solution was deposited onto the ATO coating and an mPEG-5000 (Laysan Bio, Inc.) coated glass slide was placed on top of the ATO coating and image solution. Before imaging, the sample was sealed with wax to prevent oxygen leaking into the imaging solution.

Single molecule imaging was performed on an Olympus IX-81 objective-type total internal reflection fluorescence (TIRF) microscope using a 1.40NA oil-immersion objective in HILO imaging mode for low-background data acquisition at varying sample depths.[439] Fluorescence was detected on a 512 pixel × 512 pixel EMCCD (Evolve 512, Photometrics) camera under 640 nm illumination (using a Coherent CUBE 640-100 laser) and employing a 660 nm edge BrightLine® single-edge dichroic beamsplitter.

Three types of measurements were carried out. First, for observation of immobile DNA tweezers inside the ATO coating, 40 μL infiltration solution containing 200 p*M* DNA tweezers was deposited on the coating for one hour, followed by washing with imaging solution twice before finally imaging in 20 μL imaging solution. Movies of 70 to 80 frames were collected along the z-axis throughout the coating at a rate of 500 ms/frame and a z-step size of 0.2 µm/frame. DNA tweezers were deposited and imaged along the z-axis at different Mg^{2+} concentrations of 1 mM, 10 m*M*, or 100 m*M* to study the effect of Mg^{2+} on immobilization. Second, for studying mobile DNA tweezers inside the ATO coating by single fluorescent particle tracking, a pre-bleaching process[436] was first carried out under 640 nm illumination to maximally photobleach the immobile probes, followed by taking movies of 1,000 frames with a rate of 20 ms/frame. Third, for studying the aggregation status of probes inside the ATO coating, a photobleaching experiment was performed with the oxygen scavenger system concentration reduced to 25% during sample preparation (for faster bleaching). Movies of 300 frames were recorded at a rate of 150 ms/frame at a fixed image plane until all DNA tweezers were bleached.

For the analysis of all single molecule data, custom MATLAB codes were combined with several established codes. For analyzing adsorbed DNA nanotweezers, the fluorescence signals of individual probes from different focal planes were first fitted and located by ImageJ with the QuickPALM plugin. The identified probes were further analyzed by a custom MATLAB code to calculate their z-position and 3D distribution. For the single particle tracking of mobile fluorescent probes within the ATO coating, a previously reported MATLAB code[436] was applied to, first, locate probes by 2D Gaussian function fitting and to, second, track the trajectories of probes by fitting the same probe as identified by its spatial proximity over consecutive images until it diffused out of the focal plane. To ensure the accuracy of this analysis, tracks with at least five movement steps were analyzed and only the first half of all data points were used for a diffusion coefficient calculation. A two-term CPD function using a 2D motion model was applied to fit the trajectories of individual DNA nanotweezers and bin them into two subgroups based on differential diffusion speeds. Next, mean-squared displacement (MSD) curves were plotted whereby a 2D diffusion is described as: P_{2D} $(U,\tau)=1-e^{-U/(r^2(\tau))}$.[440] P_{2D} (U,τ) is the probability of observing a squared displacement $r^2(\tau)$ value no larger than some value U during time τ. Motion modes with different diffusion coefficients were defined by expanding the equation to include multiple fractions. We found the data from diffusing DNA nanotweezers to be best described by a two-term expansion with each a fast and a slow mobile mode: P_{2D} $(U,\tau)=\alpha(1-e^{-U/(r^2(\tau))})+(1-\alpha)(1-e^{-U/(r^2(\tau))})$. Here, α represents the fraction of the faster diffusion mode (term 1) whereas 1-α represents the fraction of the slower diffusion mode (term 2) due to confinement by and interactions with the enclosing matrix. Chosen to represent tracks that contain one, three and five steps, the respective τ values of 0.020 s, 0.060 s and 0.100 s were used in fitting the tracking data with the above equation. Based on the fitting result, mean-squared displacement (MSD) versus τ were plotted (**Figure 60**). The two diffusion coefficients and the corresponding fractions of time were then calculated by from the plot. The pore size of the confining matrix was estimated from a diffusion model for restricted particle motion within a square: $MSD\,(\tau)>=\frac{L^2}{3}\bullet(1-e^{-12D_0\tau/L^2})$, where D_0 is the initial diffusion constant and L is the length of the square.[441,442] Finally, for the photobleaching data analysis a custom LabView program was used to extract time traces of DNA nanotweezers from the recorded movies, which were further analyzed in the program QuB[443] to identify the number of photobleaching steps.

4.3 Results and Discussion

The overall synthetic procedure for producing meso-macroporous ATO coatings is depicted in **Figure 51a**. Key is the use of two components in the reaction mixture: the sol-solution (red) that has both organic and inorganic components and acts as a dispersant to the carbon black particles (black). To provide well-connected and evenly distributed macropores in the final ATO material, the reaction mixture was subjected to high-shear mixing that applies sufficient force on the microscale to break up agglomerated carbon black particles into individual aggregates. To this end, PEG was included to stabilize the aqueous dispersion of carbon. Carbon black particles are added in a sufficient amount to reach the percolation threshold (5 – 10 (w/w) % or ~ 15 (w/v) %)[444,445] so that the connectivity of carbon aggregates throughout the entire volume of the dried reaction mixture should provide for the desired, openly connected network of random macropores.

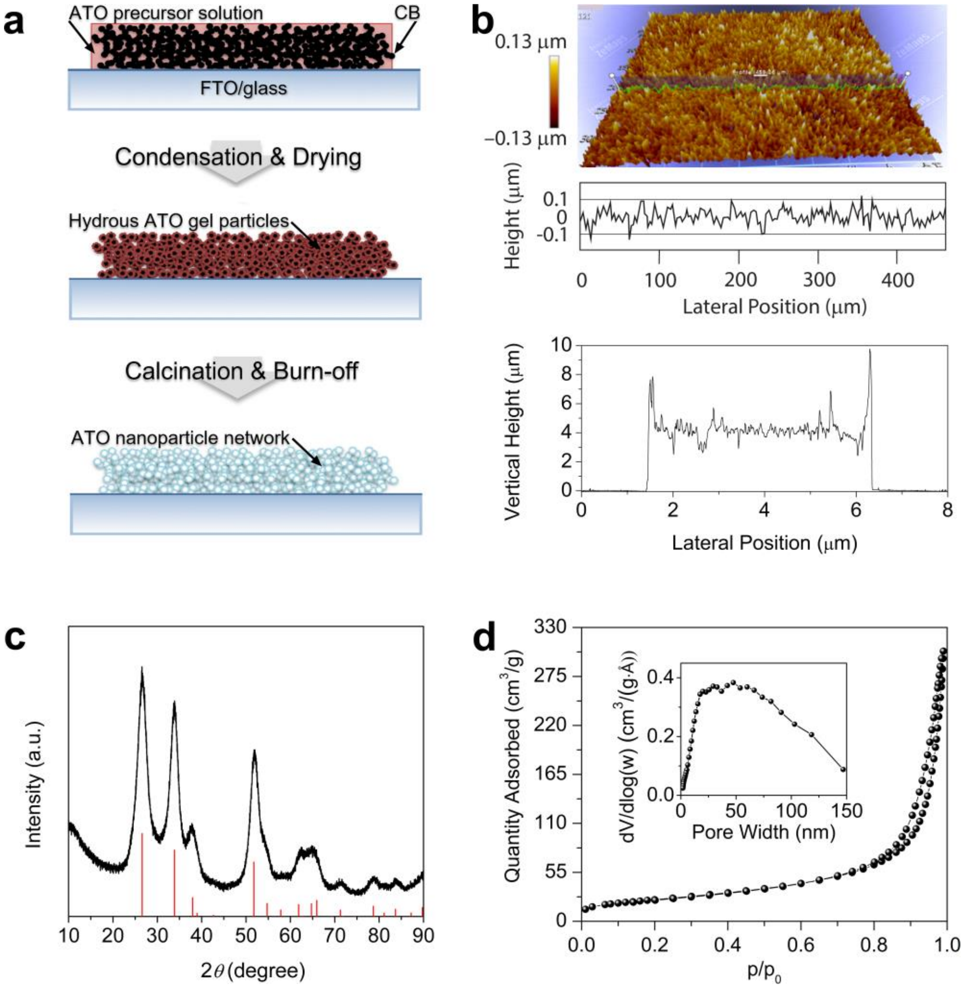

Figure 51. (a) Schematic diagram of the synthetic procedure for the fabrication of meso-macroporous ATO coatings. (b) Profilometry measurements on the meso-macroporous ATO coatings, taken by optical (top) and stylus profilometers (bottom). (c) PXRD pattern of meso-marcoporous ATO. The red lines show the simulated peaks of the previously synthesized ATO with 6.2 atom % antimony doping. (PDF # 01-075-2894) (d) Nitrogen sorption isotherms and (inset) BJH pore size distribution for the meso-macroporous ATO.

By employing carbon black and PEG, self-standing coatings of the reaction mixture can be spread as a coating. Simultaneously, the sol-gel chemistry results in atomically uniform metal oxide or hydroxide nanoparticles, which sinter into a porous material around the carbon black and PEG template. After calcination, the thickness and roughness of the resulting meso-macroporous coatings were characterized by both optical and stylus profilometry methods (**Figure 51b**). Optical profilometry (top) measured the height variations of the surface of the ATO coating, and shows that the largest peak-to-valley difference is less than 200 nm and may be attributed to the macropores exposed at the surface. The optical profilometry technique was not successful, however, in determining the overall thickness of the coating due to the highly reflective cover glass substrate. Instead, the stylus profile (**Figure 51b**, bottom) shows that the coatings have a thickness of roughly 4 µm, except for ~ 200 nm wide regions at the edges where the coating is around 8-10 µm thick. Thicker ATO coating at the edges is due to surface tension of the solvents in the reaction mixture tending to form a meniscus against the tape. These areas were not characterized further. Due to the profilometer's stylus causing damage to the ATO coating during measurement, as seen with the scanning electron microscope (SEM), 4 µm is likely an underestimation of the actual thickness. An edge-on SEM image of the coating (**Figure 52**) shows that the thickness was 4.6 µm, consistent with a slight under-reporting by stylus profile measurement.

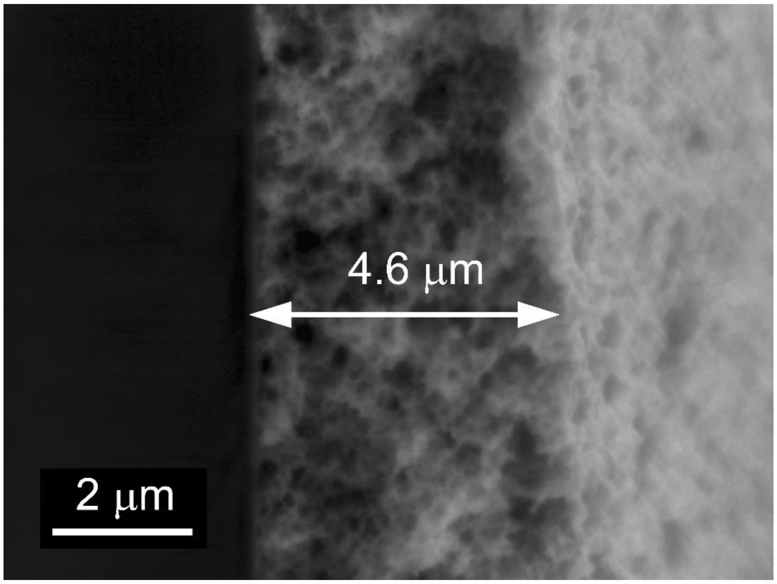

Figure 52. Edge-on SEM image of meso-macroporous ATO coating, where the thickness is measured to be 4.6 µm (scale bar = 2 µm).

The PXRD pattern of calcined ATO coatings (**Figure 51c**) shows that the crystal structure is rutile with lattice constants a = 4.730 Å and c = 3.212 Å, and the width of the Bragg peaks was used to estimate a nanoparticle size of 3.5 nm by the Scherrer formula. Other sol-gel techniques have produced larger particles, while epoxide-based sol-gel methods[54,152] or those using large amounts of multi-block co-polymer surfactants[446] can produce nanoparticles small enough to generate similarly broad Bragg peaks. Such small nanoparticles exhibit a large specific surface area, which can be measured by nitrogen sorption from which mesoporous characteristics can also be elucidated.

Figure 51d shows the results of nitrogen sorption studies, including the sorption isotherms and the resulting BJH pore size distribution. The BET surface area was measured to be 92 m^2/g, which corresponds to a spherical particle size of 9.3 nm, assuming the density of ATO is 7.02 g/cm^3 as previously calculated for other ATO coatings.[134] This size is considerably larger than the particle size of 3.5 nm estimated by applying the Scherrer equation to the PXRD pattern, which suggests that the particles are sintered to be well connected. Similar behavior has been reported for sol-gel $Sb_{0.076}Sn_{0.924}O_2$ briefly heated to 450 °C, for which the Scherrer size was determined to be 2.9 nm compared to 8.3 nm by BET analysis.[152] It is noted that an increase in the connectivity between nanoparticles leads to an increase in the conductivity, although the temperature is not high enough to cause extensive growth of the crystallites.[184] Of note, the doping amount was also based on previous studies to achieve low resistivity with a relatively small amount of dopant.[134,152,184,447]

In addition to imparting mechanical robustness to the coating, the connectivity between the particles forms a textural porosity. Both adsorption and desorption branches of the sorption isotherms exhibit a type III[392] shape that is consistent with macroporous materials (**Figure 51d**); the lack of a saturation at high partial pressures indicates that macropores are co-present with mesopores. The mesopores are evident due to the hysteresis envelope between the isotherms, which shows a type H5 behavior[448] that indicates well-connected and relatively large mesopores. Consistent with these characteristics of the isotherm curves, the BJH pore size distribution (**Figure 51d** inset) indicates the co-presence of various pore sizes. Specifically, the BJH pore size distribution shows a range of mesopore sizes of up to 50 nm, with an average pore width of 17 nm. Macropore sizes up to 150 nm are also observed, which are the maximum detectable pore sizes in nitrogen sorption studies. Compared to other epoxide-based routes to porous ATO that used similar precursor concentrations and calcination conditions, the surface area and measured pore volume are higher for our ATO coating material.[121,134]

Surface textures of both the template system and the synthesized ATO coatings were examined by SEM. **Figure 53 a – f** shows SEM images of coatings of the carbon-black template (**a – c**) and calcined ATO coatings (**d – f**) for direct comparison. The dry template shows a uniform coverage of the glass substrate (**Figure 53a**) with some small cracks associated with drying and shrinkage. The morphology of the template is more apparent in **Figure 53b**, where the carbon black aggregates form < 100 nm irregularities that are evenly distributed and are connected by PEG; some macroporosity is also observable. The individual PEG and carbon black composite particles appear to be ~ 50 nm in diameter, and form grape-like aggregates around 100-500 nm that are seen as loosely connected (**Figure 51c**). A comparison of the images in **Figure 51a** and **51d** shows that during calcination, shrinkage and cracking occur that produce islands of ATO coating material on the glass substrate that are 100-200 µm in size, separated by ~ 10 µm wide cracks. The coating does not peel, however, and maintains good contact with the underlying glass substrate. The surface features of the calcined ATO coating (**Figure 53e**) show high macroporosity with pores ranging in size from 100 to 400 nm at the surface. Furthermore, the pore walls have a thickness of ~ 30-50 nm. When compared to **Figure 53b**, it appears that the macroporosity observed in **Figure 53e** is a result of the sacrificial carbon black template, because the macropore size and distribution roughly matches those of the template. In addition, the macropore walls exhibit textural mesopores with pore widths of 10 – 30 nm (**Figure 53f**). Comparing the images of the template and the ATO coating (**Figures 53c** and **53f**, respectively), it appears that the pore structure in the ATO coating is a negative image of the carbon black and PEG template itself, considering that there was additional shrinkage during calcination. Although the extent of shrinkage is difficult to quantify based on inspection of the SEM images due to the random pore structure, a linear shrinkage of ~ 20% is in line with other methods that templated macropores by polymer beads removed during calcination.[57,135]

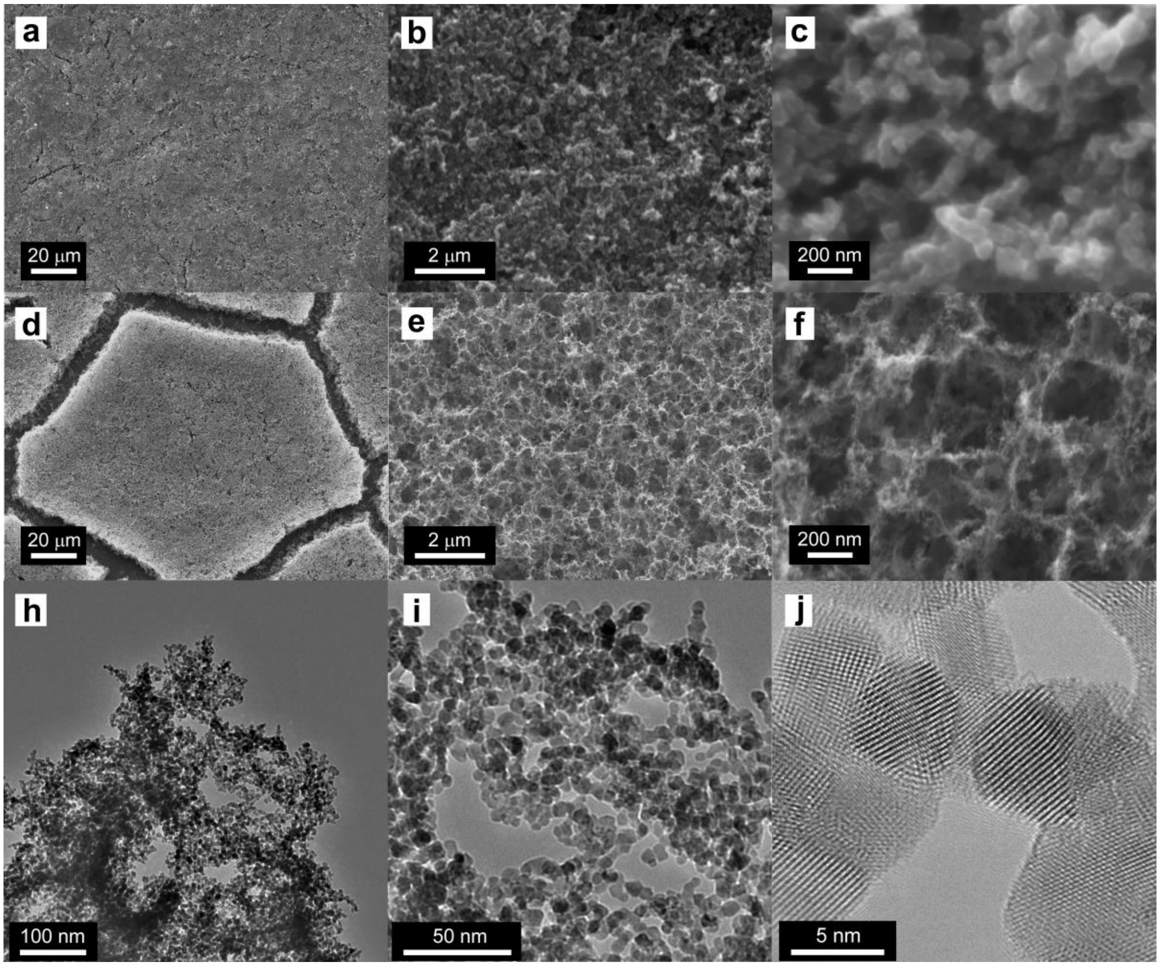

Figure 53. SEM micrographs of the carbon black/PEG template (a – c, scale bars = 20 µm, 2 µm and 500 nm, respectively) and of the meso-macroporous ATO coating itself (d – f, scale bars = 20 µm, 2 µm and 200 nm, respectively). Panels (h) and (i) are TEM micrographs, and (j) is an HR-TEM micrograph of the meso-macroporous ATO, scale bars = 100, 50 and 5 nm, respectively.

To analyze the nature of the observed shrinking, the carbon black reagent itself was imaged by TEM, and heat treatment was carried out in the absence of oxygen to study the coverage of the ATO nanoparticle formation around carbon black template. The carbon black template itself exhibits primary particle sizes around 20 – 50 nm (**Figure 53a**) with an onion-like structure, observable in the HR-TEM image (**Figure 54b**). TEM images of the pyrolyzed reaction mixture (**Figures 54c** and **54d**) show that the carbon black particles are decorated by ATO nanoparticles around 4 – 10 nm in diameter, and exhibit lattice fringes. However, the abundance of ATO nanoparticles was apparently not sufficient to form a connected network on the carbon black; instead, small groupings of ATO nanoparticles are present on the surface of the carbon black particles that come together and sinter into a continuous network as carbon black is removed during calcination.

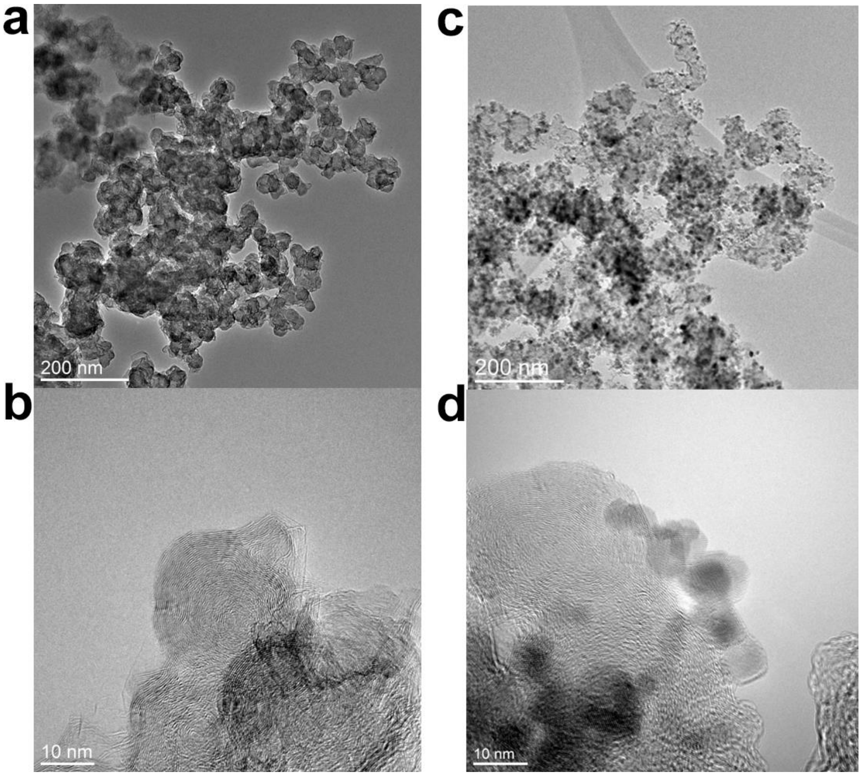

Figure 54. TEM micrographs of the carbon black template (a and b), and the pyrolyzed reaction mixture (c and d). The scale bars are 200 nm (a,c) and 10 nm (b,d).

Typical TEM and HR-TEM images of the meso-macroporous ATO structure are shown in **Figure 53g – i**. **Figure 53g** shows a piece of ATO in which the nanoparticles have a narrow size distribution, and are connected to form both mesopores and macropores. The pore structure cannot be clearly understood by TEM studies due to the 2D projection. One region where macropores penetrated through the aggregate of ATO nanoparticles was more closely examined in **Figure 53h**, and the nanoparticles around the macropores appear to be well-connected. This high nanoparticle connectivity is consistent with the large difference between Scherrer and BET sizes of the primary nanoparticles. The HR-TEM image in **Figure 53i** shows the lattice fringes of individual particles, which confirms that the particles are crystalline, and their size is around 4 nm, in agreement with the PXRD and subsequent Scherrer analysis.

To characterize the diffusion through our meso-macroporous ATO coatings, we turned to single molecule fluorescence microscopy. A published DNA nanostructure, a DNA tweezer,[437,438] was applied as a probe for characterization. The DNA probe is composed of two arms with a spacing duplex (**Figure 55b**). Each arm is ~ 14 nm in length and the distance of the ends of the two arms in the "open" conformation is ~ 16 nm,[437] resulting in a relatively large molecular size to probe the efficiency of entrance and diffusion through our meso-macroporous coatings. The DNA tweezer was modified with one Cy3 dye at the end of one arm and one Cy5 at the other. Due to the background in the Cy3 channel added by the ATO film, the lower-background Cy5 channel was generally chosen for single particle imaging. The DNA probe solution was initially loaded into the ATO coating over 1 h for adsorption, followed by the sample preparation in **Figure 55**. The prepared ATO coating sample was imaged first along the z-axis in the Cy5 channel to record the loading of immobile probes inside the coating (500 ms exposure per frame).

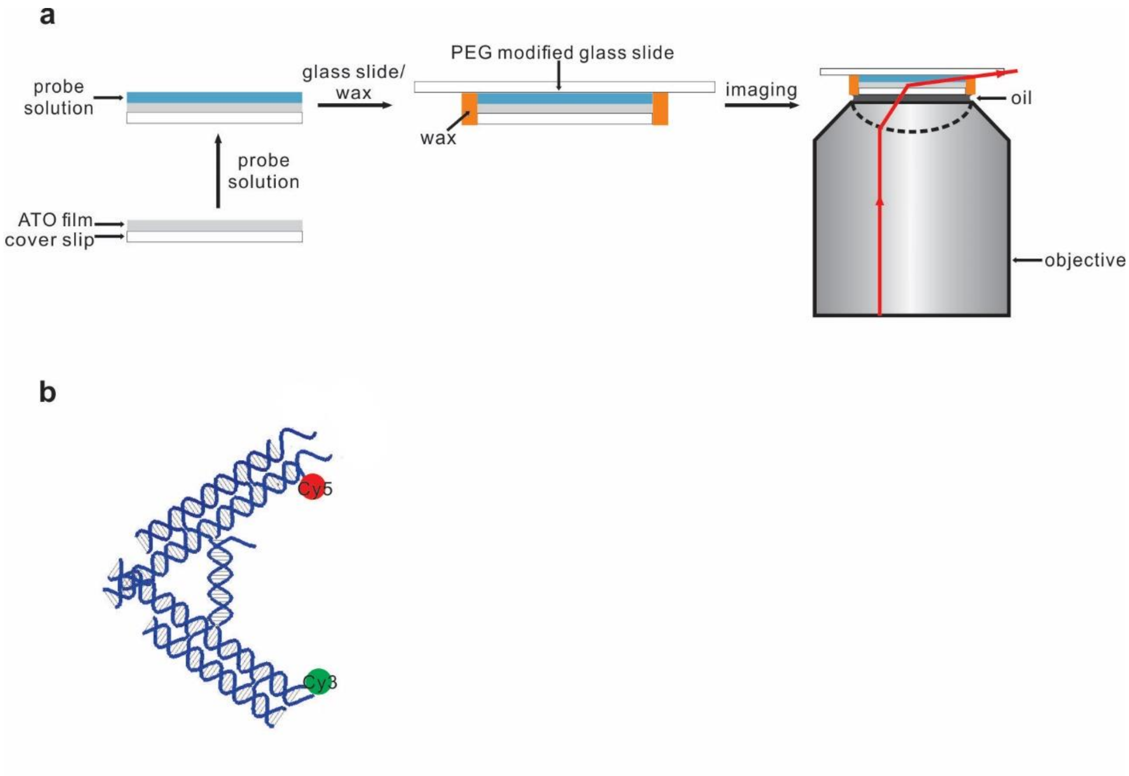

Figure 55. Characterization of our meso-macroporous ATO coatings with fluorescently labeled DNA nanotweezer probes by single particle tracking. (a) Experimental design for sample preparation and imaging. The structural details of the DNA nanotweezer are shown in (b) with the Cy3 and Cy5 fluorophore labeling sites indicated.

Figure 56a shows raw images of adsorbed DNA tweezer probes in three focal planes inside the ATO coating, with the corresponding spatial distribution highlighted below. Immobile fluorescent probes were observed over a range of ~ 7 µm in the z-direction, which is reasonably consistent with the thickness determined by both profilometery and edge-on SEM, given the localization error quantified by a control measurement of DNA tweezers deposited directly onto the cover slip, which shows a probe distribution over ~ 1 µm (**Figure 57**). The distribution of DNA probes throughout the coating, with a higher density near the surface from where the deposition occurred (**Figure 56b**), indicates that the ATO coating is highly porous and accessible. We also found evidence for small cracks in the material, as outlined by a lack of adsorbed probes in the region whose beginning and end are indicated by yellow arrows. (**Figure 56a**, z = 5 µm).

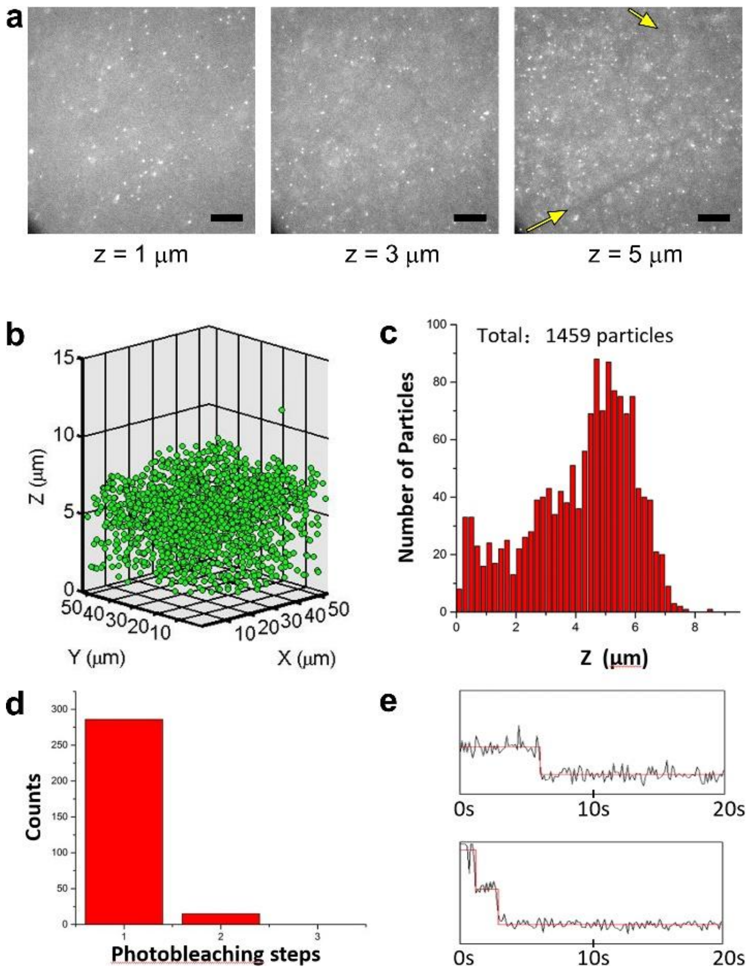

Figure 56. Distribution of fluorescence probes along z-axis inside ATO film. (a) Raw images of DNA tweezer at different focal planes; yellow arrows indicate where a crack enters and leaves the frame (scale bars = 5 µm). Probe counting results are shown in (b) 3D where green dots represent counts and (c) a histogram summarizing the counts at various z-axis heights. Results of the photobleaching study are summarized, showing (d) the number of steps for photobleaching and (e) representative traces of 1-step (top) and 2-step photobleaching (bottom).

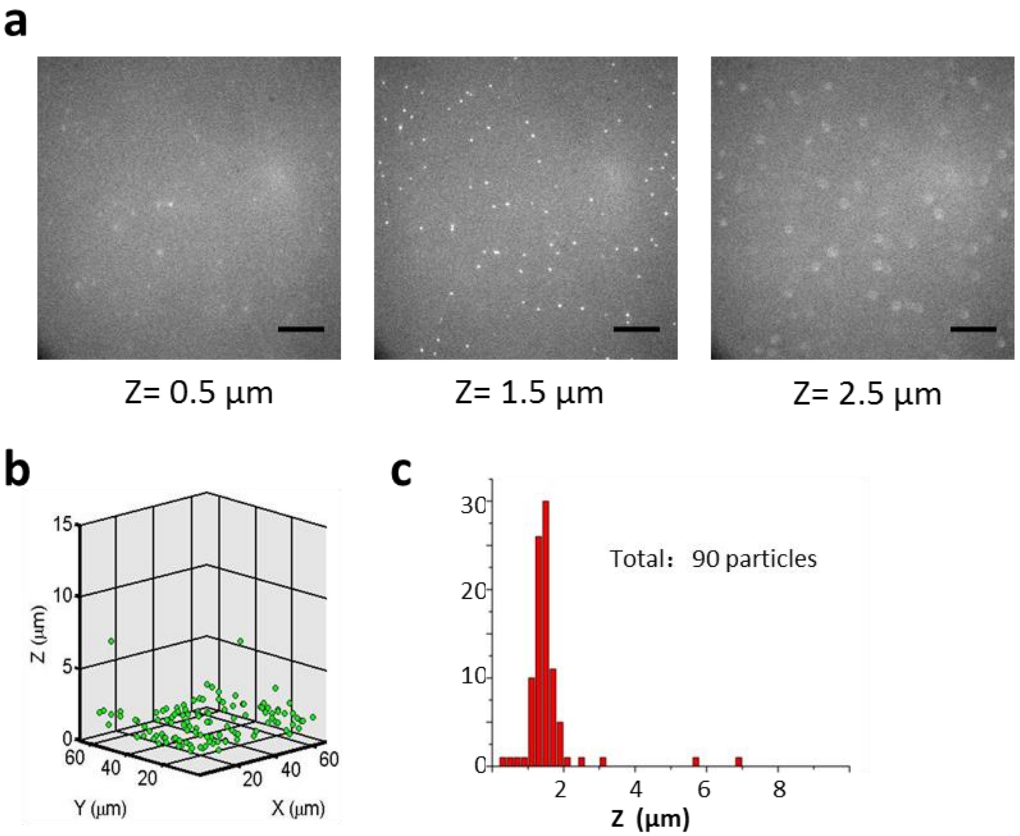

Figure 57. Distribution of DNA nanotweezers along the z-axis when directly deposited onto the glass surface. (a) Raw images of DNA tweezers at different focal planes. The 3D and z-axis distributions are summarized in (b) and (c). Scale bar = 5 µm.

The effect of Mg^{2+} ions in the buffer solution on the suitability of the porous ATO as an effective host for DNA was studied by examining the DNA distributions in solutions with two Mg^{2+} concentrations, 10 and 100 m*M* (**Figure 58**). From the distribution histograms (**Figures 56c, 58b and 58d**), we find that the total amount of DNA remaining in the coatings after the washing step increases gradually as the Mg^{2+} concentration increases. In a separate experiment, the zeta potential of aqueous dispersions of scraped ATO coatings was shown to rapidly increase from – 20 to 5 mV between 0 and 7.5 m*M* Mg^{2+} and then level off **(Figure 59**), indicating that the ATO surface becomes positively charged upon adsorption of Mg^{2+} cations at higher Mg^{2+}

concentrations over about 3 m*M* and thus can electrostatically adsorb DNA. Even at 1 m*M* Mg^{2+} in the imaging solution (**Figure 56b**), however, there is a significant amount of DNA that appears to be present within the coating. The apparent presence of DNA at the low Mg^{2+} concentration may be due to the pore structure that impedes the diffusion paths, although it is not possible to disregard transient binding of DNA in local areas of the ATO surface. A larger amount of DNA can stay in the coating at higher Mg^{2+} concentrations, which is due to the coulombic attraction between the negatively charged DNA and the positively charged ATO surface. However, the increase in DNA tweezers adsorbed at increasing Mg^{2+} concentration was modest, which is in agreement with the gradual increase of the zeta potential in that high Mg^{2+} concentration region (**Figure 59**).

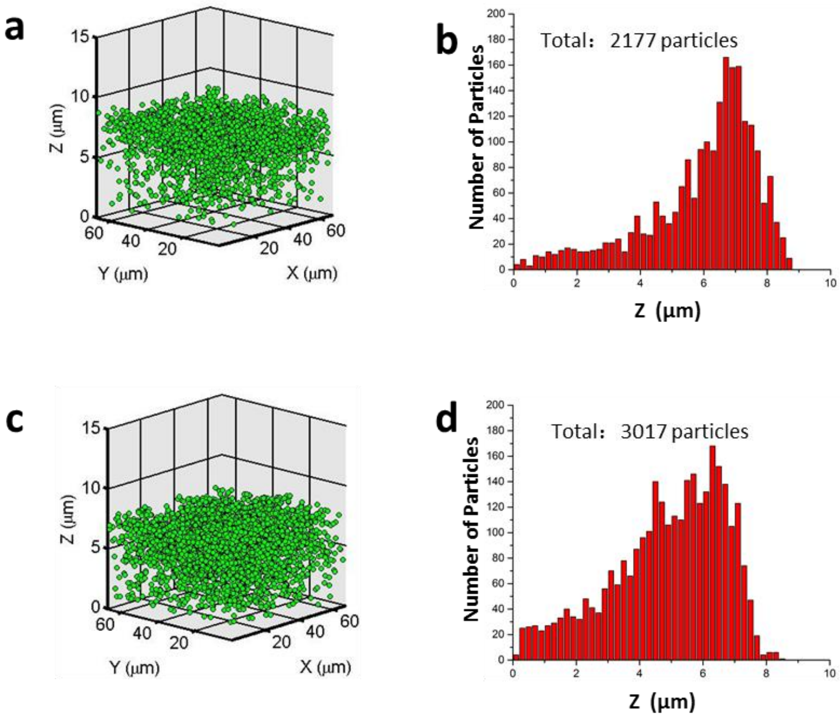

Figure 58. Distribution of DNA nanotweezers along the z-axis inside our meso-macroporous ATO coating at varying Mg^{2+} concentrations. The 3D distribution is summarized in (a) and (b) for 10 mM $MgCl_2$, and (c) and (d) for 100 mM $MgCl_2$.

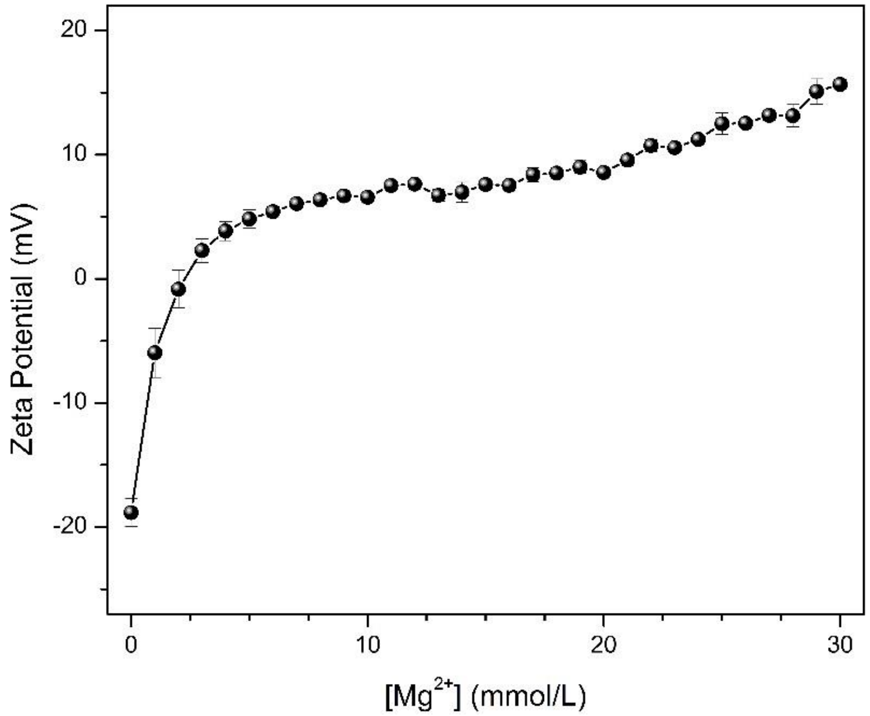

Figure 59. Zeta potential of our meso-macroporous ATO coating measured at varying Mg^{2+} concentrations.

In the next step, a photobleaching experiment was carried out to examine potential agglomeration of adsorbed DNA probes inside the coating (**Figure 53d**). This step was warranted not only because proper diffusion kinetics studies require that the guest particles in a porous medium avoid unwanted agglomeration during the span of the measurements, but also because the functionality of biomacromolecules is deleteriously affected by unwanted aggregation.[449,450] By analyzing the number of photobleaching steps as described (**Figure 56e**),[451] we found that the majority of DNA tweezers remained as single units and that no significant agglomeration occurred. We concluded that our meso-macroporous ATO coatings provide an environment compatible with hosting individual DNA nanostructures.

Successful tracking of the diffusing probes was faced by two challenges, which were the fast diffusion of the probes and the high background signal from the adsorbed probes. We observed diffusing tweezers under optimized imaging conditions, wherein we introduced 10% (w/v) PEG during imaging to slow down their diffusion and pre-photobleached most immobile probes. Movies with 1,000 frames at 20 ms/frame were recorded for particle tracking analysis. A sampling of tracks observed is shown in the **Figure 60a**, which shows the trajectories of many DNA probes, and is followed by four individual diffusion tracking events. Most DNA probes appeared to diffuse randomly (**Figure 60a**). However, a closer inspection revealed different local structures within the ATO coating, characterized by either mostly open space, since a majority of probes moved randomly, or confined space and tunnels, as evident from confined movement of a subset of probes (**Figure 60b**).

To extract kinetic information, further track analyses were carried out using custom MATLAB codes.[436] In a given focal plane, 2-dimensional (2D) random walking was observed from an analysis of the distribution of angles between successive diffusion steps, as evident from the equal angle distribution in each direction (**Figure 60c**). This result is expected since the observed 2D trajectories are projections of the 3D random motion of the probes inside the ATO coating. Moreover, most of the observed tracks had fewer than 10 steps owing to the fast 3D diffusion in and out of the imaging plane, further supporting fast 3D random motion behavior. The diffusion coefficients (D) of individual particles were calculated from the Einstein-Smoluchowski equation: MSD = $2nD\tau$, by plotting their mean square displacement (MSD) versus the time lag (τ) as shown in **Figure 60d**. The dimensionality of motion is n, which is 2 in this case. The DNA probes can be generally divided into two major groups by the slope from their linear fits, with red color used for average slopes > 0.1 μm^2/s (fast diffusion) and blue color for average slopes ≤ 0.1 μm^2/s (slow diffusion). The distribution of calculated diffusion coefficients is shown in **Figure 60e**, with a major peak around ~ 2 μm^2/s.

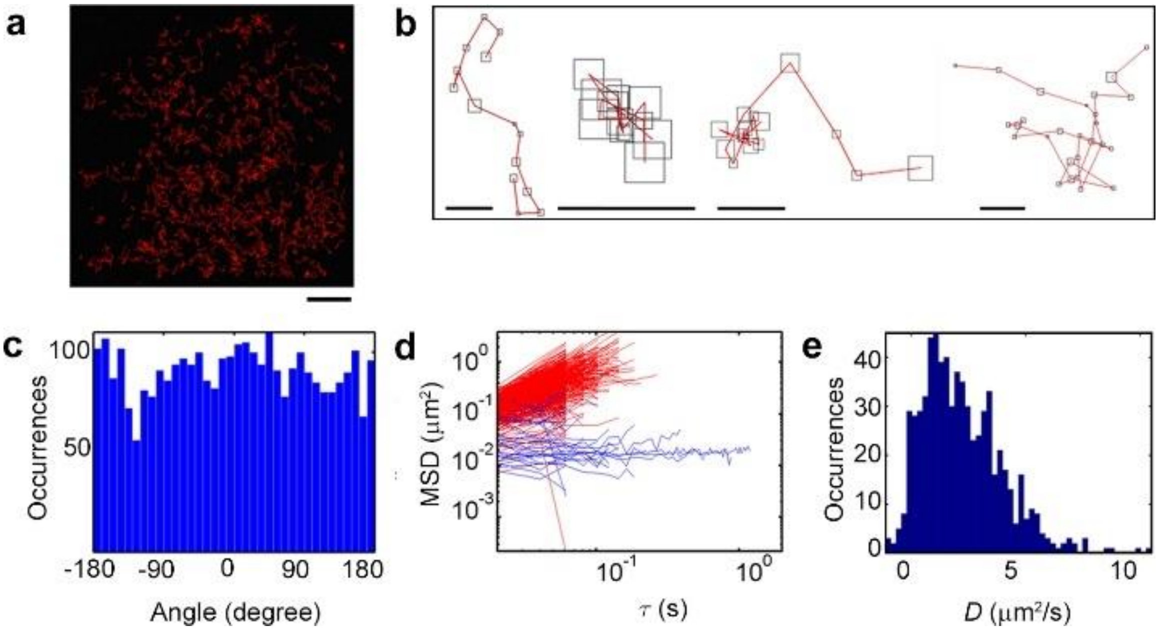

Figure 60. (a) Raw image of diffusion paths (leftmost, scale bar = 10 μm) and (b) exemplary single particle trajectories (scale bars = 500 nm). (c) Distribution of angles between successive diffusion steps. (d) MSD vs. time lag, τ; the trajectories are generally divided into two subgroups based on the slope: mobile (red) and confined (blue). (e) Distribution of apparent diffusion coefficients.

To further distinguish the motional modes of DNA tweezer probes in the ATO coating, a cumulative probability distribution (CPD) analysis was carried out by analyzing all probe trajectories together. As shown in **Figure 60c**, a 2D random motion model was chosen for the CPD plot fitting with three τ value components: $\tau = 0.020$ s, 0.060 s and 0.100 s (**Figure 61**). The best fit was obtained with two diffusion coefficients, indicating that DNA tweezers spend ~ 85% of the time in a fast motion mode ($D = 2.2$ μm^2/s) and ~ 15% of the time in a slow motion mode ($D = 0.12$ μm^2/s).

The fast motion mode accounts for all freely diffusing probes that were trackable, although the free diffusion constant may be higher since the fastest moving probes likely blur given our limiting acquisition speed of 20 ms/frame. Importantly, from the confined movement in the slow motion mode a pore size can be estimated using a diffusion model for restricted particle motion.[441,452] By fitting our data with the theoretical model, the averaged length L of confinement is calculated as ~ 210 nm. This length is within the range of pore sizes observed by SEM (**Figures 53e, 53f**). Based on its unique meso-macroporous structural features, we conclude that our ATO coatings can be readily functionalized with guest particles for a variety of applications.

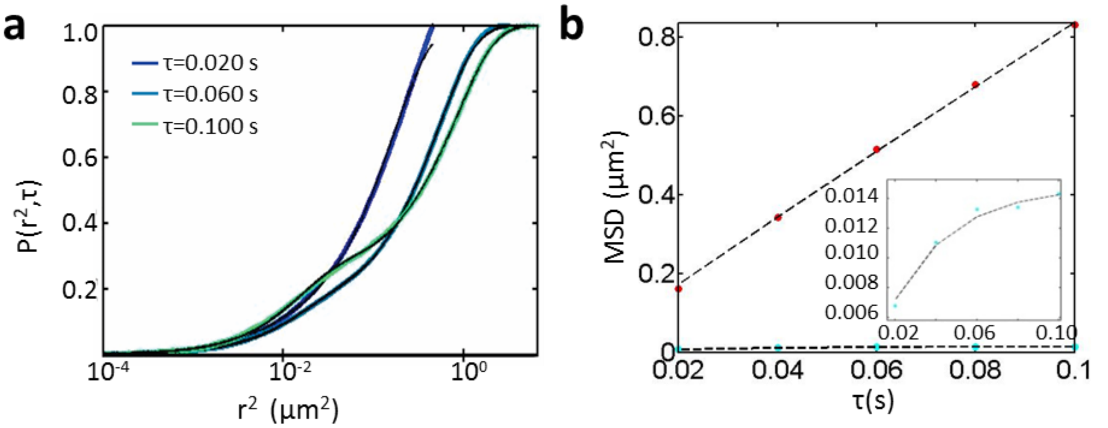

Figure 61. (a) Fitting curves of squared step sizes (r^2) of DNA probes with the 2-term 2D CPD function at three different τ values (fitting as described in Materials and Methods). Three colored lines (corresponding to three different τ) are the calculated statistic analysis from the trajectory data and the black lines are the fitting which overall overlap with the color lines. (b) MSD versus τ for the fast (red) and slow (green) subpopulations of DNA probes obtained from the 2-term CBD fitting. An inset of zoomed result of slow subpopulation is also provided.

4.4 Conclusions and Future Directions

We here have developed a sol-gel based approach for fabricating hierarchically porous, highly transparent, conductive ATO coatings with carbon black as a templating agent. Carbon black additive allows for facile and uniform coating fabrication and, upon its removal by oxidation, serves to impart an openly connected macroporous network throughout the mesoporous ATO coating. We have further applied DNA tweezers as a probe to characterize the meso-macroporous ATO, which demonstrates that the ATO pores are highly accessible to large guest molecules. Two diffusion constants were parsed from trajectory analyses that were attributed to free diffusion (diffusion constant $D = 2.2\ \mu m^2/s$) and to diffusion within an average confinement length of 210 nm ($D = 0.12\ \mu m^2/s$), consistent with the average macropore size of the coating. Overall, meso-macroporous ATO coating is a promising substrate to incorporate guest molecules such as the DNA nanostructures while retaining them as single units. Future applications may include energy applications with photosynthetic or redox-active nanodevices as guest molecules.

4.4.1. Thicker ATO Coatings with Controlled Thickness

Preliminary studies have been conducted toward establishing a procedure by which thicker ATO coatings can be fabricated, and by which the thickness can be controlled. Accordingly, we studied various absolute amounts and weight ratios of carbon black (CB) and PEG template. By increasing the amount of CB and decreasing the amount of PEG used for the template to 7 wt% and 6 wt%, respectively, the viscous behavior of the reaction mixture became shear thinning and by following the same procedure reported in **Section 4.2**, ATO coatings were applied to conducting glass slides. While the reaction mixture reported in **Section 4.2** (with 5 wt% CB and 10 wt% PEG) was too low of viscosity and runny to produce thicker coatings even with thicker masking layers, using 7 wt% CB and 6 wt% PEG instead imparted a dynamic yield stress that allowed for self-standing coatings to be made. With this new formulation, the thickness of the coatings was proportional to the thickness of the mask, as demonstrated by the stylus profiles of coatings with 3x and 4x mask thickness in **Figure 62** showing the thickness resulting from a mask with 3x tape layers as ~ 13 µm, and from a mask with 4x tape layers as ~ 17 µm. Another positive aspect of the coating profile is that the edges do not have as pronounced a spike associated with the surface tension at the tape interface. The lack of a thickness spike at the edge is a further indication that the paste is a solid at zero-shear. However, there is a streaking along the coatings that can be seen in both coating profiles using 3 and 4 tape layers, with a peak-to-valley height of ~ 3 µm.

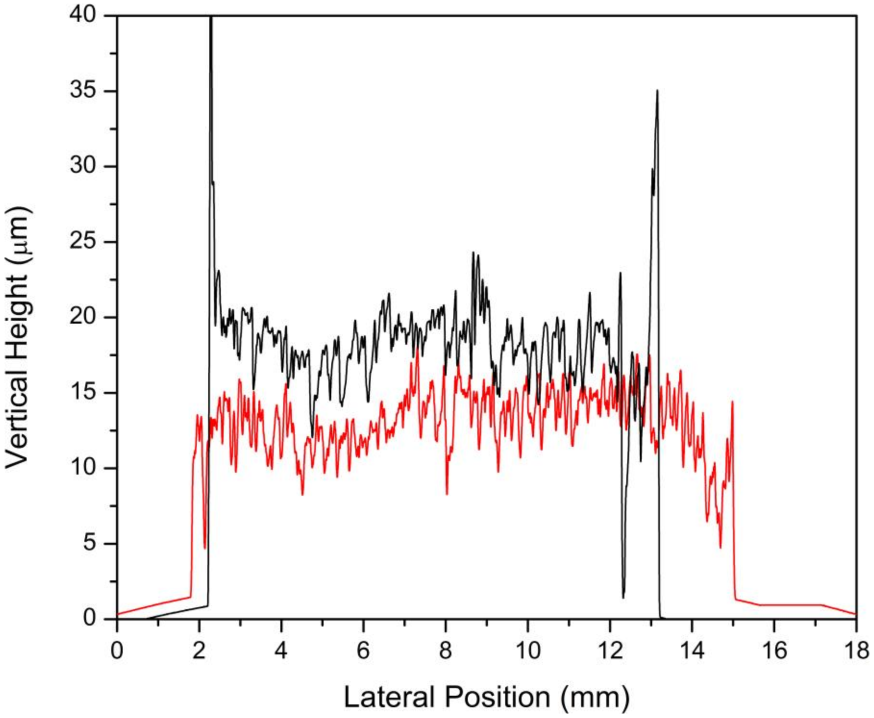

Figure 62. Stylus profilometry measurements of meso-macroporous ATO coatings with masks of 3 tape layers (red) and of 4 tape layers (black).

A synthetic method that allows for fabrication of thicker and adhering coatings of the new hierarchical meso-macroporous ATO should be of utility as the reported macroporous coatings are generally thinner than 1 μm, or peel to a significant extent.[127] Also, the SEM image in **Figure 63a** shows the lack of cracks and the uniform texture of the open pores at the surface of the thicker coating, and **Figure 63b** shows that the pores are open at the surface of the coatings, and that the structure appears to be meso-macroporous with the modified template system for thicker coatings. While these SEM images are from the thickest coating, all coatings made with this template looked similar under SEM. The macropores in the thicker ATO coatings allow for establishing an electrochemical interface with macromolecules with a substantial loading capacity, and therefore a high electrochemical response that cannot be achieved with a flat surface or with a thin macroporous film.

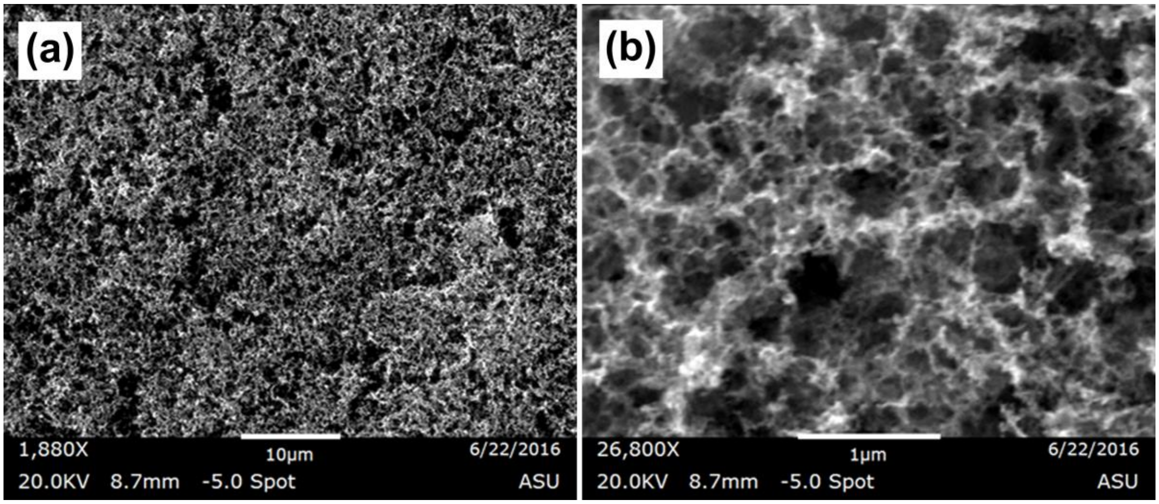

Figure 63. SEM micrographs of the meso-macroporous ATO coating made with a template system containing 7 wt% CB and 6 wt% PEG, masked with 4 layers of tape.

Future studies include fabricating DSSCs and incorporating redox active macromolecules in the thicker meso-macroporous coatings for photovoltaics.

4.4.2. Meso-Macroporous TiO_2 and ZTO

Expanding the CB and PEG template system to other systems is of great interest, since no other method has been reported to produce thick and meso-macroporous coatings that adhere to glass slides. The obvious candidate to try was TiO_2 and $Zr_{0.1}Ti_{0.9}O_2$ based on our previous works. As the mesoporous films of TiO_2 and Zr-doped TiO_2 from **CHAPTER 3** were too transparent to make efficient DSSCs, the thicker meso-macroporous coatings provide a longer path length for light absorption, and the macropores act as scattering centers to increase the absorption within the coatings. **Figure 64** shows the stylus profilometer trace across the $Zr_{0.1}Ti_{0.9}O_2$ coating, which appears to have a large variation in the thickness between ~ 4 – 12 µm.

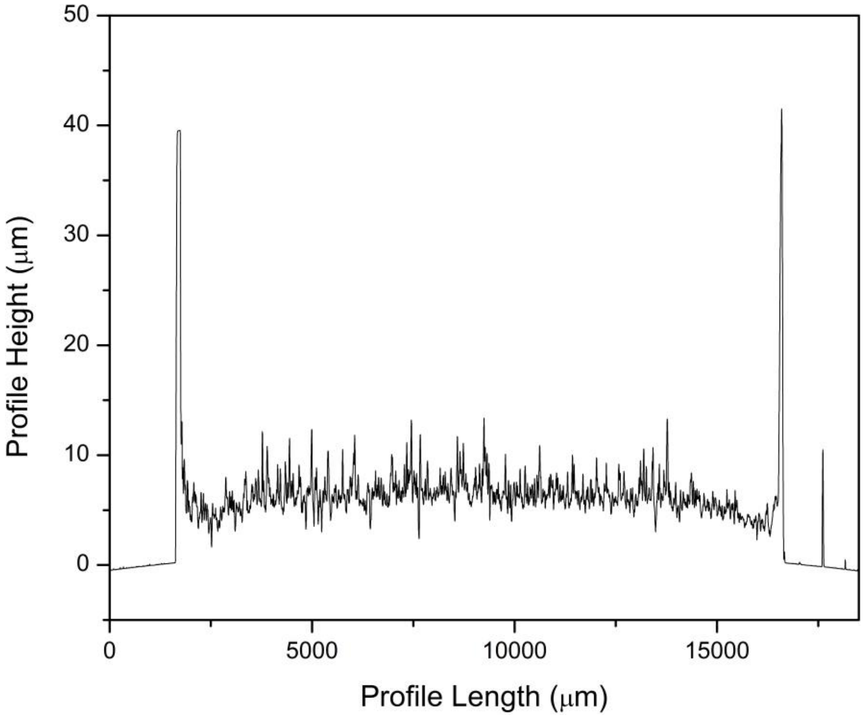

Figure 64. Stylus profilometry measurement of meso-macroporous $Zr_{0.1}Ti_{0.9}O_2$ coating.

In **Figure 65a**, showing an SEM image of the $Zr_{0.1}Ti_{0.9}O_2$ coating, it appears that the coating is highly cracked, which may be part of the explanation for the sharp variations in coating thickness measured by profilometry, although it is not peeling as to maintain the good electrical interface with the underlying conducting glass substrate. **Figure 65b** shows the open porosity at the surface of the ZTO coating material, and the texture of the underlying FTO glass is also seen where the coating is absent.

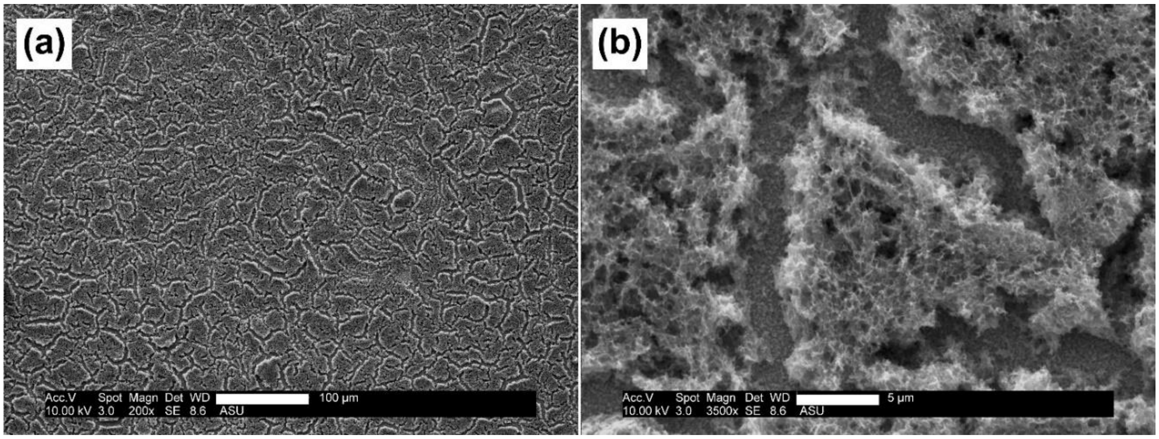

Figure 65. SEM micrographs of the meso-macroporous $Zr_{0.1}Ti_{0.9}O_2$ coating on FTO glass; scale bars are 100 µm (a) and 5 µm (b).

For studies into the performance of the meso-macroporous TiO_2 and $Zr_{0.1}Ti_{0.9}O_2$ coatings as DSSC electrodes, the porous coatings were modified by soaking in a chromophore. **Figure 66a** shows the chemical structure of the chromophore, for which a zincated porphyrin was used in this case. The $Zr_{0.1}Ti_{0.9}O_2$ electrode efficiently adsorbed the dye, as the strong purple color persisted after the coating was rinsed with solvent, a photo of which is shown in **Figure 66b**. In **Figure 66c** the performances of the DSSCs fabricated using TiO_2 and $Zr_{0.1}Ti_{0.9}O_2$ electrodes are presented. A substantial increase by nearly threefold in the photocurrent is apparent, and the open circuit voltage is also seen to increase by ~ 0.12 V upon 10% Zr-doping. The increase in voltage closely matches the increase in the conduction band edge energy measured by the Mott-Schottky technique, reported in **Figure 48b**.

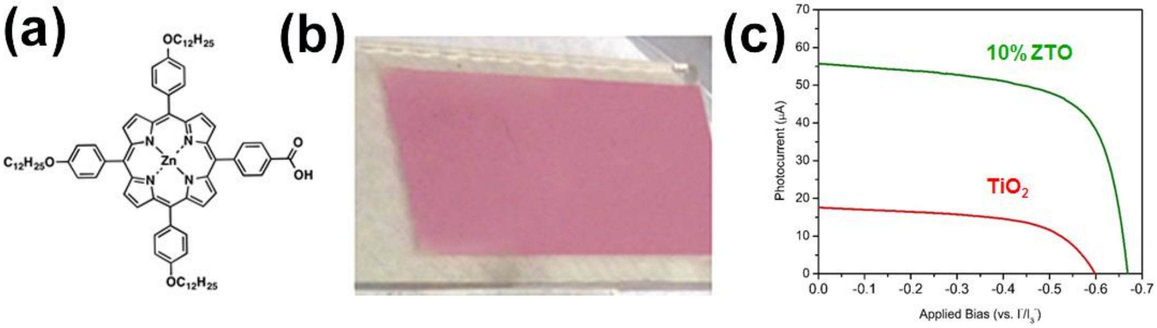

Figure 66. a) A porphyrin dye molecule used to modify the meso-macroporous TiO_2 and $Zr_{0.1}Ti_{0.9}O_2$ coatings for DSSC measurements. b) Photograph of meso-macroporous $Zr_{0.1}Ti_{0.9}O_2$ coating with adsorbed porphyrin molecule. c) I-V characteristics of DSSCs fabricated using TiO_2 (red) and $Zr_{0.1}Ti_{0.9}O_2$ (green).

The meso-macroporous coatings show a markedly higher photocurrent than the mesoporous films. The increase in the open circuit voltage of the DSSC prepared with 10% ZTO, with respect to undoped TiO_2, may be compared to the result found by Imahori *et al*., who did not observe an increase in the open circuit voltage upon Zr-addition of 5 atom% (**Figure 67**).[163]

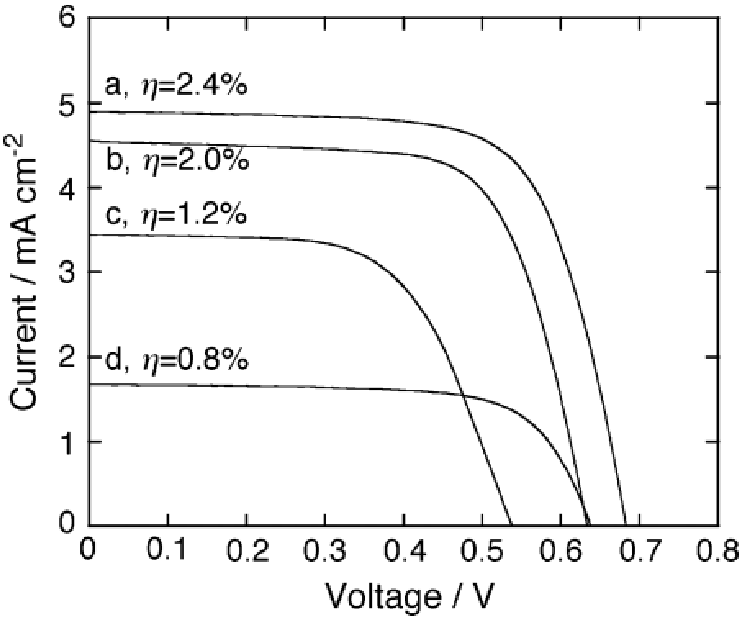

Figure 67. DSSC performance of TiO_2 (curve b) and 5% Zr-added TiO_2 (curve d). Adapted from Imahori *et al.*[163]

Based on the improved photocurrent and open circuit voltage exhibited by $Zr_{0.1}Ti_{0.9}O_2$ vs. TiO_2 in our case, as well as the good agreement between the increased open circuit voltage and the increase in the conduction band edge energy with 10% Zr-doping, it is of great interest to continue these studies for $Zr_{0.2}Ti_{0.8}O_2$ to achieve a further increase of the open circuit voltage, and also to modify the synthetic design both to increase surface coverage and to increase the coating thickness to the optimal levels.

CHAPTER 5

SYNTHESIS AND CHARACTERIZATION OF NEW SOLID ACID COMPOUNDS USING MIXED OXOANIONS, $H_{1-x}Ti_2(PO_4)_{3-x}(SO_4)_x$ (HTPS)

5.1 Introduction

Rhombohedral NASICON-type oxide compounds, $AM_2(XO_4)_3$, have been studied extensively due to their diverse properties and applications including ion exchange,[232] piezoelectricity,[453] luminescence,[454] thermal expansion,[235] chemical sensing,[455] ion-sorption,[456] proton conduction,[457] catalytic properties,[458] and solid electrolyte[249] and redox properties for battery.[310] The diversity is benefited by the flexibility of the NASICON structure that can accommodate various combinations of A, M and X cations in the structure where tetrahedral oxoanions (XO_4) are cross-linked with octahedrally coordinated metal cations (M) via corner-sharing of the oxide ions, and thus form a three-dimensional framework with connected one-dimensional ion channels that host the alkali or alkaline earth (A) cations.

In addition to common metal substitution modification of the NASICON compounds, mixing of the tetrahedral oxoanions has been very productive in discovery and optimization of the physicochemical properties of the compounds for the aforementioned applications. In fact, the original NASICON compound was prepared as a solid solution between the known compounds $NaZr_2(PO_4)_3$[260] and $Na_4Zr_2(SiO_4)_3$[258] for $Na_{1+x}Zr_2(PO_4)_{3-x}(SiO_4)_x$ with much improved ion conductivity.[255,300] The same chemistry has been extended to titanium-based NASICON-type compounds with improved Na^+ ion conductivity in titanium phosphate arsenates[314] and phosphate borates,[459] with Li^+

conductivity in titanium phosphates doped with silicate,[315-317] vanadate,[315,318-320] and niobate.[315,318-320]

Herein we report new mixed oxoanion compounds, hydrogen titanium phosphate sulfate, $H_{1-x}Ti_2(PO_4)_{3-x}(SO_4)_x$ ($x = 0.5 – 1$) through sol-gel synthesis in an acidic medium. This series constitutes a missing component upon comparison of the titanium-based NASICON oxides to the zirconium-based ones. In the literature, NASICON-type $Zr_2(PO_4)_2SO_4$ has been reported from the sol-gel synthesis using sulfuric acid, $NH_4H_2PO_4$ and zirconyl nitrate,[289,329] while the corresponding $Ti_2(PO_4)_2SO_4$ has never been discovered. Interestingly, only $Zr_2(PO_4)_2SO_4$ could be prepared among the mixed phosphate sulfate stoichiometries, even with all different nominal phosphate and sulfate amounts in the precursor solutions including the use of excess amounts of sulfuric acid. The $Zr_2(PO_4)_2SO_4$ decomposed to $Zr_2P_2O_9$ and $SO_{3,(g)}$ gradually when heated over 750 °C.

The NASICON-type $HZr_2(PO_4)_3$ proton conductor could be synthesized by exchanging the Li^+ ions in $LiZr_2(PO_4)_3$ with protons from a dilute acid,[460] or by thermal decomposition of $NH_4Zr_2(PO_4)_3$ at 600 °C.[267,461] However, the same reaction route was not applicable for the titanium system as the thermal decomposition of $NH_4Ti_2(PO_4)_3$ at 770 °C led to an oxygen-deficient NASICON-type compound, $Ti_4P_6O_{23}$ (or $Ti_2(PO_{4-1/6})_3$.[289,462] Appearance of the oxide deficient compound may be linked to the high stability of the NASICON-type framework structure, and yet it still indicates that the Ti–O bonding is not strong enough to avoid the defect formation under the high temperature condition that was necessary for the decomposition reaction.

The apparent thermal instability of sulfate ion and also the formation of oxygen deficiency at high temperatures require new synthetic routes that can crystallize the target products at relatively low reaction temperatures. Sol-gel routes are ideal for the purpose and yet our preliminary experiments indicated that a simple mixture of phosphate and sulfate with a titanium precursor would lead to immediate precipitation of titanium phosphates that do not contain sulfate. It was then discovered that the successful synthesis of the title compounds was possible by employing hydrogen peroxide as a stabilizing ligand of titanyl precursor ions[463-465] in the presence of phosphate ions in a strong acidic medium. Gradual decomposition of the formed titanyl peroxo complexes is possible upon a gentle heating, which enables much improved homogeneous gelation.

5.2 Materials Synthesis

Samples were synthesized by adjusting the synthetic parameters of phosphoric acid amount and calcination temperature, and were named systematically based on these variables. The first number of the names represents the Ti^{4+}:PO_4^{3-} ratio, which was varied between 1.0 and 1.5, and the second number stands for the highest temperature at which the products were treated, which was varied between 400 and 750 °C. The synthetic parameters were chosen based on our preliminary observations of the gelation of the precursor solutions and on the compositional variations we could achieve from the various nominal compositions. The nominal ratio of Ti^{4+}:SO_4^{2-} was that of the Ti precursor, and the weight ratio of polyethylene glycol bisphenol A epichlorohydrin copolymer (PEG) (Sigma-Aldrich, 15-20 kDa) was generally kept constant at 10 wt%.

The concentrations of Ti ions and of H_2O_2 were usually 2.1 *m*, but were varied between 0.3 and 3.5 *m*.

For a typical synthesis of samples with the nominal P/Ti ratio of 1.2 as an example, an aqueous solution of $TiOSO_4$ was produced by dissolving 6.60 g of $TiOSO_4 \cdot 0.18H_2SO_4 \cdot 3.11H_2O$ (Sigma-Aldrich) in 5.50 g of deionized water with magnetic stirring in an 80 mL glass jar, after which the stir-bar was removed. The composition of the titanyl sulfate precursor was determined from both elemental analysis and thermogravimetric analysis. To this colorless, slightly viscous solution, 6.05 g of 27 wt% H_2O_2 (Alfa Aesar) was added gradually, followed by addition of 4.39 g of PEG solution (45.5 wt% PEG in H_2O) while stirring. The nominal mole ratio of Ti:H_2O_2 was 1:1.7. Finally, 4.03 g of 83.3 wt% H_3PO_4 solution in water (Alfa Aesar) was added to the mixture solution. The sulfate and phosphate amounts in all the precursors were determined from elemental analysis. The glass jar was covered loosely with a lid and heated in a lab oven at 60 °C for 40 hrs. The cover was then removed, and the sample was heated further at the same temperature for 12 hrs to yield an orange crumbling dry gel. This resulting solid was calcined at varied temperatures from 400 to 750 °C for 10 hrs in an ashing furnace (Carbolite, AAF1100) with a heating rate of 100 °C/hr to produce a brittle, porous white compound that retained the shape of the dry gel.

5.3 Materials Characterization

Powder X-ray diffraction (PXRD) patterns were obtained primarily on a Siemens D5000 diffractometer using Cu Kα radiation. The crushed sample was spread on a zero-background quartz sample holder, and data was acquired by scanning 2θ from 10 to 90°

with a step size of 0.0403° and a scan time of 30 min. The unit cell parameters were determined by using the PANaytical X'Pert Pro software. The zero position of each PXRD pattern was first calibrated with a silicon powder internal standard (a = 5.4301 Å) and the background was subtracted with a Chebychev polynomial up to the 5th order. The thermogravimetric analysis (TGA) studies were performed using a Mettler-Toledo TGA/DSC 1 STARe system. Analysis was carried out with an air flow (40 mL/min) in addition to the N_2 cell gas (20 mL/min) by heating from 25 °C to 1200 °C at a rate of 15 °C/min and holding for 30 min, and cooling to room temperature.

Scanning electron microscopy (SEM) studies, including imaging and electron dispersive X-ray spectra (EDS), were performed using an FEI XL-30 Environmental SEM using 5 and 15 keV electrons, respectively, on dry-ground samples. For transmission electron microscopy (TEM) studies, dry samples were triturated and dusted on to TEM grids. High resolution TEM images were collected on a JEOL 2010F at an accelerating voltage of 200 kV. UV-VIS reflectance spectra were obtained on a Perkin Lambda 18 Spectrophotometer equipped with a Spectralon reflectance sphere accessory. Elemental analysis was performed on the Thermo iCAP6300 inductively coupled plasma optical emission spectrometer, (ICP-OES). Solid-state NMR data were collected on a 400 MHz Varian VNMRS wide-bore spectrometer with 10 kHz MAS. The ^{1}H spectra were collected using the DEPTH pulse sequence[466] to eliminate background signals from outside the coil, with a recycle delay of 5 seconds and 16 transients. All ^{1}H chemical shifts were indirectly referenced to TMS in the solid state using adamantane (δ = 1.63 ppm).

Nitrogen sorption isotherms were collected on a Micromeritics ASAP 2020 Surface Area and Porosity Analyzer at 77 K. Samples were degassed under vacuum at 200 °C for 8 hrs. To calculate the surface area, the Brunauer-Emmett-Teller (BET) model was applied to the partial pressure range of 0.05 – 0.2 of the adsorption branch. The desorption branch was analyzed by applying the Barrett-Joyner-Halenda (BJH) model using the Halsey thickness curve, heterogeneous surfaces and Faass correction to account for multilayer desorption in estimating the thickness of the adsorbed nitrogen to calculate pore-size distribution.[370] The total quantity of gas adsorbed at the data point closest to $p/p_0 = 0.98$ on the desorption branch was used to approximate the total pore volume.

5.4 Results and Discussion

5.4.1 Peroxide-Based Sol-Gel Synthetic Procedure

Figure 68a is a representative photograph of the aqueous solution containing all the precursors, showing the characteristic red color of peroxo titanium in sulfuric acid.[463,467] The wet gel was dried gradually at 60 °C for 40 hrs with a loosely covering lid and then for an additional 12 hrs after removing the lid. The slow decomposition of the peroxide in the later stage of the heating led to a sponge-like dry gel product (**Figure 68b**). The orange color of the dry gel indicates that a small amount of peroxo ligands still exists in the material.

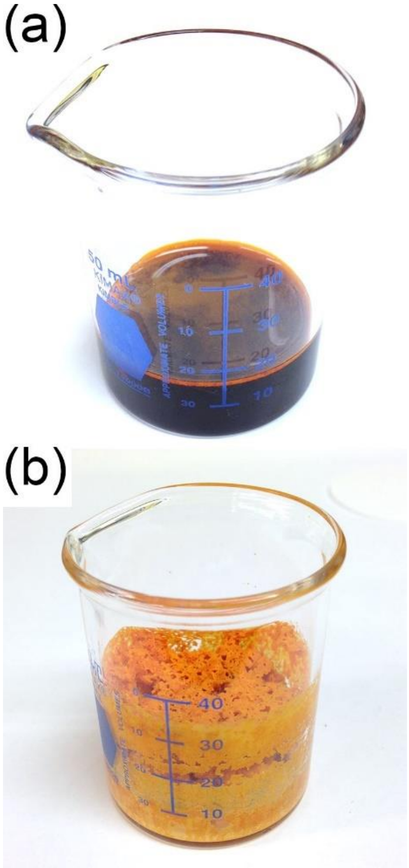

Figure 68. Photographs of the precursor solution with P/Ti = 1.2 (a) before and (b) after covered heating at 60 °C for 40 hrs.

The highly acidic condition was chosen in order to avoid the premature precipitation of the titanyl sulfate precursor and also to provide a high concentration of protons that may be incorporated in the final material. As one of the most important precursors for titanium oxide synthesis, the aqueous chemistry of titanyl sulfate is well documented.[468] Titanyl sulfate exists mainly as monomeric octahedral complex, $(TiO)(SO_4)(OH_2)_3$, in which the sulfate bidentates the titanium ion.[468,469] The covalent S−O bond in sulfate ion leads to a strong ionicity of the sulfate bond with Ti^{4+}, and therefore the complex has a tendency to dissociate in water to yield non-sulfate compounds as a precipitate when the concentration is lower than ~ 1 *M*, or when the solution is heated above ~ 60 °C in our case.[470,471] Similar uncontrolled reaction and precipitation was noticed initially when phosphoric acid was added to the $TiOSO_4$ precursor solution in our preliminary attempts at aqueous sol-gel synthesis of phosphate products.

It was found that the titanyl precursor could be sufficiently stabilized for our sol-gel synthetic route when hydrogen peroxide was added to the solution. The titanium ion can form peroxo complexes in various acidic conditions with or without the co-presence of oxo and sulfate ligands.[463,465,467] The peroxide ligand can be bidentate and yet it can act as a bridging ligand, as found in such species such as $Ti(O_2)_2(OH_2)(OH_3)^+$ and $Ti_2O(O_2)_2(OH)_2(OH_2)_4{}^{2+}$.[463] A sulfate ion can bind the peroxo titanium complex to give $Ti(O_2)(SO_4)(OH_2)_2$, in which the sulfate is also bidentate[464]. The complexing behavior of peroxide with titanyl ion ($[Ti=O]^{2+}$) is not known as much as with titanium ion (Ti^{4+}). Our preliminary results indicated that the titanyl peroxo complex is further stabilized by the copresence of sulfate in the solution, probably due to the coordination of the sulfate with the peroxo titanyl complex.[464,467,472,473] Namely, the red color of the peroxo titanyl complex diminished much more slowly in the presence of sulfuric acid in comparison to the cases of other acids such as HCl, HNO_3 and H_3PO_4. Furthermore, our experimental observations indicated that the titanyl precursor solutions containing both H_2O_2 and sulfate could be gently heated for a prolonged period to the extent that the loss of water led to a highly viscous, cold-honey-like, clear and deep red gel, without undergoing a precipitation. In the presence of HCl or HNO_3, however, precipitated particulates were formed in the same heating procedure. Therefore, it is reasonably suspected that the titanyl complex has both peroxo and sulfate anions as ligands and are strongly stabilized in our synthetic condition.

When phosphoric acid was added to the solution of the suspected peroxo sulfate titanyl complex, the complex molecules stayed stable upon a visual inspection when the peroxide was in excess with respect to the expected 1:1 peroxo titanyl complex formation. Upon heating (50 to 70 °C), a soft orange gel started to form and eventually filled the entire reaction container after 0.5 to 4 hrs, depending on the temperature and P/Ti. The gel became lighter in color during the heating, indicating that the complexes were gradually losing the peroxo ligands in the process of the gelation. The gelation must be due to the reaction of the peroxo sulfate titanyl complex with the phosphate and yet it is not clear which ligand is immediately replaced by the phosphate in the coordination sphere of the peroxo sulfate titanyl complex. The apparent polycondensation during the gelation would indicate that the titanyl complex strongly favors phosphate as a crosslinking ligand. Peroxo anion is also known for its role as a bridging ligand but this is rather unlikely under the strongly acidic condition[463] and also by the fact that the gradual loss of the orange color was observed during the gelation.

Unlike peroxide ions which act as stabilizing and yet decomposable ligands, sulfate ions play another important role as they become a part of the crystal structure of the title compounds. Although not detailed here, the same synthetic procedure using titanium *n*-butoxide as a titanium precursor led to a glassy dry gel that remained amorphous after oven drying and also after subsequent calcination. In another case, repetitive washing of the dry gel led to leaching and depletion of sulfate in the gel, and after subsequent calcination the washed dry gel sample was amorphous. The leaching of sulfate is understandable when we consider that the $Ti{-}OSO_3$ bond is more ionic than that of $Ti{-}OPO_3$. The former bond is more easily hydrolyzed by the nucleophilic attack of water. Under the strong acidic synthetic condition with excess amount of sulfate, the gelation occurs in the direction toward consumption of sulfate. The high proton concentration condition is also important for incorporating the protons in the gel and eventually in the final product. Our preliminary results indicated that the P/Ti ratio in the precursor solution effectively controls both the extent of the sulfate incorporation and the crystallinity of the products.

In our synthetic procedure, the PEG plays a role in stabilization of the gel during the synthesis and heat treatment, hence providing a high surface area to the final product. It is noted that PEG undergoes chemical changes during the sol-gel step, as indicated by the taupe color of the dry gels. In the absence of PEG, the gels became white after the drying. It may be possible that PEG reacts with hydrogen peroxide during the drying process but the presence of PEG is not required for the decomposition of hydrogen peroxide, as evidenced by the white color of the dry gel that is indicative of complete removal of peroxo ligands. Calcining the samples with and without PEG produced products with disparate qualities, where the samples made without PEG were dense and difficult to crush, while the samples containing PEG remained very crushable to produce a fine powder. Therefore, our discussions will focus on the products prepared with PEG.

5.4.2 Calcination and Phase Formation

Figure 69 shows the TGA thermographs of the dry gels with different P/Ti ratios from 1.0 to 1.5. All the samples show drastic weight losses up to 200 °C which are mainly due to the dehydration and dehydroxylation of the dry gels. Calcination at temperatures as low as 400 °C led to white products, indicating complete removal of both peroxo ligands and PEG. The weight loss in 400 – 600 °C may correspond to the decomposition of free or excess sulfates, as anhydrous $TiOSO_4$ begins thermal decomposition at around 550 °C that is completed between 600 and 700 °C.[474,475] The presence of free sulfates was examined by washing the calcined products with deionized water followed by observing the occurrence of a white precipitate when the supernatant was mixed with a $BaCl_2$ solution. None of the samples contained free sulfates after calcination at 600 °C or at a higher temperature.

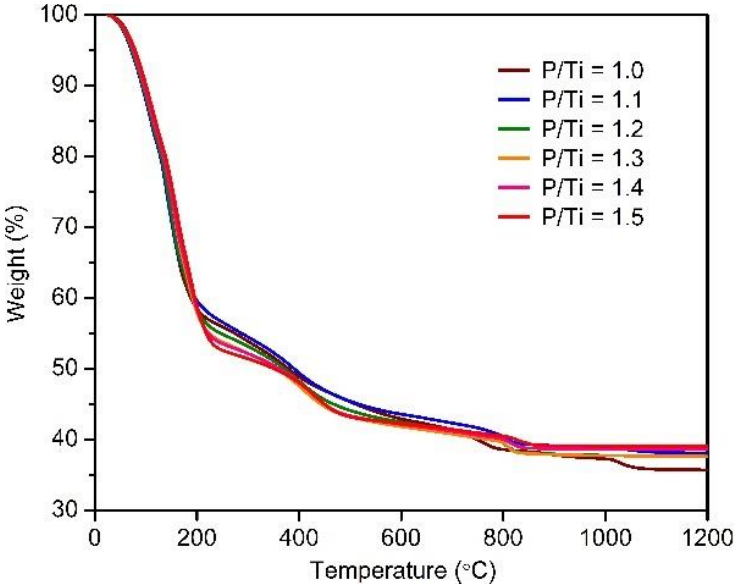

Figure 69. TGA of the dry gels prepared with nominal P/Ti ratios of 1.0, 1.1, 1.2, 1.3, 1.4 and 1.5, from room temperature up to 1200 °C.

The relatively small weight losses, continuous or abrupt, are observed about 600 °C and above in the TGA thermographs. The phase formation behavior of the samples was found to be quite subtle in the temperature range of 600 – 700 °C where a small but gradual weight loss occurs. **Figures 70a** and **70b** show the PXRD patterns of the samples with P/Ti ratios between 1.0 and 1.5, calcined at 600 and 700 °C, respectively. For the nominal P/Ti = 1.0 to 1.2, all the samples exhibit PXRD patterns in which all the

Bragg reflection peaks could be assigned for a rhombohedral NASICON-type structure, when compared with a simulated PXRD pattern of a hypothetical $HTi_2(PO_4)_3$ compound (Space Group: $R\bar{3}c$; a = 8.467 Å; c = 21.69 Å) which is derived by replacing Li^+ ions in the structure of $LiTi_2(PO_4)_3$ with protons. The PXRD patterns do not exhibit any additional Bragg peaks or peak asymmetry that might indicate a structural distortion that has been reported for similar mixed-oxoanion NASICON-type compounds such as for $Na_{1+x}Zr_2(PO_4)_{3-x}(SiO_4)_x$ ($1.8 < x < 2.2$; Space Group: $C2/c$)[255] and more remotely for monoclinic β-$Zr_2(PO_4)_2(SO_4)$.[329]

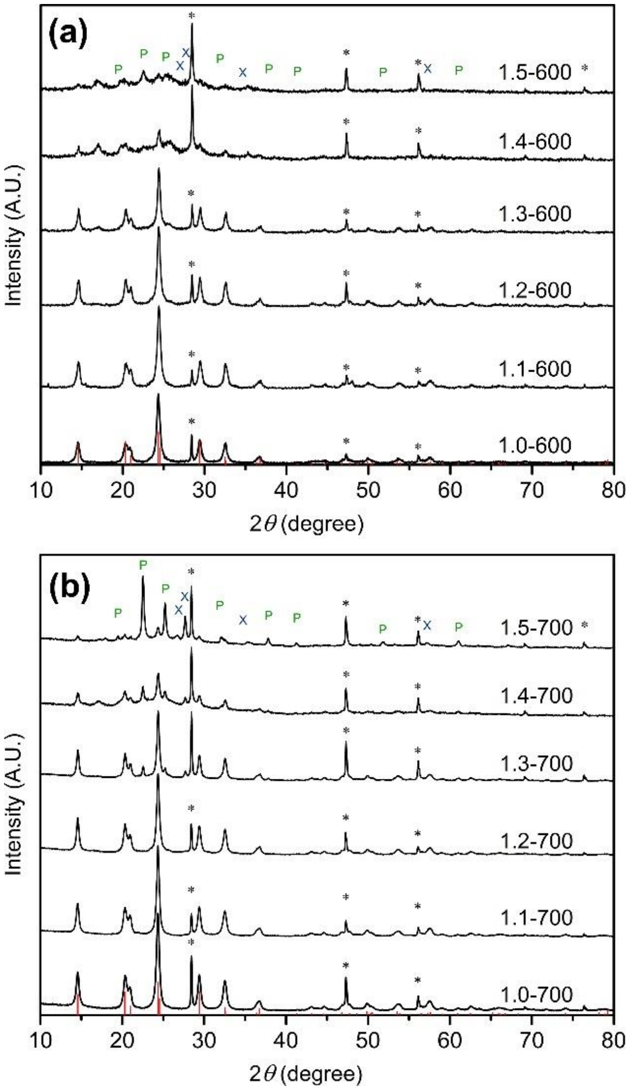

Figure 70. PXRD patterns of the products calcined at (a) 600 and (b) 700 °C, with nominal P/Ti ranging from 1.0 – 1.5. The vertical red lines represent the simulated powder pattern of hypothetical $HTi_2(PO_4)_3$, and the Bragg peaks of TiP_2O_7 (PDF # 00-052-1470), $Ti_5P_4O_{20}$ (PDF # 04-010-3935) and Si (a = 5.4301 Å) are represented by green 'P', blue 'X' and '*', respectively.

In contrast to the NASICON-type compounds formed below P/Ti = 1.3, the samples with the largest nominal P/Ti ratios (1.4 and 1.5) are poorly crystalline and contain TiP_2O_7 and $Ti_5P_4O_{20}$ phases which are more dominating in the products with a larger amount of phosphate and with increasing calcination temperature. As one might expect from the thermal instability of sulfate ion, the compounds decompose further as the temperature increases. After calcination at 1200 °C, the dominant products become TiP_2O_7 and $Ti_5P_4O_{20}$ (**Figure 71**), while the well-known $LiTi_2(PO_4)_3$ is still stable at the temperature (data not shown).

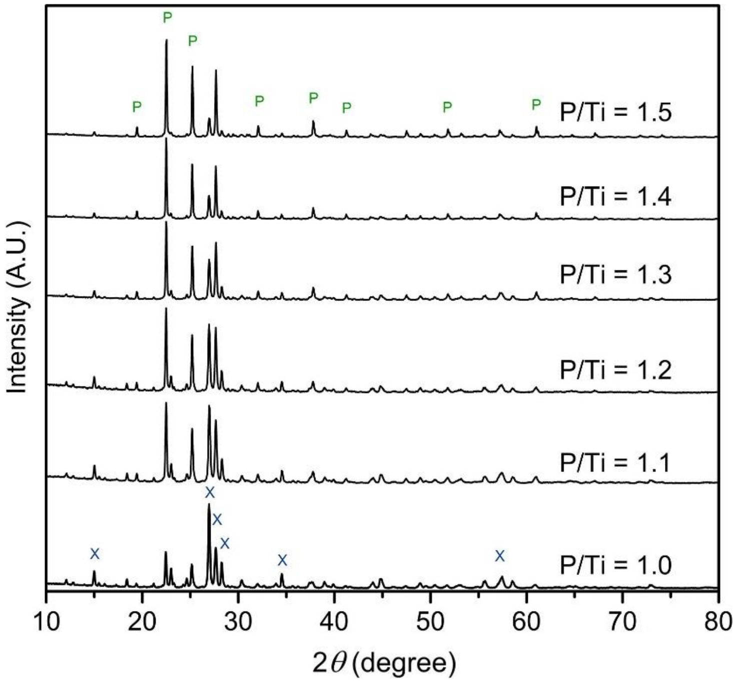

Figure 71. PXRD patterns of the samples with nominal P/Ti from 1.0 to 1.5, heated to 1200 °C. Green 'P' indicate TiP_2O_7 (PDF # 00-038-1468) and blue 'X's indicate $Ti_5P_4O_{20}$ (PDF # 04-010-3935).

Figure 72 depicts the proposed NASICON-type structure of the rhombohedral $H_{1-x}Ti_2(PO_4)_{3-x}(SO_4)_x$ compound, in which TiO_6 (blue) and XO_4 (gray) polyhedra corner-share oxygen atoms to form a three-dimensional framework. In the high-symmetry structure, only one unique Wyckoff position exists for Ti and for P, while oxygen atoms occupy two different unique positions, O1 and O2. The O1 and O2 positions are located inside two secondary building units, the so-called lantern unit (top right) and the ion cage unit (bottom right), respectively, as shown in **Figure 72**. Possible positions (small yellow dots) of the protons in the NASICON structure could be picked out, assuming an O–H length between 0.8 and 0.9 Å and a minimum interatomic distance of 2.0 Å from neighboring nonbonding oxygen sites. It is noted that the simple geometric requirements exclude the protons from the small void inside the lantern unit, like what has been found for alkali metal ions in the NASICON-type compounds.

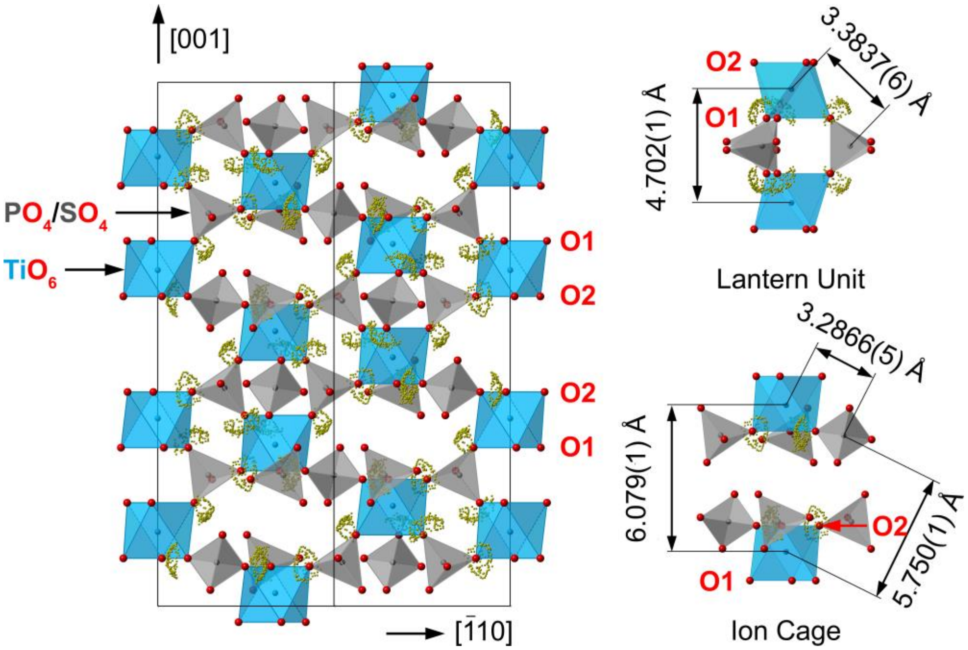

Figure 72. Unit cell of $H_{1-x}Ti_2(PO_4)_{3-x}(SO_4)_x$ projected onto the (110) plane (left) and its building blocks (right), showing possible locations of structural protons (yellow dots). The interatomic distances are given for $x = 0.4$.

Formation of NASICON-type compounds as pure phase is surprising and unprecedented in the literature for a Ti system which does not contain any alkaline element among the precursors. Furthermore, the NASICON phase formation appears to be favored with the limited amount of phosphate. With P/Ti = 1.5, the compound would have the stoichiometry of $HTi_2(PO_4)_3$ if phosphate were much superior to sulfate in the structure formation, and yet this compound does not form in our synthesis. Rather, the compounds are stabilized with the nominal P/Ti not greater than 1.3, which indicates that the sulfate ions must be incorporated into the final NASICON structure, critically assisting the formation of the compounds. The product composition must then be $H_{1-x}Ti_2(PO_4)_{3-x}(SO_4)_x$ with x in $0 < x \leq 1$, satisfying the charge neutrality of the compounds.

The presence of the structural sulfates in the new NASICON-type compounds could be further evidenced from the Raman spectra. **Figure 73** shows the Raman spectrum from 50 to 1800 cm^{-1} of the sample 1.0-700 that was prepared at P/Ti = 1.0 and calcined at 700 °C, along with the spectra of three reference samples, $LiTi_2(PO_4)_3$, TiP_2O_7 and $Ti_5P_4O_{20}$, for comparison. The 1.0-700 sample is a pure NASICON-type phase according to its PXRD pattern (**Figure 70b**) and thus, as expected, the spectrum of the 1.0-700 sample resembles only that of $LiTi_2(PO_4)_3$ and not those of TiP_2O_7 and $Ti_5P_4O_{20}$. In particular, the peaks in 940 – 1100 cm^{-1} in the spectrum of $LiTi_2(PO_4)_3$ correspond to stretching vibrations of phosphate ions in the NASICON-type structure (ν_{as} = 1091, 1083, 1050, 1034, 1005 cm^{-1}; ν_s = 976, 939 cm^{-1}).[476] Other than the noticeable broadening of the peaks, one major difference is that the 1.0-700 sample has three intense overlapping peaks in 1050 – 1130 cm^{-1}, while $LiTi_2(PO_4)_3$ exhibits only one weak peak in the region centered around 1091 cm^{-1}. Indeed, those peaks correspond to the stretching vibration modes of sulfate ions in the monoclinic NASICON-type $Fe_2(SO_4)_3$.[477] Furthermore, the weak additional peaks in both 590 – 660 cm^{-1} and 1200 – 1290 cm^{-1} in the spectrum of the 1.0-700 sample are also unique to those sulfates. The significant peak broadening observed in all the Raman spectra of all the samples also conforms to the presence of the sulfates and also to the expectation from their PXRD patterns that no structural ordering of phosphate and sulfate ions is indicated. Namely, the broad Raman peaks may be due to large local structural distortion,[478-480] originated from the random distribution of phosphate/sulfate ions, as well as from protons in the ion channels in the NASICON structure.

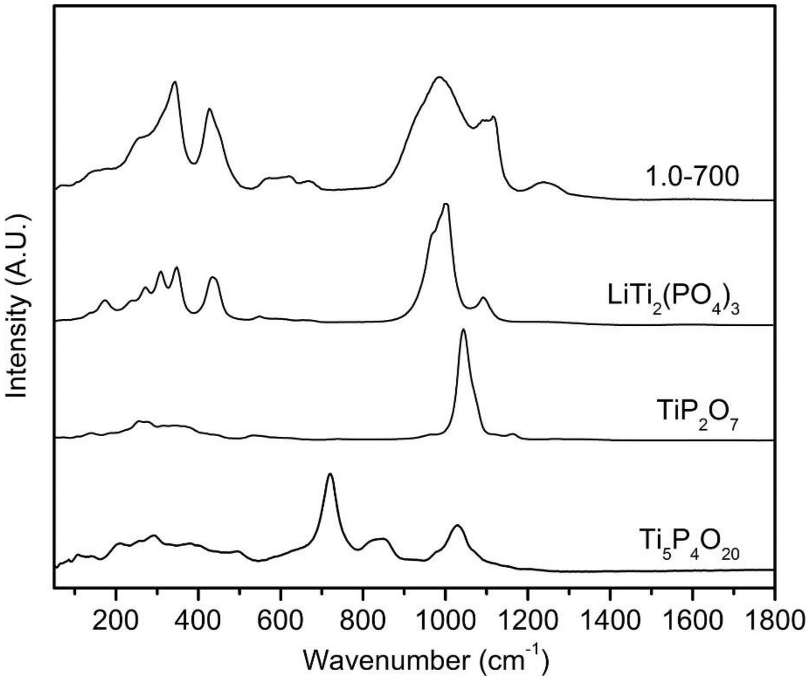

Figure 73. Raman spectra of the 1.2-700 sample, $LiTi_2(PO_4)$, TiP_2O_7 and $Ti_5P_4O_{20}$.

Further trends are found among the Raman spectra in **Figure 74** obtained for the samples with the nominal P/Ti between 1.0 and 1.5, calcined at 600 and 700 °C. Those Raman peaks indicative of the presence of the structural sulfates have the strongest intensities for the samples with lower nominal P/Ti ratios and with a lower calcination temperature (600 °C). In other words, the content of the structural sulfates decreases as the nominal P/Ti ratio and the calcination temperature increase. However, it is interesting to note that the 1.5-600 sample still shows those sulfate peaks in its Raman spectrum (**Figure 74a)**, indicating that while the material is mostly amorphous, it contains a large amount of the structural sulfates. The sulfates decompose significantly when calcined at 700 °C, which is accompanied by condensation of phosphates to pyrophosphate ions ($P_2O_7^{4-}$) which are observed around 1025 cm^{-1} in the Raman spectrum of 1.5-700 (**Figure 74b**).

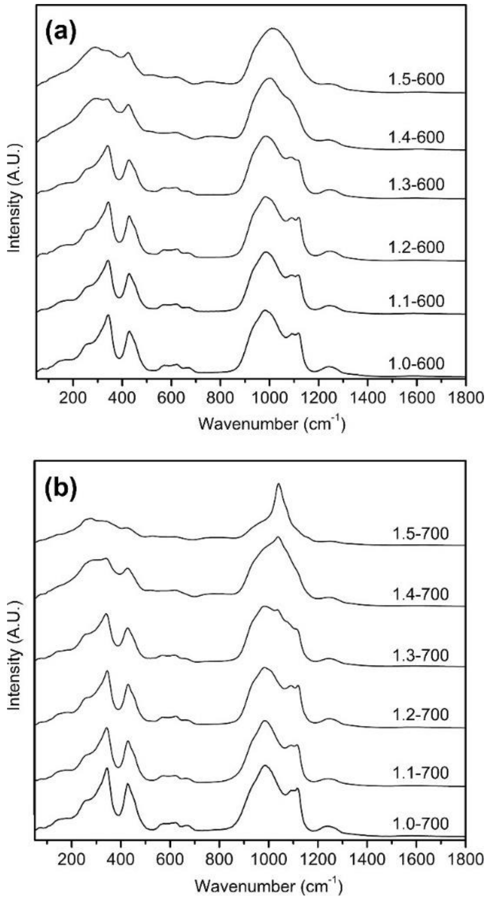

Figure 74. Raman spectra of samples calcined (a) at 600 °C and (b) at 700 °C, with nominal P/Ti ranging from 1.0 – 1.5.

5.4.3 Microscopic Morphology and Porosity

The calcined products were imaged using SEM and TEM to study their morphologies. Spherical particles around one or two µm in size are aggregated to form the bulk particles (**Figures 75a** and **75b**). Higher magnification SEM images in **Figures 75c** and **75d** reveal that these aggregated particles have a nanostructured surface texture. All SEM images shown are from 1.2-600, except **Figure 75d** which shows the 1.2-700 sample for comparison. A subtle difference in the surface textures can be seen in **Figures 75c** and **75d**, showing the coarser surface structure of the sample calcined at 700 °C. **Figure 76** shows TEM micrographs of the 1.2-600 sample which exhibits nanoparticles with diameters of 15 – 20 nm that are strongly fused together to form textural pores less than about 100 nm. Lattice fringes of individual crystallites are apparent in the HRTEM image (**Figure 76b**).

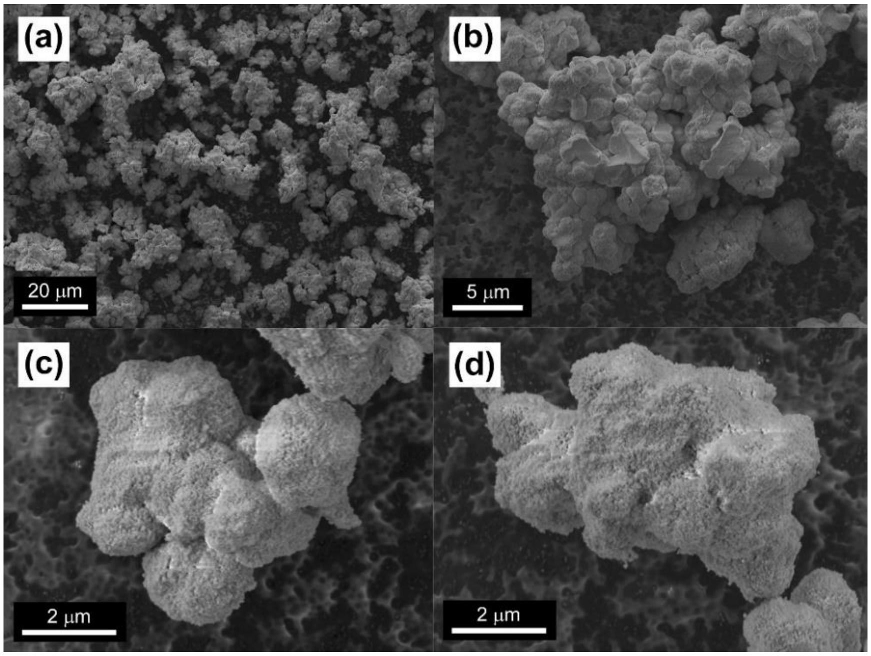

Figure 75. SEM micrographs of (a) – (c) 1.2-600 and of (d) 1.2-700. Scale bars are 20 μm for (a), 5 μm for (b) and 2 μm for both (c) and (d).

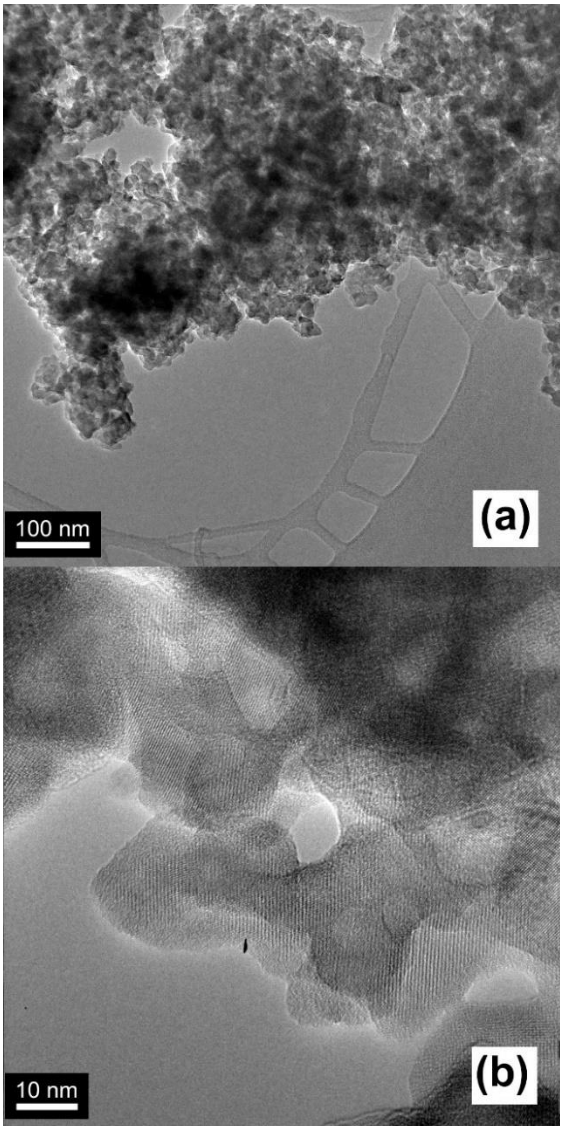

Figure 76. TEM micrographs of the sample 1.2-600. Scale bars are 100 nm for (a) and 10 nm for (b).

Figures 77a and **77b** show the N_2 sorption isotherms and BJH pore distributions of the samples with the nominal P/Ti = 1.2 calcined at different temperatures from 400 to 700 °C. The isotherms are a combination of type-III and type-V with a type H3 hysteresis, indicating presence of both mesopores and macropores.[392] It is noted that the 1.2-700 sample shows its hysteresis loop at a much higher p/p_0 position in comparison to the others, indicating that its pore sizes are much bigger than the others.

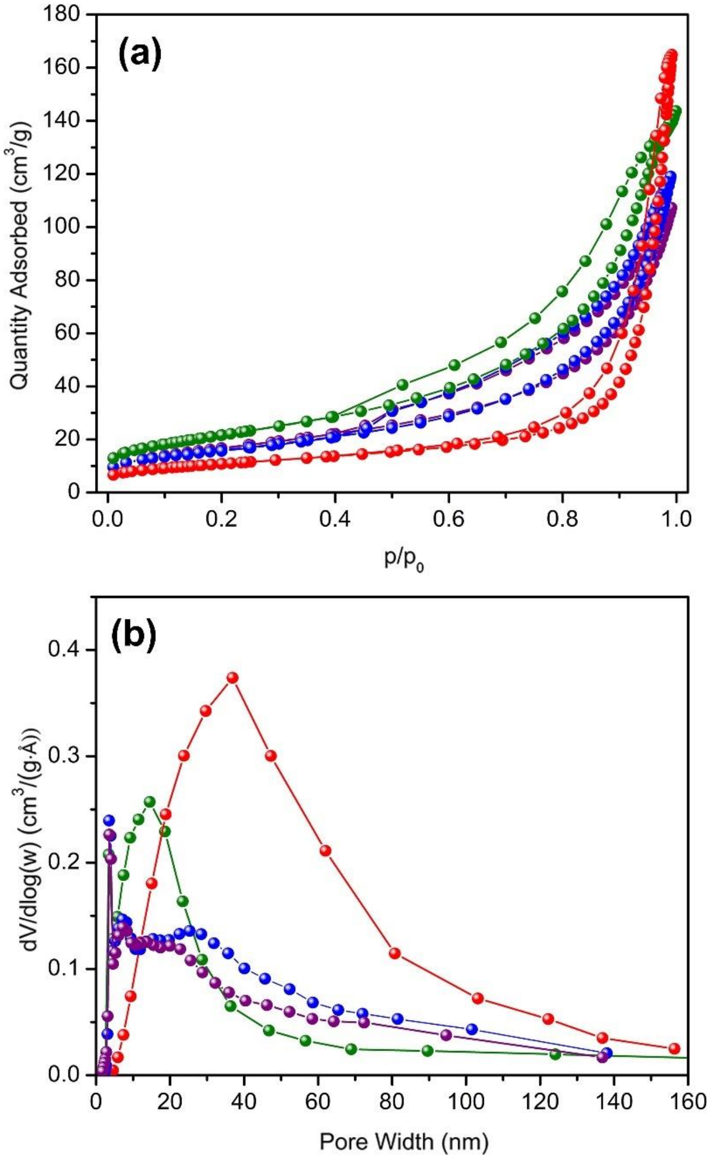

Figure 77. (a) Nitrogen sorption isotherms and (b) BJH pore size distributions for the samples 1.2-400 (purple), 1.2-500 (blue), 1.2-600 (green) and 1.2-700 (red).

This trend can be seen more clearly in the corresponding BJH pore size distributions in **Figure 77b**. The samples 1.2-400, -500 and -600 exhibit a very sharp peak around 4 nm that is usually an artifact corresponding to the sudden closure of the hysteresis loop in the desorption isotherm typically at $p/p_0 = 0.4 – 0.5$, which is due to the tensile strength effect.[481] Furthermore, 1.2-400 and -500 show a bimodal pore size distribution with ~ 8 nm pores as well as pores with a broad maximum between 15 to 27 nm. The broad peak around 20 nm becomes a main feature after calcination at 600 °C, suggesting that particles undergo sintering to some extent to eliminate the ~ 8 nm textural pores. After calcination at 700 °C, the peak maximum is shifted to ~ 40 nm with a much broader size distribution. This shift indicates that pore coarsening starts to occur drastically when calcined at 700 °C. **Table 4** summarizes the pore characteristics along with the crystallite sizes estimated with Scherrer equation. The average pore size is much larger for the 1.2-700 sample, as expected, but the other values are not as significantly different with other samples. The crystallite size is not changed even at 700 °C, implying that the pore coarsening is not due to the particle growth but rather due to softening of the pore neck structure.

Table 4. Surface areas, Scherrer crystallite diameters and pore characteristics of the products. For the sample naming convention, see the Experimental section (**Section 5.2**).

Sample	Scherrer size (nm)[a]	BET surface area (m^2/g)	Pore volume (cm^3/g)	Average pore width (nm)[b]	Porosity[c] (%)
1.2-400	22	41	0.16	15	31
1.2-500	21	47	0.19	16	35
1.2-600	18	78	0.22	11	38
1.2-700	20	39	0.25	26	41

[a] Scherrer crystallite diameter (nm) = $0.89\cdot\lambda/(\mathrm{FWHM}\cdot\cos\theta)$, Cu $k\alpha$: $\lambda = 1.5418$ Å.

[b] 4(total pore volume)/(BET surface area)

[c] Based on $\text{Porosity} = \frac{\text{Pore Volume}}{\text{Pore Volume}+\frac{1}{\rho}}$ where $\rho = 2.8$ g/cm^3 is assumed to be the true density of the products.

5.4.4 Chemical Compositions and Unit Cell Parameters

The competing coordination of phosphate and sulfate ions to Ti^{4+} ions complicates systematic control of the stoichiometry of the new NASICON-type compounds under the sol-gel reaction condition. The amount of the sulfates is always in excess in the precursor solutions and thus the relative amount of the sulfate in the final calcined products depends not only on the thermodynamic stability of the NASICON compounds, but also on the kinetics of the sulfate decomposition during the calcination and crystallization. The $BaCl_2$ test corroborates that the large amount of the sulfates observed in the Raman spectra must be from structural sulfates rather than from free sulfates that can leach out by washing.

The extent of the sulfate incorporation in the final calcined products can be seen in **Figure 78** where the graph shows the relationship of the S/Ti ratio to the P/Ti ratio that was obtained from ICP-OES elemental analysis on all the samples calcined at 600 °C. The red straight line in the graph indicates the theoretical relationship between the S/Ti and P/Ti ratios if all the phosphates in the precursor were incorporated in structure. The presence of the structural sulfates in the 1.5-600 sample is particularly revealing in that the nominal stoichiometry of P/Ti = 1.5 would give a hypothetical "sulfate-free" $HTi_2(PO_4)_3$ if all the phosphates were consumed for the NASICON structure formation. Except for the 1.0-600 sample, however, all of the samples contain more sulfates than the theoretical values and the deviation is the largest for the 1.5-600 sample with S/Ti = 0.23 instead of 0. It is noted that the 1.0-600, 1.1-600 and 1.2-600 samples show slightly decreasing sulfate amounts as the P/Ti increases and yet the similar values may indicate the maximum amount of the sulfate that can be incorporated in the structure. As the amount of phosphate increases in the precursor solution beyond the nominal P/Ti = 1.2, the sulfate amount in the final compound decreases gradually but does not reach zero. Importantly, the observed stoichiometry of the final products indicates that in the products there must be phosphates that have been left out during the gel formation and drying. At low calcination temperatures below 600 °C, these phosphates coexist with sulfates that have not been thermally decomposed yet. We suspect that these excess anions would exist at the pore surfaces of the nanoparticles in the products, although their exact nature is not known. Taking all these into account, the possible compositions of the new NASICON-type compounds are likely to be $H_{1-x}Ti_2(PO_4)_{3-x}(SO_4)_x$ with $x = 0.46 – 1$.

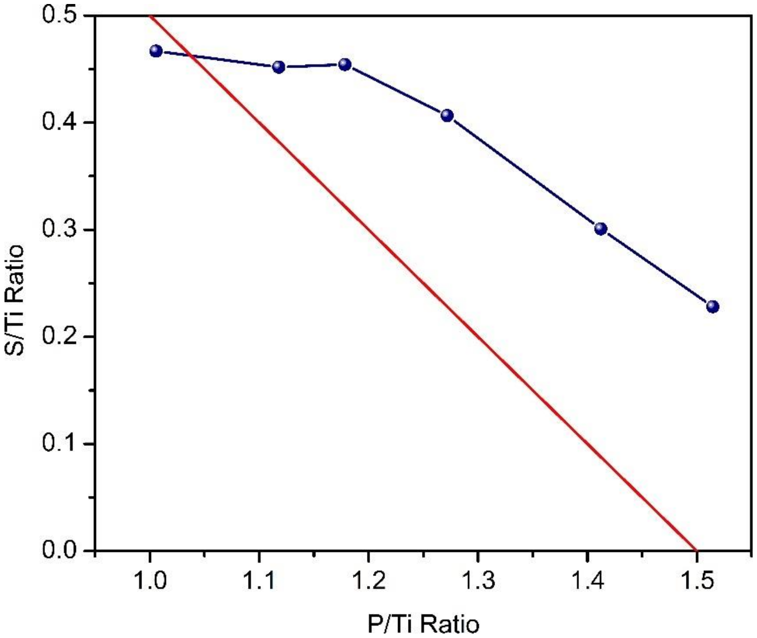

Figure 78. S/Ti vs. P/Ti relationship for the samples calcined at 600 °C, from ICP-OES elemental analysis compared to the theoretical relationship (red line) when all the phosphates are assumed to be incorporated in the structure.

The character of structural protons in the new compounds, $H_{1-x}Ti_2(PO_4)_{3-x}(SO_4)_x$ ($x = 0.46 – 1$), was investigated by using magic-angle spinning NMR (MAS-NMR) spectroscopy on the ^{1}H nucleus for the 1.2-600 and 1.2-700 samples (**Figure 79**). In the direct ^{1}H spectra of both samples, the major broad peak centered around 6 ppm is typically associated with the proton of P–O–H groups.[482,483] The dominance of the peak indicates that the protons responsible for the peak are likely the structural protons in the ion channels of the NASICON-type structure which are bonded to the oxide ions shared by P^{5+} and Ti^{4+} ions. The small split peaks around 1 ppm in the direct ^{1}H spectrum of the 1.2-600 sample correspond to the protons in hydroxyl ligands[484] which are likely due to the hydrolysis at the nanoparticle surfaces upon water adsorption. For the 1.2-700 sample, the sharp peak around 11.6 ppm in its direct ^{1}H spectrum usually indicates the presence of acidic protons[485] but their origin is not clear at the moment. The peak broadening is understandable as the oxide ions are situated in diverse local environments due to the random locations of the sulfate ions and the consequent local structural distortions and bond strength variation. There is a lower chance that the protons are associated with sulfates than with phosphates because of the stronger acidity of the former.

The solid acidity is evident upon forming a dispersion in a solution of methyl orange, that turns red as an indication of the acidity. The dispersion of the compounds in water, that acidifies the solution to pH ~ 3. Further zeta potential measurements reveal that the dispersion has a negative zeta potential, and the PZZP is reached around pH ~ 2 by titrating in acid.

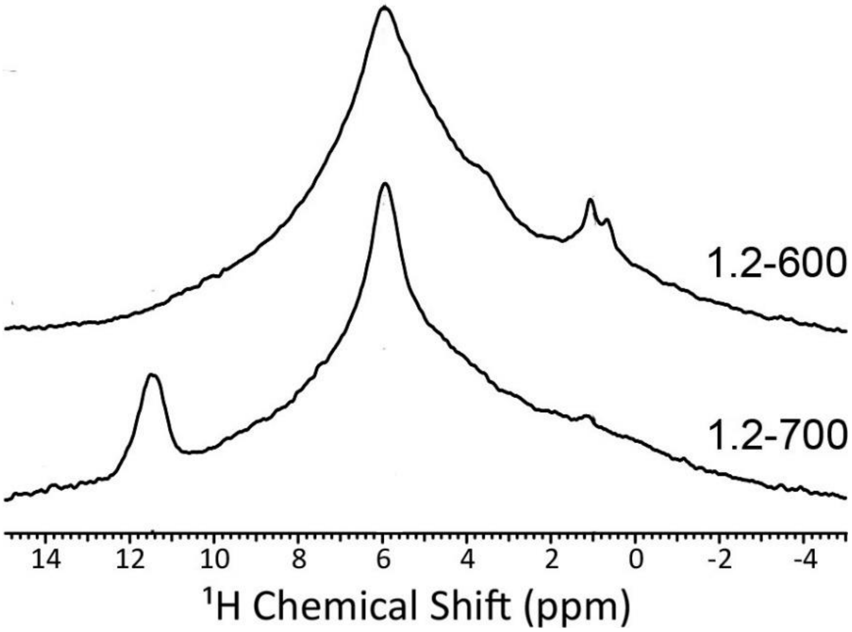

Figure 79. Direct ^{1}H MAS-NMR spectra for the sample 1.2-600 (top) and 1.2-700 (bottom).

Figure 80 shows the unit cell volumes of the pure phase samples of the nominal P/Ti = 1.0 and 1.2 calcined at different temperatures from 400 to 750 °C, as estimated from their PXRD patterns (**Figure 81**). The values were averaged among three sets of samples that were prepared independently but under the same experimental condition. For a given P/Ti, the unit cell sizes are more or less the same up to 600 °C and then increase sharply as the calcination temperature increases. For the P/Ti = 1.2 series, the sharp unit cell volume increase can be explained when we consider that the structural sulfates gradually decompose at those high temperatures and that the decomposed sulfate sites would be replaced by the phosphates migrating from the surface of the particles. This sulfate-to-phosphate replacement will increase the unit cell volume. However, the same argument is not applicable for the P/Ti = 1.0 series which is not likely to have the excess phosphates for the replacement, based on the ICP-OES results. It is suspected that the unit cell volume change is also caused by additional effects such as any impurity formation that produces excess phosphates as well as changes in bond angles and atomic arrangements. Subtle structural changes of the NASICON-type structure are noted in the peak intensity changes near $2\theta = 21°$ in **Figure 81b**.

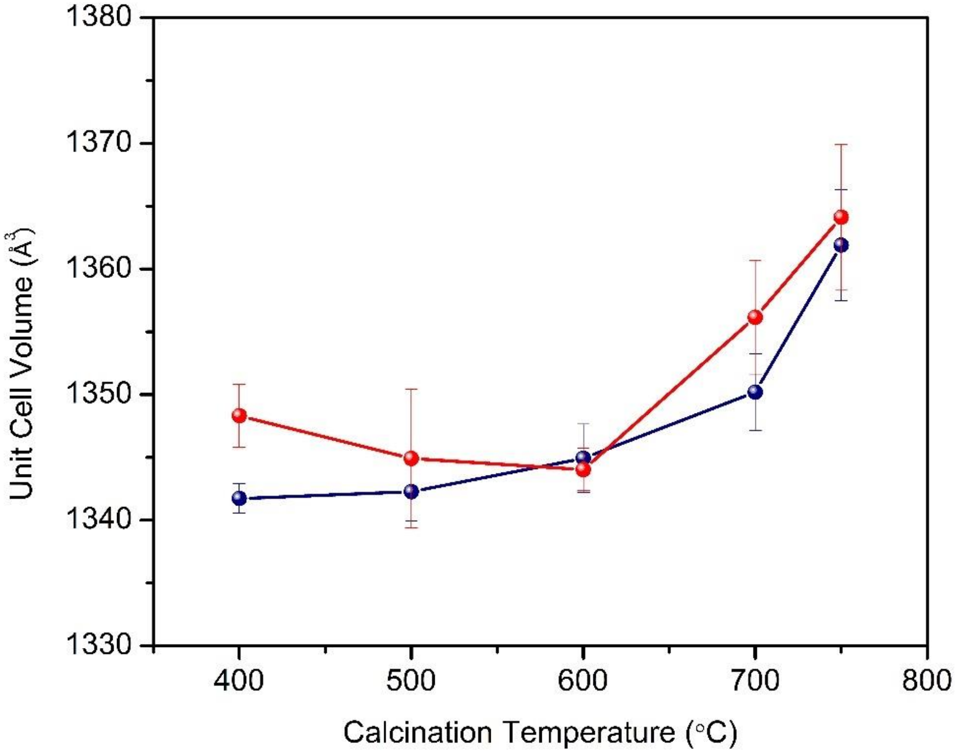

Figure 80. Unit cell volume vs. calcination temperature for the samples calcined at various temperatures, where the blue curve represents the samples with nominal P/Ti = 1.0 and red the ones with nominal P/Ti = 1.2.

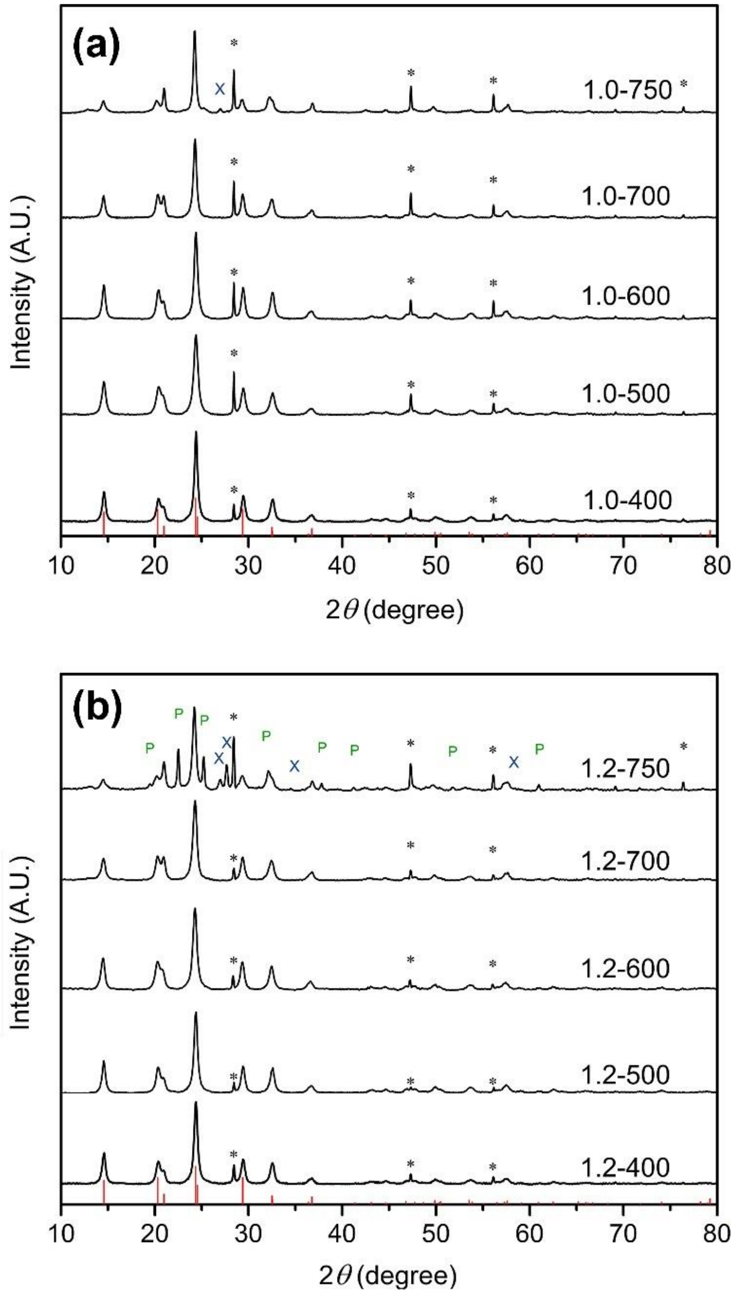

Figure 81. PXRD patterns of the samples (a) with nominal P/Ti = 1.0 and (b) with 1.2, calcined from 400 to 750 °C.

With different phosphate amounts, the samples of P/Ti = 1.2 show a slightly larger unit cell than the corresponding P/Ti = 1.0 samples by up to about 0.7%. This is not inconsistent with the facts that the former contains a slightly larger amount of phosphates than the latter and that the ionic radius of P^{5+} ion (0.17 Å) in a tetrahedral environment is larger than that of S^{6+} ion (0.12 Å).[395] A similar observation could be made for the samples calcined at 600 °C with varied P/Ti ratios from 1.0 to 1.4 where the unit cell volume increases by up to 1.3% in the series (**Figure 82**). However, the quantitative estimations must be viewed with a caution, due to the inherent error in elemental analysis and to the limited precision of unit cell parameter determination of the nanoparticles.

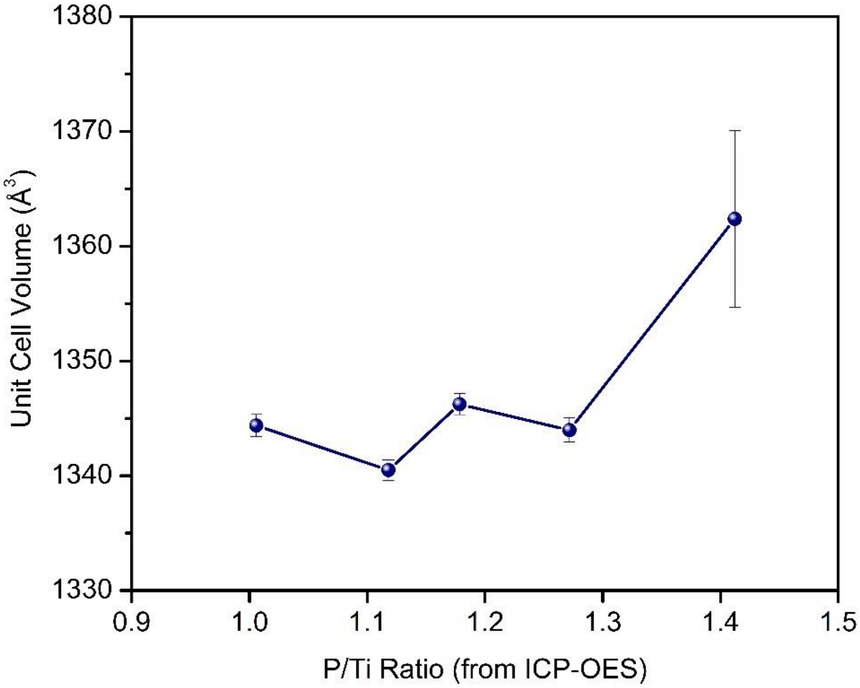

Figure 82. Unit cell volume vs. P/Ti ratio calculated for the samples synthesized with various P/Ti ratios, and calcined at 600 °C.

5.5. Concluding Remarks and Future Directions

New rhombohedral NASICON-type compounds, hydrogen titanium phosphate sulfates, have been discovered in an aggregate form of strongly fused nanoparticles (~20 nm in diameter), through a new sol-gel route that utilizes peroxide ion as a decomposable stabilizing ligand for titanyl ions in the presence of phosphates in a strong acidic medium.

TGA, PXRD, ICP-OES elemental analysis, and Raman and ^{1}H MAS-NMR spectroscopic studies have established the presence of sulfate and proton ions in the structure and the compositional range has been determined to be $H_{1-x}Ti_2(PO_4)_{3-x}(SO_4)_x$ ($x = 0.5 – 1$). Except for the case of 1:1 Ti:PO_4 nominal ratio in synthesis, all the well-calcined final products contain an excess amount of the oxoanion ligands, implying that the surface of the product nanoparticles is more likely covered with phosphates. The new synthetic method allows crystallization of the mixed oxoanion compounds under the temperature where sulfate ions decompose and thus may be expanded to explore new phosphate sulfates of other early transition metals. Future studies would determine the potential of the new compounds in various applications as battery materials, proton conductors and solid acid catalysts.

CHAPTER 6

CATALYTIC STUDIES OF HTPS

6.1 Introduction

Dehydrogenation of alcohols to aldehydes is important for producing the precursors for manufacturing downstream products, including fine chemicals, pharmaceuticals, polymers and inks.[486] Demand for formaldehyde is increasing, and currently exceeds 30 MT/year[487] while demand for acetaldehyde is around 1 MT/year,[488] respectively. Formaldehyde is primarily manufactured by oxidative dehydrogenation of methanol to formaldehyde. For the oxidative dehydrogenation of methanol to formaldehyde, industrial catalysts can achieve upwards of 98% conversion with 95% selectivity with iron molybdenum oxide and 100% conversion with ~ 92% selectivity with silver.[489,490] Both iron molybdenum oxide and silver also catalyze the oxidative dehydrogenation of ethanol with > 90% selectivity for acetaldehyde and around 50% conversion at relatively low temperatures (~180 °C).[491-493] Non-oxidative dehydrogenation of methanol and ethanol take place by the following reactions:

$$CH_3OH \rightleftarrows CH_2O + H_2 \qquad \Delta G < 0 \text{ when } T > 507\ ^\circ C^{33} \ (1)$$

$$CH_3CH_2OH \rightleftarrows CH_3CH_2O + H_2 \qquad \Delta G < 0 \text{ when } T \sim 550\ ^\circ C^{494} (2)$$

Recently, considerable interest is being paid to the non-oxidative dehydrogenation of methanol and ethanol due to the safety and sustainability aspects of the reaction compared to the oxidative route. Avoiding the use of oxygen removes the explosion risk, and produces hydrogen which is valuable as a fuel and chemical precursor. Also, the azeotropic mixture of formaldehyde and water is not formed. Ethanol, a platform chemical for biorenewable chemistry,[495] is also gaining interest as a substrate for dehydrogenation. Iron molybdenum oxide and silver catalysts are not suitable for this reaction because oxide mobility is essential for these,[490,496-498] and they become eventually deactivated under an inert carrier gas.[490]

In a thermodynamic simulation where there was no competing reaction to (1), conversion of methanol to formaldehyde began around 200 °C with tiny conversions, and increased from 20% at 400 °C to 87% at 600 °C.[499] When the competing reaction of dehydrogenation to carbon monoxide was included in the simulation, methanol conversion reached nearly 100% conversion by 200 °C, and at all temperatures the selectivity to carbon monoxide was dominating as its equilibrium constant is ~ 10^6 or 10^7 times greater than that of dehydrogenation to formaldehyde.[499] Therefore, establishing kinetic control by employing catalysts is needed to enhance conversions at low temperatures and to suppress competing reactions. Catalysts have also been sought for these reactions to eliminate the formation of coke, CO or CO_2.[33,500-503]

Even when catalysts are employed, appreciable yields of formaldehyde generally require higher temperatures (~600 – 900 °C)[499,500,504]. Supported metallic nanoparticle catalysts have been reported as having 100% selectivity for formaldehyde with conversions as high as 2% at 300 °C for $Cu^{(0)}$ nanoparticles on fluoro tetrasilicic mica, that increased to 6% conversion at 400 °C.[500,502] Adding phosphorous to copper on SiO_2 markedly increased the catalytic performance with P/Cu ratio = 0.2, maintaining the selectivity of 92% at 500 °C with 25% conversion with a ratio of catalyst mass and substrate flowrate (W/F, g_{cat} h/mol_{MeOH}) of 0.8, and 84% conversion with 52% selectivity with W/F = 4.2. Beyond metallic particles, solid bases are known to catalyze the non-oxidative dehydrogenation of methanol and $Na_{0.5}Li_{0.5}AlO_2$ showed 98% conversion and 74% selectivity with W/F = 9.3. However, the noteworthy performance is observed only at a high temperature (900 °C), while below 750 °C it generates coke which deactivates the catalyst.[505] At higher temperatures, decoking reactions take place between carbon and hydrogen to form methane.[505] Other solid bases such as Ag_2O, ZnO, $NaMgPO_4$, Ag–SiO_2–Al_2O_3–ZnO and Na_2CO_3 could be also used at the temperatures in 600 – 900 °C.[33,500,502-508] The 13X zeolites exchanged by Zn^{2+} ions showed 67% selectivity with 34% conversion at 600 °C. Although the selectivity was still low, the study interestingly found that at relatively low temperature the residual solid acidity in the aluminosilicate framework is important in preventing the complete dehydrogenation of formaldehyde to carbon monoxide.[503] Silver included in an amount of 20 wt% has been added to the solid-state base compounds within SiO_2–MgO, and also to solid acids within SiO_2–Al_2O_3, and also $Al_4Si_4O_{10}(OH)_8$ all of which produced conversions above 90% and selectivities to formaldehyde above 70% around 625 – 650 °C.[509-511] After recognizing that the solid base system produces superior conversion and carbon monoxide as the byproduct, and that the solid acid system produces super selectivity with formaldehyde as the byproduct that increased with the solid acid strength, the compounds were combined in the weight ratio Ag : SiO_2 : MgO : Al_2O_3 of 20 : 55.2 : 8.3 : 16.5 to produce a catalyst with 100% efficiency for nonoxidative dehydrogenation of methanol to formaldehyde at 650 °C.

The 100% conversion and selectivity, however, was not sustained for more than a few hours as the constant reductive conditions caused silver crystals to form at the surface; the catalyst was regenerable though by heating under oxygen gas for 2 hours restore the catalysts' performance. In another report, the nanostructured $0.045Fe_2O_3/MgO$ catalyst reportedly showed especially high selectivity of 96% at 400 °C and even 100% at 300 °C possibly due to the acidic nature of surface-Fe^{3+}, especially in mixed oxides.[225,226] But, the conversion yield was only 30% and 1%, at those respective temperatures, and also performance decreased with cycling presumably due to the formation of ferrite.[501] Recently, the NASICON-type nickel titanium phosphate ($Ni_{0.5}Ti_2(PO_4)_3$, 30 m^2/g), has shown selectivity around 80% for formaldehyde and total conversion around 70% at optimal conditions (340 – 360 °C), but unfortunately the stability of the catalyst was not reported.[225] While the good performance was attributed to redox activity, it is worth noting the expected acidity of the titanium phosphate framework structure.

For ethanol, several examples of zero-valent metal nanoparticles on various supports have been reported as efficient catalysts for its non-oxidative dehydrogenation, including Cu/mesoporous carbon at 280 °C,[512] Au/MoO_3 at 240 °C[513] and $Au/MgCuCrO_2$ at 250 °C[514] with reported conversions/selectivities of 83/95%, 94/99% and 98/94%, respectively. Adkins' catalyst, $Cu\cdot CuCr_2O_4$, has been reported to convert ethanol with 46% conversion and 99.5% selectivity for acetaldehyde at 300 °C.[515]

Herein we report NASICON-type hydrogen titanium phosphate sulfate (HTPS; $H_{1-x}Ti_2(PO_4)_{3-x}(SO_4)_x$, $x = 0.5 – 1$) as a highly efficient solid catalyst for non-oxidative dehydrogenation of methanol to formaldehyde and also as an effective catalyst for concurrent dehydrogenation and dehydration of ethanol to acetaldehyde and ethylene. In our previous report, we described sol-gel synthesis and characterization of the new compounds in a nanoporous structure form. Structural protons in the NASICON-channels were detected by solid-state nuclear magnetic resonance (SS-NMR) spectroscopy, which makes the compound the first Ti^{4+}-based NASICON-type compound that has structural protons and mixed phosphate sulfate polyanions.[516] The presence of structural protons is expected to impart Brønsted solid acidity to the compounds. Furthermore, the strongly polarizing nature of the sulfate ligand should increase the acidity of structural protons as well as the reducibility of Ti^{4+} to Ti^{3+} which has been considered to play a role in non-oxidative dehydrogenation.[225] In addition to further materials characterization, our catalysis studies indicate that the new compounds are the first solid acid catalysts showing an excellent performance with a high conversion of ethanol for non-oxidative dehydrogenation and dehydration, and with a high selectivity and stability during non-oxidative dehydrogenation of methanol to formaldehyde.

6.2 Materials Synthesis

Samples were synthesized under the same sol-gel condition but at three different calcination temperatures, and were named accordingly. The first part of the name stands for hydrogen titanium phosphate sulfate (HTPS), and the postfix is the calcination temperature (600, 650 and 700 °C). The nominal ratio of Ti^{4+}:PO_4^{3-} was kept at 1.2, and the ratio of Ti^{4+}:SO_4^{2-} was that of the Ti precursor. Polyethylene glycol bisphenol A epichlorohydrin copolymer (PEG) (Sigma-Aldrich, 15-20 kDa) was added in an amount of 10 wt% of the reaction mixture. The concentration of Ti ions was 2.1 *m*, and the molar ratio of Ti:H_2O_2 was 1.8.

For a typical synthesis, an aqueous solution of $TiOSO_4$ was produced by dissolving 4.41 g of $TiOSO_4 \cdot 0.18H_2SO_4 \cdot 3.11H_2O$ (Sigma-Aldrich) in 3.43 g of deionized water with magnetic stirring in an 80 mL glass jar, after which the stir-bar was removed. Into this solution, 3.82 g of 27 wt% H_2O_2 (Alfa Aesar) was added gradually followed by 2.77 g of PEG solution (45.5 wt% PEG in H_2O) while stirring. Next, 2.44 g of 83.3 wt% H_3PO_4 solution in water (Alfa Aesar) was added to the solution. Determination of the composition of the precursors was carried out by elemental analysis and that of titanyl sulfate was also measured by thermogravimetric analysis. A lid was loosely placed on top of the jar, which was placed in a lab oven heated at 60 °C for 40 h. The cover was then removed, and the sample was heated further at the same temperature for 12 h to yield an orange crumbling dry gel. This resulting substance was calcined at various temperatures for 10 h in an ashing furnace (Carbolite, AAF1100) with a heating rate of 100 °C/h to produce a brittle, porous white compound that retained the shape of the dry gel.

6.3 Materials Characterization

6.3.1 Material Characterization

Powder X-ray diffraction (PXRD) patterns were obtained on a PANalytical diffractometer using Cu Kα radiation. The sample was crushed together with internal standard (Si, a = 5.4301 Å), and spread on a zero-background quartz sample holder. Data was acquired by scanning 2θ from 10 to 90° with a step size of 0.0251° and a scan time of 30 min. Scanning electron microscopy (SEM) imaging studies were performed using an FEI XL-30 Environmental SEM using 20 keV electrons on lightly ground samples.

Transmission electron microscopy (TEM) studies were performed on triturated catalysts that were dusted on to TEM grids. High resolution TEM images were collected on a JEOL 2010F at an accelerating voltage of 200 kV. Elemental analysis was performed on a Thermo iCAP6300 inductively coupled plasma optical emission spectrometer, (ICP-OES).

For sorption measurements, samples were degassed under vacuum at 200 °C for 8 h prior to sorption measurements. Nitrogen sorption isotherms were obtained on a Micromeritics ASAP 2020 Surface Area and Porosity Analyzer at 77 K. The Brunauer-Emmett-Teller (BET) model was applied to the partial pressure range of 0.05 – 0.2 of the adsorption branch to calculate surface area. The desorption branch was used for analysis of the pore characteristics. To estimate the pore size distribution, the Barrett-Joyner-Halenda (BJH) model using the Halsey thickness curve, heterogeneous surfaces and Faass correction to account for multilayer desorption, was applied.[370] The total quantity of gas adsorbed at p/p_0 ~ 0.98 was used to approximate the total pore volume.

6.3.2 Catalysis Characterization

The NH_3-TPD profiles were obtained using a Micromeritics Auto-ChemII apparatus equipped with a programmable temperature furnace and thermal conductivity detector. 0.05 g of sample was purged for 2 h with 40 mL/min He at 500 °C, after which the temperature was increased from ambient to 500 °C using a heating rate of 5 °C/min, followed by lowering the temperature to 40 °C. Then, 3% NH_3/He was flushed for 30 min at 40 °C, and purged with 40 mL/min He at 40 °C for 1 h. After that, under the same flow of He, the temperature was raised from 40 °C to 700 °C at 10 °C/min, analyzing the desorbed ammonia. The weak, medium, and strong acidities were assigned to the peaks of NH_3-TPD profiles at temperatures lower than 350 °C, between 350 and 500 °C, and above 500 °C, respectively.[517]

6.3.3 Catalytic Test

The measurements for methanol and ethanol dehydrogenation were carried out in a continuous-flow, tubular fixed-bed glass reactor (10 mm i.d.) over the temperature range of 250 – 400 °C at atmospheric pressure. Before the reaction, the reactor was purged with N_2 to remove air. The experiments were carried out with catalyst weight of 0.1 – 0.3 g and with methanol flow rate from 0.08 to 0.3 mL/min. Reaction products were collected every 30 min and were analyzed by a gas chromatograph equipped with a hydrogen flame ionization detector (FID), a capillary column with DB5 stationary phase (30 m length and 0.324 mm diameter), and highly pure N_2 (99.999%) as carrier gas.

6.4 Results and Discussion

6.4.1 Characterization of the Catalysts

PXRD diffraction patterns of the three samples, HTPS-600, -650 and -700, are shown in **Figure 83**, and the drop-lines show the reference PXRD pattern of HTPS-600 (Space Group: $R\bar{3}c$; a = 8.4717 Å; c = 21.663 Å), and the samples themselves were found to have unit cell volumes of 1346.46, 1348.49 and 1356.59 $Å^3$, respectively. All of the catalysts are phase-pure by PXRD, with the same respective average crystallite sizes determined by the Scherrer equation to be 15.3, 15.3 and 16.8 nm. As previously reported, sintering during calcination at 700 °C coincides with an increase in the crystallite size as well as the enlargement of the unit cell volume which is associated with sulfate loss.[516] By elemental analysis of Ti, P and S, and by satisfying the charge neutrality, the samples HTPS-600, -650 and -700 were reported to have compositions within $H_{1-x}Ti_2(PO_4)_{3-x}(SO_4)_x$ where $x \approx 0.42$, 0.33 and 0.15, respectively.

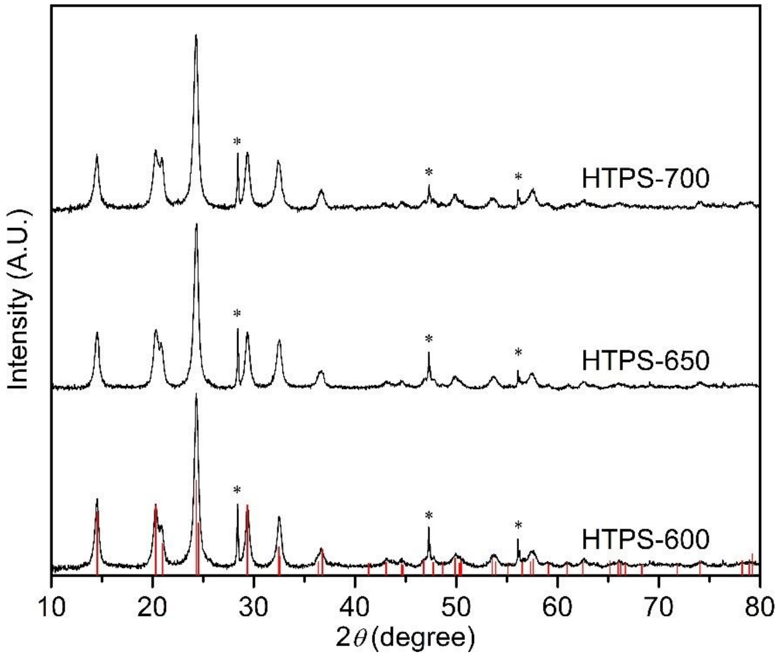

Figure 83. PXRD patterns of the catalysts HTPS-600 (bottom), HTPS-650 (middle) and HTPS-700 (top).

The catalyst HTPS-650 was imaged using SEM and TEM to study the morphology and microstructure. Aggregates of nanoparticles form spherical bulk particles (**Figure 84a)** with sizes around one to two µm. The nanostructured surface texture of the aggregates was visible in the higher magnification SEM image (**Figure 84b**), and TEM studies were used to image the primary nanoparticles. TEM micrographs of HTPS-650 (**Figure 85**) show that the primary nanoparticles with diameters of 15 – 20 nm are strongly fused to form textural pores, and individual crystallites exhibit lattice fringes under HRTEM (**Figure 85b**). Characteristics of the textural pores among the fused crystallites were further elucidated by nitrogen sorption measurements.

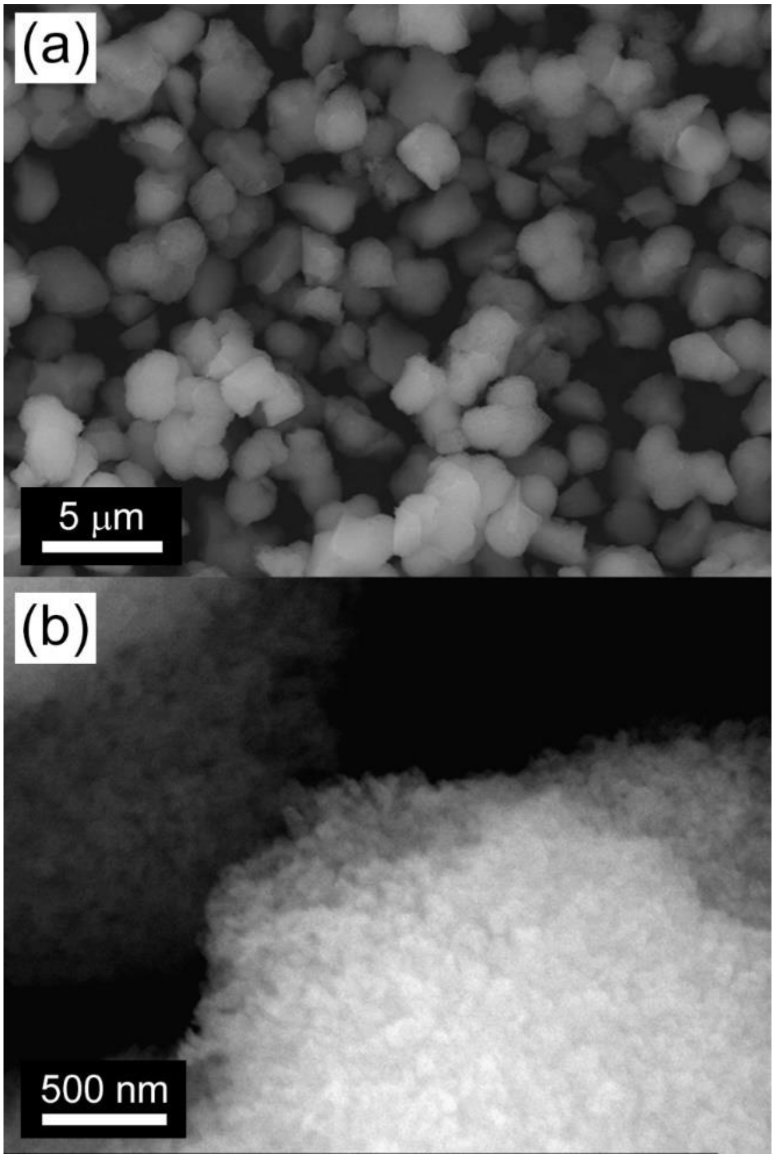

Figure 84. SEM micrographs of HTPS-650; scale bars are 5 µm for (a) and 500 nm for (b).

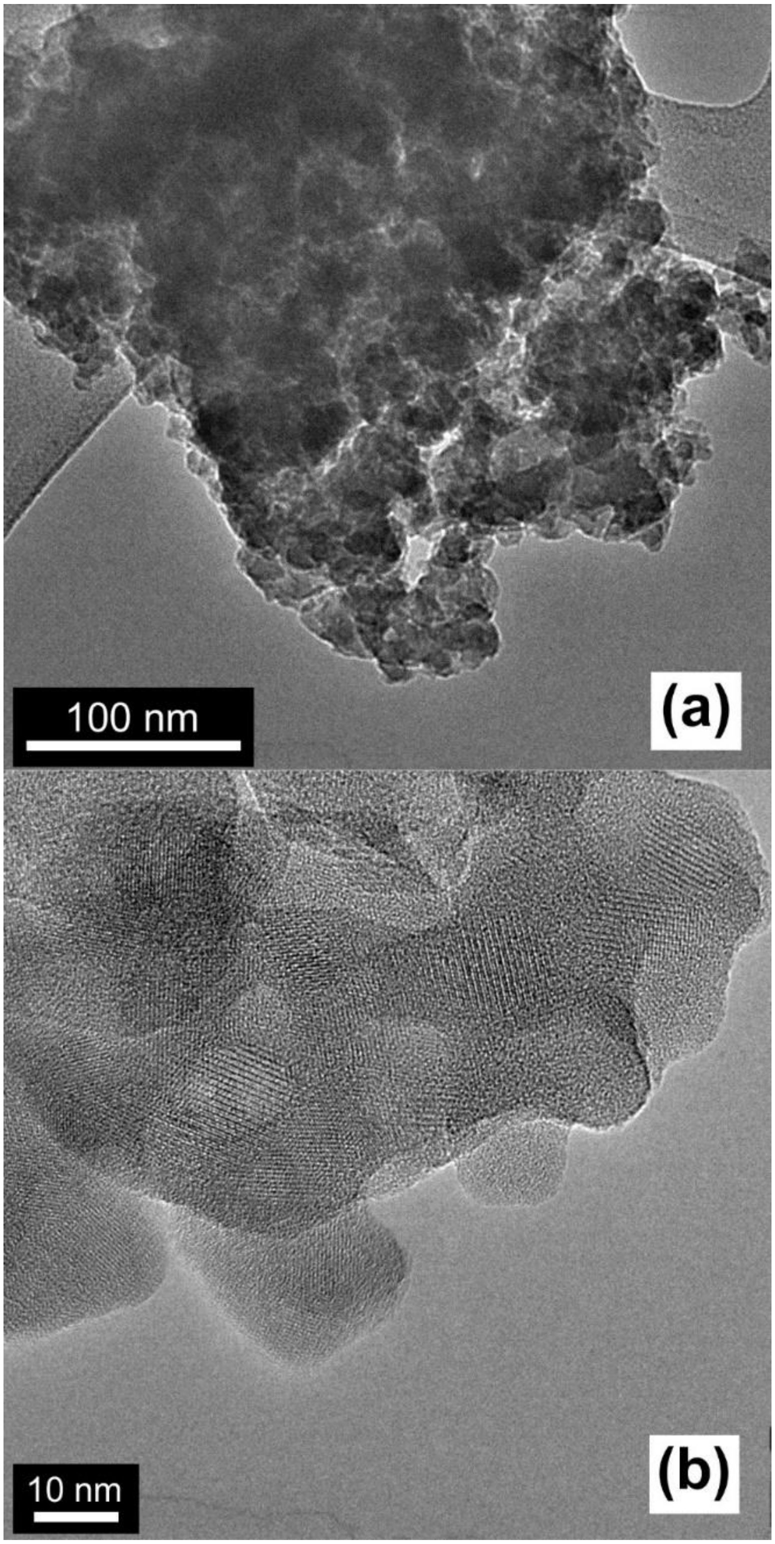

Figure 85. TEM and HRTEM micrographs of HTPS-650; scale bars are 100 nm for (a) and 10 nm for (b).

Nitrogen sorption isotherms and BJH pore distributions of the catalysts are shown in **Figures 86a** and **86b**. The sorption isotherms are a combination of type-III and type-V, and show a type H3 hysteresis indicating that both mesopores and macropores are present.[392] The hysteresis loop of the catalyst HTPS-700 appears at a significantly higher p/p_0 compared to the other catalysts, which indicates that the pore sizes are the biggest among the catalysts. BJH analysis of pore size distributions (**Figure 86b**), shows peak maxima of 18 nm, 23 nm, and 40 nm for the samples HTPS-600, HTPS-650 and HTPS-700, respectively, with average pore diameters of 16, 20 and 29 nm confirming that HTPS-700 had the largest pore diameters. In addition to shifting to wider pore sizes, the peaks become broadened with higher calcination temperatures. Despite a broader distribution of pore sizes, the pore volume was comparable between HTPS-650 and -700, with pore volumes of 0.25 and 0.24 cm^3/g, respectively, although the sample HTPS-600 had slightly lower surface area with 0.22 cm^3/g. While pore coarsening occurs to a larger extent with higher calcination temperatures, the primary crystallite size does not significantly increase which suggests that the increased pore widths may be associated with widening of the necks between connected primary particles due to the greater extent of sintering while maintaining their original crystallite domains. Pore characteristics and crystallite sizes estimated with Scherrer equation are summarized in **Table 5**. The lower pore volume that exists from the lower calcination temperature indicates that some material inside the pores was removed with the higher calcination temperature.

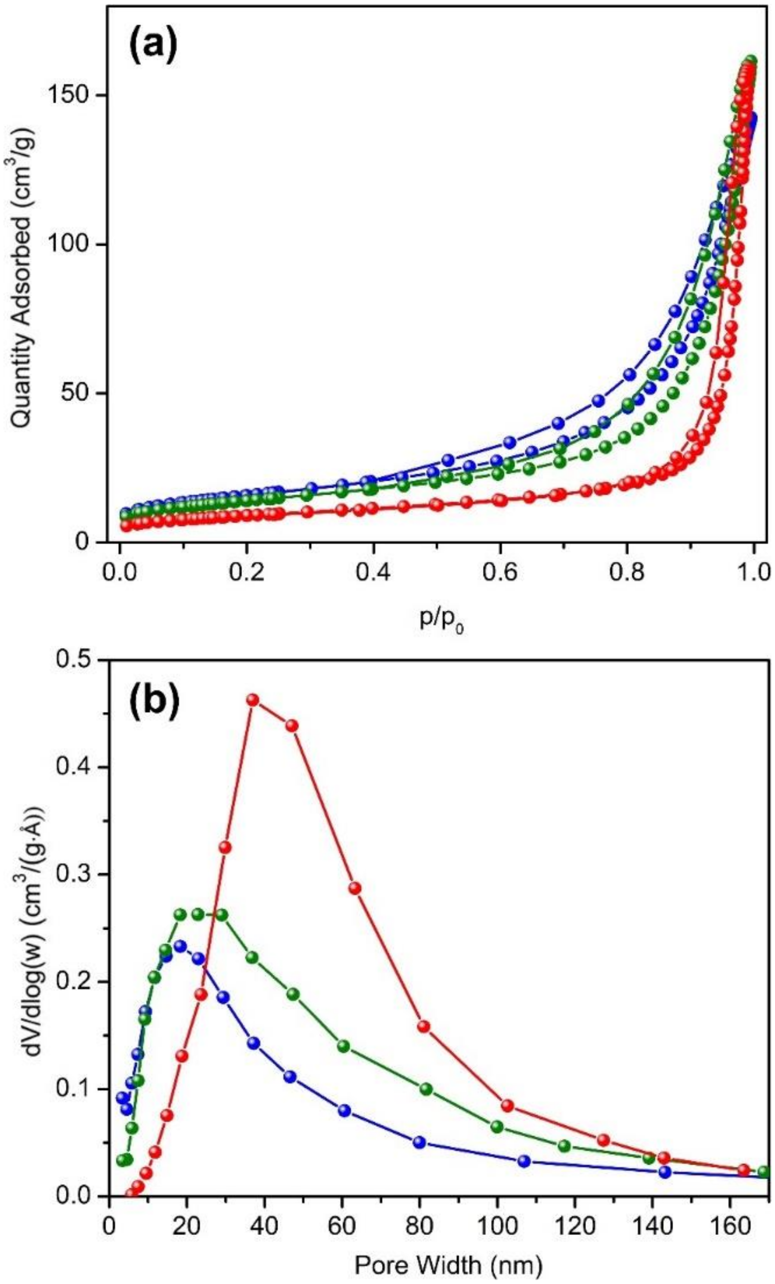

Figure 86. (a) Nitrogen sorption isotherms and (b) BJH pore size distributions for the samples HTPS-600 (blue), HTPS-650 (green) and HTPS-700 (red).

Table 5. Surface areas and pore characteristics of the products. See the Experimental section for the sample naming convention.

Sample	BET Surface Area (m^2/g)	Pore Volume (cm^3/g)	Average Pore Size (nm)	Crystallite Size (nm)
HTPS-600	56	0.22	16	15.5
HTPS-650	50	0.25	20	15.3
HTPS-700	32	0.24	29	16.8

The NH_3-TPD profiles for adsorbed ammonia are presented in **Figure 91** for the temperature region from room temperature to 700 °C where the catalysts are thermally stable.[516] An initial desorption peak was observed near 90 °C for all samples, which is due to physisorbed ammonia. HTPS-600 shows a broad peak from 200 to 400 °C with a maximum at 300 °C and an acid site density of 0.47 g/cm^3. The same broad peak appears in the TPD profile of HTPS-650 from 200 to 500 °C with a slightly higher maximum position (335 °C) and a higher acid site density (0.57 g/cm^3), indicating that HTPS-650 has a slightly stronger acidity than HTPS-600. Meanwhile, HTPS-700 does not show any peak in that temperature region and thus the presence of the presence of acid sites with moderate strength is not apparent. It can be concluded that calcination at 650 °C leads to the highest acidity for the HTPS system. However, HTPS is more thermally stable than sulfated titania as it has been reported that when the sulfated titania was calcined to 650 °C, its NH_3-sorption capacity was greatly diminished and it showed almost no surface acid sites due to sulfate decomposition.[518]

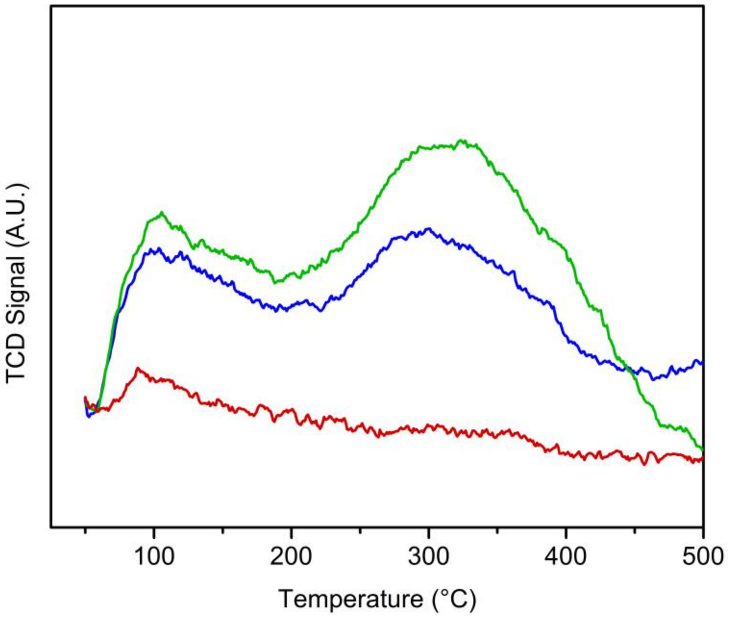

Figure 87. NH_3-TPD profiles of catalysts HTPS-600 (blue), -650 (green) and -700 (red).

6.4.2 Catalyst Performance

In order to evaluate the catalytic activity of HTPS samples for methanol under non-oxidative conditions, the catalytic tests were performed at various temperatures between 250 °C and 400 °C. Under these conditions, the products from methanol include formaldehyde, dihydrogen and methane by the following reactions:

$CH_3OH \rightleftarrows CH_2O + H_2$ [500]

$2CH_3OH + \rightleftarrows CO_2 + 3CH_4$ [519]

The methanol conversion and products selectivities as function of reaction temperature between 250 and 400 °C are shown in **Figure 87**. The alcohol flow rate was 0.08 ml/min and the catalyst mass was 0.1 g. Formaldehyde was the main product of dehydrogenation and CH_4 was observed as a side product. **Figure 88a** shows that all the samples exhibit catalytic activities for the reaction. The conversion yield increases sharply to over 45% above 250 °C for both HTPS-600 and -650, reaching 52% at 400 °C. However, HTPS-700 shows a more or less linear increase in the same range. Interestingly, the selectivity to formaldehyde is close to 100% for all the samples in the entire temperature range. In other words, the selectivity for formaldehyde is not affected by the surface acidity of HTPS, while a high conversion yield is possible at low temperatures only when HTPS has acidic sites.

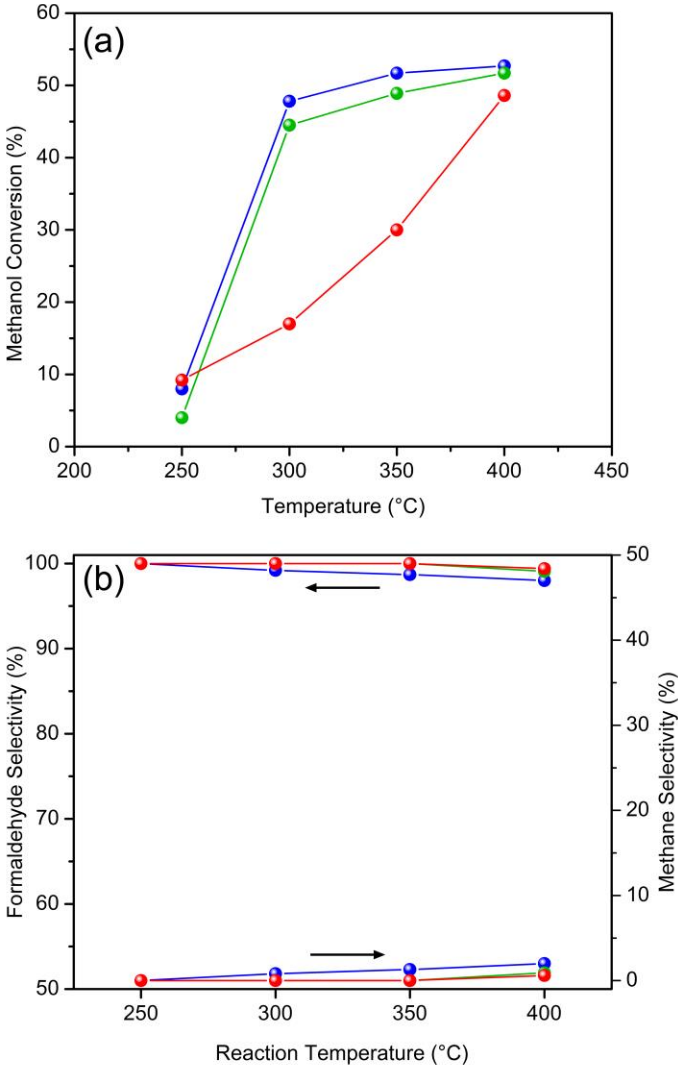

Figure 88. Effect of the temperature on the methanol conversion (a) and formaldehyde (H_2) selectivity (b) over HTPS-600 (blue), -650 (green) and -700 (red) (methanol flow rate 0.08 ml/min, catalyst loading 0.1 g).

Figure 89 shows the influence of the ratio of contact time (W/F) on the conversion and formaldehyde yield. The conversion of methanol increases with increasing contact time, and the calcination temperature of 600 °C seems to give the higher activity and formaldehyde yield. The higher activity is likely due to the higher surface area, although the lowered selectivity is not simply understood by a higher surface area. Instead, the surface chemistry may be different among the samples based on the composition. Elemental analysis showed the sulfate content decreasing with higher calcination temperature, and the different compositions will present different surface site availability. Furthermore, ^{1}H SS-NMR studies were reported for HTPS-600 and -700, which both show a dominating peak around 6 ppm. Contrastingly, the HTPS-600 sample exhibited a chemical shift at ~ 1 ppm that was associated with surface protons, which was not observed in the SS-NMR spectrum of HTPS-700, which instead showed a significant peak at ~ 11.5 ppm. The differences in the compositions and the proton environments are noteworthy, although their interpretation as it pertains to the selectivity is unknown, as the sample with the strongest acid sites catalyze the non-oxidative dehydrogenation of methanol to formaldehyde with 100% selectivity under our conditions.

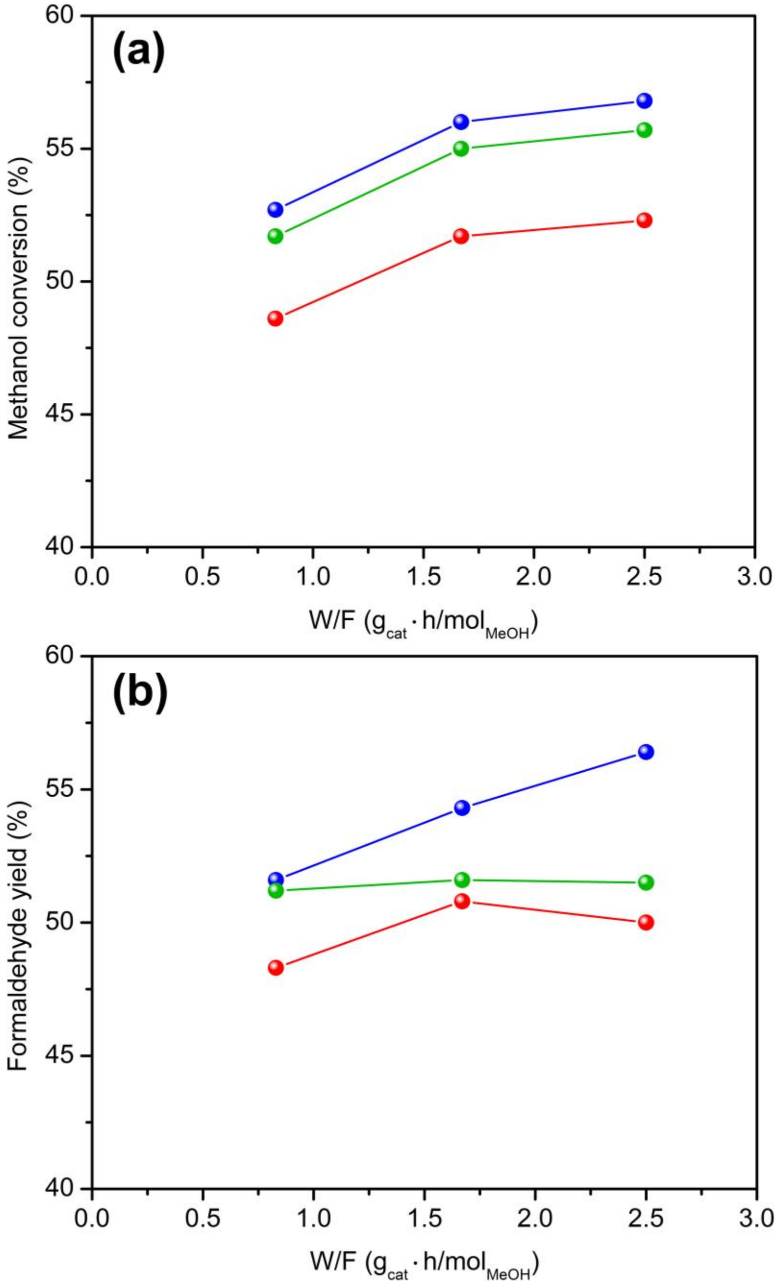

Figure 89. The methanol conversion (a) and formaldehyde yield (b) as a function of methanol mass to flow rate ratio W/F (0.12 mol/h methanol, 400 °C) for catalysts HTPS-600 (blue) -650 (green) and -700 (red).

Figure 90 presents results of stability experiments for non-oxidative dehydrogenation of methanol that were conducted over HTPS 600 at 350 °C for 15 h, with a methanol flow rate 0.08 ml/min and a catalyst loading of 0.3 g. The methanol conversion is constant around 52% and the selectivity remains at 100% for 7 h, after which it decreases to 99% where it remains stable. The unchanging conversion and selectivity indicate that the catalyst deactivation does not occur. In the literature, catalyst deactivation is generally most pronounced during the initial hours, as has been measured for ZnO-based catalysts at 600 °C that lose zinc due to the reduction of Zn^{2+} to zinc and its and subsequent evaporation, and zeolite-based catalysts that are deactivated due to coking at 500 – 600 °C.[503] The appearance of species at the surface such as nanoparticles of carbon or copper (reduced from Cu-ZSM-5 or CuO/SiO_2) can also improve selectivity for formaldehyde but decrease methanol conversion during the initial hours on-stream.[500,503,507] The fact that there was virtually no change in either the methanol conversion or the selectivity for formaldehyde, using HTPS-600 as a catalyst, indicates and that the surface is not modified during catalysis by either coke or by the buildup of reduced titanium species.

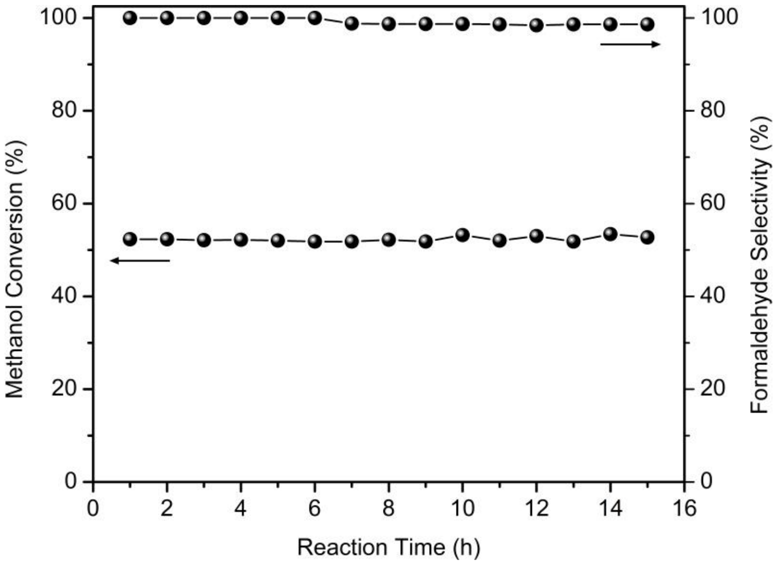

Figure 90. Stability of methanol conversion and selectivity for formaldehyde on HTPS-600 at 350 °C.

Solid acids have previously been tested as catalysts for the dehydration of alcohols, however solid acids themselves are not generally associated with the non-oxidative dehydrogenation of alcohols; in fact, dehydrogenation is characteristic of solid bases.[520] Rather, catalysts with increasing acidity as indicated by higher NH_3-TPD temperatures show higher activity for the dehydration of alcohols. For example, at 300 °C methanol dehydration occurred to produce dimethyl ether with conversion and selectivity less than 20% for titania-silica catalysts with NH_3-TPD temperatures around 170 °C, and around 80 to 90% for the aluminum phosphate catalysts with NH_3-TPD temperatures around 270 °C.[521] It follows that sulfated ZrO_2 with the NH_3-TPD temperature around 625 °C[522] converted methanol to dimethyl ether at 275 °C with 83% conversion and 100% selectivity.[523] Disparately, the acidic NASICON-type compounds $Li_{0.9}Zr_2(PO_4)_{2.9}(MoO_4)_{0.1}$ and $Li_1Zr_{1.8}In_{0.1}Nb_{0.1}(PO_4)_3$ show a NH_3-TPD desorption signal ranging from 100 to 450 °C, with a peak around 200 °C, and were efficient at catalyzing the non-oxidative dehydrogenation of ethanol with conversions of 100% and acetaldehyde selectivities of ~ 60% and 80%, respectively, in a membrane reactor.[227] Based on the typical behavior of solid acids as catalysts for dehydration of alcohols instead of for dehydrogenation, the origin of the catalytic activity of HTPS is not clear, though solid acids have been previously used for the non-oxidative dehydrogenation of alcohols.

From the recognition that solid basicity leads to superior conversions and that solid acidity leads to superior selectivity, a ceramic catalyst was synthesized that combines the solid acid SiO_2-Al_2O_3 and MgO with Ag. The NH_3-TPD peak at 136 °C indicates a mild acidity, and there is no solid basicity judged by the lack of CO_2

sorption.[510] This compound, in addition to exhibiting mild surface acidity, also showed 100% conversion and efficiency for methanol conversion to formaldehyde for a short duration, after which it needed to be regenerated under a reductive gas to reincorporate silver that crystallized on the surface.

In the case of HTPS, methanol conversion is directly proportional with weak and medium acid sites, and increases in the order: HTPS-700 ($0.11\ cm^3/g$) < HTPS-650 ($0.73\ cm^3/g$) < HTPS-600 ($0.85\ cm^3/g$). In contrast, non-oxidative methanol dehydrogenation carried out over the catalysts $Na_{1-y}Zr_2(MoO_4)_y(PO_4)_{3-y}$ showed increasing selectivity for formaldehyde when y increased from 0 to 0.25, from around 10% to 50-60%, despite the decrease in acid site density from 243.1 to 107.2 µmol/g, respectively.[321] This inverse relationship between surface acidity and methanol conversion to formaldehyde is known in the literature, the acid sites promoting dehydration instead of dehydrogenation.[33,277] Instead of acidity, the reducibility of the transition metals present at the surface may be responsible for the non-oxidative dehydrogenation of methanol[225,277] and of ethanol[227] for that matter. In the case of HTPS, the only redox-active metal is Ti^{4+}.

Figure 91 plots the conversion of methanol and selectivity for formaldehyde at 350 °C, showing that the conversion increases with decreasing particle dimensions in concordance with the literature data,[524,525] while the selectivity drops from 100% to 98% with the smallest particles. Increasing surface area clearly increases the activity due to an increased interface between catalyst and substrate, however it is not clear how different the surface chemistry is between the samples. While sulfate reportedly decomposes from $TiOSO_4$ between 600 and 700 °C during thermogravimetry,[474] we observed in our own experiments that the decomposition of $TiOSO_4$ to TiO_2 was complete after 10 hours of calcination at 650 °C. However, this is clearly not the case with HTPS which is stable to 700 °C although the sulfate amount decreases with higher calcination temperature. The kinetic aspect of the sulfate decomposition suggests that sample HTPS-600 may have sulfate present at the surface that is slightly less thermally stable than those of HTPS-650 and HTPS-700. Since lower thermal stability is correlated with a higher reactivity, the presence of more reactive sulfate groups may explain the slight drop in selectivity with the sample HTPS-600.

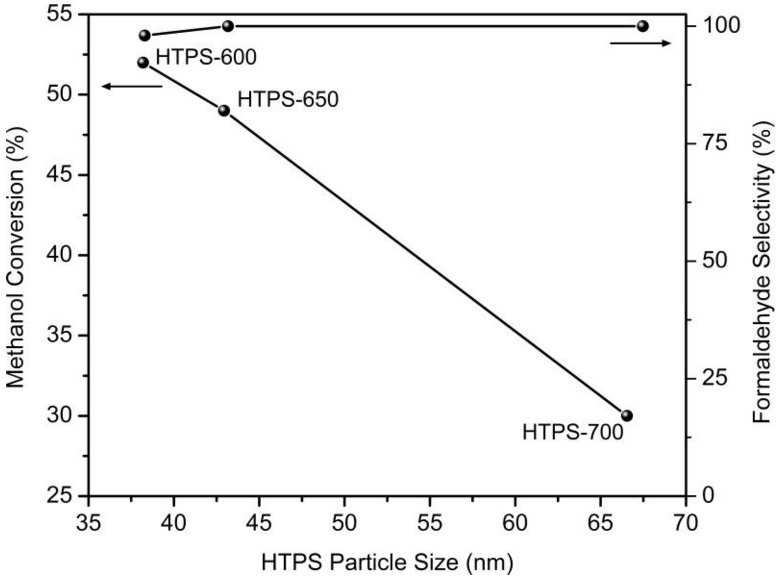

Figure 91. The methanol conversion and selectivity for formaldehyde at 350 °C.

While the mild to moderate surface acidity was also measured by NH_3-TPD for the NASICON-type compounds that are effective for non-oxidative dehydrogenation of ethanol, the catalyst activity was attributed to redox chemistry. With oxygen in the feed gas, dehydrogenation of methanol by iron molybdenum oxide proceeds not by reaction of gaseous oxygen with the substrate molecule, but by surface oxide oxidizing the methanol to produce temporary surface oxide vacancies.[487] Subsequently, O_2 reacts with the reduced Mo species to oxidize them to Mo^{6+} and filling the oxide vacancy.[526] Since the HTPS-650 catalyst activity was shown to be stable over 15 h under non-oxidative conditions (**Figure 90**), the oxide vacancies could not be responsible for the oxidation of methanol to formaldehyde since methanol was converted by four orders of magnitude fewer moles of catalyst. Even though the nature of the redox reaction at the surface of the NASICON-type catalysts has not been investigated, we may suggest a catalytic mechanism unique to HTPS, such as:

$$H_{0.4}Ti_2(PO_4)_{2.4}(SO_4)_{0.6} + CH_3OH \rightarrow H_{1.4}Ti^{4+}Ti^{3+}(PO_4)_{2.4}(SO_4)_{0.6} + CH_3O\cdot$$

$$H_{1.4}Ti_2(PO_4)_{2.4}(SO_4)_{0.6} + CH_3O\cdot \rightarrow CH_2O + H_{2.4}Ti^{3+}{}_2(PO_4)_{2.4}(SO_4)_{0.6}$$

$$H_{2.4}Ti^{3+}{}_2(PO_4)_{2.4}(SO_4)_{0.6} \rightarrow H_2 + H_{0.4}Ti_2(PO_4)_{2.4}(SO_4)_{0.6}$$

Relatively mild surface acidity may be beneficial based on the results obtained by Florek-Milewska *et al.*[527] who noted that the stronger acidity of the catalyst did not allow CH_2O molecules to desorb from the surface in the gas phase leading to the formation of methyl formate, which was not observed for our catalysts. The importance of solid acidity for the non-oxidative dehydrogenation was also mentioned for the Na-ZSM-5 catalysts,[503] although the specific role of the acid site during dehydrogenation has not been established.

While the Scherrer size of the samples was nearly the same around 15 – 17 nm, BET surface area was correlated to the effective particle sizes that are larger than the primary crystallite particles due to their sintering, and the samples HTPS-600, -650 and -700 exhibited particle sizes of 38.2, 42.9 and 66.5 nm, respectively, assuming a particle density of 2.8 cm^3/g. Despite the decreasing sulfate amount in the samples calcined at higher temperatures, the activity of samples were nonetheless compared by the particle size based on BET surface area. The small particle size and uniform nanoporous structure are present from the sol-gel route, although sol-gel chemistry is generally not the best route for fabricating metal phosphate due to the strong tendency for phosphate to react with transition metal ions in solution to form precipitates.[528] To get the correct product, re-grinding steps and high firing temperatures have been necessary that greatly reduced the surface area to ~ 1 m^2/g.[225] It is noteworthy that in contrast, our new catalyst is a product of sol-gel chemistry that was enabled by sulfuric acid and peroxide, that served to stabilize titanium and phosphate together in solution. After gelation, a high surface-area and porous material was yielded with one-step calcination.

For comparative studies of the catalytic activity, ethanol conversion was carried out over the catalyst HTPS-650 and the results obtained on this sample are presented in **Figure 92**. Two products, acetaldehyde and ethane, are competitively formed.

$$C_2H_5OH \rightleftarrows C_2H_4O + H_2$$

$$C_2H_5OH \rightleftarrows C_2H_4 + H_2O \quad \Delta H \approx 45.7 \text{ kJ/mol}$$

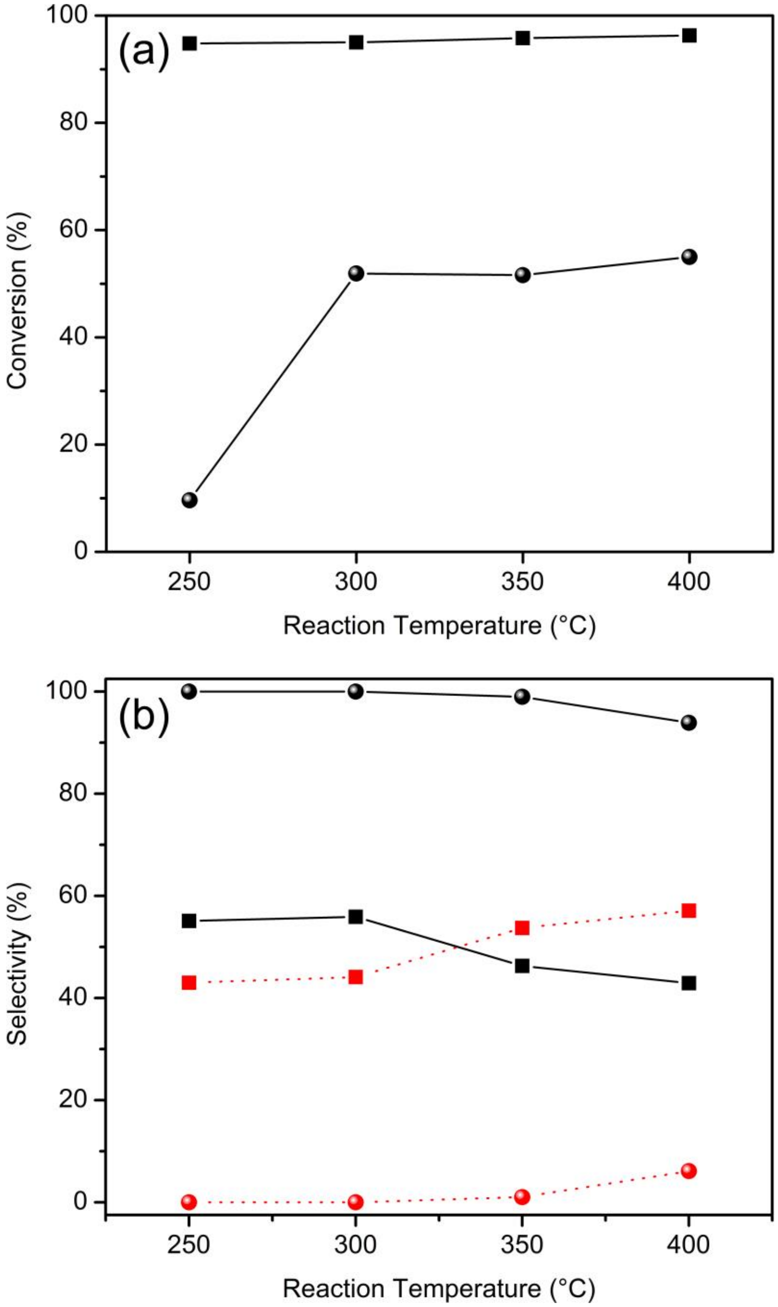

Figure 92. (a) Effect of the temperature on the methanol (spheres) and ethanol (squares) conversion, and (b) the selectivities for methanol conversion to formaldehyde (black spheres) and methane (red spheres), and ethanol selectivity to acetaldehyde (black squares) and ethylene (red squares) over HTPS-650 catalysts (methanol flow rate 0.08 ml/min, catalyst loading 0.2 g).

In terms of conversion the ethanol is more reactive than methanol, the conversion for ethanol exceeding 95% as compared to methanol where the conversion has a maximum value at 55%. For the ethanol reaction, the selectivity to acetaldehyde decreases from 56% to 43% while the selectivity to ethene increased from 43% to 57% when the reaction temperature is increased from 250 to 400 °C. It should be noted that, in case of ethanol, dehydrogenation and dehydration occur simultaneously. Dehydration of ethanol is attributable to the solid acidity of HTPS,[529] although as mentioned, dehydrogenation reactions are not generally catalyzed by solid acid catalysts themselves. Over the same temperature range, a recent report found that the NASICON-type compound $Li_{0.9}Zr_2(PO_4)_{2.9}(MoO_4)_{0.1}$ increased in its conversion of ethanol around 30% to 100%, with the selectivity for acetaldehyde decreasing from 20% to < 5%, while selectivity to ethane increased from 1 to 30 % and while also producing diethyl ether and C_4 hydrocarbons.[530] HTPS exhibits a high conversion at lower temperatures and a simpler effluent mixture with higher selectivity for both acetaldehyde and ethane. Other catalysts for ethanol were not found in the literature that produce these two chemicals without selectivity for other compounds.

6.5 Conclusion

The non-oxidative dehydrogenation of methanol and ethanol to the respective aldehydes was carried out over a new catalyst material, HTPS. Selectivity for formaldehyde was nearly 100%, and at and above 300 °C the conversion was ~ 50%. The catalyst performance was steady for at least 15 h at 350 °C. While the absence of water as a product is desirable for the subsequent purification of formaldehyde, hydrogen gas produced instead offers the potential for purifying the hydrogen as a green fuel. Although the industrial processes for oxidative dehydrogenation of methanol have a conversion around 100%, the inferior selectivity and production of water with the current Ag and $Fe_2(MoO_4)_3$ catalysts make HTPS an interesting catalyst to explore for scaling up.

CHAPTER 7

FUTURE DIRECTIONS

7.1 Future Directions of Interest

Several ongoing projects have already been mentioned, although many of those are application based. These include photocatalytic studies (**Figure 10**), achieving better control over the thickness of meso-macroporous coatings (**Figure 62**), and using them for dye-sensitized solar cells (**Figure 66**) and for electrochemical communication with redox active biomacromolecules. Not to mention studying the catalytic activities of various porous materials for different reactions, beyond those studied in **CHAPTER 6**. In addition to catalytic activity of the solid acids, HTPS may show good proton conductivity, which could be studied by ion conductivity measurements. However, since the focus of the work was to pursue new sol-gel synthetic routes, the discussion of future directions is mainly about synthesis and characterization.

Our main interests for the fabrication of new materials include the following points: 1. Finding new methods for stabilizing molecular precursors and sols such that we can control the gelation to form a homogeneous gel, 2. Finding ways to use green chemicals, 3. Exploring new template systems to control the pore characteristics of the final porous materials, with specific interest in macropores, 4. Exploring new elemental compositions and synthetic procedures to identify new compounds and materials, where the atomic-level homogeniety allowed by solution-based chemistry can lead to new materials, 5. Refining the synthetic and characterization techniques that we employ to better study the fundamentals of sol-gel synthetic chemistry, and specifically of interest is oxoanion chemistry with peroxide-ligated metal solutes. As progress opens more questions than it answers, below is some brief discussion on these 5 points pertaining to the specific directions that are currently of interest in our research.

7.2 Improving Control of Sol-Gel Chemistry for Multinary Metal Oxides

One main limitation of sol-gel chemistry is that sol-gel systems with different compositions undergo a sol-gel transition at different pH. The reaction conditions required to form a volume-filling gel can be quite narrow, as demonstrated in **Figure 8** which also indicates that conditions for gelation can be more narrow at lower concentrations. Experimental conditions that we considered for modifying the reaction conditions included pH, concentration, solvents, ligands, reaction temperature, ageing time, atmosphere, and whether the system was closed or open during the reaction. Some of the steps were dynamic during the course of the synthetic process (i.e. exothermic reactions, ligand decomposition, change in atmosphere, etc.) which could be difficult to monitor and control especially on a larger scale.

Only a few options are available to destabilize an aqueous solution of metal ions in a homogeneous way as to produce a volume-filling gel. These include increasing the pH by a reactive solute such as epoxides or urea, or using reactive ligands to control the types of polycondensation reactions. These routes generally require highly reactive organic reagents such as organometallics and epoxides, and volatile alcohols as solvents. While we took advantage of these somewhat conventional routes for the ZTO work in **CHAPTER 3**, they are still limited by both the types of mixed metal oxides that they can make and by the low sustainability and difficulty of increasing the scale of the reaction.

However, in some cases we were unable to obtain the phase-pure sol-gel products that we targeted, some of which included mullite, $LiFePO_4$, $Li_4Ti_5O_{12}$, $NaGa_{1-x}Al_xO_2$, $AgGa_{1-x}Al_xO_2$ and $Zr_xTi_{1-x}P_2O_7$. Problems encountered were phase separation in the solution, or unanticipated formation of other crystal structures during calcination.

7.3 Emphasizing Green Chemistry in Design of Sol-Gel Syntheses

It is crucial to consider the environmental impacts of our research in the context of today's chemical industry. Glycerol has come in large supply as a byproduct of biodiesel production, and its low toxicity and volatility as well as its ability as a polar solvent make it a strong candidate for use in green sol-gel chemistry. In this direction, we found that many hydrous metal nitrate salts are highly soluble in glycerol, and furthermore that urea has good solubility in glycerol. Gentle heating over hours to days of a solution containing certain dissolved metal salts and urea yields a gel, and combustion produces a nanostructured product that contains carbon. Subsequent calcination serves to remove carbon and to produce the crystalline metal oxide products.

Several phase-pure products were synthesized by this route including MgO (BET SA = 140 m^2/g, pore volume = 0.47 cm^3/g, average pore width = 14 nm), Al_2O_3 (BET SA = 150 m^2/g, pore volume = 0.21 cm^3/g, average pore width = 6.2 nm), ZrO_2, (BET SA = 5 m^2/g, pore volume = 0.02 cm^3/g, average pore width = 16 nm), CeO_2 (BET SA = 45 m^2/g, pore volume = 0.15 cm^3/g, average pore width = 13 nm), and ternary compounds including $Ce_xZr_{1-x}O_2$ (CZS), $MgAl_2O_4$, $LiNi_{0.5}Mn_{1.5}O_4$ and $LaPO_4$. **Figure 93** shows PXRD patterns of the $MgAl_2O_4$ and $Ce_{0.2}Zr_{0.8}O_2$ products, along with the respective reference patterns of $MgAl_2O_4$ and the tetragonal ZrO_2 structure. The compounds are phase-pure, exhibiting nanoparticle sizes calculated by the Scherrer equation to be 10 and 8 nm respectively, and the Bragg peaks of CZS are slightly shifted to a lower angle, corresponding to the enlargement of the unit cell consistent with Ce doping in ZrO_2. **Figure 93** also shows TEM images of some compounds including the $Ce_{0.2}Zr_{0.8}O_2$ (BET SA = 60 m^2/g, pore volume = 0.21 cm^3/g, average pore width = 13 nm) (**Figure 93a**) and $MgAl_2O_4$ (BET SA = 80 m^2/g, pore volume = 0.14 cm^3/g, average pore width = 6.2 nm) (**Figure 93b**) products, as well as MgO (**Figure 93c**) and $LaCoO_3$ (**Figure 93d**).

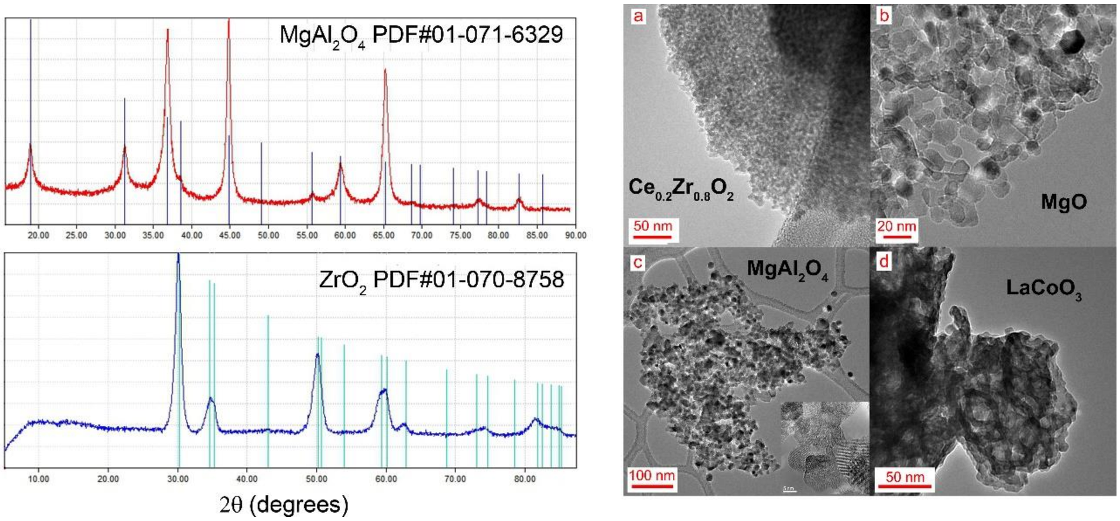

Figure 93. (left) PXRD patterns of $MgAl_2O_4$ and $Ce_{0.2}Zr_{0.8}O_2$ overlaid with the reference Bragg reflections from $MgAl_2O_4$ and ZrO_2, and (right) TEM images of (a) $Ce_{0.2}Zr_{0.8}O_2$ (scale bar = 50 nm), (b) MgO, (scale bar = 20 nm), (c) $MgAl_2O_4$, (scale bar = 100 nm), (d) $LaCoO_3$ (scale bar = 50 nm).

Another green solvent is water, although obtaining a uniform inorganic gel in pure water can be difficult. Peroxide is also a green reagent, and we found that some peroxide-ligated metals remain highly soluble in water where they would otherwise react to form a precipitate. One specific instance that we found is that the titanium peroxide in sulfuric acid solution does not precipitate in the presence of phosphate. This finding opens a route for exploring new materials. In addition to the solvent, another synthetic factor that can be modified to improve the green aspect is the method of generating and controlling the pore structure. Expensive surfactants such as copolymers and tetra-alkylamines, and templating agents such as polymer and silica beads, are frequently added both to increase the porosity of the final products and to impart pores of a specific size. Carbon black is a renewable and economical reagent that can be used as a template to fabricate hierarchically meso-macroporous coatings on glass. While we have explored this template system for ATO, TiO_2 and 10% ZTO, it can be used in many sol-gel systems when used in conjunction with poly(ethylene glycol) (PEG) compounds, which are often commodity chemicals.

7.4 Synthesis of Macroporous Materials With a Focus on Coating Fabrication

In addition to being a green reagent, carbon black also offers a unique combination of making a paste that spreads and dries with minimal to no cracking, and has a high structure that creates macropores as the gel solidifies and dries. Also, it can be removed by heat treatment under oxygen gas at 500 °C which is compatible with making coatings on glass. Future avenues include optimizing the formulation of the templating system, which has already been done to some extent as far as the concentration and ratios of carbon black and PEG.

This carbon black and PEG template system can be applied to a variety of aqueous sol-gel systems; other systems of interest include luminescent materials, *p*-type semiconductors and photochromic or electrochromic materials. Although the high calcination temperature precluded the direct fabrication on glass,[187] we also have made bulk meso-macroporous $CuAlO_2$. Another novel templating agent is the oxygen gas formed by the decomposition of hydrogen peroxide and peroxide ligands, as well as the CO_2 gas generated during the reaction of urea and water. The gas can be caught in the highly viscous products, forming closed macropores as shown in **Figure 11** (the TiO_2 floats for weeks).

7.5 Extension of Oxoanion-Based Sol-Gel Chemistry

The synthetic procedure for HTPS reported in **CHAPTER 5** is designed to produce phase-pure NASICON-type HTPS products, and is not optimized for any application. Many variations in the synthetic route can be performed to obtain HTPS. Phase-pure products were also obtained by modifying the concentration, the temperature and duration of heating during both covered and heating, and without PEG additive. Also, the high acidity allows for complete dissolution of titanium precursors in water, including $TiOSO_4$ which is more economical than the alkoxides or the tetrachloride. The choice of reagents has a large impact on the pore structure. As one example, when HTPS is synthesized using $TiOSO_4$ as the acidic Ti-precursor, the pore structure is distinctly different than when $Ti(OBu)_4$ and H_2SO_4 are used.

Figure 94a shows the PXRD pattern of the HTPS compound synthesized with $Ti(OBu)_4$ as the Ti precursor and H_2SO_4 as the acidifying agent in water, and calcined to 600 °C to make the sample ‘HTPS-600-B’. The sample is phase-pure by PXRD, and the nanoparticle size calculated by the Scherrer equation is 14 nm. Those samples (with P/Ti = 1.2) made with $TiOSO_4$ and calcined to 600, 650 and 700 °C are abbreviated as HTPS-600, -650 and -700, respectively, which are also phase-pure and have nanoparticles of 17, 16 and 18 nm, respectively, as calculated by the Scherrer equation. **Figure 94b** shows the nitrogen sorption isotherms of these samples, and the BET surface area of samples HTPS-600, -650 -700 and -600-B are 61, 53, 35 and 91 m^2/g, respectively. The larger surface area of HTPS-600-B is consistent with the smaller nanoparticle size determined from the PXRD analysis. Further, the hysteresis loop between the adsorption and desorption branches of HTPS-600-B occurs between p/p_0 ~ 0.7 – 0.85, while the hysteresis loop occurs between p/p_0 ~ 0.45 – 1.0 for those products using $TiOSO_4$ precursor. Comparing the lower limits of these ranges indicates that the mesopores of HTPS-600-B contain fewer blockages and are more easily accessible than those of HTPS-600, -650 and -700; also, the closure of the hysteresis loop of HTPS-600-B around $p/p_0 = 0.85$ indicates the absence of large mesopores and macropores. **Figure 94c** shows the pore size distributions, and the pore volumes and average pore widths were found to be 0.22 cm^3/g and 14 nm, 0.27 cm^3/g and 21 nm, 0.21 cm^3/g and 25 nm, and 0.33 cm^3/g and 15 nm, respectively for samples HTPS-600, -650 -700 and -600-B. There is a clear difference in the pore size distribution between the products that used $TiOSO_4$ vs. $Ti(OBu)_4$ in that the pores are relatively widely distributed and include mesopores and macropores for HTPS-600, -650 -700, while the sample HTPS-600-B has almost all its pore volume in pores around 15 nm. Under certain synthetic conditions, HTPS-600-B is formed as transparent monolithic particles while HTPS-600, -650 and -700 are fine powders.

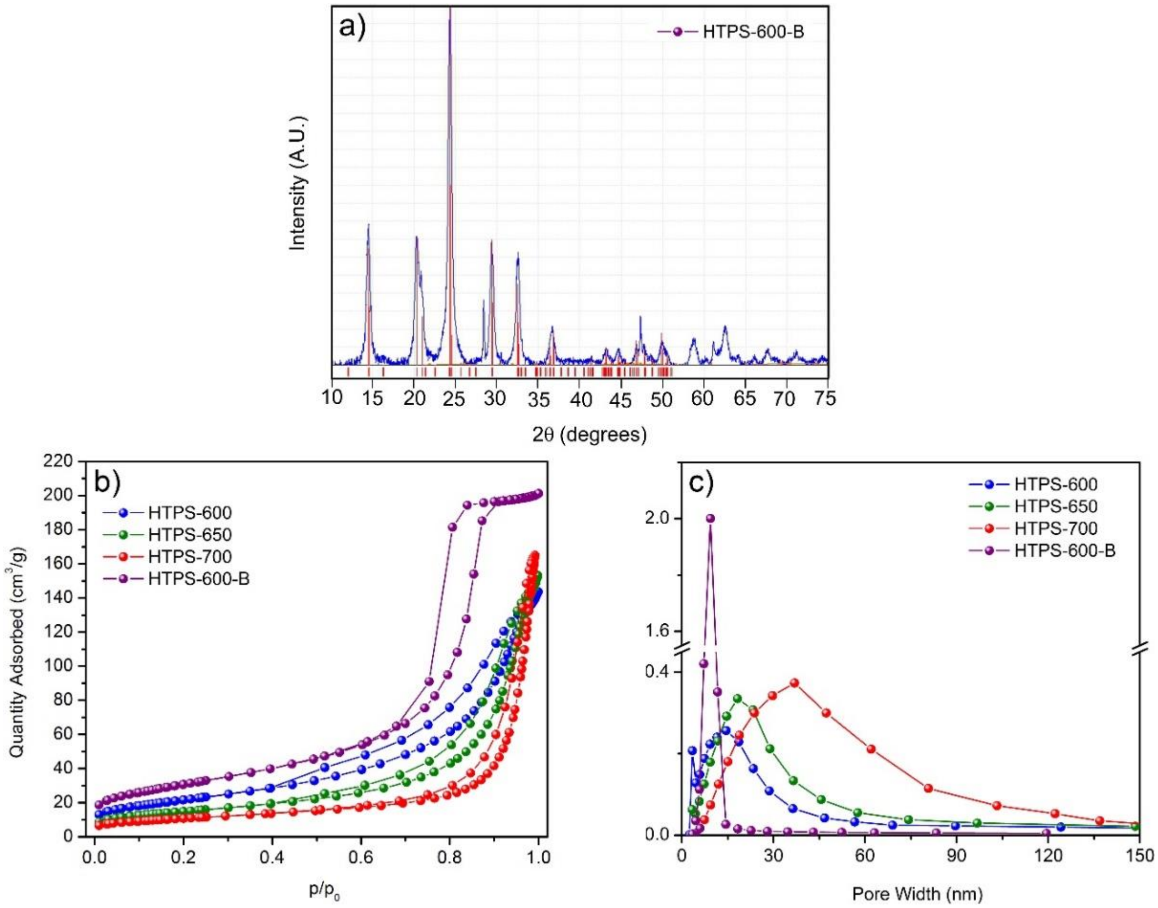

Figure 94. Characterizations of HTPS made with titanium butoxide and sulfuric acid precursors as opposed to titanyl sulfate, including PXRD pattern (a), nitrogen sorption isotherms (b) and pore size distributions (c).

A main goal of our research became to discover new compounds. This goal was motivated because we discovered a facile way to do sol-gel chemistry with titanium and phosphate, which was previously difficult if at all possible. HTPS was discovered and can be produced by a range of synthetic conditions. Several variations of the synthetic procedure led to promising avenues for further research. For example, we realized that even at 110 °C, the dry gel crystallizes and I am interested in this specific phase behavior, and also of titanium phosphate in sulfate solutions more generally.

Another variation of the synthesis of HTPS is evaporating the water from the gel, and heating the dry gel at 110 °C for several days during which the gel exhibits an interesting phase behavior. **Figures 95a** and **b** show series of PXRD patterns that illustrate this phase behavior for products synthesized with a nominal P/Ti ratio of 1.0 and 1.2 respectively, and omitting PEG. Bragg peaks belonging to the NASICON-type structure, which is presumably HTPS, form over one or two days for both P/Ti ratios, although additional Bragg peaks appear for the P/Ti ratio of 1.2 which were largely unidentified. The black lines indicate the main Bragg peak of the Si internal standard. The red line indicates the most intense Bragg peak corresponding to the NASICON-type structure of HTPS, although reflections appear at low angles around $2\theta = 5.51$ and 6.96 degrees (green and blue lines) which may be associated with stacking of titanium phosphate layers (TEM images showed what looked like layered particles). The titanium phosphate layers have a P/Ti ratio of 2, which may be related to their appearance upon increasing the nominal P/Ti ratio beyond 1. The NASICON-type products form as larger crystals without PEG, and when PEG is added the NASICON-type crystallites do not grow as large, possibly due to surface capping during the growth of the crystallites into larger crystals. Initial studies suggest that the lattice constants increase as the crystallites grow, (**Figure 95c**) which possibly indicates that the crystals are enriched in phosphate content as they grow larger. The fact that sulfate remains in not only the NASICON-type titanium phosphate product after calcination at 700 °C, but also in the compound with P/Ti = 1.3 from which the NASICON-type structure was absent, suggests that sulfate may occupy sites in the amorphous and TiP_2O_7 phases. Furthermore, the fact that crystallization took place at 110 °C suggests that sulfate affects the types of metastable phases, which may allow for the synthesis of new compounds without calcination. One study of interest may be to use surfactants to see whether new crystal structures or morphologies can be found.

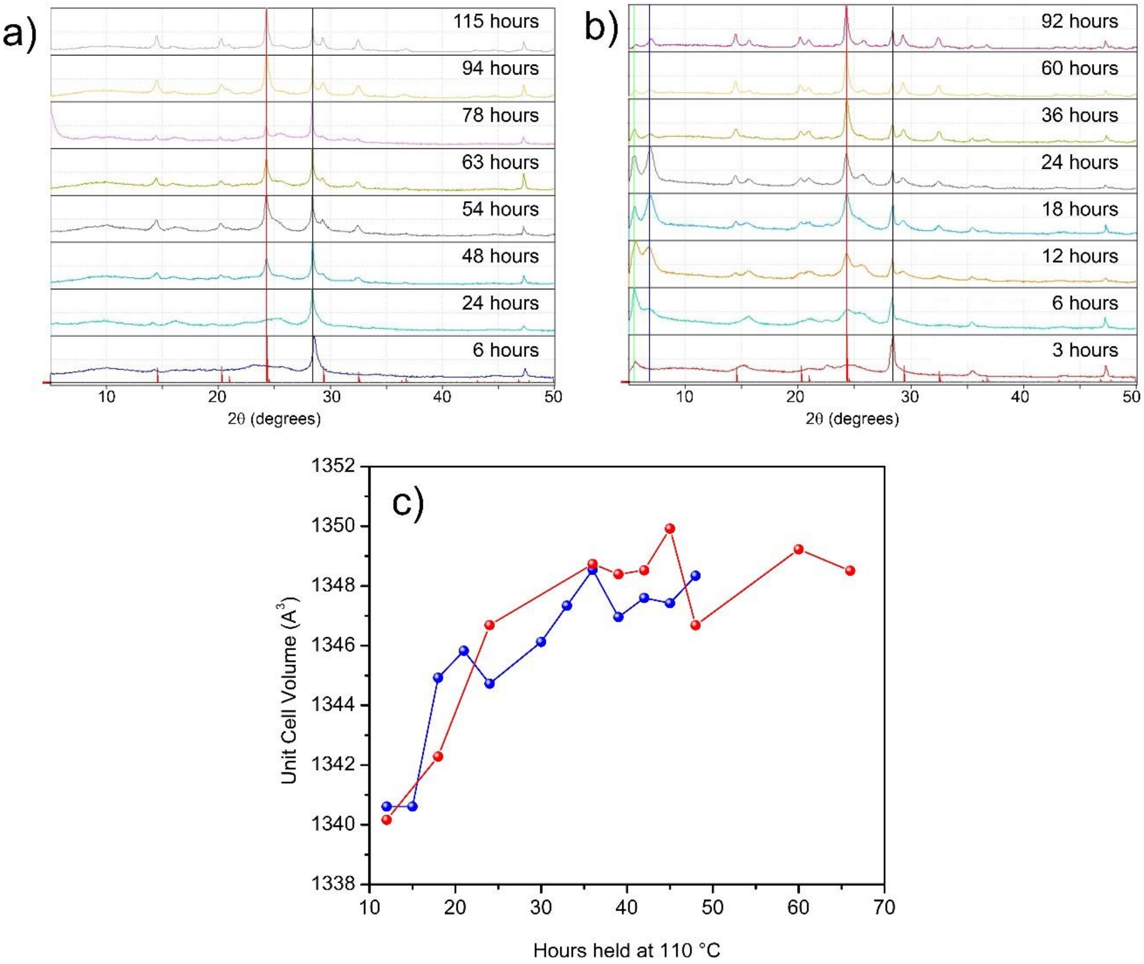

Figure 95. PXRD patterns taken at various times of heating the dry gel precursor to HTPS with P/Ti = 1.0 in (a) and 1.2 in (b), at 110 °C for various times. The unit cell volume also increases with the increased heating time, where the red line is for samples with P/Ti = 1.0, and the blue line is for samples with P/Ti = 1.2.

A suite of titanium phosphates and hydrous titanium phosphate compounds have been reported in the literature. As characterized by methods such as diffraction, thermogravimetric analysis and ion exchange, the anhydrous compounds include TiP_2O_7,[531,532] $Ti_5P_4O_{20}$,[533] and $Ti_4P_6O_{23}$,[289,462] and hydrous compounds include

$Ti(HPO_4)_2$,[534] $Ti(HPO_4)_2\cdot 1/2H_2O$,[535,536] $Ti(HPO_4)_2\cdot H_2O$,[534,536-539] $Ti(HPO_4)_2\cdot 2H_2O$,[531,534,537,539-541] $Ti(PO_4)(H_2PO_4)$,[531,542] $Ti_4(HPO_4)_7(H_2PO_4)_2\cdot{\sim}3(H_2O)$ $TiO(OH)(H_2PO_4)_2\cdot 2(H_2O)$,[543,544] $Ti_2O(PO_4)_2\cdot(H_2O)$,[545] $Ti_2O(PO_4)_2(H_2O)_2$,[546] $Ti_2O(H_2O(PO_4)$,[547] $Ti_2O(PO_4)_2\cdot(H_2O)$,[538,545] $Ti_2O_3(H_2PO_4)_2\cdot 2(H_2O)$,[545,548] $Ti(PO_4)(H_2P_2O_7)_{0.5}$,[531] and $Ti(PO_4)(H_2PO_4)\cdot(2\text{-}x)H_2O$.[531] Also, titanium phosphate molecular sieves have been reported with tetrahedral Ti centers, synthesized using structure-directing surfactants during their synthesis.[549] There are several directions that could potentially yield new materials based on our new peroxide-based synthetic route. One route is exploring the partial substitution of sulfate in the compounds and studying the effect on ion-exchange ability, solubility and applications in catalysis. Another is to attempt the synthesis of these compounds with the partial or full substitution of Ti^{4+} by Zr^{4+} (or other metal cations), such as previously demonstrated for $Ti_{(1-x)}Zr_xP_2O_7$;[550] although the peroxo-zirconium compounds still precipitate with the addition of phosphate which precludes the desired sol-gel route, various synthetic conditions could be explored to produce new zirconium phosphate or phosphate sulfate materials. It may also be possible to synthesize new hydrous titanium phosphate compounds or to isolate new peroxotitanium phosphate compounds.

Another avenue to explore is what metals will form vacant NASICON-type compounds with phosphate and sulfate oxoanions. One example of such a compound can be produced by partial substitution of titanium for iron, and the iron appears to be Fe^{2+} based on the off-white color of the TFPS compound, depicted in (**Figure 96a**). The PXRD pattern shown in **Figure 96b** matches that of the simulated NASICON-type

$H_{1.1}Fe_{0.5}Ti_{1.5}(PO_4)_{2.1}(SO_4)_{0.9}$ structure (Space Group: R3*c*; *a* = 8.461 Å; *c* = 21.69 Å) which is a contraction of the unit cell volume by 0.4% from HTPS (**CHAPTER 3**). The elemental ratios are from ICP-OES and from SEM-EDS, and the average crystallite size is 17 nm by the Scherrer equation. Nitrogen sorption isotherms of TFPS are shown in **Figure 96c** with the corresponding pore size distributions shown in **Figure 96d**. The severe hysteresis between adsorption and desorption isotherm branches indicates that there is a severe inefficiency of diffusion through the pores, which appear to consist of nanopores of ~ 10 nm that are copresent with larger mesopores and macropores; the compound has an overall pore volume of 0.11 cm^3/g, and an average pore width of 16 nm. While the compound has a surface area of 27 m^2/g, this corresponds to the average particle size of 77 nm considering a density of 2.9 g/cm^3, which is not consistent with the Scherrer size of 17 nm.

Figure 96e and **f** show transmission electron microscopy images of the compound, and the nanoporous texture is apparent as is the severe sintering of the crystallites, whose lattice fringes are visible in **Figure 96f**. This strong fusion of the nanoparticles explains the discrepancy between the nanoparticle size as calculated by the Scherrer equation and by the surface area. The compound was a solid acid, exhibiting a pH of zero zeta-potential at pH = 2.7, and is of interest to explore as a catalyst for various reactions (we already tried it as a photo-Fenton catalyst[551] with negative results). We presumed that iron took this oxidation state based on the white color, which was also understandable because Fe^{2+} has almost the same ionic radius as Ti^{4+} (75 pm). This finding made us interested to explore synthetic procedures targeting new compounds of

HTPS with partial substituents such as Mo^{6+}, Co^{3+}, Cr^{3+}, W^{5+}, W^{6+}, Ni^{2+}, Ga^{3+}, that have similar ionic radii as Ti^{4+}.

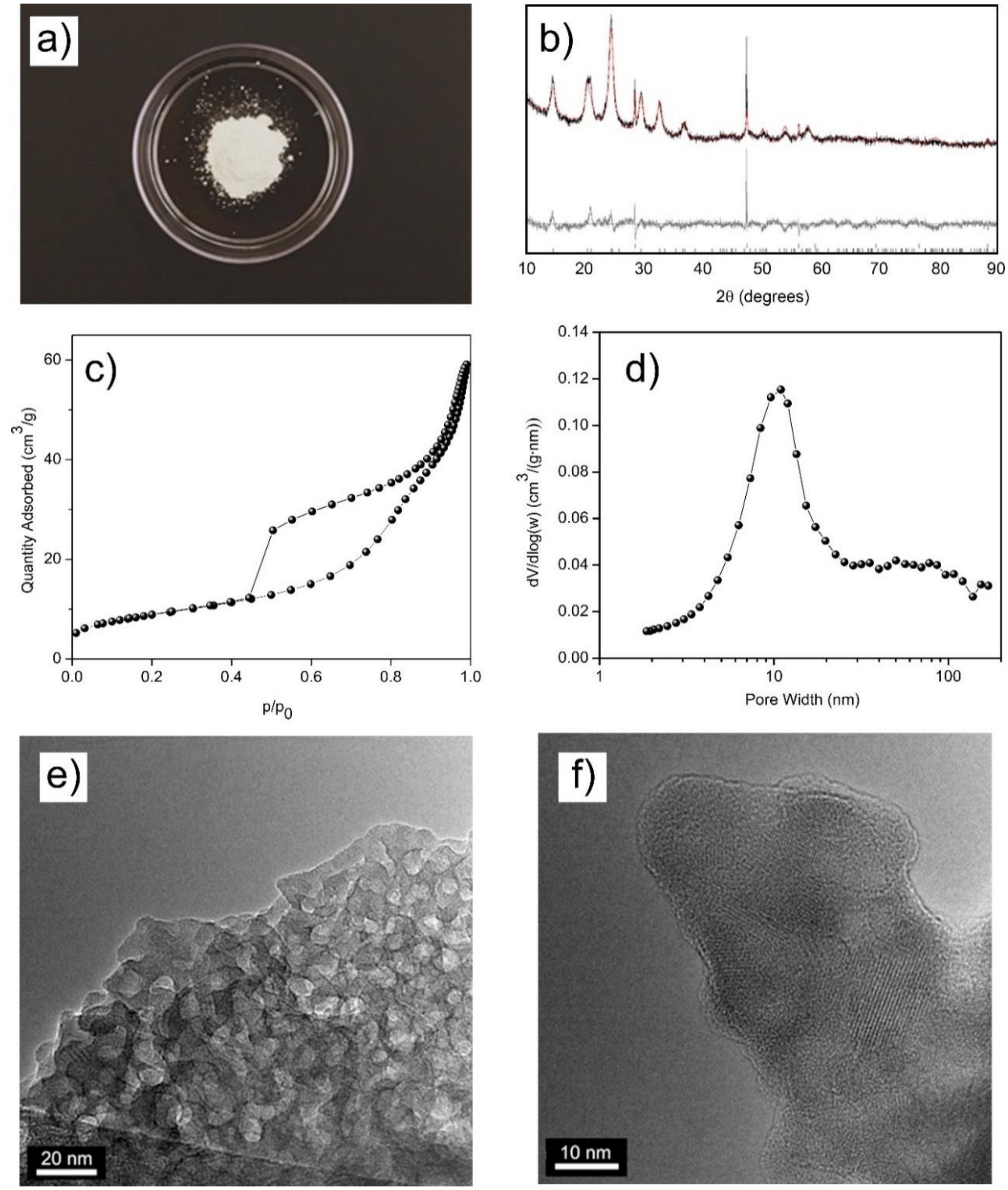

Figure 96. Characterizations of TFPS, including a photograph (a), PXRD pattern shown with the Rietveld-refined model (b), nitrogen gas sorption isotherms (c) and pore size distributions (d), as well as TEM images in (e, scale bar = 20 nm) and (f, scale bar = 10 nm).

More broadly, an area of interest is to understand the chemistry involved with the decomposition of peroxide as it pertains to the polycondensation reactions. For example, Raman and NMR spectroscopy studies could serve both to identify the dissolved peroxo-species and to determine their reactivities. Understanding the reactivities of the peroxo-complexes, and relating them to the gel structure and to the formation of metastable phases, may enable the green synthesis of important porous and nanostructured mixed metal oxide and doped metal oxide materials with a high degree of control. The same types of studies involving various oxoanions and mixed oxoanions is also of interest, and has been of interest in recent literature reports.[297,552-556]

7.6 Better Understanding of Fundamentals of Synthesis and Characterization

There are areas where improved understanding both of the synthetic chemistry and of the characterization techniques was to be desired. One main limitation in the characterization of the HTPS materials was accurate elemental analysis of phosphorous and sulfur. Due to a systematic error in the measurement we applied a correction factor to the P/Ti ratio from ICP-OES results as to match the nominal ratio. We could not definitively determine the source of this error since elemental analysis of the precursors was verified by ICP-OES and checked by TGA, and consideration of the experimental conditions precluded any loss of either phosphate or titanium.

We found that the copresence of titanium and phosphate gave difficulties in developing an appropriate method for the elemental analysis. There was a severe random error that was solved by increasing the power of the RF source from 1150 to 1200 W that presumably mitigated a problem of titanium and phosphorous complexing with each other. Although this higher power solved the random error, some interference may have been responsible for the systematic error causing the measured value of P/Ti to be ~ 10% greater than the nominal ratio. Applying a correction by setting P/Ti to the nominal ratios allowed for understandable data interpretation. The maximum allowable wattage was 1250 W, which did not solve this systematic error.

Since ICP-OES is the primary tool for accurately measuring the elemental ratios, my lack of understanding of the primary elemental analysis technique (ICP-OES) in the copresence of titanium and phosphate leads to the problem that exploring the various potential phases of titanium phosphate sulfate materials cannot be done satisfactorily. To exacerbate the elemental analysis problem, sulfate has a relatively low emission signal in ICP-OES that further limits the accuracy of calculating S/Ti and S/P. A large uncertainty is present with SEM-EDS, although this technique is expected to be semi-quantitative when the proper conditions are met (such as having a flat surface and being non-porous) along with using the proper calibration references. I was not successful at growing large crystals of HTPS to provide such a flat surface and dense bulk volume, and the nanostructured HTPS material that was synthesized was not suitable to form a flat surface or dense material; furthermore, the material is insulating that makes analyzing pellets difficult due to the sample charging.

REFERENCES

(1) In *Merriam-Webster* 2016.

(2) Davis, M. E. *Nature* **2002**, *417*, 813.

(3) Taguchi, A.; Schüth, F. *Microporous and Mesoporous Materials* **2005**, *77*, 1.

(4) Ferey, G. *Chemical Society Reviews* **2008**, *37*, 191.

(5) Li, W.; Liu, J.; Zhao, D. *Nature Reviews Materials* **2016**, *1*, 16023.

(6) Farnan, D.; Frey, D. D.; Horváth, C. *Journal of Chromatography A* **2002**, *959*, 65.

(7) Woerly, S.; Doan, V. D.; Evans-Martin, F.; Paramore, C. G.; Peduzzi, J. D. *Journal of Neuroscience Research* **2001**, *66*, 1187.

(8) Perez-Ramirez, J.; Christensen, C. H.; Egeblad, K.; Christensen, C. H.; Groen, J. C. *Chemical Society Reviews* **2008**, *37*, 2530.

(9) Hormann, K.; Tallarek, U. *Journal of Chromatography A* **2014**, *1365*, 94.

(10) Schmidt, I.; Boisen, A.; Gustavsson, E.; Ståhl, K.; Pehrson, S.; Dahl, S.; Carlsson, A.; Jacobsen, C. J. H. *Chemistry of Materials* **2001**, *13*, 4416.

(11) Park, C.-W.; Kim, T.-K.; Ahn, W.-S. *Synthesis of Mesoporous TS-1 for Catalytic Oxidative Desulfurization*; Korean Chemical Society: Seoul, Coree, Republique De. 2009; Vol. 30.

(12) Egeblad, K.; Kustova, M.; Klitgaard, S. K.; Zhu, K.; Christensen, C. H. *Microporous and Mesoporous Materials* **2007**, *101*, 214.

(13) Jacobsen, C. J. H.; Madsen, C.; Houzvicka, J.; Schmidt, I.; Carlsson, A. *Journal of the American Chemical Society* **2000**, *122*, 7116.

(14) Li, X.; Sun, M.; Rooke, J. C.; Chen, L.; Su, B.-L. *Chinese Journal of Catalysis* **2013**, *34*, 22.

(15) Sun, M.-H.; Chen, L.-H.; Li, X.-Y.; Yang, Y.; Ouyang, Y.-T.; Geng, W.; Li, Y.; Yang, X.-Y.; Su, B.-L. *Microporous and Mesoporous Materials* **2013**, *182*, 122.

(16) Stoeckel, D.; Kübel, C.; Hormann, K.; Höltzel, A.; Smarsly, B. M.; Tallarek, U. *Langmuir* **2014**, *30*, 9022.

(17) Li, Y.; Guijarro, N.; Zhang, X.; Prévot, M. S.; Jeanbourquin, X. A.; Sivula, K.; Chen, H.; Li, Y. *ACS Applied Materials & Interfaces* **2013**.

(18) Reeder, D. H.; Carr, P. W.; Flickinger, M. C.; McCormick, A. V. *Journal of Colloid and Interface Science* **2000**, *226*, 277.

(19) Gritti, F.; Guiochon, G. *Journal of Chromatography A* **2009**, *1216*, 4752.

(20) Sun, M.-H.; Huang, S.-Z.; Chen, L.-H.; Li, Y.; Yang, X.-Y.; Yuan, Z.-Y.; Su, B.-L. *Chemical Society Reviews* **2016**, *45*, 3479.

(21) Ravikovitch, P. I.; Neimark, A. V. *Langmuir* **2002**, *18*, 9830.

(22) Zeng, Y.; Fan, C.; Do, D. D.; Nicholson, D. *Industrial & Engineering Chemistry Research* **2014**, *53*, 15467.

(23) Sun, T.; Xu, L.; Li, S.; Chai, W.; Huang, Y.; Yan, Y.; Chen, J. *Applied Catalysis B: Environmental* **2016**, *193*, 1.

(24) Stein, A.; Wilson, B. E.; Rudisill, S. G. *Chemical Society Reviews* **2013**, *42*, 2763.

(25) Zhang, H.; Cooper, A. I. *Soft Matter* **2005**, *1*, 107.

(26) Imhof, A.; Pine, D. J. *Nature* **1997**, *389*, 948.

(27) Hess, S. C.; Kohll, A. X.; Raso, R. A.; Schumacher, C. M.; Grass, R. N.; Stark, W. J. *ACS Applied Materials & Interfaces* **2015**, *7*, 611.

(28) Vukovic, I.; Brinke, G. t.; Loos, K. *Polymer* **2013**, *54*, 2591.

(29) Yang, P.; Zhao, D.; Margolese, D. I.; Chmelka, B. F.; Stucky, G. D. *Chemistry of Materials* **1999**, *11*, 2813.

(30) Yang, P.; Zhao, D.; Margolese, D. I.; Chmelka, B. F.; Stucky, G. D. *Nature* **1998**, *396*, 152.

(31) Zhang, F.; Meng, Y.; Gu, D.; Yan; Chen, Z.; Tu, B.; Zhao, D. *Chemistry of Materials* **2006**, *18*, 5279.

(32) Mezedur, M. M.; Kaviany, M.; Moore, W. *AIChE Journal* **2002**, *48*, 15.

(33) Clark, S. J.; Segall, M. D.; Pickard, C. J.; Hasnip, P. J.; Probert, M. I. J.; Refson, K.; Payne, M. C. *Zeitschrift für Kristallographie* **2005**, *220*.

(34) Kumar, P.; Agrawal, K. V.; Tsapatsis, M.; Mkhoyan, K. A. *Nature Communications* **2015**, *6*, 7128.

(35) Yan, Y.; Li, K.; Dai, Y.; Chen, X.; Zhao, J.; Yang, Y.; Lee, J.-M. *Electrochimica Acta* **2016**, *208*, 231.

(36) Li, H.; Bian, Z.; Zhu, J.; Zhang, D.; Li, G.; Huo, Y.; Li, H.; Lu, Y. *Journal of the American Chemical Society* **2007**, *129*, 8406.

(37) Huang, Y.; Kang, S.; Yang, Y.; Qin, H.; Ni, Z.; Yang, S.; Li, X. *Applied Catalysis B: Environmental* **2016**, *196*, 89.

(38) Xu, J.; Wang, L.; Zhang, J.; Qian, J.; Liu, J.; Zhang, Z.; Zhang, H.; Liu, X. *Journal of Alloys and Compounds* **2016**, *688, Part B,* 933.

(39) Xu, J.; Su, D.; Bao, W.; Zhao, Y.; Xie, X.; Wang, G. *Journal of Alloys and Compounds* **2016**, *684*, 691.

(40) Huang, S.-Z.; Jin, J.; Cai, Y.; Li, Y.; Deng, Z.; Zeng, J.-Y.; Liu, J.; Wang, C.; Hasan, T.; Su, B.-L. *Scientific Reports* **2015**, *5*, 14686.

(41) Liu, X.; Yi, R.; Zhang, N.; Shi, R.; Li, X.; Qiu, G. *Chemistry – An Asian Journal* **2008**, *3*, 732.

(42) Hwang, J.; Jo, C.; Hur, K.; Lim, J.; Kim, S.; Lee, J. *Journal of the American Chemical Society* **2014**, *136*, 16066.

(43) Fears, T. M.; Sotiriou-Leventis, C.; Winiarz, J. G.; Leventis, N. *Journal of Sol-Gel Science and Technology* **2016**, *77*, 244.

(44) Sadakane, M.; Horiuchi, T.; Kato, N.; Takahashi, C.; Ueda, W. *Chemistry of Materials* **2007**, *19*, 5779.

(45) Zhu, W.; Zhang, L.; Tian, G.-L.; Wang, R.; Zhang, H.; Piao, X.; Zhang, Q. *CrystEngComm* **2014**, *16*, 308.

(46) Wang, Q.; Yuan, L.; Dun, M.; Yang, X.; Chen, H.; Li, J.; Hu, J. *Applied Catalysis B: Environmental* **2016**, *196*, 127.

(47) Lee, C.; Jeon, Y.; Hata, S.; Park, J.-I.; Akiyoshi, R.; Saito, H.; Teraoka, Y.; Shul, Y.-G.; Einaga, H. *Applied Catalysis B: Environmental* **2016**, *191*, 157.

(48) Jun, L.; Dongfeng, X. *Advanced Materials* **2008**, *20*, 2622.

(49) Liang, Z.; Dongyuan, Z.; Xiong Wen, L. *Advanced Materials* **2012**, *24*, 745.

(50) Deville, S. *Journal of Materials Research* **2013**, *28*, 2202.

(51) Ahn, H.; Lee, H.; Lee, S.-B.; Lee, Y. *Journal of Membrane Science* **2007**, *291*, 46.

(52) Frasca, S.; Molero Milan, A.; Guiet, A.; Goebel, C.; Pérez-Caballero, F.; Stiba, K.; Leimkühler, S.; Fischer, A.; Wollenberger, U. *Electrochimica Acta* **2013**, *110*, 172.

(53) Luo, H.; Fang, Z.; Song, N.; Garvey, T.; Lopez, R.; Meyer, T. J. *ACS Applied Materials & Interfaces* **2015**, *7*, 25121.

(54) Baena, J. P. C.; Agrios, A. G. *Journal of Physical Chemistry C* **2014**, *118*, 17028.

(55) Arsenault, E.; Soheilnia, N.; Ozin, G. A. *ACS Nano* **2011**, *5*, 2984.

(56) Benrabah, B.; Bouaza, A.; Kadari, A.; Maaref, M. A. *Superlattices and Microstructures* **2011**, *50*, 591.

(57) Liu, Y.; Peters, K.; Mandlmeier, B.; Müller, A.; Fominykh, K.; Rathousky, J.; Scheu, C.; Fattakhova-Rohlfing, D. *Electrochimica Acta* **2014**, *140*, 108.

(58) Tétreault, N.; Arsenault, É.; Heiniger, L.-P.; Soheilnia, N.; Brillet, J.; Moehl, T.; Zakeeruddin, S.; Ozin, G. A.; Grätzel, M. *Nano Letters* **2011**, *11*, 4579.

(59) Ding, J.; Li, Y.; Hu, H.; Bai, L.; Zhang, S.; Yuan, N. *Nanoscale Research Letters* **2013**, *8*, 9.

(60) Chen, Z.; Wei, C.; Li, S.; Diao, C.; Li, W.; Kong, W.; Zhang, Z.; Zhang, W. *Nanoscale Research Letters* **2016**, *11*, 295.

(61) Wei, D.; Scherer, M. R. J.; Bower, C.; Andrew, P.; Ryhänen, T.; Steiner, U. *Nano Letters* **2012**, *12*, 1857.

(62) Parlett, C. M. A.; Wilson, K.; Lee, A. F. *Chemical Society Reviews* **2013**, *42*, 3876.

(63) Zhang, R.; Feng, J.; Cheng, X.; Gong, L.; Li, Y.; Zhang, H. *Energy and Buildings* **2014**, *81*, 262.

(64) K. Lien, T.; Gao, T.; Sandberg, L. I. C.; Jelle, B. P. *Procedia CIRP* **2014**, *15*, 490.

(65) http://curator.jsc.nasa.gov/stardust/aerogel.cfm# (Accessed August 6, 2016)

(66) Wales, D. J.; Grand, J.; Ting, V. P.; Burke, R. D.; Edler, K. J.; Bowen, C. R.; Mintova, S.; Burrows, A. D. *Chemical Society Reviews* **2015**, *44*, 4290.

(67) Roszak, R.; Firlej, L.; Roszak, S.; Pfeifer, P.; Kuchta, B. *Colloids and Surfaces A: Physicochemical and Engineering Aspects* **2016**, *496*, 69.

(68) Niaz, S.; Manzoor, T.; Pandith, A. H. *Renewable and Sustainable Energy Reviews* **2015**, *50*, 457.

(69) Prachi, P. R.; Mahesh, W. M.; Aneesh, G. C. *Advances in Energy and Power* **2016**, *4*, 11.

(70) Makal, T. A.; Li, J.-R.; Lu, W.; Zhou, H.-C. *Chemical Society Reviews* **2012**, *41*, 7761.

(71) Arico, A. S.; Bruce, P.; Scrosati, B.; Tarascon, J.-M.; van Schalkwijk, W. *Nature Materials* **2005**, *4*, 366.

(72) Vu, A.; Qian, Y.; Stein, A. *Advanced Energy Materials* **2012**, *2*, 1056.

(73) Hamann, T. W.; Martinson, A. B. F.; Elam, J. W.; Pellin, M. J.; Hupp, J. T. *Journal of Physical Chemistry C* **2008**, *112*, 10303.

(74) Luc, W.; Jiao, F. *Accounts of Chemical Research* **2016**, *49*, 1351.

(75) Takenoiri, S.; Kadokawa, N.; Koseki, K. *Journal of Thermal Spray Technology* **2000**, *9*, 360.

(76) Weckmann, H.; Syed, A.; Ilhan, Z.; Arnold, J. *Journal of Thermal Spray Technology* **2006**, *15*, 604.

(77) Sherman, B. D.; Bergkamp, J. J.; Brown, C. L.; Moore, A. L.; Gust, D.; Moore, T. A. *Energy & Environmental Science* **2016**, *9*, 1812.

(78) O'Regan, B.; Gratzel, M. *Nature* **1991**, *353*, 737.

(79) Tiemann, M. *Chemistry – A European Journal* **2007**, *13*, 8376.

(80) Madhi, I.; Bouzid, B.; Saadoun, M.; Bessaïs, B. *Ceramics International* **2015**, *41*, 6552.

(81) Kwan, P.; Schmitt, D.; Volosin, A. M.; McIntosh, C. L.; Seo, D.-K.; Jones, A. K. *Chemical Communications* **2011**, *47*, 12367.

(82) Müller, V.; Rathousky, J.; Fattakhova-Rohlfing, D. *Electrochimica Acta* **2014**, *116*, 1.

(83) Topoglidis, E.; Astuti, Y.; Duriaux, F.; Grätzel, M.; Durrant, J. R. *Langmuir* **2003**, *19*, 6894.

(84) Topoglidis, E.; Cass, A. E. G.; O'Regan, B.; Durrant, J. R. *Journal of Electroanalytical Chemistry* **2001**, *517*, 20.

(85) Topoglidis, E.; Lutz, T.; Durrant, J. R.; Palomares, E. *Bioelectrochemistry* **2008**, *74*, 142.

(86) Sheng, S.; Fang, G.; Li, C.; Xu, S.; Zhao, X. *Physica Status Solidi (A)* **2006**, *203*, 1891.

(87) Gardner, G.; Al-Sharab, J.; Danilovic, N.; Go, Y. B.; Ayers, K.; Greenblatt, M.; Charles Dismukes, G. *Energy & Environmental Science* **2016**, *9*, 184.

(88) Jolivet, J. P.; Henry, M.; Livage, J. *Metal Oxide Chemistry and Synthesis: From Solution to Solid State*; Wiley, 2000.

(89) Baumann, T. F.; Gash, A. E.; Chinn, S. C.; Sawvel, A. M.; Maxwell, R. S.; Satcher, J. H. *Chemistry of Materials* **2004**, *17*, 395.

(90) Einaga, H.; Komatsu, Y. *Journal of Inorganic and Nuclear Chemistry* **1981**, *43*, 2443.

(91) Johnson, J. S.; Kraus, K. A. *Journal of the American Chemical Society* **1956**, *78*, 3937.

(92) Johnson, G. K.; Schlemper, E. O. *Journal of the American Chemical Society* **1978**, *100*, 3645.

(93) Livage, J.; Sanchez, C. *Journal of Non-Crystalline Solids* **1992**, *145*, 11.

(94) Klabunde, K. J.; Stark, J.; Koper, O.; Mohs, C.; Park, D. G.; Decker, S.; Jiang, Y.; Lagadic, I.; Zhang, D. *Journal of Physical Chemistry* **1996**, *100*, 12142.

(95) Medine, G. M.; Zaikovskii, V.; Klabunde, K. J. *Journal of Materials Chemistry* **2004**, *14*, 757.

(96) Djerdj, I.; Arčon, D.; Jagličić, Z.; Niederberger, M. *Journal of Solid State Chemistry* **2008**, *181*, 1571.

(97) Müller, V.; Rasp, M.; Štefanić, G.; Ba, J.; Günther, S.; Rathousky, J.; Niederberger, M.; Fattakhova-Rohlfing, D. *Chemistry of Materials* **2009**, *21*, 5229.

(98) Yuan, C.; Wu, H. B.; Xie, Y.; Lou, X. W. *Angewandte Chemie International Edition* **2014**, *53*, 1488.

(99) Arakaki, A.; Masuda, F.; Amemiya, Y.; Tanaka, T.; Matsunaga, T. *Journal of Colloid and Interface Science* **2010**, *343*, 65.

(100) Lee, K.; Kim, M.; Kim, H. *Journal of Materials Chemistry* **2010**, *20*, 3791.

(101) Stark, J. V.; Park, D. G.; Lagadic, I.; Klabunde, K. J. *Chemistry of Materials* **1996**, *8*, 1904.

(102) Khaleel, A.; Li, W.; Klabunde, K. J. *Nanostructured Materials* **1999**, *12*, 463.

(103) Yan, W.-Y.; Zhou, Q.; Chen, X.; Yang, Y.; Zhang, Y.; Huang, X.-J.; Wu, Y.-C. *Journal of Hazardous Materials* **2016**, *314*, 41.

(104) Alivisatos, A. P. *Science* **1996**, *271*, 933.

(105) Ranade, M. R.; Navrotsky, A.; Zhang, H. Z.; Banfield, J. F.; Elder, S. H.; Zaban, A.; Borse, P. H.; Kulkarni, S. K.; Doran, G. S.; Whitfield, H. J. *Proceedings of the National Academy of Sciences of the United States of America* **2002**, *99*, 6476.

(106) Navrotsky, A. *Geochemical Transactions* **2003**, *4*, 34.

(107) Navrotsky, A. *The Journal of Chemical Thermodynamics* **2007**, *39*, 1.

(108) Navrotsky, A. *International Journal of Quantum Chemistry* **2009**, *109*, 2647.

(109) Afkhami, A.; Moosavi, R. *Journal of Hazardous Materials* **2010**, *174*, 398.

(110) Jacinto, M. J.; Kiyohara, P. K.; Masunaga, S. H.; Jardim, R. F.; Rossi, L. M. *Applied Catalysis A: General* **2008**, *338*, 52.

(111) Klaine, S. J.; Alvarez, P. J. J.; Batley, G. E.; Fernandes, T. F.; Handy, R. D.; Lyon, D. Y.; Mahendra, S.; McLaughlin, M. J.; Lead, J. R. *Environmental Toxicology & Chemistry* **2008**, *27*, 1825.

(112) Yang, W.; Peters, J. I.; Williams Iii, R. O. *International Journal of Pharmaceutics* **2008**, *356*, 239.

(113) Gopalakrishnan, J. *Chemistry of Materials* **1995**, *7*, 1265.

(114) Adschiri, T.; Hakuta, Y.; Sue, K.; Arai, K. *Journal of Nanoparticle Research* **2001**, *3*, 227.

(115) P, P. M.; Google Patents (US3330697): 1967.

(116) Strelko, V. In *Sol-Gel Methods for Materials Processing*; Innocenzi, P., Zub, Y., Kessler, V., Eds.; Springer Netherlands: 2008, p 227.

(117) Danks, A. E.; Hall, S. R.; Schnepp, Z. *Materials Horizons* **2016**, *3*, 91.

(118) Emanuela, Z. *Journal of Physics: Condensed Matter* **2007**, *19*, 323101.

(119) Trappe, V.; Sandkühler, P. *Current Opinion in Colloid & Interface Science* **2004**, *8*, 494.

(120) Baumann, T. F.; Kucheyev, S. O.; Gash, A. E.; Satcher, J. H. *Advanced Materials* **2005**, *17*, 1546.

(121) Sharma, S.; Volosin, A. M.; Schmitt, D.; Seo, D.-K. *Journal of Materials Chemistry A* **2013**, *1*, 699.

(122) Trinh, T. T.; Tran, K.-Q.; Zhang, X.-Q.; van Santen, R. A.; Meijer, E. Journal of Physical Chemistry C*hem. Phys.* **2015**, *17*, 21810.

(123) Babonneau, F.; Sanchez, C.; Livage, J. *Journal of Non-Crystalline Solids* **1988**, *106*, 3.

(124) Kallala, M.; Sanchez, C.; Cabane, B. *Physical Review E* **1993**, *48*, 3692.

(125) Nedelec, J.-M.; Courtheoux, L.; Jallot, E.; Kinowski, C.; Lao, J.; Laquerriere, P.; Mansuy, C.; Renaudin, G.; Turrell, S. *Journal of Sol-Gel Science and Technology* **2008**, *46*, 259.

(126) Scherer, G. W. *Journal of Non-Crystalline Solids* **1988**, *100*, 77.

(127) Scherer, G. W. *Journal of Non-Crystalline Solids* **1992**, *144*, 210.

(128) Yoldas, B. E. *Journal of Materials Science* **1986**, *21*, 1087.

(129) Scherer, G. W. *Journal of Non-Crystalline Solids* **1990**, *121*, 104.

(130) Rolison, D. R.; Dunn, B. *Journal of Materials Chemistry* **2001**, *11*, 963.

(131) Thouless, M. D. *Acta Metallurgica* **1988**, *36*, 3131.

(132) Drory, M. D.; Thouless, M. D.; Evans, A. G. *Acta Metallurgica* **1988**, *36*, 2019.

(133) Yang, J.; Ferreira, J. M. F. *Materials Research Bulletin* **1998**, *33*, 389.

(134) Volosin, A. M.; Sharma, S.; Traverse, C.; Newman, N.; Seo, D.-K. *Journal of Materials Chemistry* **2011**, *21*, 13232.

(135) Nandiyanto, A. B. D.; Suhendi, A.; Kisakibaru, Y.; Ogi, T.; Okuyama, K. *International Journal of Chemical and Biological Engineering* **2012**, *6*, 1142.

(136) de Lima, R. K. C.; da Silva, E. D.; Urquieta-González, E. A. In *Studies in Surface Science and Catalysis*; Gaigneaux, E. M.; Devillers, M.; Hermans, S.; Jacobs, P. A.; Martens, J. A.; Ruiz, P. Eds.; Elsevier: 2010; Vol. Volume 175, p 657.

(137) Koo, H.-J.; Park, J.; Yoo, B.; Yoo, K.; Kim, K.; Park, N.-G. *Inorganica Chimica Acta* **2008**, *361*, 677.

(138) Thapliyal, P. C.; Singh, K. *Journal of Materials* **2014**, *2014*, 10.

(139) Fujishima, A.; Honda, K. *Nature* **1972**, *238*, 37.

(140) Oregan, B.; Grätzel, M. *Nature* **1991**, *353*, 737.

(141) Leem, G.; Sherman, B. D.; Burnett, A. J.; Morseth, Z. A.; Wee, K.-R.; Papanikolas, J. M.; Meyer, T. J.; Schanze, K. S. *ACS Energy Letters* **2016**, 339.

(142) Fajans, K. *Naturwissenschaften* **1923**, *11*, 165.

(143) Hanaor, D. A. H.; Sorrell, C. C. *Journal of Materials Science* **2011**, *46*, 855.

(144) Ribeiro, C.; Vila, C.; Stroppa, D. B.; Mastelaro, V. R.; Bettini, J.; Longo, E.; Leite, E. R. *Journal of Physical Chemistry C* **2007**, *111*, 5871.

(145) Burdett, J. K.; Hughbanks, T.; Miller, G. J.; Richardson, J. W.; Smith, J. V. *Journal of the American Chemical Society* **1987**, *109*.

(146) Bolzan, A. A.; Fong, C.; Kennedy, B. J.; Howard, C. J. *Acta Crystallographica Section B* **1997**, *53*, 373.

(147) Matthews, A. *American Mineralogist* **1976**, *61*, 419.

(148) Patra, S.; Davoisne, C.; Bouyanfif, H.; Foix, D.; Sauvage, F. *Scientific Reports* **2015**, *5*, 10928.

(149) Campbell, L. K.; Na, B. K.; Ko, E. I. *Chemistry of Materials* **1992**, *4*, 1329.

(150) Ladd, D. M.; Volosin, A.; Seo, D.-K. *Journal of Materials Chemistry* **2010**, *20*, 5923.

(151) Gázquez, M.; Bolívar, J.; Garcia-Tenorio, R.; Vaca, F. *Materials Sciences and Applications* **2014**, *5*, 441.

(152) Correa Baena, J. P.; Agrios, A. G. *ACS Applied Materials & Interfaces* **2014**, *6*, 19127.

(153) Rickert, K.; Sedefoglu, N.; Malo, S.; Caignaert, V.; Kavak, H.; Poeppelmeier, K. R. *Chemistry of Materials* **2015**, *27*, 5072.

(154) Dürr, M.; Rosselli, S.; Yasuda, A.; Nelles, G. *Journal of Physical Chemistry B* **2006**, *110*, 21899.

(155) Chen, W.-C.; Lien, H.-T.; Cheng, T.-W.; Su, C.; Chong, C.-W.; Ganguly, A.; Chen, K.-H.; Chen, L.-C. *ACS Applied Materials & Interfaces* **2015**, *7*, 4616.

(156) Stadler, A. *Materials* **2012**, *5*, 661.

(157) Minami, T.; Miyata, T. *Thin Solid Films* **2008**, *517*, 1474.

(158) Umar Sidik; Jung Hee Kim; Hae-Kyoung Kim; Hee Young Lee; Lee, J.-Y. *Micro & Nano Letters* **2014**, *9*, 854.

(159) Lewis, B. G.; Paine, D. C. *MRS Bulletin* **2000**, *August*, 22

(160) Fujishima, A.; Zhang, X.; Tryk, D. A. *Surface Science Reports* **2008**, *63*, 515.

(161) Ni, M.; Leung, M. K. H.; Leung, D. Y. C.; Sumathy, K. *Renewable and Sustainable Energy Reviews* **2007**, *11*, 401.

(162) Kambe, S.; Murakoshi, K.; Kitamura, T.; Wada, Y.; Yanagida, S.; Kominami, H.; Kera, Y. *Solar Energy Materials and Solar Cells* **2000**, *61*, 427.

(163) Imahori, H.; Hayashi, S.; Umeyama, T.; Eu, S.; Oguro, A.; Kang, S.; Matano, Y.; Shishido, T.; Ngamsinlapasathian, S.; Yoshikawa, S. *Langmuir* **2006**, *22*, 11405.

(164) Li, B.; Wang, L.; Kang, B.; Wang, P.; Qiu, Y. *Solar Energy Materials and Solar Cells* **2006**, *90*, 549.

(165) Sanderson, R. T. *Journal of the American Chemical Society* **1983**, *105*, 2259.

(166) Mulliken, R. S. *The Journal of Chemical Physics* **1934**, *2*, 782.

(167) Song, J.; Kulinich, S. A.; Li, J.; Liu, Y.; Zeng, H. *Angewandte Chemie International Edition* **2015**, *54*, 698.

(168) Banerjee, A.; Chattopadhyay, K. In *Open Physics* 2008; Vol. 6, p 57.

(169) Wang, Y.; Djerdj, I.; Smarsly, B.; Antonietti, M. *Chemistry of Materials* **2009**, *21*, 3202.

(170) Koebel, M. M.; Nadargi, D. Y.; Jimenez-Cadena, G.; Romanyuk, Y. E. *ACS Applied Materials & Interfaces* **2012**, *4*, 2464.

(171) Floriano, E. A.; Scalvi, L. V. A.; Sambrano, J. R.; de Andrade, A. *Applied Surface Science* **2013**, *267*, 164.

(172) Guzman, G.; Dahmani, B.; Puetz, J.; Aegerter, M. A. *Selected Papers from the 5th International Conference on Coatings on Glass (ICCG5)- Advanced Coatings on Glass and Plastics for Large-Area or High-Volume Products ICCG-5 Selected Papers from the 5th International Conference on Coatings on Glass (ICCG5)- Advanced Coatings on Glass and Plastics for Large-Area or High-Volume Products* **2006**, *502*, 281.

(173) Mazloom, J.; Ghodsi, F. E.; Gholami, M. *Journal of Alloys and Compounds* **2013**, *579*, 384.

(174) Senguttuvan, T. D.; Malhotra, L. K. *Thin Solid Films* **1996**, *289*, 22.

(175) Seo, M.; Akutsu, Y.; Kagemoto, H. *Ceramics International* **2007**, *33*, 625.

(176) Zhang, D.; Tao, L.; Deng, Z.; Zhang, J.; Chen, L. *Materials Chemistry and Physics* **2006**, *100*, 275.

(177) Kong, J.; Deng, H.; Yang, P.; Chu, J. *Materials Chemistry and Physics* **2009**, *114*, 854.

(178) Dua, L.; Biswas, P. K. *Chemical Physics Letters* **2013**, *572*, 66.

(179) Liu, T. J.; Jin, Z. G.; Feng, L. R.; Wang, T. *Applied Surface Science* **2008**, *254*, 6547.

(180) Song, I. S.; Heo, S. W.; Lee, J. H.; Haw, J. R.; Moon, D. K. *Journal of Industrial and Engineering Chemistry* **2012**, *18*, 312.

(181) Simmons, C. R.; Schmitt, D.; Wei, X.; Han, D.; Volosin, A. M.; Ladd, D. M.; Seo, D.-K.; Liu, Y.; Yan, H. *ACS Nano* **2011**, *5*, 6060.

(182) Scheideler, W. J.; Jang, J.; Karim, M. A. U.; Kitsomboonloha, R.; Zeumault, A.; Subramanian, V. *ACS Applied Materials & Interfaces* **2015**, *7*, 12679.

(183) Gong, J.; Chen, Q.; Lian, M.-R.; Liu, N.-C.; Stevenson, R. G.; Adami, F. *Sensors and Actuators B: Chemical* **2006**, *114*, 32.

(184) Skoromets, V.; Němec, H.; Kopeček, J.; Kužel, P.; Peters, K.; Fattakhova-Rohlfing, D.; Vetushka, A.; Müller, M.; Ganzerová, K.; Fejfar, A. *Journal of Physical Chemistry C* **2015**, *119*, 19485.

(185) Stefik, M.; Cornuz, M.; Mathews, N.; Hisatomi, T.; Mhaisalkar, S.; Grätzel, M. *Nano Letters* **2012**, *12*, 5431.

(186) Roy, B.; Perkins, J. D.; Kaydanova, T.; Young, D. L.; Taylor, M.; Miedaner, A.; Curtis, C.; Kleebe, H. J.; Readey, D. W.; Ginley, D. S. *Thin Solid Films* **2008**, *516*, 4093.

(187) Das, B.; Renaud, A.; Volosin, A. M.; Yu, L.; Newman, N.; Seo, D.-K. *Inorganic Chemistry* **2015**, *54*, 1100.

(188) Renaud, A.; Chavillon, B.; Le Pleux, L.; Pellegrin, Y.; Blart, E.; Boujtita, M.; Pauporte, T.; Cario, L.; Jobic, S.; Odobel, F. *Journal of Materials Chemistry* **2012**, *22*, 14353.

(189) Powar, S.; Xiong, D.; Daeneke, T.; Ma, M. T.; Gupta, A.; Lee, G.; Makuta, S.; Tachibana, Y.; Chen, W.; Spiccia, L.; Cheng, Y.-B.; Götz, G.; Bäuerle, P.; Bach, U. *Journal of Physical Chemistry C* **2014**, *118*, 16375.

(190) Wang, Y.; Chen, T. *Electrochimica Acta* **2009**, *54*, 3510.

(191) Chen, F.; Li, N.; Shen, Q.; Wang, C.; Zhang, L. *Solar Energy Materials and Solar Cells* **2012**, *105*, 153.

(192) Forman, A. J.; Chen, Z.; Chakthranont, P.; Jaramillo, T. F. *Chemistry of Materials* **2014**, *26*, 958.

(193) Tran, Q. P.; Fang, J. S.; Chin, T. S. *Materials Science in Semiconductor Processing* **2015**, *40*, 664.

(194) Regoutz, A.; Egdell, R. G.; Morgan, D. J.; Palgrave, R. G.; Téllez, H.; Skinner, S. J.; Payne, D. J.; Watson, G. W.; Scanlon, D. O. *Applied Surface Science* **2015**, *349*, 970.

(195) Knapp, C. E.; Hyett, G.; Parkin, I. P.; Carmalt, C. J. *Chemistry of Materials* **2011**, *23*, 1719.

(196) Shan, C.; Huang, T.; Zhang, J.; Han, M.; Li, Y.; Hu, Z.; Chu, J. *Journal of Physical Chemistry C* **2014**, *118*, 6994.

(197) Ohsawa, T.; Okubo, J.; Suzuki, T.; Kumigashira, H.; Oshima, M.; Hitosugi, T. *Journal of Physical Chemistry C* **2011**, *115*, 16625.

(198) Pasquarelli, R. M.; Curtis, C. J.; Miedaner, A.; van Hest, M. F. A. M.; O'Hayre, R. P.; Ginley, D. S. *Inorganic Chemistry* **2010**, *49*, 5424.

(199) Hoel, C. A.; Mason, T. O.; Gaillard, J.-F.; Poeppelmeier, K. R. *Chemistry of Materials* **2010**, *22*, 3569.

(200) Allhusen, J. S.; Conboy, J. C. *ACS Applied Materials & Interfaces* **2013**, *5*, 11683.

(201) Grätzel, M. *Journal of Photochemistry and Photobiology C: Photochemistry Reviews* **2003**, *4*, 145.

(202) Nakata, K.; Fujishima, A. *Journal of Photochemistry and Photobiology C: Photochemistry Reviews* **2012**, *13*, 169.

(203) Zhang, H.; Ruan, S.; Xie, T.; Feng, C.; Qu, P.; Chen, W.; Dong, W. *IEEE Electron Device Letters* **2011**, *32*, 653.

(204) Zhang, H.; Li, H.; Zhang, M.; Feng, C.; Gu, X.; Xu, Y.; Zhou, J.; Ruan, S. *Applied Optics* **2013**, *52*, 750.

(205) Zhang, H.; Feng, C.; Liu, C.; Xie, T.; Zhou, J.; Ruan, S. *IEEE Electron Device Letters* **2011**, *32*, 934.

(206) Wu, J.; Zhang, C.; Li, Q.; Wu, L.; Jiang, D.; Xia, J. *Solid State Ionics* **2016**, *292*, 32.

(207) Mor, G. K.; Varghese, O. K.; Paulose, M.; Shankar, K.; Grimes, C. A. *Solar Energy Materials and Solar Cells* **2006**, *90*, 2011.

(208) Ko, K. H.; Lee, Y. C.; Jung, Y. J. *Journal of Colloid and Interface Science* **2005**, *283*, 482.

(209) Lee, J.-H.; Park, N.-G.; Shin, Y.-J. *Solar Energy Materials and Solar Cells* **2011**, *95*, 179.

(210) Nang Dinh, N.; Bernard, M.-C.; Hugot-Le Goff, A.; Stergiopoulos, T.; Falaras, P. *Comptes Rendus Chimie* **2006**, *9*, 676.

(211) Basu, K.; Benetti, D.; Zhao, H.; Jin, L.; Vetrone, F.; Vomiero, A.; Rosei, F. *Scientific Reports* **2016**, *6*, 23312.

(212) Rechberger, F.; Ilari, G.; Niederberger, M. *Chemical Communications* **2014**, *50*, 13138.

(213) Takahashi, R.; Sato, S.; Sodesawa, T.; Suzuki, K.; Tafu, M.; Nakanishi, K.; Soga, N. *Journal of the American Ceramic Society* **2001**, *84*, 1968.

(214) Chu, N.; Wang, J.; Zhang, Y.; Yang, J.; Lu, J.; Yin, D. *Chemistry of Materials* **2010**, *22*, 2757.

(215) Janssen, A. H.; Schmidt, I.; Jacobsen, C. J. H.; Koster, A. J.; de Jong, K. P. *Microporous and Mesoporous Materials* **2003**, *65*, 59.

(216) Koo, J.-B.; Jiang, N.; Saravanamurugan, S.; Bejblová, M.; Musilová, Z.; Čejka, J.; Park, S.-E. *Journal of Catalysis* **2010**, *276*, 327.

(217) Madsen, C.; Madsen, C.; J. H. Jacobsen, C. *Chemical Communications* **1999**, 673.

(218) Guo, Y.-G.; Hu, J.-S.; Wan, L.-J. *Advanced Materials* **2008**, *20*, 2878.

(219) Hao, X.; Bartlett, B. M. *Advanced Energy Materials* **2013**, *3*, 753.

(220) Jinka, K.; Bajaj, H.; Jasra, R.; Prasetyanto, E.; Park, S.-E. *Topics in Catalysis* **2010**, *53*, 238.

(221) Schüth, F. *Angewandte Chemie International Edition* **2003**, *42*, 3604.

(222) Schwickardi, M.; Johann, T.; Schmidt, W.; Busch, O.; Schüth, F. In *Studies in Surface Science and Catalysis*; Gaigneaux, E.; De Vos, D. E.; Grange, P.; Jacobs, P. A.; Martens, P.; Ruiz, P.; Poncelet, G. Eds.; Elsevier: 2000; Vol. 43, p 93.

(223) Schwickardi, M.; Johann, T.; Schmidt, W.; Schüth, F. *Chemistry of Materials* **2002**, *14*, 3913.

(224) Wang, D.; Yu, Y.; He, H.; Wang, J.; Zhou, W.; Abruña, H. D. *ACS Nano* **2015**, *9*, 1775.

(225) Asabina, E. A.; Orekhova, N. V.; Ermilova, M. M.; Pet’kov, V. I.; Glukhova, I. O.; Zhilyaeva, N. A.; Yaroslavtsev, A. B. *Inorganic Materials* **2015**, *51*, 793.

(226) Shchelokov, I.; Asabina, E.; Sukhanov, M.; Ermilova, M.; Orekhova, N.; Pet'kov, V.; Tereshchenko, G. *Solid State Sciences* **2008**, *10*, 513.

(227) Ilin, A. B.; Orekhova, N. V.; Ermilova, M. M.; Yaroslavtsev, A. B. *Catalysis Today* **2016**, *268*, 29.

(228) Auborn, J. J.; Johnson Jr, D. W. *Solid State Ionics* **1981**, *5*.

(229) Hogarth, W. H. J.; Diniz da Costa, J. C.; Drennan, J.; Lu, G. Q. *Journal of Materials Chemistry* **2005**, *15*, 754.

(230) Alamo, J. *Solid State Ionics* **1993**, *63–65*, 547.

(231) Asabina, E. A.; Lukutsov, A. A.; Pet’kov, V. I. *Russian Journal of Applied Chemistry* **2012**, *85*, 867.

(232) Hirose, N.; Kuwano, J. *Journal of Materials Chemistry* **1994**, *4*, 9.

(233) Hosono, H.; Imai, K.; Abe, Y. *Journal of The Electrochemical Society* **1993**, *140*, L7.

(234) Jia, K.; Pan, B.; Zhang, Q.; Zhang, W.; Jiang, P.; Hong, C.; Pan, B.; Zhang, Q. *Journal of Colloid and Interface Science* **2008**, *318*, 160.

(235) Pet'kov, V.; Asabina, E.; Shchelokov, I. *Inorganic Materials* **2013**, *49*, 502.

(236) Arbi, K.; Tabellout, M.; Sanz, J. *Solid State Ionics* **2010**, *180*, 1613.

(237) Arun, N.; Aravindan, V.; Ling, W. C.; Madhavi, S. *Journal of Alloys and Compounds* **2014**, *603*, 48.

(238) Nanjundaswamy, K. S.; Padhi, A. K.; Goodenough, J. B.; Okada, S.; Ohtsuka, H.; Arai, H.; Yamaki, J. *Solid State Ionics* **1996**, *92*, 1.

(239) Nuspl, G.; Takeuchi, T.; Weiß, A.; Kageyama, H.; Yoshizawa, K.; Yamabe, T. *Journal of Applied Physics* **1999**, *86*, 5484.

(240) Ortiz, G. F.; López, M. C.; Lavela, P.; Vidal-Abarca, C.; Tirado, J. L. *Solid State Ionics* **2014**, *262*, 573.

(241) Dang, H.-Y.; Guo, X.-M. *Sensors and Actuators B: Chemical* **2013**, *178*, 163.

(242) Dang, H.-Y.; Guo, X.-M. *Solid State Ionics* **2011**, *201*, 68.

(243) Jasinski, P.; Strzelczyk, A.; Chachulski, B. A.; Gazda, M.; Jasinski, G. *Sensors and Actuators B: Chemical* **2013**, *189*, 141.

(244) Liang, X.; Wang, B.; Zhang, H.; Diao, Q.; Quan, B.; Lu, G. *Sensors and Actuators B: Chemical* **2013**, *187*, 522.

(245) Paściak, G.; Mielcarek, W.; Prociów, K.; Warycha, J. *Ceramics International* **2014**, *40*, 12783.

(246) Boilot, J. P.; Colomban, P. *Journal of Materials Science Letters* **1985**, *4*, 22.

(247) Cretin, M.; Khireddine, H.; Fabry, P. *Sensors and Actuators B: Chemical* **1997**, *43*, 224.

(248) Ziyad, M.; Ahmamouch, R.; Rouimi, M.; Gharbage, S.; Védrine, J. C. *Solid State Ionics* **1998**, *110*, 311.

(249) Essoumhi, A.; Favotto, C.; Mansori, M.; Ouzaouit, K.; Satre, P. *Solid State Sciences* **2007**, *9*, 240.

(250) Aono, H.; Sugimoto, E.; Sadaoka, Y.; Imanaka, N.; Adachi, G. Y. *Journal of The Electrochemical Society* **1993**, *140*, 1827.

(251) Matkovic, B.; Prodic, B.; Sljukic, M. *Bulletin de la Societe Chimique de France*, 1777.

(252) Brik, Y.; Kacimi, M.; Bozon-Verduraz, F.; Ziyad, M. *Microporous and Mesoporous Materials* **2001**, *43*, 103.

(253) Ahmamouch, R.; Arsalane, S.; Kacimi, M.; Ziyad, M. *Materials Research Bulletin* **1997**, *32*, 755.

(254) Ilyushin *Kristallografiia / Akademiia nauk SSSR* **1989**, *34*, 839.

(255) Hong, H. Y. P. *Materials Research Bulletin* **1976**, *11*, 173.

(256) Jrifi, A.; El Jazouli, A.; Chaminade, J. P.; Couzi, M. *Powder Diffraction* **2009**, *24*, 200.

(257) Borovikova, E. Y.; Kurazhkovskaya, V. S.; Boldyrev, K. N.; Sukhanov, M. V.; Pet’kov, V. I.; Kokarev, S. A. *Vibrational Spectroscopy* **2014**, *73*, 158.

(258) Sizova *Kristallokhimii͡a i struktura mineralov* **1974**, 10.

(259) Yue, Y.; Pang, W. *Journal of Materials Science Letters* **1991**, *10*, 1009.

(260) Hagman, L.-O.; Kierkegaard, P. *Acta Chemica Scandinavica* **1968**, *22*, 1822.

(261) Hirayama, M.; Sonoyama, N.; Yamada, A.; Kanno, R. *Journal of Solid State Chemistry* **2009**, *182*, 730.

(262) Masui, T.; Koyabu, K.; Tamura, S.; Imanaka, N. *Journal of Alloys and Compounds* **2006**, *418*, 73.

(263) Mouline, A.; Alami, M.; Brochu, R.; Olazcuaga, R.; Parent, C.; Le Flem, G. *Journal of Solid State Chemistry* **2000**, *152*, 453.

(264) Mouline, A.; Alami, M.; Brochu, R.; Olazcuaga, R.; Parent, C.; Le Flem, G. *Materials Research Bulletin* **2000**, *35*, 899.

(265) Tamura, S.; Imanaka, N.; Adachi, G. *Journal of Alloys and Compounds* **2001**, *323–324*, 540.

(266) Anuar, N. K.; Adnan, S. B. R. S.; Mohamed, N. S. *Ceramics International* **2014**, *40*, 13719.

(267) Clearfield, A.; Roberts, B. D.; Subramanian, M. A. *Materials Research Bulletin* **1984**, *19*, 219.

(268) Subramanian, M. A.; Roberts, B. D.; Clearfield, A. *Materials Research Bulletin* **1984**, *19*, 1471.

(269) Imanaka, N.; Itaya, M.; Ueda, T.; Adachi, G. *Solid State Ionics* **2002**, *154–155*, 319.

(270) Imanaka, N.; Adachi, G. Y. *Journal of Alloys and Compounds* **2002**, *344*, 137.

(271) Pet’kov, V. I.; Asabina, E. A.; Markin, A. V.; Smirnova, N. N.; Kitaev, D. B. *Journal of Thermal Analysis and Calorimetry* **2005**, *80*, 695.

(272) Bykov, D. M.; Orlova, A. I.; Tomilin, S. V.; Lizin, A. A.; Lukinykh, A. N. *Radiochemistry* **2006**, *48*, 234.

(273) Petkov, V. I.; Orlova, A. I. *Journal of Thermal Analysis and Calorimetry* **1998**, *54*, 71.

(274) Orlova, A. I.; Samoĭlov, S. G.; Kazantsev, G. N.; Volgutov, V. Y.; Bykov, D. M.; Golubev, A. V.; Borovikova, E. Y. *Crystallography Reports* **2009**, *54*, 431.

(275) Gorodylova, N.; Kosinova, V.; Sulcova, P.; Belina, P.; Vlcek, M. *Dalton Transactions* **2014**, *43*, 15439.

(276) Pet’kov, V. I.; Kurazhkovskaya, V. S.; Orlova, A. I.; Spiridonova, M. L. *Crystallography Reports* **2002**, *47*, 736.

(277) Pet’kov, V. I.; Sukhanov, M. V.; Ermilova, M. M.; Orekhova, N. V.; Tereshchenko, G. F. *Russian Journal of Applied Chemistry* **2010**, *83*, 1731.

(278) Limaye, S. Y.; Agrawal, D. K.; McKinstry, H. A. *Journal of the American Ceramic Society* **1987**, *70*, 232.

(279) Nomura, K.; Ikeda, S.; Ito, K. *Bulletin of the Chemical Society of Japan* **1992**, *65*, 3221.

(280) Yaakoubi, A.; Jouini, T.; Jouini, N. *Solid State Chemistry* **1991**, *312*, 451.

(281) Yahia, H. B.; Rodewald, U. C.; Pottgen, R. *Verlag der Zeitschrift für Naturforschung* **2010**, 65b, 639.

(282) Mbandza, A.; Bordes, E.; Courtine, P. *Materials Research Bulletin* **1985**, *20*, 251.

(283) Takahashi, H.; Takamura, H. *Key Engineering Materials* **2012**, *508*, 291.

(284) Fakrane, H.; Lamire, M.; El Jazouli, A.; Le Flem, G.; Olazcuaga, R. *Annales de Chimie Science des Matériaux* **1998**, *23*, 77.

(285) Dressler, M.; Börnstein, J.; Meinel, M.; Ploska, U.; Reinsch, S.; Hodoroaba, V. D.; Nicolaides, D.; Wenzel, K. J. *Journal of Sol-Gel Science and Technology* **2012**, *62*, 273.

(286) Duhlev, R. *Acta Crystallographica Section C* **1994**, *50*, 1525.

(287) El Jazouli, A.; Soubeyroux, J. L.; Dance, J. M.; Le Flem, G. *Journal of Solid State Chemistry* **1986**, *65*, 351.

(288) McCarron Iii, E. M.; Calabrese, J. C.; Subramanian, M. A. *Materials Research Bulletin* **1987**, *22*, 1421.

(289) Horiuchi, S.; Ono, A. *Journal of Solid State Chemistry* **1986**, *62*, 335.

(290) Bussereau, I.; Olazcuaga, R.; Dance, J. M.; Delmas, C.; Le Flem, G.; El Jazouli, A. *Journal of Alloys and Compounds* **1992**, *188*, 110.

(291) Schöneborn, M.; Glaum, R. *Zeitschrift für anorganische und allgemeine Chemie* **2008**, *634*, 1843.

(292) El Bouari, A.; El Jazouli, A. *Phosphorous Research Bulletin* **2004**, *15*, 136.

(293) Olazcuaga, R.; Dance, J. M.; Flem, G. L.; Derouet, J.; Beaury, L.; Porcher, P.; Bouari, A. E.; Jazouli, A. E. *Journal of Solid State Chemistry* **1999**, *143*, 224.

(294) Pinus, I.; Bok, T.; Yaroslavtsev, A. *Inorganic Materials* **2010**, *46*, 412.

(295) Senguttuvan, P.; Rousse, G.; Arroyo y de Dompablo, M. E.; Vezin, H.; Tarascon, J. M.; Palacín, M. R. *Journal of the American Chemical Society* **2013**, *135*, 3897.

(296) Senguttuvan, P.; Rousse, G.; Vezin, H.; Tarascon, J. M.; Palacín, M. R. *Chemistry of Materials* **2013**, *25*, 2391.

(297) Ruther, R. E.; Baker, B. M.; Son, J.-H.; Casey, W. H.; Nyman, M. *Inorganic Chemistry* **2014**, *53*, 4234.

(298) Walsh, J. J.; Zhu, J.; Bond, A. M.; Forster, R. J.; Keyes, T. E. *Journal of Electroanalytical Chemistry* **2013**, *706*, 93.

(299) Botar, B.; Kogerler, P.; Hill, C. L. *Chemical Communications* **2005**, 3138.

(300) Goodenough, J. B.; Hong, H. Y. P.; Kafalas, J. A. *Materials Research Bulletin* **1976**, *11*, 203.

(301) Wang, C.; Chalkova, E.; Lee, J. K.; Fedkin, M. V.; Komarneni, S.; Lvov, S. N. *Journal of The Electrochemical Society* **2011**, *158*, B690.

(302) Pradhan, G. K.; Swain, D.; Guru Row, T. N.; Narayana, C. *Journal of Physical Chemistry A* **2009**, *113*, 1505.

(303) Sunajadevi, K. R.; Sugunan, S. *Catalysis Letters* **2005**, *99*, 263.

(304) Sunajadevi, K. R.; Sugunan, S. *Materials Letters* **2006**, *60*, 3813.

(305) Sugunan, S.; Seena, C. R. K.; Jyothi, T. M. *React Kinet Catalysis Letters* **1999**, *67*, 49.

(306) Zheng, A.; Huang, S.-J.; Chen, W.-H.; Wu, P.-H.; Zhang, H.; Lee, H.-K.; Ménorval, L.-C. d.; Deng, F.; Liu, S.-B. *Journal of Physical Chemistry A* **2008**, *112*, 7349.

(307) Su, F.; Guo, Y. *Green Chem.* **2014**, *16*, 2934.

(308) Corma, A. *Chemical Reviews* **1995**, *95*, 559.

(309) Guo, C.; Liao, S.; Quan, Z.; Tanabe, K. *Applied Catalysis A: General* **1994**, *107*, 239.

(310) Goodenough, J. B. *Accounts of Chemical Research* **2013**, *46*, 1053.

(311) Patoux, S.; Masquelier, C. *Chemistry of Materials* **2002**, *14*, 5057.

(312) Manthiram, A.; Goodenough, J. B. *Journal of Power Sources* **1989**, *26*, 403.

(313) Manthiram, A. *The Electrochemical Society Interface* **2009**, 44.

(314) Shimanouchi-Futagami, R.; Nishimori, M.; Nishizawa, H. *Journal of Materials Science Letters* **2001**, *20*, 1881.

(315) Gromov, O. G.; Kunshina, G. B.; Kuzmin, A. P.; Kalinnikov, V. T. *Russian Journal of Applied Chemistry* **1996**, *69*, 385.

(316) Xu, X.; Yang, T.; Shui, M.; Lu, Z.; Gao, S.; Shu, J.; Zheng, W.; Cheng, L.; Feng, L.; Ren, Y. *Ceramics International* **2014**, *40*, 3819.

(317) Zhang, T.; Imanishi, N.; Hasegawa, S.; Hirano, A.; Xie, J.; Takeda, Y.; Yamamoto, O.; Sammes, N. *Journal of The Electrochemical Society* **2008**, *155*, A965.

(318) Wong, S.; J. Newman, P.; S. Best, A.; M. Nairn, K.; R. Macfarlane, D.; Forsyth, M. *Journal of Materials Chemistry* **1998**, *8*, 2199.

(319) Best, A. S.; Newman, P. J.; MacFarlane, D. R.; Nairn, K. M.; Wong, S.; Forsyth, M. *Solid State Ionics* **1999**, *126*, 191.

(320) Forsyth, M.; Wong, S.; Nairn, K. M.; Best, A. S.; Newman, P. J.; MacFarlane, D. R. *Solid State Ionics* **1999**, *124*, 213.

(321) Sukhanov, M. V.; Shchelokov, I. A.; Ermilova, M. M.; Orekhova, N. V.; Pet'kov, V. I.; Tereshchenko, G. F. *Russian Journal of Applied Chemistry* **2008**, *81*, 17.

(322) Cetinkol, M.; Wilkinson, A. P.; Lee, P. L. *Journal of Solid State Chemistry* **2009**, *182*, 1304.

(323) Cetinkol, M.; Wilkinson, A. P. *Solid State Communications* **2009**, *149*, 421.

(324) Evans, J. S. O.; Mary, T. A.; Sleight, A. W. *Journal of Solid State Chemistry* **1995**, *120*, 101.

(325) Isobe, T.; Umezome, T.; Kameshima, Y.; Nakajima, A.; Okada, K. *Materials Research Bulletin* **2009**, *44*, 2045.

(326) Evans, J. S. O.; Mary, T. A.; Sleight, A. W. *Journal of Solid State Chemistry* **1997**, *133*, 580.

(327) Blasse, G.; Piffard, Y.; Struye, L. *Chemical Physics Letters* **1988**, *147*, 514.

(328) Piffard, Y.; Verbaere, A.; Kinoshita, M. *Journal of Solid State Chemistry* **1987**, *71*, 121.

(329) Alamo, J.; Roy, R. *Journal of Solid State Chemistry* **1984**, *51*, 270.

(330) Morrison, S. R. *Electrochemistry at semiconductor and oxidized metal electrodes*; Plenum Press, 1980.

(331) Xu, Y.; Schoonen, M. A. A. *American Mineralogist* **2000**, *85*, 543.

(332) Pecharsky, V.; Zavalij, P. *Fundamentals of Powder Diffraction and Structural Characterization of Materials, Second Edition*; 2 ed.; Springer US, 2009.

(333) Coppens, P. *The structure factor*, 2006; Vol. B.

(334) Keller, J. U.; Staudt, R. *Gas adsorption equilibria: experimental methods and adsorptive isotherms*; Springer: New York, 2005.

(335) Rouquerol, J.; Rouquerol, F.; Sing, K. S. W. *Adsorption by Powders and Porous Solids : Principles, Methodology and Applications*; Academic Press: London, GB, 1998.

(336) Micromeritics *ASAP 2020 Accelerated Surface Area and Porosimetry System Operator's Manual V 4.01*, 2011.

(337) Kaszuba, M.; Corbett, J.; Watson, F. M.; Jones, A. *Philosophical Transactions of the Royal Society of London A: Mathematical, Physical and Engineering Sciences* **2010**, *368*, 4439.

(338) Yates, M. Z.; O'Neil, M. L.; Johnston, K. P. *Macromolecules* **1997**, *30*, 5060.

(339) Pencer, J.; Hallett, F. R. *Langmuir* **2003**, *19*, 7488.

(340) Malvern Instruments, *Frequently Asked Questions*. Worcestershire, UK.

(341) Akpan, U. G.; Hameed, B. H. *Applied Catalysis A: General* **2010**, *375*, 1.

(342) Inturi, S. N. R.; Boningari, T.; Suidan, M.; Smirniotis, P. G. *Applied Catalysis B: Environmental* **2014**, *144*, 333.

(343) Park, J.-Y.; Lee, K.-H.; Kim, B.-S.; Kim, C.-S.; Lee, S.-E.; Okuyama, K.; Jang, H.-D.; Kim, T.-O. *RSC Advances* **2014**, *4*, 9946.

(344) Feth, M. P.; Weber, A.; Merkle, R.; Reinöhl, U.; Bertagnolli, H. *Journal of Non-Crystalline Solids* **2002**, *298*, 43.

(345) Gao, B.; Lim, T. M.; Subagio, D. P.; Lim, T.-T. *Applied Catalysis A: General* **2010**, *375*, 107.

(346) Kokporka, L.; Onsuratoom, S.; Puangpetch, T.; Chavadej, S. *Materials Science in Semiconductor Processing* **2013**, *16*, 667.

(347) Merkle, R.; Bertagnolli, H. *Journal of Materials Chemistry* **1998**, *8*, 2433.

(348) Reidy, D. J.; Holmes, J. D.; Morris, M. A. *Journal of the European Ceramic Society* **2006**, *26*, 1527.

(349) Schiller, R.; Weiss, C.; Landfester, K. *Nanotechnology* **2010**, *21*, 405603.

(350) Wang, J.; Yu, Y.; Li, S.; Guo, L.; Wang, E.; Cao, Y. *Journal of Physical Chemistry C* **2013**, *117*, 27120.

(351) Zou, H.; Lin, Y. S. *Applied Catalysis A: General* **2004**, *265*, 35.

(352) Bhosale, R. R.; Pujari, S. R.; Muley, G. G.; Patil, S. H.; Patil, K. R.; Shaikh, M. F.; Gambhire, A. B. *Solar Energy* **2014**, *103*, 473.

(353) Bineesh, K. V.; Kim, D.-K.; Park, D.-W. *Nanoscale* **2010**, *2*, 1222.

(354) Fresno, F.; Hernández-Alonso, M. D.; Tudela, D.; Coronado, J. M.; Soria, J. *Applied Catalysis B: Environmental* **2008**, *84*, 598.

(355) Gnatyuk, Y.; Smirnova, N.; Korduban, O.; Eremenko, A. *Surface and Interface Analysis* **2009**, *42*, 1276.

(356) Goswami, P.; Ganguli, J. N. *Dalton Transactions* **2013**, *42*, 14480.

(357) Huang, B.; Liu, M.; Zhang, Y.; Li, P.; Zheng, Z. *Ionics* **2013**, *19*, 681.

(358) Venkatachalam, N.; Palanichamy, M.; Arabindoo, B.; Murugesan, V. *Journal of Molecular Catalysis A: Chemical* **2007**, *266*, 158.

(359) Gnatyuk, Y.; Smirnova, N.; Korduban, O.; Eremenko, A. *Surface and Interface Analysis* **2010**, *42*, 1276.

(360) Bineesh, K. V.; Kim, D. K.; Park, D. W. *Nanoscale* **2010**, *2*, 1222.

(361) Fan, M.; Hu, S.; Ren, B.; Wang, J.; Jing, X. *Powder Technology* **2013**, *235*, 27.

(362) Hernández-Alonso, M. D.; Coronado, J. M.; Bachiller-Baeza, B.; Fernández-García, M.; Soria, J. *Chemistry of Materials* **2007**, *19*, 4283.

(363) Huang, Q.; Ma, W.; Yan, X.; Chen, Y.; Zhu, S.; Shen, S. *Journal of Molecular Catalysis A: Chemical* **2013**, *366*, 261.

(364) Manríquez, M. E.; López, T.; Gómez, R.; Navarrete, J. *Journal of Molecular Catalysis A: Chemical* **2004**, *220*, 229.

(365) Pérez-Hernández, R.; Mendoza-Anaya, D.; Fernández, M. E.; Gómez-Cortés, A. *Journal of Molecular Catalysis A: Chemical* **2008**, *281*, 200.

(366) Shang, Y.-L.; Huo, L.; Jia, Y.-L.; Liao, F.-H.; Li, J.-R.; Li, M.-X.; Zhang, S.-H. *Colloids and Surfaces A: Physicochemical and Engineering Aspects* **2008**, *325*, 160.

(367) Vishwanathan, V.; Roh, H.-S.; Kim, J.-W.; Jun, K.-W. *Catalysis Letters* **2004**, *96*, 23.

(368) Yu, J. C.; Lin, J.; Kwok, R. W. M. *Journal of Physical Chemistry B* **1998**, *102*, 5094.

(369) Livage, J.; Henry, M.; Sanchez, C. *Progress in Solid State Chemistry* **1988**, *18*, 259.

(370) Halsey, G. *The Journal of Chemical Physics* **1948**, *16*, 931.

(371) Randles, J. E. B. *Discussions of the Faraday Society* **1947**, *1*, 11.

(372) Brug, G. J.; van den Eeden, A. L. G.; Sluyters-Rehbach, M.; Sluyters, J. H. *Journal of Electroanalytical Chemistry and Interfacial Electrochemistry* **1984**, *176*, 275.

(373) Chong, M. N.; Vimonses, V.; Lei, S.; Jin, B.; Chow, C.; Saint, C. *Microporous and Mesoporous Materials* **2009**, *117*, 233.

(374) Chong, M. N.; Jin, B. *Synthesis and Reactivity in Inorganic, Metal-Organic, and Nano-Metal Chemistry* **2012**, *42*, 68.

(375) Vimonses, V.; Chong, M. N.; Jin, B. *Microporous and Mesoporous Materials* **2010**, *132*, 201.

(376) Suh, D. J.; Park, T.-J. *Chemistry of Materials* **1996**, *8*, 509.

(377) Leventis, N.; Chandrasekaran, N.; Sadekar, A. G.; Mulik, S.; Sotiriou-Leventis, C. *Journal of Materials Chemistry* **2010**, *20*, 7456.

(378) Durairaj, R. B. In *Resorcinol: Chemistry, Technology and Applications*; Springer Berlin Heidelberg: Berlin, Heidelberg, 2005, p 179.

(379) Mulik, S.; Sotiriou-Leventis, C.; Leventis, N. *Chemistry of Materials* **2007**, *19*, 6138.

(380) Kapusuz, D.; Park, J.; Ozturk, A. *Journal of Physics and Chemistry of Solids* **2013**, *74*, 1026.

(381) Lucky, R. A.; Medina-Gonzalez, Y.; Charpentier, P. A. *Langmuir* **2010**, *26*, 19014.

(382) Onsuratoom, S.; Chavadej, S.; Sreethawong, T. *International Journal of Hydrogen Energy* **2011**, *36*, 5246.

(383) Shang, Y.-L.; Jia, Y.-L.; Liao, F.-H.; Li, J.-R.; Li, M.-X.; Wang, J.; Zhang, S.-H. *Journal of Materials Science* **2007**, *42*, 2586.

(384) Venkatachalam, N.; Palanichamy, M.; Murugesan, V. *Journal of Molecular Catalysis A: Chemical* **2007**, *273*, 177.

(385) Holbig, E. S., Universität Bayreuth, 2008.

(386) Lejon, C.; Österlund, L. *Journal of Raman Spectroscopy* **2011**, *42*, 2026.

(387) Liu, S. W.; Song, C. F.; Lü, M. K.; Wang, S. F.; Sun, D. L.; Qi, Y. X.; Xu, D.; Yuan, D. R. *Catalysis Communications* **2003**, *4*, 343.

(388) Naumenko, A.; Gnatiuk, I.; Smirnova, N.; Eremenko, A. *Thin Solid Films* **2012**, *520*, 4541.

(389) Zhang, M.; Gu, X.; Lv, K.; Dong, W.; Ruan, S.; Chen, Y.; Zhang, H. *Applied Surface Science* **2013**, *268*, 312.

(390) Zhu, L. Y.; Yu, G.; Wang, X. Q.; Xu, D. *Journal of Non-Crystalline Solids* **2009**, *355*, 68.

(391) Troitzsch, U.; Ellis, D. *Journal of Materials Science* **2005**, *40*, 4571.

(392) Alothman, Z. *Materials* **2012**, *5*, 2874.

(393) Grosman, A.; Ortega, C. *Langmuir* **2008**, *24*, 3977.

(394) Mattsson, A.; Leideborg, M.; Persson, L.; Westin, G.; Österlund, L. *Journal of Physical Chemistry C* **2009**, *113*, 3810.

(395) Shannon, R. *Acta Crystallographica Section A* **1976**, *32*, 751.

(396) Hoffmann, M. R.; Martin, S. T.; Choi, W.; Bahnemann, D. W. *Chemical Reviews* **1995**, *95*, 69.

(397) Reyes-Coronado, D.; Rodríguez-Gattorno, G.; Espinosa-Pesqueira, M. E.; Cab, C.; de Cross, R.; Oskam, G. *Nanotechnology* **2008**, *19*, 145605.

(398) Li, Y.; Xiang, Y.; Peng, S.; Wang, X.; Zhou, L. *Electrochimica Acta* **2013**, *87*, 794.

(399) Yin, W.-J.; Tang, H.; Wei, S.-H.; Al-Jassim, M. M.; Turner, J.; Yan, Y. *Physical Review B* **2010**, *82*.

(400) Nozik, A. J. *Annual Review of Physical Chemistry* **1978**, *29*, 189.

(401) Butler, M. A.; Ginley, D. S. *Journal of The Electrochemical Society* **1978**, *125*, 228.

(402) Gerischer, H. *Electrochimica Acta* **1989**, *34*, 1005.

(403) Matsumoto, Y.; Yoshikawa, T.; Sato, E. i. *Journal of The Electrochemical Society* **1989**, *136*, 1389.

(404) Butler, M. A.; Ginley, D. S. *Chemical Physics Letters* **1977**, *47*, 319.

(405) Oosawa, Y.; Takahashi, R.; Yonemura, M.; Sekine, T.; Goto, Y. *New Journal of Chemistry* **1989**, *13*, 435.

(406) Fabregat-Santiago, F.; Garcia-Belmonte, G.; Bisquert, J.; Bogdanoff, P.; Zaban, A. *Journal of The Electrochemical Society* **2003**, *150*, E293.

(407) Poole, R. T.; Williams, D. R.; Riley, J. D.; Jenkin, J. G.; Liesegang, J.; Leckey, R. C. G. *Chemical Physics Letters* **1975**, *36*, 401.

(408) Castelli, I.; Olsen, T.; Datta, S.; Landis, D.; Dahl, S.; Thygesen, K. S.; Jacobsen, K. W. *Energy & Environmental Science* **2012**, *5*, 5814.

(409) Stevanovic, V.; Lany, S.; Ginley, D. S.; Tumas, W.; Zunger, A. *Physical Chemistry Chemical Physics* **2014**, *16*, 3706.

(410) El Halouani, F.; Deschanvres, A. *Materials Research Bulletin* **1982**, *17*, 1045.

(411) Kung, H. H.; Jarrett, H. S.; Sleight, A. W.; Ferretti, A. *Journal of Applied Physics* **1977**, *48*, 2463.

(412) Lee, M.-S.; Cheon, I.-C.; Kim, Y.-I. *Bulletin of the Korean Chemical Society* **2003**, *24*, 1155.

(413) Möllers, F.; Tolle, H. J.; Memming, R. *Journal of The Electrochemical Society* **1974**, *121*, 1160.

(414) Oosawa *New Journal of Chemistry* **1989**, *13*, 435.

(415) van de Krol, R.; Goossens, A.; Schoonman, J. *Journal of The Electrochemical Society* **1997**, *144*, 1723.

(416) Taylor, M. A.; Alonso, R. E.; Errico, L. A.; López-García, A.; de la Presa, P.; Svane, A.; Christensen, N. E. *Physical Review B* **2012**, *85*, 155202.

(417) Winterer, M.; Delaplane, R.; McGreevy, R. *Journal of Applied Crystallography* **2002**, *35*, 434.

(418) Ballirano, P.; Caminiti, R. *Journal of Applied Crystallography* **2001**, *34*, 757.

(419) Howard, C. J.; Sabine, T. M.; Dickson, F. *Acta Crystallographica Section B-structural Science* **1991**, *47*, 462.

(420) Leinekugel-le-Cocq-Errien, A. Y.; Deniard, P.; Jobic, S.; Gautier, E.; Evain, M.; Aubin, V.; Bart, F. *Journal of Solid State Chemistry* **2007**, *180*, 322.

(421) Hughbanks, T. *Journal of the American Chemical Society* **1985**, *107*, 6851.

(422) Ghicov, A.; Schmuki, P. *Chemical Communications* **2009**, 2791.

(423) Sreethawong, T.; Yoshikawa, S. *Materials Research Bulletin* **2012**, *47*, 1385.

(424) Masařík, M.; Stobiecka, A.; Kizek, R.; Jelen, F.; Pechan, Z.; Hoyer, W.; Jovin, T. M.; Subramaniam, V.; Paleček, E. *Electroanalysis* **2004**, *16*, 1172.

(425) Tong, J.; Anderson, J. L. *Biophysical journal* **1996**, *70*, 1505.

(426) Stone, M. C.; Carta, G. *Journal of Chromatography A* **2007**, *1160*, 206.

(427) Lévesque, S. G.; Lim, R. M.; Shoichet, M. S. *Biomaterials* **2005**, *26*, 7436.

(428) Serrano, D. P.; Escola, J. M.; Pizarro, P. *Chemical Society Reviews* **2013**, *42*, 4004.

(429) Yuan, Z.-Y.; Su, B.-L. *Journal of Materials Chemistry* **2006**, *16*, 663.

(430) Smått, J.-H.; Sayler, F. M.; Grano, A. J.; Bakker, M. G. *Advanced Engineering Materials* **2012**, *14*, 1059.

(431) Smått, J.-H.; Weidenthaler, C.; Rosenholm, J. B.; Lindén, M. *Chemistry of Materials* **2006**, *18*, 1443.

(432) Davis, M.; Ramirez, D. A.; Hope-Weeks, L. J. *ACS Applied Materials & Interfaces* **2013**, *5*, 7786.

(433) Skaug, M. J.; Schwartz, D. K. *Industrial & Engineering Chemistry Research* **2015**, *54*, 4414.

(434) Zurner, A.; Kirstein, J.; Doblinger, M.; Brauchle, C.; Bein, T. *Nature* **2007**, *450*, 705.

(435) Kirstein, J.; Platschek, B.; Jung, C.; Brown, R.; Bein, T.; Brauchle, C. *Nature Materials* **2007**, *6*, 303.

(436) Liao, Y.; Yang, S. K.; Koh, K.; Matzger, A. J.; Biteen, J. S. *Nano Letters* **2012**, *12*, 3080.

(437) Dhakal, S.; Adendorff, M. R.; Liu, M.; Yan, H.; Bathe, M.; Walter, N. G. *Nanoscale* **2016**, *8*, 3125.

(438) Liu, M.; Fu, J.; Hejesen, C.; Yang, Y.; Woodbury, N. W.; Gothelf, K.; Liu, Y.; Yan, H. *Nature Communications* **2013**, *4*.

(439) Pitchiaya, S.; Krishnan, V.; Custer, T. C.; Walter, N. G. *Methods* **2013**, *63*, 188.

(440) Sonnleitner, A.; Schütz, G. J.; Schmidt, T. *Biophysical journal* **1999**, *77*, 2638.

(441) Kusumi, A.; Sako, Y.; Yamamoto, M. *Biophysical journal* **1993**, *65*, 2021.

(442) Lommerse, P. H. M.; Blab, G. A.; Cognet, L.; Harms, G. S.; Snaar-Jagalska, B. E.; Spaink, H. P.; Schmidt, T. *Biophysical journal* **2004**, *86*, 609.

(443) Blanco, M.; Walter, N. G. In *Methods in Enzymology*; Nils, G. W., Ed.; Academic Press: 2010; Vol. 472, p 153.

(444) Han, B.; Li, C.; Zhang, C.; Li, C. *Advanced Materials Research* **2014**, *989-994*, 629.

(445) Xiliang, C.; Peng, C.; Yanpei, J. *Applied Mechanics and Materials* **2013**, *333-335*, 1872.

(446) Wang, Y.; Brezesinski, T.; Antonietti, M.; Smarsly, B. *ACS Nano* **2009**, *3*, 1373.

(447) Puyane, R.; Kato, I. *Proceedings of SPIE, the International Society for Optical Engineering* **1983** *401*, 190.

(448) Mayagoitia, V. In *Studies in Surface Science and Catalysis*; F. Rodriguez-Reinoso, J. R. K. S. W. S., Unger, K. K., Eds.; Elsevier: 1991; Vol. Volume 62, p 51.

(449) Aguzzi, A.; O'Connor, T. *Nature Reviews Drug Discovery* **2010**, *9*, 237.

(450) Siddhanta, S.; Barman, I.; Narayana, C. *Soft Matter* **2015**, *11*, 7241.

(451) Pitchiaya, S.; Androsavich, J. R.; Walter, N. G. *EMBO Reports* **2012**, *13*, 709.

(452) Lommerse, P. H. M.; Blab, G. A.; Cognet, L.; Harms, G. S.; Snaar-Jagalska, B. E.; Spaink, H. P.; Schmidt, T. *Biophysical Journal*, **2004**, *86*, 609.

(453) Sarapulova, A. E.; Bazarov, B.; Namsaraeva, T.; Dorzhieva, S.; Bazarova, J.; Grossman, V.; Bush, A. A.; Antonyshyn, I.; Schmidt, M.; Bell, A. M. T.; Knapp, M.; Ehrenberg, H.; Eckert, J.; Mikhailova, D. *Journal of Physical Chemistry C* **2014**, *118*, 1763.

(454) He, Y.; Quan, B.; Wang, Y.; Cheng, C.; Wang, B. *Materials Letters* **2007**, *61*, 4519.

(455) Zhong, T.; Zhao, W.; Jiang, F.; Liang, X. *Sensors and Actuators B: Chemical* **2014**, *202*, 1103.

(456) Zhu, Y.; Shimizu, T.; Kitajima, T.; Morisato, K.; Moitra, N.; Brun, N.; Kiyomura, T.; Kanamori, K.; Takeda, K.; Kurata, H.; Tafu, M.; Nakanishi, K. *New Journal of Chemistry* **2015**, *39*, 2444.

(457) Ding, F.; Xu, W.; Shao, Y.; Chen, X.; Wang, Z.; Gao, F.; Liu, X.; Zhang, J.-G. *Journal of Power Sources* **2012**, *214*, 292.

(458) Palla, S.; Ravi, G.; Reddy, J. R.; Veldurthi, N.; Velchuri, R.; Prasad, G.; Munirathnam, N. R.; Vithal, M. *Journal of Sol-Gel Science and Technology* **2013**, *67*, 507.

(459) Shimanouchi-Futagami, R.; Nishimori, M.; Nishizawa, H. *Journal of Materials Science Letters* **2000**, *19*, 405.

(460) Stenina, I. A.; Kislitsyn, M. N.; Ghuravlev, N. A.; Yaroslavtsev, A. B. *Materials Research Bulletin* **2008**, *43*, 377.

(461) Ono, A. *Journal of Materials Science* **1984**, *19*, 2691.

(462) Ono, A. *Journal of Solid State Chemistry* **1985**, *56*, 260.

(463) Schwarzenbach, G.; Muehlebach, J.; Mueller, K. *Inorganic Chemistry* **1970**, *9*, 2381.

(464) Jere, G. V.; Patel, C. C. *Canadian Journal of Chemistry* **1962**, *40*, 1576.

(465) O'Sullivan, D. W.; Tyree, M. *International Journal of Chemical Kinetics* **2007**, *39*, 457.

(466) Cory, D. G.; Ritchey, W. M. *Journal of Magnetic Resonance (1969)* **1988**, *80*, 128.

(467) Patel, C. C.; Mohan, M. S. *Nature* **1960**, *186*, 803.

(468) Szilagyi, I.; Konigsberger, E.; May, P. M. *Dalton Transactions* **2009**, 7717.

(469) Wang, W.; Liu, Y.; Xue, T.; Li, J.; Chen, D.; Qi, T. *Chemical Engineering Science* **2015**, *134*, 196.

(470) Gerasimova, L. G.; Maslova, M. V. *Russian Journal of Inorganic Chemistry* **2012**, *57*, 313.

(471) Grzmil, B. U.; Grela, D.; Kic, B. *Chemical Papers* **2008**, *62*, 18.

(472) Ge, L.; Xu, M.; Sun, M.; Fang, H. *Journal of Sol-Gel Science and Technology* **2006**, *38*, 47.

(473) Ge, L.; Xu, M. X.; Sun, M. *Materials Letters* **2006**, *60*, 287.

(474) Byrappa, K.; Jain, A. *Journal of Materials Science Letters* **1994**, *13*, 1430.

(475) Naka, S.; Tanaka, K.; Suwa, Y.; Takeda, Y. *Journal of Inorganic and Nuclear Chemistry* **1977**, *39*, 1240.

(476) Pikl, R.; de Waal, D.; Aatiq, A.; El Jazouli, A. *Materials Research Bulletin* **1998**, *33*, 955.

(477) Ling, Z. C.; Wang, A. *Icarus* **2010**, *209*, 422.

(478) Barj, M.; Lucazeau, G.; Delmas, C. *Journal of Solid State Chemistry* **1992**, *100*, 141.

(479) Francisco, B. E.; Stoldt, C. R.; M’Peko, J.-C. *Chemistry of Materials* **2014**, *26*, 4741.

(480) Venkateswara Rao, A.; Veeraiah, V.; Prasada Rao, A. V.; Kishore Babu, B.; Kumar, K. V. *Ceramics International* **2014**, *40*, 13911.

(481) Groen, J. C.; Pérez-Ramírez, J. *Applied Catalysis A: General* **2004**, *268*, 121.

(482) Mafra, L.; Almeida Paz, F. A.; Rocha, J.; Espina, A.; Khainakov, S. A.; García, J. R.; Fernandez, C. *Chemistry of Materials* **2005**, *17*, 6287.

(483) Mafra, L.; Rocha, J.; Fernandez, C.; Castro, G. R.; García-Granda, S.; Espina, A.; Khainakov, S. A.; García, J. R. *Chemistry of Materials* **2008**, *20*, 3944.

(484) Crocker, M.; Herold, R. H. M.; Wilson, A. E.; Mackay, M.; Emeis, C. A.; Hoogendoorn, A. M. *Journal of the Chemical Society, Faraday Transactions* **1996**, *92*, 2791.

(485) Blanchard, J. W.; Groy, T. L.; Yarger, J. L.; Holland, G. P. *Journal of Physical Chemistry C* **2012**, *116*, 18824.

(486) American Chemistry Council, Inc. https://www.formaldehydefacts.org/applications/common_uses (Accessed Aug. 8, 2016)

(487) Brookes, C.; Bowker, M.; Wells, P. *Catalysts* **2016**, *6*, 92.

(488) Global Industry Analysts, Inc. http://www.prweb.com/releases/acetaldehyde/acetic_ether_pyridine/prweb8070299.htm (Accessed Aug. 8, 2016)

(489) Soares, A. P. V.; Portela, M. F.; Kiennemann, A. *Catalysis Reviews* **2005**, *47*, 125.

(490) Waterhouse, G. I. N.; Bowmaker, G. A.; Metson, J. B. *Applied Catalysis A: General* **2004**, *265*, 85.

(491) Srihari, V.; Viswanath, D. S. *Journal of Chemical Technology and Biotechnology* **1982**, *32*, 868.

(492) Gatt, J. E.; Nair, H.; Baertsch, C. D. *Applied Catalysis B: Environmental* **2010**, *99*, 127.

(493) Li, Z.; Xu, J.; Gu, X.; Wang, K.; Wang, W.; Zhang, X.; Zhang, Z.; Ding, Y. *ChemCatChem* **2013**, *5*, 1705.

(494) Happel, J.; Chao, J. C.; Mezaki, R. *Journal of Chemical & Engineering Data* **1974**, *19*, 110.

(495) Sun, J.; Wang, Y. *ACS Catalysis* **2014**, *4*, 1078.

(496) Brookes, C.; Wells, P. P.; Cibin, G.; Dimitratos, N.; Jones, W.; Morgan, D. J.; Bowker, M. *ACS Catalysis* **2014**, *4*, 243.

(497) Brookes, C.; Wells, P. P.; Dimitratos, N.; Jones, W.; Gibson, E. K.; Morgan, D. J.; Cibin, G.; Nicklin, C.; Mora-Fonz, D.; Scanlon, D. O.; Catlow, C. R. A.; Bowker, M. *Journal of Physical Chemistry C* **2014**, *118*, 26155.

(498) House, M. P.; Carley, A. F.; Bowker, M. *Journal of Catalysis* **2007**, *252*, 88.

(499) Ruf, S.; May, A.; Emig, G. *Applied Catalysis A: General* **2001**, *213*, 203.

(500) Usachev, N. Y.; Krukovskii, I. M.; Kanaev, S. A. *Petroleum Chemistry* **2004**, *44*, 379.

(501) El-Molla, S. A.; Mahmoud, H. R. *Materials Research Bulletin* **2013**, *48*, 4105.

(502) Takagi, K.; Morikawa, Y.; Ikawa, T. *Chemistry Letters* **1985**, *14*, 527.

(503) Musˇicˇ, A.; Batista, J.; Levec, J. *Applied Catalysis A: General* **1997**, *165*, 115.

(504) Ilolov, A. M.; Tret'yakov, V. F.; Talyshinskii, R. M.; Lermontov, A. S. *Petroleum Chemistry* **2009**, *49*, 127.

(505) Wiesgickl, G.; Beck, H. P.; Emig, G. *Applied Catalysis* **1990**, *59*, L1.

(506) Yamamoto, T.; Shimoda, A.; Okuhara, T.; Misono, M. *Chemistry Letters* **1988**, *17*, 273.

(507) Su, S.; Prairie, M. R.; Renken, A. *Applied Catalysis A: General* **1992**, *91*, 131.

(508) Ren, L.-P.; Dai, W.-L.; Yang, X.-L.; Cao, Y.; Li, H.; Fan, K.-N. *Applied Catalysis A: General* **2004**, *273*, 83.

(509) Cao, Y.; Dai, W.-L.; Deng, J.-F. *Materials Letters* **2001**, *50*, 12.

(510) Ren, L.-P.; Dai, W.-L.; Cao, Y.; Li, H.; Fan, K. *Chemical Communications* **2003**, 3030.

(511) Dong, Y.; Dai, W.-L.; Li, J.-L.; Deng, J.-F. *Chemistry Letters* **2001**, *30*, 534.

(512) Wang, Q. N.; Shi, L.; Lu, A. H. *ChemCatChem* **2015**, *7*, 2846.

(513) Takei, T.; Iguchi, N.; Haruta, M. *New Journal of Chemistry* **2011**, *35*, 2227.

(514) Liu, P.; Zhu, X.; Yang, S.; Li, T.; Hensen, E. J. M. *Journal of Catalysis* **2015**, *331*, 138.

(515) Prasad, R. *Materials Letters* **2005**, *59*, 3945.

(516) Mieritz, D.; Davidowski, S. K.; Seo, D.-K. *Journal of Solid State Chemistry*.

(517) Liu, D.; Yuan, P.; Liu, H.; Cai, J.; Tan, D.; He, H.; Zhu, J.; Chen, T. *Applied Clay Science* **2013**, *80–81*, 407.

(518) Zhao, H.; Jiang, P.; Dong, Y.; Huang, M.; Liu, B. *New Journal of Chemistry* **2014**, *38*, 4541.

(519) Su, S.; Zaza, P.; Renken, A. *Chemical Engineering Technology* **1994**, *17*, 34.

(520) Hattori, H.; Ono, Y. *Solid acid catalysis : from fundamentals to applications*; Pan Stanford Publishing: Singapore, 2015.

(521) Yaripour, F.; Baghaei, F.; Schmidt, I.; Perregaard, J. *Catalysis Communications* **2005**, *6*, 542.

(522) Barthos, R.; Lónyi, F.; Onyestyák, G.; Valyon, J. *Journal of Physical Chemistry B* **2000**, *104*, 7311.

(523) Said, A. E.-A. A.; Abd El-Wahab, M. M.; El-Aal, M. A. *Journal of Molecular Catalysis A: Chemical* **2014**, *394*, 40.

(524) Sobczak, I.; Kozlowska, M.; Ziolek, M. *Journal of Molecular Catalysis A: Chemical* **2014**, *390*, 114.

(525) Kon, K.; Hakim Siddiki, S. M. A.; Shimizu, K.-i. *Journal of Catalysis* **2013**, *304*, 63.

(526) Bowker, M. *Topics in Catalysis* **2015**, *58*, 606.

(527) Florek-Milewska, J.; Decyk, P.; Ziolek, M. *Applied Catalysis A: General* **2011**, *393*, 215.

(528) Livage, J.; Barboux, P.; Vandenborre, M. T.; Schmutz, C.; Taulelle, F. *Journal of Non-Crystalline Solids* **1992**, *147–148*, 18.

(529) Takahara, I.; Saito, M.; Inaba, M.; Murata, K. *Catalysis Letters* **2005**, *105*, 249.

(530) Il'in, A. B.; Ermilova, M. M.; Orekhova, N. V.; Yaroslavtsev, A. B. *Inorganic Materials* **2015**, *51*, 711.

(531) Krogh Andersen, A. M.; Norby, P. *Inorganic Chemistry* **1998**, *37*, 4313.

(532) Helluy, X.; Marichal, C.; Sebald, A. *Journal of Physical Chemistry B* **2000**, *104*, 2836.

(533) F. Reinauer, R. G., R. Gruehn *European Journal of Solid State and Inorganic Chenistry* **1994**, *31*, 779.

(534) Alberti, G.; Constantino, U.; Luciani Giovagnotti, M. L. *Journal of Inorganic and Nuclear Chemistry* **1979**, *41*, 643.

(535) Yin, Z.; Sakamoto, Y.; Yu, J.; Sun, S.; Terasaki, O.; Xu, R. *Journal of the American Chemical Society* **2004**, *126*, 8882.

(536) Etsuro, K. *Bulletin of the Chemical Society of Japan* **1975**, *48*, 3114.

(537) Christensen, A. N.; Andersen, E. K.; Andersen, I. G. K.; Alberti, G.; Nielsen, M.; Lehmann, M. S. *Acta Chemica Scandinavica* **1990**, *44*, 865.

(538) Guo, S.-y.; Han, S.; Chi, B.; Pu, J.; Li, J. *International Journal of Hydrogen Energy* **2014**, *39*, 2446.

(539) Espina, A.; García, J. R.; Guil, J. M.; Jaimez, E.; Parra, J. B.; Rodríguez, J. *Journal of Physical Chemistry B* **1998**, *102*, 1713.

(540) Allulli, S.; Ferragina, C.; La Ginestra, A.; Massucci, M. A.; Tomassini, N. *Journal of Inorganic and Nuclear Chemistry* **1977**, *39*, 1043.

(541) Tegehall, P.-E. *Acta Chemica Scandinavica* **1989**, *43*, 322.

(542) La Ginestra, A.; Ferragina, C.; Patrono, P. *Materials Research Bulletin* **1979**, *14*, 1099.

(543) Li, Y. J.; Whittingham, M. S. *Solid State Ionics* **1993**, *63–65*, 391.

(544) Maheria, K. C.; Chudasama, U. V. *Industrial & Engineering Chemistry Research* **2007**, *46*, 6852.

(545) Bereznitski, Y.; Jaroniec, M.; Bortun, A. I.; Poojary, D. M.; Clearfield, A. *Journal of Colloid and Interface Science* **1997**, *191*, 442.

(546) Poojary, D. M.; Bortun, A. I.; Bortun, L. N.; Clearfield, A. *Journal of Solid State Chemistry* **1997**, *132*, 213.

(547) Benmokhtar, S.; El jazouli, A.; Chaminade, J. P.; Gravereau, P.; Ménétrier, M.; Bourée, F. *Journal of Solid State Chemistry* **2007**, *180*, 2713.

(548) Bortun, A. I.; Khainakov, S. A.; Bortun, L. N.; Poojary, D. M.; Rodriguez, J.; Garcia, J. R.; Clearfield, A. *Chemistry of Materials* **1997**, *9*, 1805.

(549) Bhaumik, A.; Inagaki, S. *Journal of the American Chemical Society* **2001**, *123*, 691.

(550) Wang, R.; Ye, J.; Rauf, A.; Wu, X.; Liu, H.; Ning, G.; Jiang, H. *Journal of Hazardous Materials* **2016**, *315*, 76.

(551) Zepp, R. G.; Faust, B. C.; Hoigne, J. *Environmental Science & Technology* **1992**, *26*, 313.

(552) Oleksak, R. P.; Ruther, R. E.; Luo, F.; Fairley, K. C.; Decker, S. R.; Stickle, W. F.; Johnson, D. W.; Garfunkel, E. L.; Herman, G. S.; Keszler, D. A. *ACS Applied Materials & Interfaces* **2014**, *6*, 2917.

(553) Anderson, J. T.; Munsee, C. L.; Hung, C. M.; Phung, T. M.; Herman, G. S.; Johnson, D. C.; Wager, J. F.; Keszler, D. A. *Advanced Functional Materials* **2007**, *17*, 2117.

(554) Son, J.-H.; Park, D.-H.; Keszler, D. A.; Casey, W. H. *Chemistry – A European Journal* **2015**, *21*, 6727.

(555) Mal, S. S.; Nsouli, N. H.; Carraro, M.; Sartorel, A.; Scorrano, G.; Oelrich, H.; Walder, L.; Bonchio, M.; Kortz, U. *Inorganic Chemistry* **2010**, *49*, 7.

(556) Goberna-Ferrón, S.; Park, D.-H.; Amador, J. M.; Keszler, D. A.; Nyman, M. *Angewandte Chemie International Edition* **2016**, *55*, 6221.

(557) Lide, D. R. E. *CRC Handbook of Chemistry and Physics*; 88th ed.; CRC Press:: Boca Raton, FL, 2007.

APPENDIX A

ELECTRONEGATIVITY (χ) AND OPTICAL ENERGY GAP (E_g, eV) VALUES USED IN THE SCISSOR RELATIONSHIP TO PREDICT THE CONDUCTION BAND ENERGIES (E_{CB}), AND THE MEASURED FLAT BAND ENERGIES (U_{fb}), COMBINED WITH THE POINT OF ZERO ZETA POTNEITIAL (PZZP) AND pH DURING THE MEASUREMENT (pH_{Meas}), USED TO OBTAIN THE CORRECTED FLAT BAND ENERGY (U_{fb}^0).

Compound	χ[a]405	E_g	E_{CB}	U_{fb}	PZZP	pH_{Meas}	U_{fb}^0	Ref.
TiO_2, anatase	5.812	3.19	-4.22	−4.26	5.45	5.05	−4.24	this study
$Zr_{0.1}Ti_{0.9}O_2$	5.816	3.24	-4.20	−4.10	5.45	5.05	−4.08	this study
$Zr_{0.2}Ti_{0.8}O_2$	5.820	3.29	-4.18	−4.03	5.58	5.05	−4.00	this study
TiO_2, anatase	5.812	3.32	-4.15	−4.30	5.80	0.00	−3.96	405
TiO_2, anatase	5.812	3.40	-4.11	−4.42	5.45[b]	3.00	−4.28	412
TiO_2, anatase	5.812	3.40	-4.11	−4.27	5.45[b]	6.00	−4.30	412
TiO_2, anatase	5.812	3.40	-4.11	−4.07	5.45[b]	11.00	−4.40	412
TiO_2, anatase	5.812	3.20	-4.21	−3.82	5.80	7.00	−3.89	376
TiO_2, anatase	5.812	3.20	-4.21	−3.77	5.80	13.70	−4.24	415
TiO_2, anatase	5.812	3.20	-4.21	−4.45	5.80	1.00	−4.17	413
TiO_2, anatase	5.812	3.20[b]	-4.21	−4.42	5.45[b]	7.00	−4.51	163
$Zr_{0.05}Ti_{0.95}O_2$	5.814	3.23[c]	-4.20	−4.31	5.45[b]	7.00	−4.40	163
ZrO_2	5.854	5.00	-3.35	−2.71	6.70	13.30	−3.10	401
ZrO_2	5.854	5.00	-3.35	−2.75	6.70	13.30	−3.14	400
Bi_2O_3	5.917	2.80	-4.52	−5.20	6.20	0.00	−4.83	410
CdO	5.823	2.20	-4.72	−4.55	11.60	13.30	−4.65	400
CuO	5.812	1.70	-4.96	−5.05	9.50	7.00	−4.90	400
Fe_2O_3	5.867	2.20	-4.77	−4.65	8.60	9.00	−4.67	400
Nb_2O_5	6.211	3.40	-4.51	−3.72	6.06	13.30	−4.14	411
PbO	5.416	2.80	-4.02	−4.96	8.29	0.00	−4.47	410
SnO_2	6.217	3.50	-4.47	−4.82	4.30	0.00	−4.57	410
Ta_2O_5	6.262	4.00	-4.26	−3.31	2.90	13.30	−3.93	401
TiO_2, rutile	5.812	3.00	-4.31	−3.75	5.80	13.00	−4.18	400
TiO_2, rutile	5.812	3.05	-4.29	−4.50	5.80	0.00	−4.16	405
TiO_2, rutile	5.812	3.00	-4.31	−3.88	5.80	7.00	−3.95	376
V_2O_5	6.121	2.80	-4.72	−5.55	6.54	7.00	−5.58	400
WO_3	6.567	2.70	-5.22	−4.55	0.43	13.30	−5.31	401
ZnO	5.951	3.20	-4.35	−4.91	8.80	0.00	−4.39	410
$BaTiO_3$	5.244	3.30	-3.59	−3.95	9.00	13.60	−4.22	400
$CdFe_2O_4$	5.854	2.30	-4.70	−4.55	7.22	13.30	−4.91	400
$FeTiO_3$	5.689	2.80	-4.29	−3.66	6.30	13.30	−4.07	401
$Hg_2Nb_2O_7$	6.233	1.80	-5.33	−4.82	6.25	13.30	−5.24	411

$KTaO_3$	5.275	3.50	-3.52	−3.52	8.55	13.30	−3.80	[411]
$PbFe_{12}O_{19}$	5.837	2.30	-4.69	−5.75	7.17	13.30	−6.11	[404]
$SrTiO_3$	5.317	3.40	-3.62	−3.35	8.60	13.00	−3.61	[404]

[a] All values calculated by the geometric mean of Mulliken electronegativity. Ionization and electron affinity energies taken from ref. 557.

[b] Measured in this study

[c] Extrapolated from values measured in this study